UNIVERSITY OF SOUTHAMPTON
Faculty of Engineering, Science and Mathematics
School of Engineering Sciences

Damage and Stress Analysis on Pipework using Thermoelastic Stress Analysis

by

Nuttaphon Sathon

Thesis for the degree of Doctor of Philosophy

June 2006

UNIVERSITY OF SOUTHAMPTON

ABSTRACT

FACULTY OF ENGINEERING, SCIENCE AND MATHEMATICS
SCHOOL OF ENGINEERING SCIENCES

Doctor of Philosophy

Damage and Stress Analysis on Pipework using Thermoelastic Stress Analysis

by Nuttaphon Sathon

Pipework plays many important roles in various engineering applications. In a real component, inherent damage such as imperfections of materials and damage from the manufacturing process are not unusual. These small imperfections or damage can grow and become cracks which lead to structure failure particularly when the structure is subjected to fatigue load.

In Linear Elastic Fracture Mechanics (LEFM), the Stress Intensity Factor (SIF) is used to assess the damage severity of the crack-like flaws on a component which requires knowledge of the flaw shape, dimensions, component geometries as well as the stress states surrounding the cracks. It is demanding to calculate the SIF in real components as the crack often occurs in a complex stress field and the geometry of the component is often complex.

In this thesis, a technique that uses the non-adiabatic thermoelastic response from a standard Thermoelastic Stress Analysis (TSA) system to evaluate the severity of the damage is proposed. The theoretical basis of the new approach is described. A procedure for finite element simulation of TSA incorporating non-adiabatic behaviour is also developed to be used as a basis to understand the behaviour of the non-adiabatic response around the sub-surface damage. Both TSA and FEA are used to examined severity of the sub-surface flaws in details. It is found that a unique relation between the phase response from TSA and a dimensionless parameter (the ratio between the thermal diffusion length and the ligament length) can be used to identify the level of the contribution that made to the surface material which can then be related to the damage severity in terms of sub-surface stress.

In this investigation, attention has been paid to the analysis of damage on the inner surface of a cylindrical section which can not be observed from the outside surface. This means that the approach can be used to determine the

damage severity of the internal damage of the pipework or pressure vessel components.

As composite materials have been widely used in Marine applications recently, **G**lass **R**einforced **P**lastic (GRP) pipe is employed in pipe network and tubular structure. However, information about strength behaviour and stress analysis in this pipe component is very rare particularly on tee-intersection where the most complex stress occurs. A preliminary study of stress analysis of GRP and steel pipe structure is included in this thesis to demonstrate that TSA technique can also be used on large cylindrical structure component in both composite and metallic pipework structure.

Contents

List of Figures

List of Tables

Nomenclature

A	Calibration factor $[\mathrm{MPa} \cdot \mathrm{U}^{-1}]$
A^*	Calibration factor for an orthotropic material $[\mathrm{MPa} \cdot \mathrm{U}^{-1}]$
a/t	Damage extent parameter (crack depth/thickness)
B	Physical constant depending on the IR detector
B_s, B_c	Amplitude of the signal
C_1, C_2	Constants
c_ρ	Specific heat capacity at constant stress (per unit mass)($= c_p$) $[\mathrm{J} \cdot \mathrm{kg}^{-1} \cdot \mathrm{K}^{-1}]$
c_ϵ	Specific heat capacity at constant strain(per unit mass)($= c_v$) $[\mathrm{J} \cdot \mathrm{kg}^{-1} \cdot \mathrm{K}^{-1}]$
D_o	Outer diameter of a running pipe [mm]
d_o	Outer diameter of a branch pipe [mm]
E	Young's Modulus [GPa]
F_0	Applied load amplitude [N]
e	Surface emissivity
f	Loading frequency [Hz]
J	Moment of inertia of the beam cross-section $[\mathrm{m}^4]$
K	Thermoelastic constant $(= \frac{\alpha}{\rho c_p})$
k	Thermal conductivity $[\mathrm{W} \cdot \mathrm{m}^{-1} \cdot \mathrm{K}^{-1}]$
L	Beam half thickness [m]
N	The number of samples
N_λ	Number of photons striking detector (between operating wave length)
n	A constant
P	Applied load [N]
Q	Amount of heat absorbed by an element [J]
q	Heat source gain by the system from the surrounding per unit volume $[\mathrm{J} \cdot m^{-3}]$
R	Amplitude of the absolute signal [U]
S	Thermoelastic signal from TSA system [U]
S_{nom}	Thermoelastic signal from DeltaTherm system at a uniform region [U]
S_x	In-phase thermoelastic signal from DeltaTherm system [U]
S_y	Out-of-phase thermoelastic signal from DeltaTherm system [U]
T	Absolute temperature or average temperature of a body subjected to oscillation loading [K]
T_0	Reference temperature [K]

t	Time [sec.]
ΔT	Temperature increment ($\Delta T = T - T_0$) [K]
V	Volume fraction
Y_n	Sampled signal
y	Distance in y-direction [m]
Z	Detector response factor
z_1	Distance in z-direction [m]
α	Coefficient of linear thermal expansion [K^{-1}]
α_p, α_t	Coefficient of linear thermal expansion in the principal material directions
ϵ_{ij}	Strain tensor
γ	Thermal diffusion length [m]
ν	Poisson's ratio
ρ	Material density [$\mathrm{kg} \cdot \mathrm{m}^{-3}$]
σ	An instantaneous stress of a stress function [MPa]
σ_a	Amplitude of stress of a stress function [MPa]
σ_m	Mean stress of a stress function [MPa]
σ_{ij}	Stress tensor [MPa]
σ_I	The change of the sum of the principal stress [MPa]
$\Delta\sigma_{\mathrm{app}}$	Applied stress [MPa]
$\Delta\sigma_p, \Delta\sigma_t$	The change in the direct stresses in the principal material directions [MPa]
φ	Phase angle between the reference signal and the temperature response [Degrees]
ω	Angular velocity [rad/s]

Acknowledgements

I would like to thanks a number of individuals gave me generous help and support.

First of all, I am greatly indebted to the Royal Thai Navy for their financial support throughout my study in UK. I would also like to thank my supervisor, Dr. Janice Barton, for her uniformly generous help and guidance during the course of my PhD. She showed heroic reserve of patience when reading my thesis and I want to thank her for offering valuable suggestions as well as correcting the English grammar. This contribution is far beyond the duty of a supervisor and is profoundly appreciated. I could not have imagined to have a better supervisor. I would like to thank to my examiners, Dr Simon Quinn (internal) and Dr Rachel Tomlinson (external) for their time spent reading my thesis and for a very fruitful viva.

I also would like to say a big thanks to my officemates, turn friends, Mr James Eaton-Evans and Mr Trystan Emery who are always available to help either in or out of the working hours. Your help and support is greatly appreciated. I would also like to take this opportunity to extend a special appreciation to all my friends and family back home in Thailand for their support. Finally, thanks to my dear, patient and incomparable wife who keeps my motivation alive.

Moss.

Chapter 1

Introduction

Pipework is used extensively in the offshore and marine industries. The pipes are mainly used in fluid transmission systems as well as in tubular construction of load-bearing structures, such as the foundation of an offshore platform. The pipework is usually designed conservatively to sustain internal pressure load and unexpectedly large deflections, as well as to prevent failure under severe loading conditions during sea service. However, fatigue failure can occur as a consequence of progressive damage from material imperfections and cracks under fluctuating stresses.

In most engineering structures, existing flaws from the manufacturing process as well as material discontinuities are inevitable. It is well-known that these defects are a primary cause of failure of load-bearing structures. When the structures or components are in service, they are generally subjected to fatigue load under severe conditions. If the small defects and/or material imperfections happen to exist in the regions of high stress concentrations, these situations will cause the propagation of cracks and lead to unexpected structural failure. Consequently, prediction of damage levels in those components is a vital element of structural assessment for safe design and timely maintenance.

To assess the integrity of a structure in service, taking full-field measurements that relate to the stress distribution in a component is an attractive proposition. The full-field stress analysis can be used to locate the peak stress or high stress gradient regions of the component under service loads. It is critical to identify these locations because these are regions where cracks usually initiate and propagate. Consequently, they become the potential failure locations in the structure. Full-field stress analysis can be achieved using various experimental techniques. Thermoelastic Stress Analysis (TSA) [1] allows reliable and rapid assessment of full-field stresses in a structure under dynamic loading. TSA is essentially an optical technique that allows collection of high resolution stress related data from practically any structure, even those with complex geometries. Modern TSA systems use a focal plane array IR (infra-red) detector in conjunction with high speed digital signal processing that enable collection of data in virtually real time. TSA is based on the measurement of the small temperature change in a material or component caused by the thermoelastic effect in a linear elastic solid. The technique has been successfully used in a broad range of engineering applications such as in nuclear power plant components [2], automotive industries [3], and marine industries [4], as well as in aviation industries [5]. In fracture mechanics, TSA has been proved to be an effective technique to determine Stress Intensity Factors (SIFs) from crack tip stress fields [6]. A review of the relevant literature associated with TSA studies of structures is given in Chapter 2.

As the need for energy conservation inspires the use of lightweight materials in engineering structures, applications of composite materials in components used in offshore and marine applications is becoming popular. One of the most successful applications is in the field of tubular construction and pipework. This is because the performance of the plastic pipes is superior to conventional metallic pipes in many aspects, particularly regarding weight saving and corrosion resistance. There is a reluctance to use GRP pipes in some high integrity applications because not only are they costly to fabricate, but also their mechanical behaviour is not well documented when compared to that of conventional metallic pipes. Therefore, a study of composite pipe performances is vital to establish reliable design data or a design procedure using this material. Little research work has been dedicated to the behaviour of pipe-intersections which are necessary in all pipework applications. For practical uses of GRP intersections, a general recommendation from international standards such as BS 7159 (Code for practice for design and construction of glass-reinforced plastics (GRP) piping systems for individual plants or sites) is that the strength of the joint shall be equal or superior in strength to the pipework. However, a simple theory for predicting the stress distribution on the composite tee-section is not available. Consequently, considerable effort in devising a testing procedure that produces reliable experimental stress values is necessary. Application of conventional strain gauge techniques would be laborious and therefore a full-field optical technique is more attractive for this application. To demonstrate that TSA can be used for stress analysis on large cylindrical structure such as pipework and to show that TSA is an effective full-field technique for stress analysis in both metal and composite pipes, Chapter 3 of this thesis examines the application of TSA on GRP pipes.

The objective of this research is to explore and develop an approach so that TSA can be used as a tool to determine the extent of an internal surface flaw. Therefore, in this thesis, a new approach for sub-surface damage analysis using TSA is devised. The TSA equipment is used to obtain the thermoelastic response from a component containing internal damage. The data is collected from the undamaged surface and then evaluated to obtain the extent of internal damage. The approach exploits non-adiabatic conditions caused by the large stress gradient developed in the neighbourhood of the internal damage. This non-adiabatic condition results in nonlinearity in thermoelastic response and a time-lag between the applied stress change and resultant temperature change. Since the TSA data contains both the amplitude of the temperature change and the phase of thermal response in relation to the applied stresses, the effect of non-adiabatic behaviour can be evaluated over a range of load frequencies and related to the damage extent enabling a new approach for damage detection and evaluation. The theoretical basis of the new approach is that of classical thermoelasticity incorporating a generalised heat conduction equation. Therefore, the thermoelastic response under both adiabatic and non-adiabatic conditions can be described. A preliminary feasibility study is presented in Chapter 4 that shows the non-adiabatic response can be related to damage severity.

The approach is devised for a standard IR system designed for TSA in which the IR signal, S is described as a linear relationship with the magnitude of the sum of the principal stresses, $\Delta(\sigma_{11} + \sigma_{22} + \sigma_{33})$ [7]:

$$\Delta(\sigma_{11} + \sigma_{22} + \sigma_{33}) = A\,S \tag{1.1}$$

where A is a calibration factor. It can be seen that the relationship does not contain any useful information about non-adiabatic behaviour because the system is designed to measure only the adiabatic temperature change. To make use of the new approach, the relationship has to be described by time dependent parameters, therefore, the phase relation can be identified. The underlying theory is presented in Chapter 5. Moreover, the TSA system must be able to supply both the signal response and the phase relationship between the thermoelastic response and the excitation stress. Modern TSA systems can supply this information effectively as they use advanced digital signal processing techniques. To show how the IR signal can be used for non-adiabatic behaviour analysis, a derivation of a time dependent signal output is given in Chapter 5.

In order to study the effect of non-adiabatic behaviour in a thermoelastic problem, a mathematical model of the physical situation needs to be established so that the effect of individual parameters in the governing equation can be investigated. The derivation of the mathematical model is also given in Chapter 5. Since the exact solution for real geometries of damage is arbitrary and may be laborious to obtain, a numerical simulation technique was chosen as the most efficient approach. A procedure for Finite Element (FE) simulation of TSA incorporating non-adiabatic behaviour using a commercial FE software package, ANSYS, has been developed and is presented in Chapter 6. The approach has been confirmed by comparisons between the FE simulations and TSA on a range of case studies. First, the approach was applied on a bar specimen containing an idealised damage in the form of a through slot. This situation allows the simple damage geometry to be modelled using two dimensional (2-D) analysis. Details are presented in Chapter 7. Second, a more realistic specimen of a flat plate with a series of semi-circular part-through slots has been tested and compared with the simulations (see Chapter 8). Finally, tests were carried out on a pressured steel cylinder containing artificial part-through damage (see Chapter 9). The part-through damage in a cylindrical section is of most interest because this type of damage models that experienced in pipes and is most frequently found [8, 9, 10] but cannot be detected visually from the outside surface. The work described in Chapter 8 and 9 demonstrates the potential of TSA for non-destructive assessment of sub-surface damage.

In summary, the thesis combines new applications of TSA on damage and stress analysis in pipe structure. Both metallic and composite pipework were studied. In metals an evaluation of the non-adiabatic behaviour from the thermoelastic response in the neighbourhood of damage has been carried out and theory has been developed to describe this. A non-adiabatic response can also be derived from the other complex stress regions such as pipe connections or pipe intersections where the crack is often initiated. However, the same approach cannot be used in composite pipe because of the low thermal conductivity of the materials. In addition, the potential failure site of composite pipe is at the joints [11]. Therefore an approach for stress factor evaluation at the joints is introduced as an alternative.

There are 10 chapters in this thesis. Chapter 1 is an introduction which is dedicated to the background information for this research. Chapter 2 provides a review of previous work related to TSA applications, particularly in the field of fracture mechanics and damage analysis to point out the potential of using TSA for damage assessment. In Chapter 3, the application of TSA to large pipe sections is introduced. TSA is used to study the stress distribution intersections of various component pipes with different nozzle to running pipe ratios and demonstrates the technique is viable for large scale structure. The work in this chapter provides confirmation that it is worthwhile exercise to pursue TSA as a damage assessment technique for cylindrical structures. In Chapter 4, the results of a preliminary feasibility study on damage assessment are presented. In Chapter 5, theoretical development of classical thermoelastic equations and generalised heat conduction is described. This emphasizes the use of a new relationship in damage analysis. A description of the mode of operation of a commercial infra-red system designed for TSA is also included in this chapter. In Chapter 6, a numerical simulation of the non-adiabatic thermoelastic effect is developed using FE simulation software. The simulation is validated by comparisons with results from the published literature and with the TSA results. In Chapter 7, thermoelastic work under non-adiabatic conditions on a specimen with idealised damage (a bar specimen with a central through crack) is presented. The results are compared with the numerical simulation developed in Chapter 6 and a relationship that defines the non-adiabatic thermoelastic response is presented.

In the real world, the damage is arbitrary in shape and location; therefore a more realistic damage type is studied in Chapter 8, in the form of part-through damage in a flat aluminium plate. In Chapter 9, the approach is applied on the more complex geometry of a cylindrical section component, where a pipe sample containing damage on the inside surface has been manufactured and tested. Chapter 10 provides an overarching discussion in the context of future development of the findings in this thesis. In Chapter 11, an overall summary of the achievements and conclusions of this research work is presented.

Chapter 2

Previous work and motivation for current studies

2.1 Introduction

It has been stated in the introduction chapter that the ultimate goal of the work in this thesis is to use TSA for damage and stress analysis on pipework. In pipe system cracks develop from sub-surface flaws. The standard equipment used for TSA is briefly described in Section 2.2. Then a brief summary of the classical approach based on Linear Elastic Fracture Mechanics (LEFM) for surface flaws is described in Section 2.3. However, the main purpose of this chapter is to bring together information from other TSA studies to identify the potential of using TSA as a damage assessment tool. Therefore, previous studies to analyse crack tip stress fields are reviewed and a detailed description of the related TSA work on this topic is given in Section 2.4. However, the existing approaches cannot be applied to the problem of a sub-surface flaw or defect. Therefore further development of the technique is required. Recently, it has been reported that TSA can be used to reveal a hidden crack [12], nevertheless, the technique was not used to evaluate the severity. Instead, in this thesis, a new approach is developed in order that TSA can be used to assess the damage extent. The proposed approach is based on the use of TSA to evaluate non-adiabatic behaviour from the thermoelastic response which has been successful in an internal stress evaluation. A summary of TSA applications on part-through crack problems as well as internal stress evaluations is given in Section 2.5. Previous work related to the non-adiabatic thermoelastic response are also reviewed in Section 2.6. As TSA is a full-field and non-contacting approach, this make in-service inspection or taking measurements on a complex structure possible. A number of successful TSA applications on real structures is exemplified in Section 2.7.

In order to demonstrate the application of TSA to large structural pipework, particularly for marine applications, the application of TSA on composite pipes is investigated in this thesis (see Section 2.8 and 2.9). The application of TSA to composite materials is well-documented [13]. Several papers about TSA of composite material are available [14, 15, 16]. In general, most of the studies have focused on material characterisation and work on real components was limited to only ideal specimens. The applications of TSA to composite materials is discussed further in Section 2.10.

2.2 DeltaTherm system

In general, the main component of a TSA system is the IR detector used to measure the thermal emission associated with the thermoelastic temperature change. The means by which the thermal emission from the test specimen is converted to a voltage signal is described in detail in Chapter 5. For this section of work it is only necessary to understand how the voltage signal is processed into a digital image. Since the magnitude of the useful signal is very small. a special technique for noise rejection and correlation is used to process the electrical signal into 'thermoelastic signal', S (see Equation 1.1).

The first commercial TSA instrument was released the early 1980s and named SPATE (**S**tress **Pat**tern **A**nalysis by the measurement of **T**hermal **E**missions) [1]. The system contains a single point Cadmium Mercury Telluride (CMT) IR detector. The thermal variation is measured and processed one point at a time. A full-field image is achieved by using scanning mirrors. The IR signal was correlated by an analogue lock-in signal processing system. The disadvantage of the system is that the data acquisition time is relatively long. A single full-field stress image could take 1-2 hours. In 1994, a modern TSA system was presented by Stress Photonics and named as DeltaTherm. The system uses an Indium Antimonide (InSb) Focal Plane Array (FPA) detector and an advanced digital processing unit. As a result, the system reduces the operating time for thermoelastic testing considerably. The DeltaTherm system is the system used in all of the work in this thesis[1] and is therefore described in detail in this section. A diagram of DeltaTherm system is shown in Figure 2.1.

In Figure 2.1, the IR detector receives input from IR radiation associated with temperature variation caused by the thermoelastic effect on the specimen. The input data is then passed into the signal processing unit to correlate with the reference signal. As a result of the correlation IR background noise is eliminated and the thermoelastic data is obtained in terms of magnitude and phase. The reference signal can be obtained either directly from a strain gauge attached to the specimen or from a function generator from the load cell of the servo-hydraulic testing machine. The resulting correlated data is passed through the personal computer to display as a colour contour stress map in virtually real time ready for post processing and further analysis.

---

[1] In Chapter 3 and 4 DT1000 (128 × 128 FPA detector) was used. A higher resolution system, DT1400 (256 × 256 FPA detector), was available later and used in the rest of the work in this thesis.

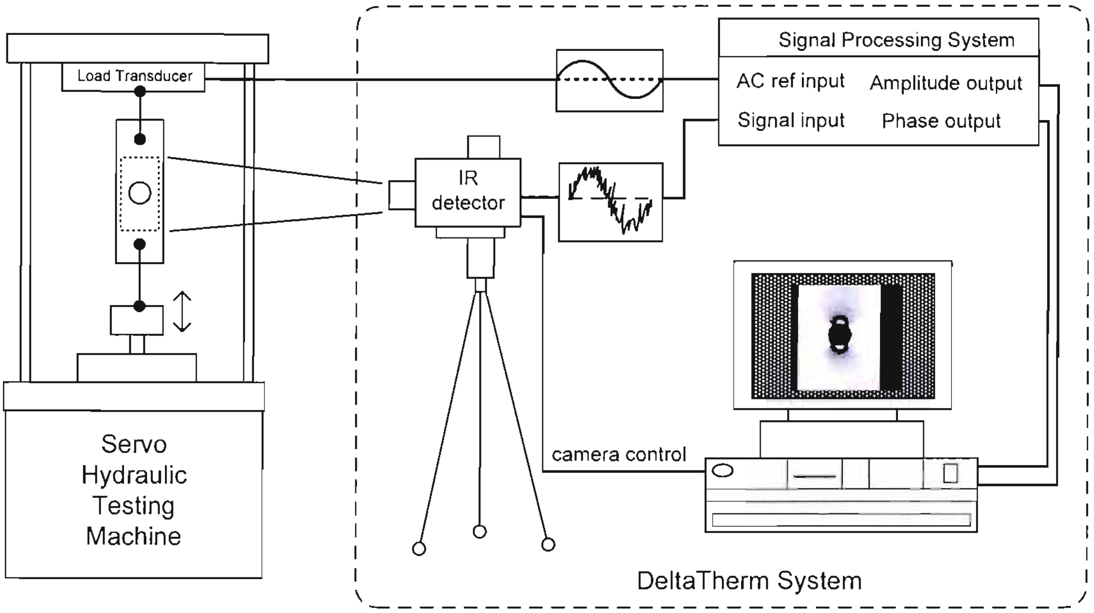

FIGURE 2.1: A schematic diagram of the DeltaTherm system

The DeltaTherm system uses a focal plane array detector to measure the temperature variation on the target surface. Each detector (pixel) measures the IR radiation at a specific point on the surface and converts the photon striking the detector into electrical signal proportional to the number of photons. All points in the visible frame are monitored by the array of sensors. The data is read out by row from the array of detectors into an analogue to digital converter. As the data is interrogated by row, there is a slightly different phase with respect to the load/stress cycle. However, it has been reported that the correction can be made at the output stage [17]. The sampled images are then transmitted to the signal processing unit to be processed before sending to display on the computer monitor.

The DeltaTherm system processes the data using digital a Fast Fourier Transform (FFT) analyser. It functions in a practically identical manner to the analogue type lock-in analyser used in SPATE and determines the magnitude and phase from the sampled signal. This is done by correlating the sampled signal with the reference signal using the following function [17]:

$$B_s = \frac{2}{N}\sum_{n=1}^{N} Y_n \sin\beta(n) \tag{2.1}$$

where B_s is the amplitude of the signal, Y_n is the sampled signal, N is the number of samples, and $\sin\beta(n) = \frac{2\pi}{N}\left(n - \frac{1}{2}\right)$ is a reference or weight function. The resulting processed signal is the signal that is in-phase with the reference signal and termed the X-signal in the DeltaTherm software (see Figure 2.2 (a)) and denoted S_x in this thesis.

The process described by Equation 2.1 also removes any input caused by background radiation, i.e. the in-phase signal is derived using only the input at the reference frequency of the applied stress.

The other output obtained from the correlation is the signal which is correlated with an offset-reference signal (shifted by 90 degrees from the reference signal). This out-of-phase data is known as the Y-signal (see Figure 2.2 (b)) in the DeltaTherm software, denoted S_Y in this thesis, and can be described as:

$$B_c = \frac{2}{N}\sum_{n=1}^{N} Y_n \cos\beta(n) \tag{2.2}$$

The resulting absolute magnitude of the signal output is known as R-signal (see Figure 2.2 (c)) in the DeltaTherm software and can be calculated from:

$$R = \sqrt{B_s^2 + B_c^2} \tag{2.3}$$

and the phase angle between the reference signal and the instantaneous temperature response is obtained from:

$$\varphi = \tan^{-1}\left(\frac{B_c}{B_s}\right) \tag{2.4}$$

and can be plotted as phase image as shown in Figure 2.2 (d). The phase image provides the phase angle of each data point relative to a reference datum. This datum is set by the operator by adjusting the phase setting on the system. Ideally, it should be set to synchronise with the load signal.

This cross correlation technique is very useful in that the out-of phase correlation, B_c, component in the TSA image can be used to identify the localised out-of-phase signal caused by heat conduction [1].

2.3 Application of LEFM to surface flaws

As stated in Chapter 1, small defects such as surface flaws can propagate and cause structural failure under a normal operating loads. Components need to be inspected at appropriate times to assess their integrity. This can be done by using any suitable non-destructive evaluation method to define damage locations and estimate geometric detail of the defect. To assess the integrity, knowledge of the stress field in the vicinity of the crack-tip is required. In practice, the stress intensity factor approach is widely used. The shape and size of the defects obtained from the inspection are compared

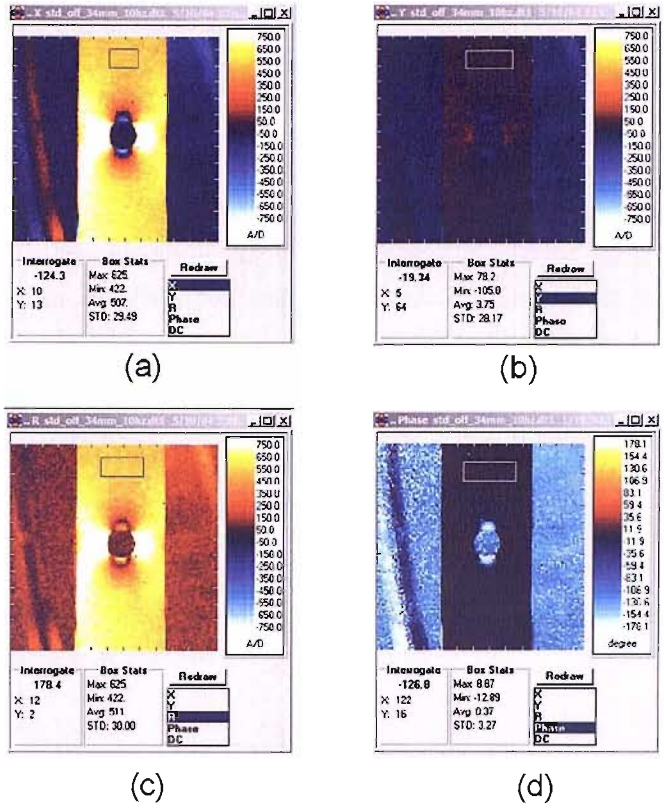

(a) (b) (c) (d)

FIGURE 2.2: Typical images from DeltaTherm system: (a) maximised X image, (b) minised Y image, (c) R-image and (d) phase image of the same data

with established standards or handbooks such as [18], [19], [20] and [21]. As most of the techniques used to obtain SIFs are based on analytical and numerical methods only idealised crack/flaw geometries are available. Finally, the SIF as well as geometric factors from the handbooks for the particular crack shape are obtained. These parameters are essential to predict the growth rate and fatigue life of the components. However, it should be pointed out that most of the analytical solutions of the SIFs in the standard handbooks are derived for infinite or semi-infinite plates and they are based on the function of crack size, shape and far-field stress. Consequently, the crack-tip stress field is not expressed explicitly in a closed form and applications of the analytical solution are quite limited.

In pressure vessels and piping, a number of approaches have been proposed to solve the SIF problem for various circumstances. Atluri and Kathiresan [22] used a displacement hybrid FE method to solve three dimensional-crack problems on surface flaws in thick-walled reactor pressure vessels. Raju and Newman [23] used a three dimensional FE method. Their FE results cover a wide range of crack shapes and sizes for both internal and external locations and are generally regarded as one of the most accurate solutions [24]. Nishioka and Atluri [25] developed a new 3-D alternating method. The solution was shown to be an inexpensive FE procedure for a routine evaluation of the SIFs for a flaw in pressure vessels. Chen et al. [26] modified the conventional body force method to evaluate SIFs for surface flaws in cylindrical pressure vessels.

Nevertheless, these available SIF solutions are not always adequate for particular engineering applications. A complex situation occurs when the cracks initiate in a non uniform stress field such as that caused by residual stress or thermal stress. This makes SIFs evaluation more problematic and special treatment is required [27]. Furthermore, it has been argued in Ref [28] that fracture in real applications is irregular and may not strictly fit with generic configurations and could introduce errors in the growth data as well as the estimated fatigue life. A similar issue has been also emphasized in Ref [24]. It can be concluded that some difficulties in damage severity evaluation in LEFM for actual cracks can be attributed to the irregularity of the actual crack front and the complex stress field due to the complicated boundary conditions.

Full-field experimental analysis such as TSA can be considered as an alternative technique to achieve a better understanding of the problem. The experimental results can also be used to validate any numerically proposed solutions.

2.4 TSA applied to through-cracks

The non-contact features of TSA and the ability to obtain relatively high resolution full-field stress data directly from the component has made it an attractive technique for crack-tip studies. An extensive review by Tomlinson and Olden [29] describes four main approaches available to determine SIFs from the crack tip stress data. Firstly, Stanley and Chan proposed a method that related the thermoelastic signal to the Westergaard equation under mode I [6] and mode II [30] loading. Second, Stanley and Dulieu-Smith [31] introduced an approach based on the isopachic contours around the crack tip region for mixed-mode analysis. Third, Lin et al. [32] suggested a method based on the equilibrium and compatibility equation with J-integral concept. Fourth, Tomlinson et al. [33] proposed a concept using Muskhelishvili's stress field equations. A step further in the application of TSA to fracture mechanics has been recently carried out by Diaz et al. [34], where TSA was used to measure the SIFs during fatigue crack growth. The considerable effort in these works has meant that the technique of using TSA to evaluate SIFs in through cracks has become widely recognised and the reliability of the technique in fracture mechanics applications has been confirmed.

The studies mentioned above were aimed to identify the SIFs from a through crack. These works are mainly based on the use of LEFM stress field equations to define the stress field near the crack tip in an infinite body. The thermoelastic response is obtained directly from the surface which can be monitored directly as shown in Figure 2.3 (a). When a surface flaw (see Figure 2.3 (b))or a part-through crack in a body of finite thickness is in question, these techniques are not applicable. This is because the thermoelastic response from a surface flaw can be obtained only from the free surfaces, i.e. either the damaged side or undamaged side. Furthermore, a direct relationship between the stress field on the free surfaces and the part-through crack does not exist. Therefore, further investigations using TSA to evaluate damage severity of surface flaws is required and is one of the objectives of the work described in this thesis.

2.5 TSA applied to part-through cracks and internal stress

TSA has been used to evaluate the SIF from surface cracks [35]. In this investigation the TSA data was obtained directly from the damaged side of the plate and the solution of mode I SIF was derived from the Westergaard equations. The derived SIFs is an approximation as the characteristics of a surface crack are not the same as those of a through crack. Therefore, the Westergaard equation is not adequate for this boundary condition. However, the author showed that TSA has great potential as a non-destructive technique for damage evaluation of complicated stress states where there is no available closed form solution.

Generally, it is understood that TSA gives no indication of subsurface stress because the temperature change is observed from the specimen surface only. However, Lesniak [36] showed that it is possible to measure internal stress by using TSA. He developed a thermal model to study how heat created by the internal stress conducts to the surface. This heat transfer model is analogous to A.C. circuit analysis. He also concluded that the method can be applied to TSA to detect internal damage in materials. Therefore, it is possible to obtain internal stress information by observing the thermoelastic response from the surface resulting from heat conduction from within the material.

For crack detection, Silva et al. [12] used SPATE to detect a hidden crack in an aluminium flat plate. A series of specimens with different damage severities were tested to identify the sensitivity of the technique. All 1.6 mm-thick specimens were machined to simulate a part-through crack. The rectangular part-through cracks were made by the electro-erosion process. Damage severities were varied by a parameter representing the crack depth, a, to thickness, t, ratio (see Figure 2.3). SPATE was used as non-destructive evaluation tool to detect the part-through crack from the face without a crack. The location of damage was observed by a perturbation of the stress distribution along the crack axis. According to their results the crack of depth to thickness ratio, a/t, of 0.375 (see Figure 2.3) was the shallowest crack that can be detected by the technique. It was also expected that the in-service induced crack may produce a greater thermoelastic response because the actual crack front is sharper than the simulated crack and hence results in a very high stress gradient. Therefore, stress at the crack front is much more extreme and as a consequence, shallower defects may be observed.

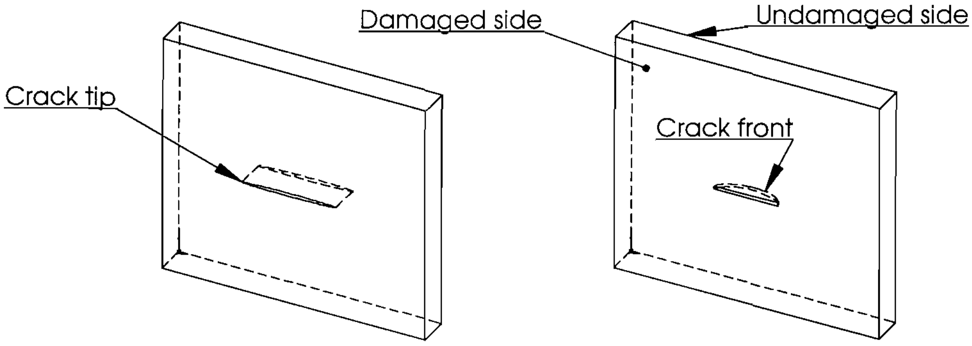

(a) Through crack (b) Part- through crack

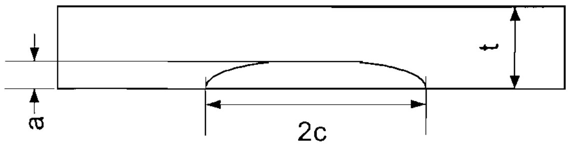

(c) cross-sectional view of the part- through crack

FIGURE 2.3: Crack descriptions

The work in Ref [12] indicated that TSA could be applied to subsurface crack detection. A preliminary feasibility study, described in Chapter 4, confirms the findings of Ref [12]. Chapter 4 also shows that care must be taken when TSA is used to interpret the results at the region of high stress gradient such as cracks or notches, as these regions are prone to non-adiabatic behaviour in TSA and may lead to some error in the interpretation. A theoretical derivation of the TSA signal in Chapter 5 shows how the non-adiabatic condition can bias the thermoelastic signal. Therefore, a further investigation of using TSA for subsurface flaw detection is necessary. In this thesis the study of non-adiabatic behaviour is carried out in order to understand the physical effect of the damage extent to the detected thermoelastic signal as well as the ability to evaluate the severity from the damage.

2.6 Non-adiabatic behaviour in TSA

Non-adiabatic behaviour has been analysed using several numerical approaches. Dunn [37] used a finite difference technique to solve the two-dimensional heat conduction equation, where the heat input term (heat generated in the body) was calculated from the stress field obtained from the FE model. Offermann et al. [38] used the FE technique to quantify the solutions of a simple two dimensional model of a bar with a centre hole, where non-adiabatic behaviour was observed over various load frequencies. Another recent study of the non-adiabatic effect has been carried out by Inoue and Kishimoto [39]. The Boundary Element Method (BEM) was used in their study. They showed that under non-adiabatic conditions, heat diffusion effects lead to an underestimation of stress concentration.

Recent studies of the non-adiabatic behaviour [39, 40] focused on correction procedures to recover the adiabatic thermoelastic response so that TSA data taken under non-adiabatic conditions can be used for stress analysis. In this study, the non-adiabatic behaviour was investigated in order to relate the non-adiabatic thermoelastic response to the damage severity of the sub-surface flaw.

It has been shown that more detail of internal stress conditions can be assessed from the non-adiabatic behaviour [36]. For this reason, the non-adiabatic behaviour created from the damage beneath the surface could lead to some relationship between the signal response and the extent of the damage. Therefore, fully understanding the non-adiabatic behaviour in the thermoelastic effect is essential. To do this it is necessary to revisit the theory to understand the nature of the heat transfer as a result of the stress gradient and thermal conductivity as well as the theory behind the TSA via IR detecting system. This will enable better interpretation of the thermoelastic response to elicit detailed information on non-adiabatic behaviour. In the author's knowledge, there is no published information on the use of TSA in damage evaluations of part-through crack-like flaws by considering the undamaged surface. Moreover, analytical solutions to relate the three-dimensional stress distribution around arbitrary damage to the thermoelastic response do not exist. Therefore, it is necessary to develop a suitable numerical simulation procedure to solve for a three-dimensional case. Ref [38] has provided some information on the use of FEA to model the non-adiabatic behaviour on their specimen, however, the procedure necessary to reproduce such a simulation is unclear. Therefore, in Chapter 6 a detailed account of using FEA to obtain the thermoelastic response is provided.

2.7 Practical applications of TSA on curved shell structures

As the objective of this work is to apply TSA on actual pipework structure, under pressurised load in particular, further considerations in this review are to justify the technique based on real applications on full-scale structure which features complex geometry as well as complex operating loads. Under dynamic pressurised loading, there is only one reported work on TSA used in conjunction with this type of loading condition. Stanley and Chan [41] carried out TSA work on a thin free-formed pressure vessel end. They showed that the technique can provide stress distribution of a thin-walled structure under a simulated in-service loading. The design of the pressure loading system used by Stanley and Chan forms the basis for the design of pressure loading system used in the work described in Chapter 9. For the applications of TSA under full-scale testing, many TSA applications have shown the that TSA possesses some advantages over other experimental techniques, examples are the measurement of the stress distribution on large tubular welded tee joints and cross tee joints of an off-shore platform [1] and in nuclear power plant components [2]. These works demonstrate the reliability and practical viability of the technique. Therefore, it can be seen that the approach possess great potential for a novel application on any pressurised cylindrical structure. Moreover, the pipework is often subjected to a cyclic load when it is in service, therefore, it may be possible to perform an *in situ* thermoelastic measurement.

2.8 GRP pipes in marine applications

GRP piping systems have been used successfully over the past 20 years in the offshore industries. This type of piping is expensive to manufacture but possesses key advantages over typical metal or alloy pipe systems in that it is highly resistant to corrosion and is lightweight. However, composite piping systems have not been widely adopted by ship building industries where these advantages could be realised.

The nature of pipe networks in ships is generally more complex than that has been found in ordinary engineering plants. This is because the routing of the pipework is more compact within the limited space available among many machines in a single compartment. In addition, a large number of complicated pipe intersections and connections are required to allow access for machinery maintenance. Under service loading, complex stress distributions are developed at those intersections according to the joint geometry. Apart from the pipe weight. loads are applied from a combination of internal pressure and moment force due to pipe deformation. others are from the vibration transmitted from the machinery to which the pipes are connected. Consequently, failure may occur if the pipework is not properly designed. It has been reported [42] that a current application of plastic pipes in commercial vessels to replace steel pipework in non-critical areas is cost effective. On that account, the practice of using GRP pipe in critical areas could be expected to produce similar savings. A rigorous study of the practicality and economics of using GRP pipes in ships had been carried out [42] and demonstrated the feasibility of the approach in both cost and structural terms.

2.9 GRP pipe intersections

Pipe intersections are necessary in any pipe network to facilitate the introduction of branch pipes and nozzles. The intersections are generally the weakest part of the pipework network and are usually subjected to complex loading conditions. A large amount of work has been dedicated to investigating the stress distribution around the metallic pipe intersections subjected to various loading conditions using both experimental and numerical methods. However. there is little data on the behaviour of intersections in Glass Reinforced Plastic (GRP) pipe. To the author's knowledge, only one extensive experimental investigation on composite pipe intersections is reported in the literature [43].

In Ref [43] the strength of the tee-section components was assessed using conventional strain gauge technique and tests destruction. Four types of tee-sections were manufactured to meet the BS 7159 requirement for the offshore use. Strain gauges were attached to both the inside and outside surfaces around the joints to observe the behaviour of the sections under in-plane bending and pressure loading. Elastic strain distribution around the intersection profiles due to pressure, in-plane and out-of-plane bending loads was reported extensively based on their experimental results. The conventional strain gauge technique is very laborious for this application as a large number of strain gauges are required to observe the strain behaviour around the pipe intersection profile. Moreover, in practice, making all connections to meet all dimensions required by the standard would be difficult since most of the GRP/FRP pipe-connection fabrications have to be carried out by hand lay-up particularly on-site fabrications. It was also argued in Ref [43] that the strain gauges did not supply sufficient data to identify the maximum stress because of the high stress gradients involved at the surface discontinuity. Therefore, introducing a high resolution full-field technique such as TSA to analyse the stresses in such structure allows both a convenient and efficient means of performing stress/strain analysis.

Considering that numerical techniques such as FE simulations are currently in favour, the FE analysis of GRP pipe intersection is very limited. One of the very few investigations using FEM was carried out by Xue et al. [44]. They used three dimensional FE to estimate the stress and strength of FRP tee sections subjected to internal pressure. Incompatible element types were used in the model to deal with the problem of different principal directions of the material at the interface of branch and nozzle regions. The analysis showed the reinforcement at the joint was necessary, as the strength criterion derived from the Tsai-Wu strength criterion [45] was exceeded in all cases.

In the current work the piping sections are reinforced at the joint by over-lamination with Chopped Strand Mat (CSM) material which is wrapped around the joint. This reinforcement will affect the stress distribution at the joint considerably because both the localised stiffness at the reinforced region and the geometry at intersection area will change substantially. In this case, detailed FEA may not be the most preferable option since hand lay-up fabrication at the reinforcement region results in highly non-uniform geometries and material properties. This issue was also mentioned in Ref [43]. An experimental approach is a more realistic solution for the stress analysis in this situation. Therefore, the objective of this work is to assess the applicability of TSA in obtaining the stresses around composite pipe intersections.

2.10 TSA for composite materials

TSA has a unique feature over other experimental techniques in that both stresses on the component surface and internal damage such as delaminations can be identified simultaneously. The applications of TSA to composite materials have been monitoring damage evolution on composite materials [46, 47], measuring stress concentration factors [46], determining complex stress in the composite structure [4, 48] and detecting sub-surface damage on a large wind turbine blade [49]. In this current study, TSA is used to observe the stress distribution on composite pipe sections particularly around the connection region where not only a complex stress distribution occurs but the material properties around this region are highly heterogeneous.

To apply TSA to orthotropic materials where the mechanical properties vary with directions, the governing equation (Equation 1.1) needs to be developed for an anisotropic elastic solid [13]. For orthotropic materials, the temperature change (ΔT) due to the thermoelastic effect can be expressed in the following form:

$$\Delta T = -\frac{T}{\rho\, c_{\mathrm{p}}}(\alpha_p \Delta\sigma_p + \alpha_t \Delta\sigma_t) \tag{2.5}$$

where T is the absolute temperature, ρ is the material density, c_p is the specific heat at constant pressure, α_p and α_t are the coefficients of thermal expansion in the directions of the principal material axes and $\Delta\sigma_p$ and $\Delta\sigma_t$ are the stress changes along the axes.

Similar to the case of isotropic materials, when the temperature change is measured using an IR detector, this expression can be rewritten in terms of thermoelastic signal (S) and calibration constants (A^*). Equation 2.5 can be expressed as:

$$A^* S = (\alpha_t \Delta\sigma_t + \alpha_p \Delta\sigma_p) \tag{2.6}$$

Equation 2.6 shows that data related to the stress (in the principal material directions) can be obtained. This theoretical development has been validated by experimental work [13]. Further development of the thermoelastic theory for composite materials has improved the accuracy of the technique [50].

The applications of TSA to composite materials may be separated into two categories: damage evaluations and stress/strain analysis. In a damage characterisation study, Mackin et al. [46] used TSA to monitor damage evolution of the fatigue damage on double notch samples of several composite systems. The in-phase images (see Section 2.2) were used to measure redistribution of stress caused by the fatigue damage and the out-of-phase images were used to identify the level of damage. They concluded that the heat from frictional work influences the thermoelastic signal and this causes the phase-shift in the phase image and hence alters the magnitude of the in-phase images. Cunningham et al. [47] conducted a similar investigation on fatigue damage on a composite sample with a centre hole. They also found that thermoelastic data was affected by the increase in temperature from friction and viscoelastic heating. In this study on the composite pipe sections, it is believed that the same phenomenon will occur around the joint area of the pipe section but the CSM used as a reinforcement material is relatively thick around the joint area therefore the above effect may not be observed as the CSM has a very low thermal conductivity.

Apart from the damage evaluation on composite structure, TSA can also be used to determine stress distribution quantitatively. Dulieu-Smith et al [4] have demonstrated that TSA can be applied to obtain full-field stress distribution on a complex GRP structure (a GRP tee joint commonly used in marine applications). Reasonable agreement between the TSA and FEA was achieved. Another quantitative work on foam-cored sandwich construction composite tee joints carried out by Dulieu-Barton et al [48] also demonstrates applicability and usefulness of the technique to determine stress distribution on the real GRP structures. These works established TSA as a means of validating FE simulations.

A study of the effect of ply lay-up on the thermoelastic response of laminated composites has been carried out by Cunningham et al. [51]. Their investigation shows that the resin-rich layer plays an important role in quantitative stress analysis. They concluded that the thermoelastic response obtained from a component with a resin-rich layer is a function of the global stiffness of the component. A similar finding was made by El-Hajjar and Haj-Ali [16]. They proposed a method to measure the surface strain on a pultruded composite component by taking advantage of an in-plane isotropic surface layer with an assumption that the surface layer is responsible for the thermoelastic response. They verified their results with FE simulation and a good agreement was obtained.

2.11 Justification for current work

In view of damage and stress assessment on composite pipe component, very few studies have been dedicated to the stress analysis in the actual component particularly on GRP pipe intersections. The conventional strain gauge technique is laborious and is not sufficient to evaluate the distribution of stress at a complex region. FEA can be considered to be a good option for full-field analysis on a complex structure. However, for the stress analysis of a GRP pipe intersection the approach may not be suitable. This is because the accuracy of the physical response of the FE model depends on a good approximation of various input parameters such as geometries, material properties and boundary conditions which are difficult to achieve in GRP pipe intersection. Therefore, TSA is proposed as an experimental technique for this purpose.

According to the above review on damage assessment, it can be concluded that traditional methods to obtain damage parameters in fracture mechanics rely upon the effectiveness of the detection technique to estimate the geometry of the defects and the accuracy of the methods used to evaluate the fracture parameters. It has been pointed out that difficulties occur when the defect shape is irregular or the flaws occur in a complex stress field. Since the exact solutions for particular cases are not available, experimental techniques need to be developed not only to provide a comparative validation of the existing techniques but to gain more knowledge about the behaviour of the defect.

A new approach is proposed here based on TSA. TSA provides full-field data that can be directly related to the stresses and provides the opportunities to obtain detailed information from the actual structures. The approach has the potential to provide sub-surface information from cracks and damage. To implement the approach, it is necessary to understand the non-adiabatic thermoelastic response. To achieve this it will be necessary to develop a generic FE computational model to simulate the thermoelastic effect under non-adiabatic conditions. To demonstrate the effectiveness of the approach TSA will be used on a variety of specimens with sub-surface defects. This has not been attempted in any previous studies. To demonstrate the approach in a practical context in a pressurised pipe section, internal damage is also analysed using TSA. This is a new contribution to the field of TSA. Furthermore, considerable design effort was required to develop the pressurisation facilities, which are also described in this thesis.

Chapter 3

Demonstration of TSA on pipe components

3.1 Introduction

It has been mentioned in Chapter 2 that using conventional strain gauges to obtain the stress distribution around the complex geometry of a composite pipe is laborious. Therefore in this chapter, TSA is introduced as an experimental stress analysis technique for this application. The objective of this work is to demonstrate that TSA is an effective tool for stress evaluation, particularly in a real structure. In this work, full-scale GRP (Glass Reinforced Plastic) pipe intersections manufactured from off-the-shelf filament wound tube, were tested using a rig specially designed for full-scale pipe testing. To obtain quantitative stress values, it is necessary to calibrate the thermoelastic signal. Therefore, a calibration procedure for the pipe-intersection material is developed. A stress factor approach is also proposed to allow a quick evaluation of the pipe-intersection. This is compared with the results obtained from the similar pipe-intersection made from steel. An FE stress analysis of the stress distribution around the pipe-junction was also carried out for comparison with TSA.

3.2 Fundamental theory

It has been mentioned in Section 2.10 that the classical thermoelastic equation for TSA defined in Equation 1.1, i.e. $AS = \Delta(\sigma_{11} + \sigma_{22})$ is not applicable for orthotropic materials. For orthotropic materials the theory must be modified because the temperature change, ΔT, caused by the thermoelastic effect does not simply relate to the stress change but is also related to a combination of the coefficients of linear thermal expansion in each principal material direction and the stresses change in those axes. In a biaxial stress system, the thermoelastic temperature change, ΔT, can be expressed as [13]:

$$\Delta T = -\frac{T}{\rho c_p}(\alpha_p \Delta\sigma_p + \alpha_t \Delta\sigma_t) \tag{3.1}$$

where, α_p and α_t are the linear coefficients of thermal expansion in the principal material directions and $\Delta\sigma_p$ and $\Delta\sigma_t$ are the stress change in the corresponding directions. For TSA using the DeltaTherm system, Equation 3.1 can be rewritten as:

$$A^* S = (\alpha_p \Delta\sigma_p + \alpha_t \Delta\sigma_t) \tag{3.2}$$

3.3 Specimen descriptions

Plain cylindrical GRP sections were produced using a filament winding technique by Halyard so that a balanced, symmetric winding was obtained with an angle of 67.5° to the axis of the cylinder. The fibre content of the wound pipe was approximately 70%, the resin material was polyester. Tee-joints were produced by cutting the tube sections that form the running pipe to a length of 900 mm and then cutting an appropriate hole in the running section to accommodate the branch pipe. The branch pipe was adhesively bonded to the running pipe and then overlaminated with E-glass/polyester chopped strand mat (CSM) material to form a rigid connection, see Figure 3.1. Four GRP pipe sections were used in this work and are shown in Figure 3.2. The dimensions are given in Table 3.1: T-01, T-02, T-03 and T-04 denote the pipes. Two different wall thickness were studied, which gave three branch to running pipe outside diameter (d_o/D_o) ratios. It should be noted that because the cylindrical sections were formed on a mandrel of fixed diameter the thicker wall provides a different d_o/D_o ratio. For comparison a welded steel tee-joint was also included and is denoted T-05. The steel tee-joint was coated with two passes of matt black paint prior to testing.

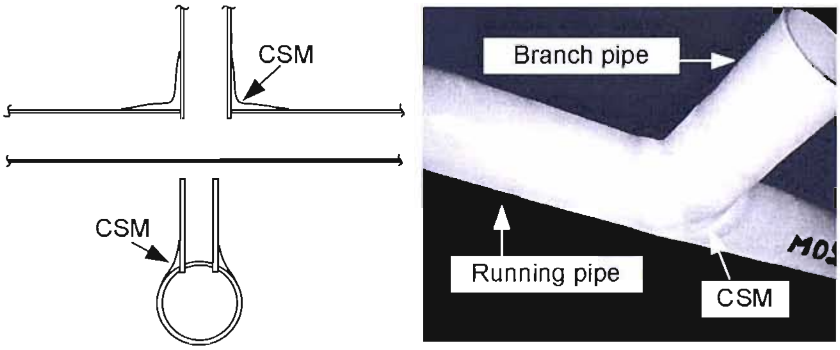

FIGURE 3.1: GRP pipe connection

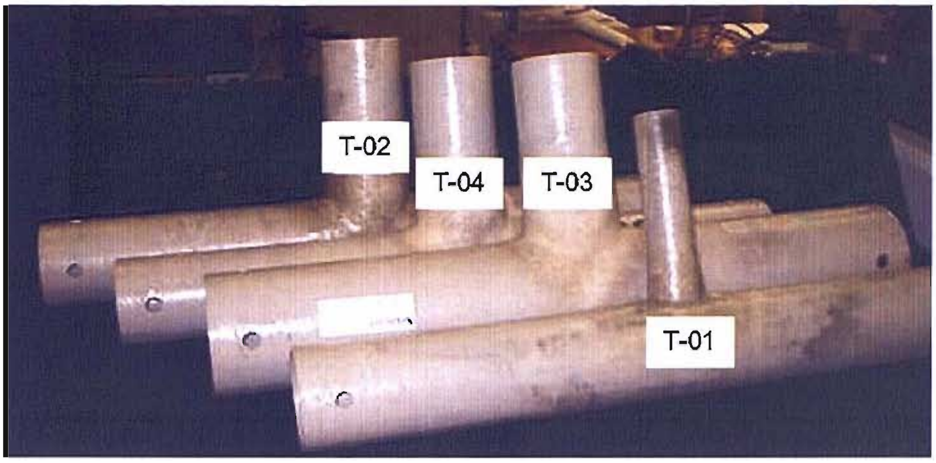

FIGURE 3.2: GRP pipe specimens

TABLE 3.1: GRP and steel pipe specimen dimensions

Specimen Reference	Running pipe(mm)		Branch pipe(mm)		Wall thickness (mm)	Dia. ratio $(\frac{d_o}{D_o})$
	OD	ID	OD	ID		
T-01 (GRP)	127	119	64	56	4	0.5
T-02 (GRP)	127	119	127	119	4	1.0
T-03 (GRP)	161	145	124	107	9	0.77
T-04 (GRP)	124	107	124	107	9	1.0
T-05 (steel)	140	127	76	63	6	0.5

3.4 Loading rig

To simulate the operating load experienced by a pipe section in a laboratory environment, it is necessary to have a test facility that can accommodate the pipe section specimen and distribute the load from a standard test machine into the branch pipe specimen in various directions. The pipe testing facility was designed and built [52] to allow a full-scale pipe section with a branch to be tested on a typical test machine. The rig was designed to be able to load the pipe specimen in both in-plane and out-of-plane directions. Moreover, the base of the rig can be adjusted to position the applied load on the branch of the specimen. As a result, an oblique branch can also be tested. Figure 3.3 shows a simple bending load configuration on a perpendicular junction which is used in this experiment. The photograph shows the specimen assembled with the rig mounted on the testing machine. It can be seen that , in this configuration the load can be applied directly through the branch pipe.

3.5 Thermoelastic calibration of pipe materials

Before the full-scale bending tests were performed, two experiments had to be carried out to obtain calibration constants for the relavent materials, i.e. the CSM and filament

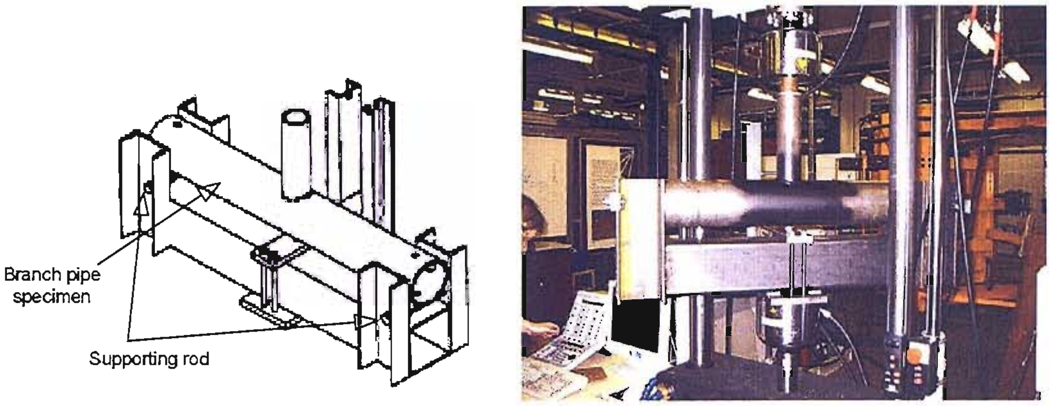

FIGURE 3.3: Bending rig used in the experiment

wound material. The specimens was not coated with the matt black paint as the surface emissivity of the material is relatively high.

3.5.1 CSM specimen

Four CSM coupons (4mm × 40mm × 200mm) were made from the materials used to over laminate the tee joint and supplied by the pipe manufacturer. Firstly it was decided to perform a tensile test to mechanically characterise the material. A tensile test until failure was performed to obtain the behaviour of the material. Due to the limited number of specimens, two of the CSM specimens were tested. A strain gauge was mounted onto the specimen in the direction of applied load to record the strain during the test.

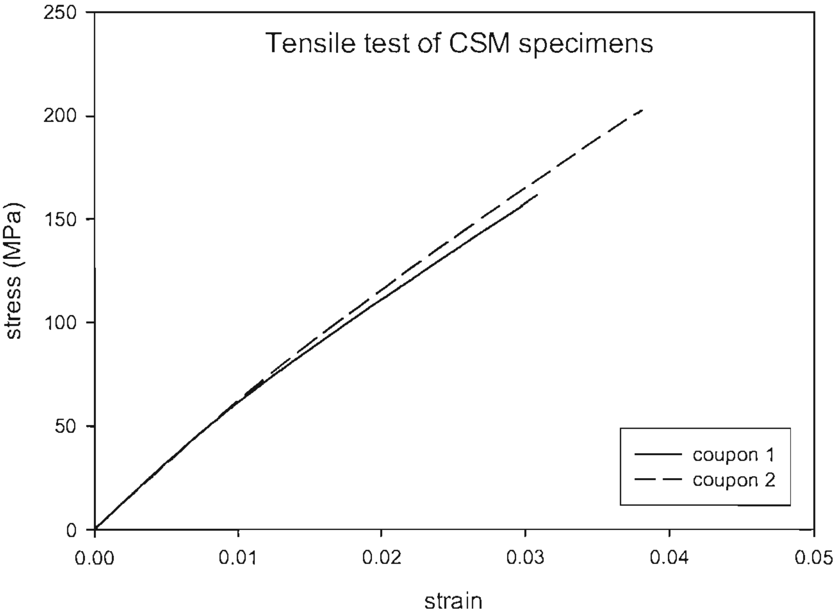

FIGURE 3.4: Stress-Strain curve from the tensile test of the two CSM coupons: loading rate = 1 mm per second.

The stress-strain curve obtained from the tests is given in Figure 3.4 and shows that the yield stress of the material is approximately 60 MPa or less. Although the failure stress and strain are substantially different, there is a good agreement in the elastic range. The two tests were considered sufficient to establish the elastic range of the material.

To obtain the calibration factor for the CSM specimen, the CSM coupons were loaded cyclically at 4.5 ± 4 kN which results in 28 ± 25 MPa, i.e. below 60 MPa. A typical thermoelastic image is shown in Figure 3.5. The box indicated in the figure is the area where the data was interrogated and the test results from all the tests are provided in Table 3.2.

The average signal and standard deviation values provided in the table are the average values within the rectangular region shown in the image. It can be seen that the results were repeatable within an error of approximately 5%. The averaged thermoelastic signal (S) was used with the calculated stress [53] and a calibration factor of **0.052** MPa/U was obtained.

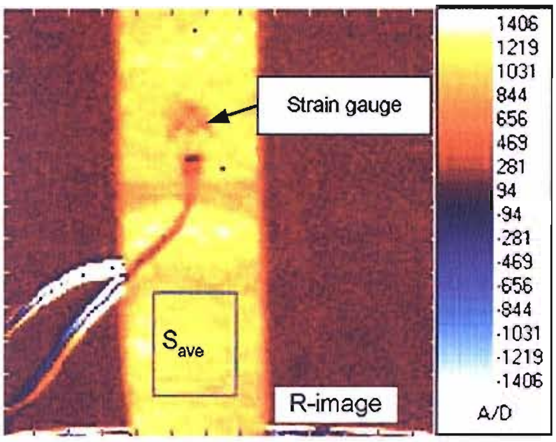

FIGURE 3.5: An example R-image observed from the CSM specimen

TABLE 3.2: Thermoelastic signal (R-signal) from each specimen under load 4.5 ± 4 kN

Specimen no.	Signal (U)	SD	Coef of variation
1	1155	90.4	0.08
2	1145	91.3	0.08
3	1123	92.7	0.08
4	1180	95.2	0.08

3.5.2 Pipe section

As the manufacturer did not supply a straight pipe section, a section of straight pipe was cut from a tee specimen of 4 mm thickness and 127 mm outer diameter for the calibration test of the pipe. A diagram of the filament wound pipe is shown in Figure 3.6.

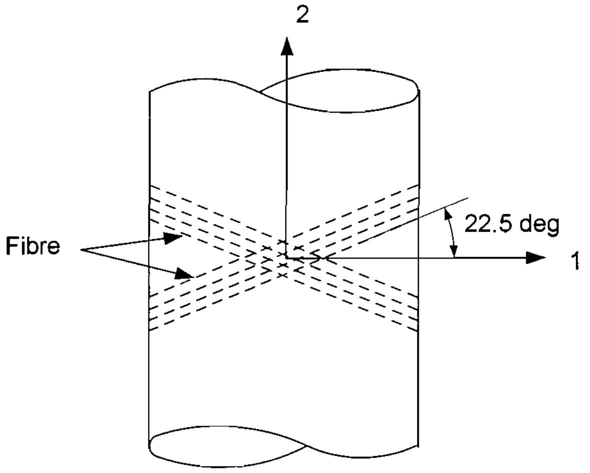

FIGURE 3.6: Orthotropic cylinder: 1 and 2 are the principal stress directions

The pipe was subjected to a cyclic load of −4.4 ± 3kN (compression) in the axial direction at 10 Hz using the same rig as described in Figure 9.10. This yields $\Delta\sigma_{\mathrm{app}} = 3.8$ MPa which is high enough to produce a good signal quality for general glass/polyester materials. The filament wound pipe was considered as an orthotropic material with principal material symmetry axes in the direction of circumferential and axial directions, i.e. direction 1 and 2 respectively in Figure 3.6. The thermoelastic equation for this case can be expressed as:

$$A^*S = \alpha_{11}\Delta\sigma_1 + \alpha_{22}\Delta\sigma_2 \tag{3.3}$$

where $\Delta\sigma_1$ and $\Delta\sigma_2$ are the stress changes in the direction of the principal stress axeses and α_{11} and α_{22} are the linear coefficients of thermal expansion in the corresponding directions which can be obtained by the standard tensorial transformation as:

$$\alpha_{11} = \alpha_p \cos^2\phi + \alpha_t \sin^2\phi \tag{3.4}$$

$$\alpha_{22} = \alpha_p \sin^2\phi + \alpha_t \cos^2\phi \tag{3.5}$$

where ϕ is the angle between the principal stress direction and the fibre direction, i.e. 22.5 degrees (see Figure 3.6)

As the cylinder was loaded in uniaxial compression $\Delta\sigma_1$ in Equation 3.3 can be eliminated and $\Delta\sigma_2 = \Delta\sigma_{\text{app}}$ so that:

$$A^{**}S = \frac{\alpha_{22}}{\alpha_{11}}\Delta\sigma_{\text{app}} \tag{3.6}$$

where $A^{**} = \frac{A^*}{\alpha_{11}}$.

In this work, the coefficients of linear thermal expansion α_p and α_t are obtained by using a formulation proposed in Ref [54]:

$$\alpha_p = \frac{E_f\alpha_f V_f + E_m\alpha_m V_m}{E_f V_f + E_m V_m} \tag{3.7}$$

$$\alpha_t = \alpha_f(1+\nu_f)V_f + \alpha_m V_m(1+\nu_m) - \nu_{pt}\alpha_p \tag{3.8}$$

$$\nu_{pt} = \nu_f V_f + \nu_m V_m \tag{3.9}$$

where E is the Young's modulus, ν is Poisson's ratio and V is the volume fraction and the subscripts f and m denote the fibre and matrix respectively. Since the exact material properties of the materials (E-glass/polyester) used to make these specimens are not available and a range of typical material properties values for polyester is relatively large, the material properties used in the calculation are assumed from generic values from Ref [55] and shown in Table 3.3.

By substituting the assumed material properties in Equations 3.7 and 3.8, and then substituting the results into Equations 3.4 and 3.5, the coefficient of thermal expansion in the principal stress directions can be obtained as: $\alpha_{11} = 11.06 \times 10^{-6}$/K and $\alpha_{22} = 22.24 \times 10^{-6}$/K. Therefore the calibration factor A^{**} could be determined.

An example of the thermoelastic data in terms of R-image from the calibration test on the GRP pipe is shown in Figure 3.7. The box in the image indicates where the average data were interrogated for this calibration exercise. The averaged signal from six tests was calculated to assess the repeatability of the results and given in Table 3.4.

TABLE 3.3: Material properties using in the coefficient of thermal expansion (CTE) calculation

Material properties		unit
Young's modulus of fibre, E_f	80	GPa
CTE of fibre, α_f	5×10^{-6}	$^{\circ}C^{-1}$
Volume fraction of fibre, V_f	0.7	-
Possion's ratio of fibre, ν_f	0.27	
Young's modulus of matrix, E_m	3.5	GPa
CTE of matrix, α_m	60×10^{-6}	$^{\circ}C^{-1}$
Volume fraction of matrix, V_m	0.3	-
Possion's ratio of matrix, ν_m	0.37	-

TABLE 3.4: Thermoelastic signal in the box area shown in Figure 3.7 under a cyclic load of -4.4 ± 3kN

Specimen no.	Signal (U)	SD	Coef of variation
1	517	79.1	0.15
2	495	90	0.18
3	482	91	0.18
4	490	88.2	0.18
5	480	79.3	0.16
6	504	77	0.15

It was found that the signal was relatively noisy. The coefficient of variation of each data set was approximately 16.7%. A similar irregularity in the signal was also observed in an experimental validation performed by Stanley and Chan [13]. With the average thermoelastic signal, S, of 485 U acquired from the test, the thermoelastic constant, A^{**}, of **0.02** MPa/U was calculated from Equation 3.6.

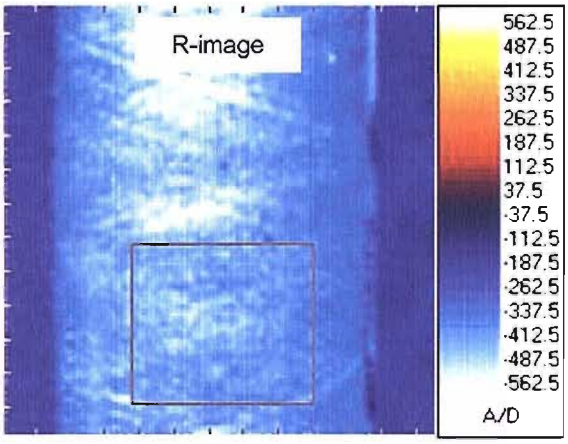

FIGURE 3.7: R-image of a pipe section under compressive load

3.6 Experimental arrangement

3.6.1 Load arrangement

Figure 3.8 shows the loading configuration used for the tee-joints. To achieve this, the rig was set up in the configuration shown in Figure 3.3 (a). The rig was rested on the lower jaws of the test machine, four pins were used to secure the tee-joint in the rig. This allows for fine adjustments during the set-up and eliminates any misalignment. The load **P** was applied towards the running pipe (see Figure 3.8). The free-end of the branch pipe was placed against the top jaw of the test machine. The load applied to each specimen is given in Table 3.5 ; in all cases the loading frequency was 10 Hz.

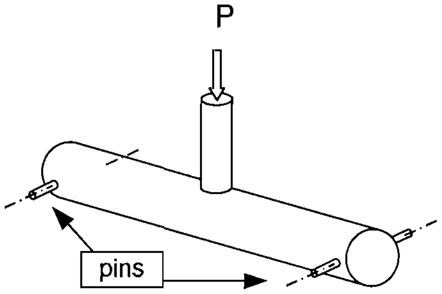

FIGURE 3.8: Load arrangement for in-plane simple bending

TABLE 3.5: Load setting for the in-plane bending test

Specimen	Mean Load (kN)	Load Range (kN)
T-01	0.5	0.9
T-02	0.5	0.9
T-03	1.0	1.5
T-04	1.0	1.5
T-05	6.0	10.0

3.6.2 Detector setting

The area of interest for the thermoelastic stress analysis is around the connection. The stress distribution on the uppermost surface was analysed first. To obtain a view of the junction area two approaches were investigated (see Figure 3.9) using the pipe configuration T-04. Firstly the detector was tilted at an angle of 30° so that both the running pipe and the branch pipe could be observed directly. The second approach was to use a front coated mirror positioned at a 45° above the area of interest. This meant that the DeltaTherm detector could remain upright during the tests. Figure 3.9 shows DeltaTherm images from both approaches and it can be clearly seen that the quality of the image from the mirror is poor. It should be also noted that the colour scale between both thermoelastic images in the figure are different. Line plots were taken from the data from the uppermost surface and are also given in the figure. Here it can be seen a clear indication of significant signal attenuation due to the use of mirror. The minimum values of each line plot signifies the location of joint region. Therefore it was decided that the Deltatherm detector would be positioned in a tilted configuration.

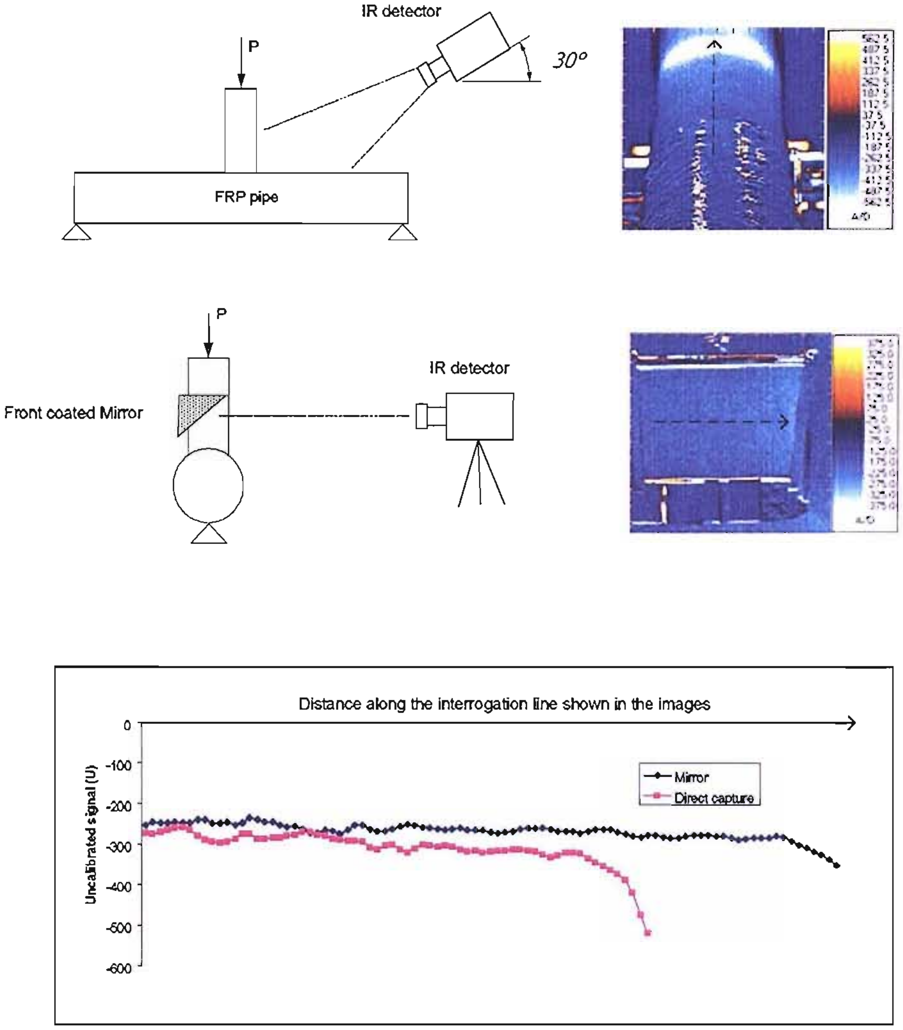

FIGURE 3.9: Top: Viewing angle and TSA image from each viewing angle, Bottom: Line plot from different view angles along the topmost surface

3.7 Results

3.7.1 Simple bending test results

A typical DeltaTherm image is shown in Figure 3.10. Alongside the DeltaTherm data a photograph of the tee-joint is given with the viewing angle identical to that of the DeltaTherm detector. In the DeltaTherm image the stress concentration at the pipe junction can be seen clearly.

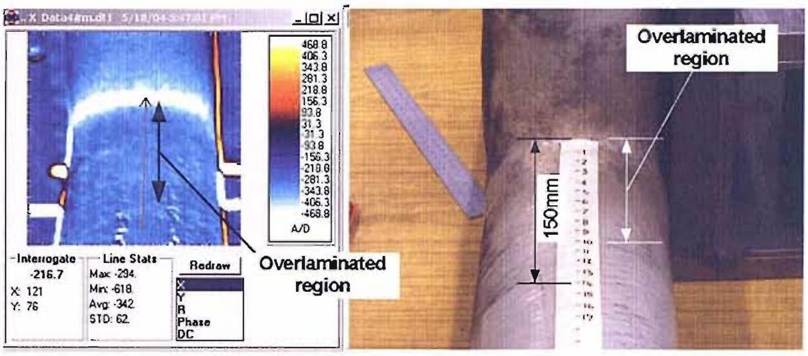

(a) (b)

FIGURE 3.10: Typical DeltaTherm image and photograph of the tee-joint from the same viewing angle

To analyse the data, line plots were taken from each of the five joints along the line indicated in Figure 3.10; these are given in Figure 3.11 (a). In each case the line was taken from 150 mm away from the branch pipe and ended at the junction. As the loads used in each test were different and T-05 is the steel joint, these plots are not directly comparable. However, all five plots show a linear region of decreasing negative signal. Four of the five plots then show a sharp decrease in signal in the proximity of the junction. The thickest pipe with the d_o/D_o ratio of 0.77 does not show the pronounced departure from the linear decrease.

It was expected that the discrepancy of signal response should be observed at the reinforced region due to the different material properties between CSM and wound pipe as the calibration factors are different. However, there was no change in signal at the 'overlaminated region'.

3.7.1.1 Stress factor evaluation

In order to compare the results, a simple "stress factor" approach was used. In the running pipe away from the junction (approx 100 mm from the starting point of each line plot in Figure 3.11) the pipe will be in simple bending. Therefore only one stress in the axial direction will exist as if it was a straight pipe loaded in simple bending. The

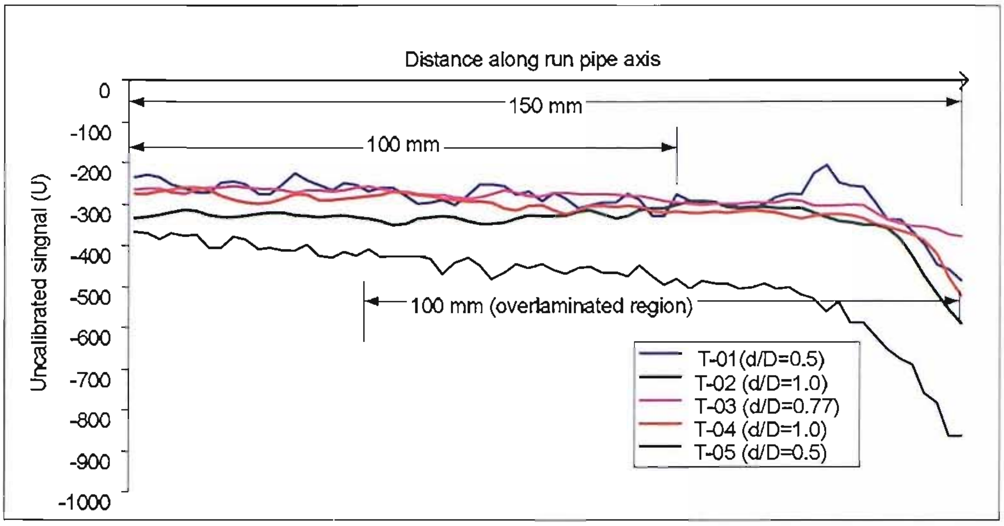

FIGURE 3.11: Line plots of TSA data: it appears that the linear region starts from the beginning of the line plot until approximately 100 mm away from the starting point. Note: d/D ≡ d_0/D_0 inTable 3.1

linear region shown at the start of the line plot in Figure 3.11 could be regarded as the equivalent signal from the situation. Extrapolating a best-fit line through this data will provide a signal value equivalent to that which would be obtained for a plain pipe in simple bending. Dividing the actual signal by these values gives a stress factor value for each point in the line plot and a means of comparing the data (see Appendix A.7). A plot of stress factors is shown in Figure 3.12. Here it can be seen that the smallest wall thickness of GRP pipe, with the greatest d_o/D_o ratio, provides a stress factor of 1.63. A stress factor of 1.50 results from the GRP configuration with $d_o/D_o = 0.5$ for the thin pipe and $d_o/D_o = 1.0$ for the thick pipe. The smallest stress factor is reported for the thickest pipe with $d_o/D_o = 0.77$ which was 1.20.

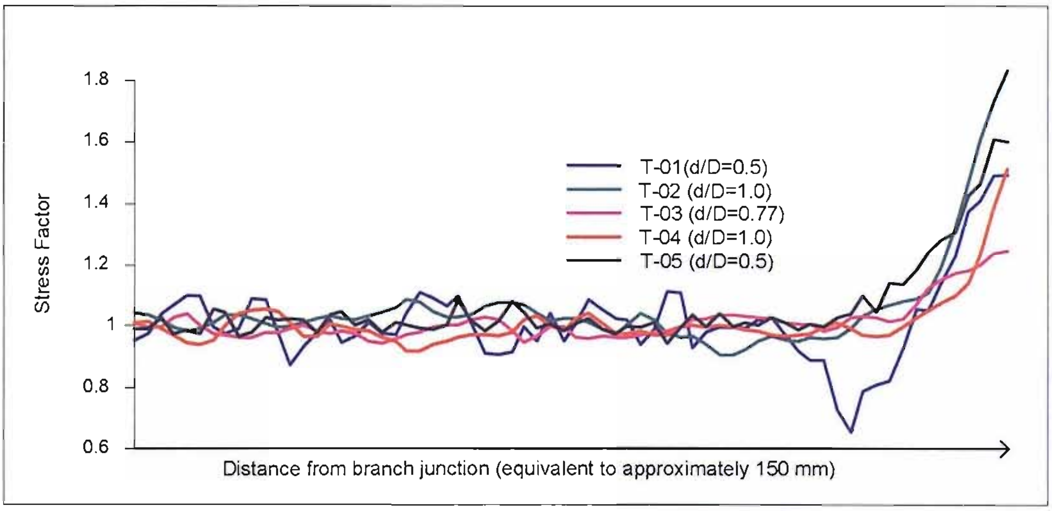

FIGURE 3.12: Stress Factors derived from TSA results

3.8 Discussion

It has been shown that both calibration factors (A and A^{**}) can be obtained by using calibration procedures described in Ref [53]. However, the CSM material will act as *strain witness* on the wound material and a complex calibration approach needs to be adopted based on the strain in the joint and not the stress. The over laminated region starts approximately 100 mm into the line plots shown in Figure 3.11. At this point there is no change in the signal, so a question must be posed: if the thermoelastic response is different for the CSM and woven material, why are the two materials providing practically identical signals. One explanation may be that the matrix is dominating the response from both. In the running pipe away from the junction the pipe will be in simple bending. Therefore only one stress in the axial direction will exist. As the winding angle was 67.5° from the axis of the running pipe and the resin content of the CSM was estimated to be greater than 70% this is a likely explanation. Further work is required to verify this.

As there is no data in the literature with which to compare the TSA data, it was decided to build a simple finite element model in ANSYS for each joint configuration. A SHELL93 (8-node-structural shell) element was used and the added thickness of the CSM was neglected. Material properties were calculated by using the fibre volume fraction for the wound structure and laminate theory. The applied load range given in Table 3.5 was used and stress sum data was produced from the FEA in order to compare with TSA data. Figure 3.13 shows a TSA plot from a T-01 joint and the equivalent FEA model. The FEA stress sum data shows excellent correspondence with the TSA qualitatively, even though the effects of the CSM overlaminated region and the coefficients of thermal expansion have been neglected. For comparison stress sum line plots were obtained from equivalent positions (see Figure 3.10) in the FEA model; these are given in Figure 3.14. The plots show similar characteristics to the line plots given in Figure 3.11. The stress sum is shown to be very small in T-02, T-03 and T-04. To compare with the TSA data stress factors were derived in a practically identical manner to those derived from the TSA data and are given in Figure 3.15. These show a very close correspondence to the TSA data.

In order to obtain quantitative stress data, it is necessary to calibrated the thermoelastic signal. However, the non-uniform and non-homogeneous of the reinforcement material (CSM) around the pipe junction may cause some difficulty in TSA interpretation. Further work is required to study the effect of the thickness as well as non-uniformity of material properties of the resin-rich region to the thermoelastic signal. Figure 3.16 shows a proposed approach to obtain strain and thermoelastic data information at various locations with different material properties.

The FE models of the specimens are also needed to be validated. Strain gauge measurement can be used to verify the results. A number of strain gauges can be mounted on

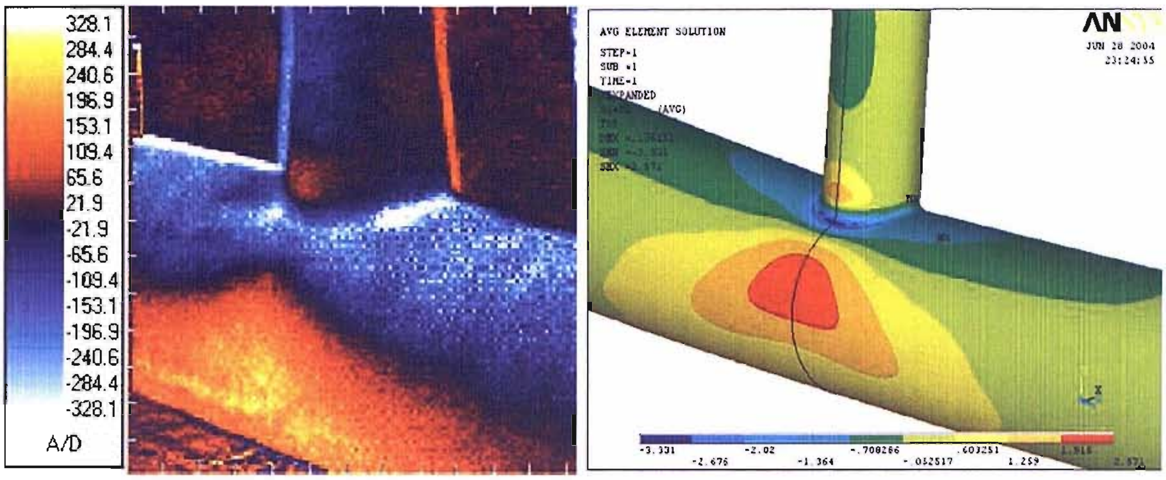

FIGURE 3.13: TSA and FEA data from T-01 joint

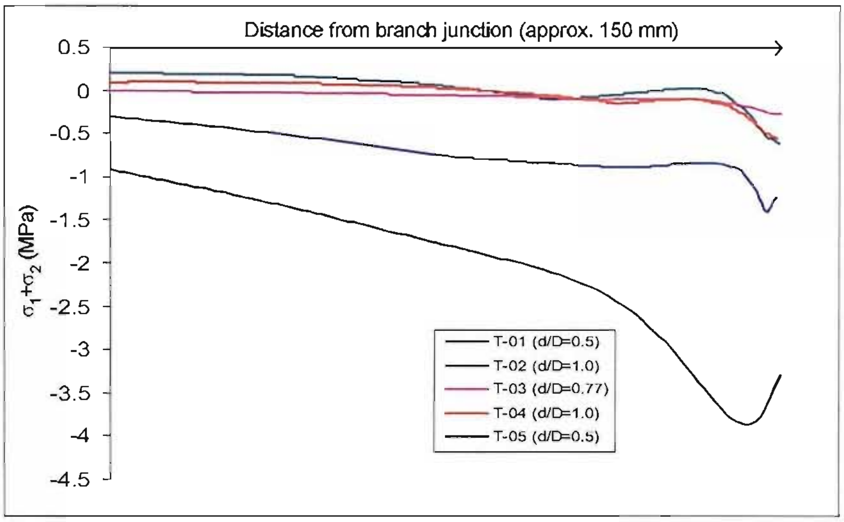

FIGURE 3.14: Line plots from FEA corresponding to the plot on Figure 3.11

the specimens at the approximate positions shown in Figure 3.17. Consequently, global behaviour of the specimens can be used to verify the FE model.

Following the logical step of the GRP pipe stress analysis is to study the stress distribution of the Tee intersection under various load conditions. As pressure rig and bending rig are available, the GRP pipe can be tested at various loading conditions. However, developing a calibration technique is considered to be more important for GRP pipe work.

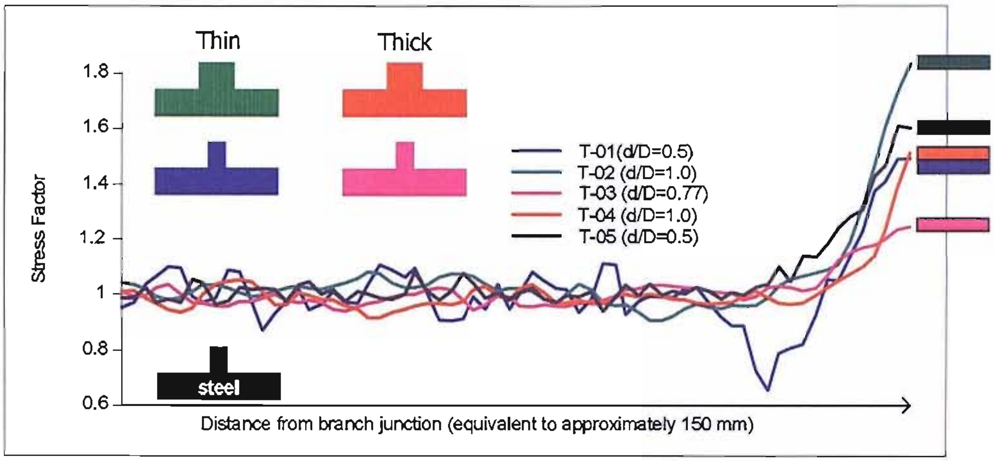

(a) TSA

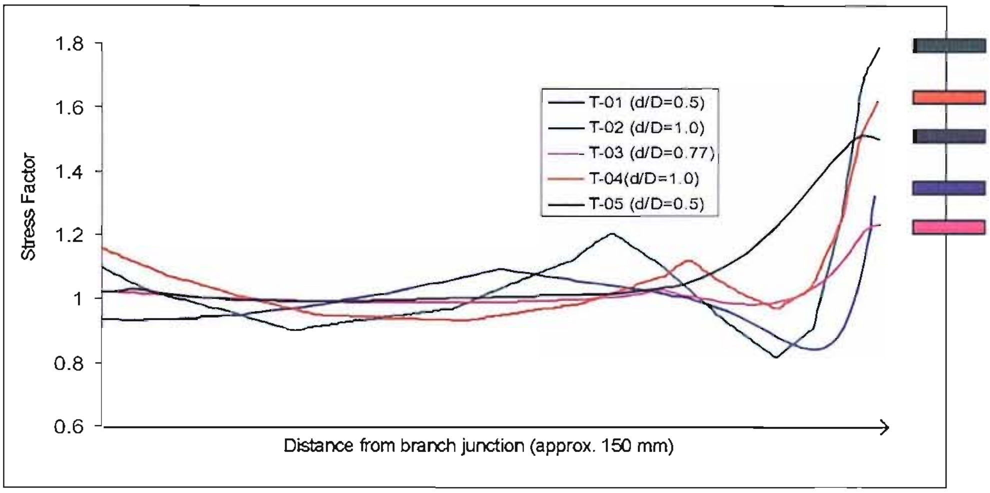

(b) FEA

FIGURE 3.15: TSA and FEA stress factor comparison

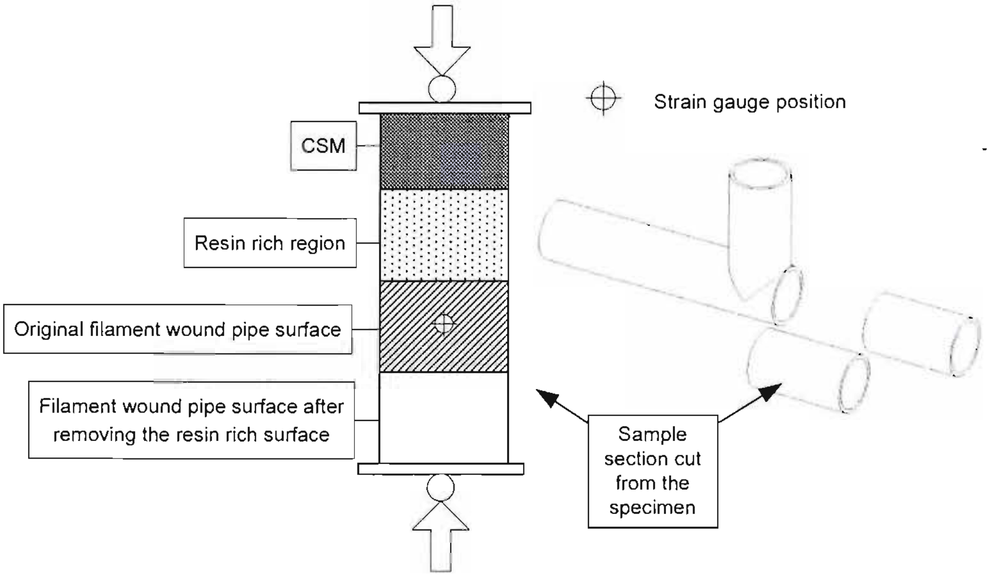

FIGURE 3.16: A sample section used in calibration exercise

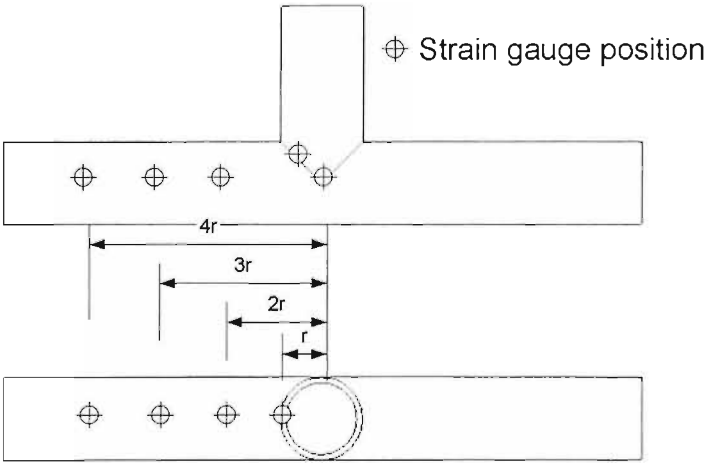

FIGURE 3.17: Strain gauge positions. Note: r is the nominal branch pipe radius ($r = OD/2$)

3.9 Conclusions

In this chapter, experimental stress analysis using TSA on GRP pipes under in-plane bending loads has been completed. The results showed that accurate stress data can be obtained from the GRP components using TSA. Stress factors obtained from the GRP components showed that the composite-pipe joints outperform a similar steel joint. The stress factors for the steel and the composite-pipe joints of similar geometry were different, indicating that the manufacturing technique causes a change in geometry that enhances the composite joint performance. In general, the results from the FE simulation showed excellent correspondence with the TSA results, qualitatively. To ensure that the FE models are correctly representing the actual behaviour of the GRP specimens, these models need validation. Due to the fact that an analytical solution is not available and may not be possible, in the future the FE models should also be validated against the results from strain measurement using strain gauges.

The main purpose of this chapter was to show that TSA can be used for stress analysis on large cylindrical structure components such as pipework. The work has shown this can be successfully achieved and therefore pursuing TSA as a technique for damage assessment on pipe structure is worthwhile. Therefore the remainder of this thesis concentrates on developing the theory and application of TSA to damaged metallic pipework structure.

Chapter 4

Preliminary feasibility study

4.1 Introduction

The objectives of the initial experiments described in this chapter are to demonstrate that typical sub-surface flaws can be detected using TSA. In Chapter 2, it was determined from the literature that SPATE could be used to detect sub-surface flaws of $a/t = 0.375$ [12]. In this chapter the idea will be explored in further detail. It is known that sub-surface stresses can be revealed by non-adiabatic behaviour [36]. Non-adiabatic behaviour occurs when the loading frequency is not sufficient to minimise heat conduction [56]. Therefore, the thermoelastic response over a range of loading frequencies will be studied.

In general damage in materials is of arbitrary configurations. The geometry of the damage determines the damage severity and hence stress gradient around the damage. To examine the effect of damage geometry to the thermoelastic response, two types of artificial sub-surface flaws were machined in flat aluminium alloy plate specimens. The DeltaTherm system (DT1000) was used to record the thermoelastic response from both the damaged and undamaged side of the specimen. A brief description of the DeltaTherm system's mode of operation is described in the following section with more details provided on IR thermography in Chapter 5.

4.2 Experimental work

4.2.1 Test specimens

Two aluminium plate specimens of 5.3 mm thickness were fabricated. The width of the plates was 340 mm and the length was 460 mm. Diagrams of the test specimens are provided in Figure 4.1 with a cross-sectional view across the damage.

Figure 4.1 (a) shows a drawing of 'specimen 1' containing three part-through slots machined using EDM. The slot width was 0.8 mm. The profile of the slot is semi-circular and each of the slots was machined using an electrode of diameter 20 mm. This means for different depth slots there are different slot lengths. For comparison purposes, a dimensionless parameter of the ratio of the flaw depth and the thickness of the specimen, a/t, was established to give three defect extents : $a/t = 0.75$, 0.50 and 0.25. Figure 4.1 (b) shows a diagram of 'specimen 2' that contains three flat bottomed part-through holes of diameter 10 mm positioned along the centre line of the plate. Three flaws of $a/t =$ 0.75, 0.50 and 0.25 were machined.

Essentially, the specimens were initially "damaged" by the machining of the simulated flaws therefore it was necessary to determine the maximum load range to prevent specimen failure during testing. As the crack-like slot in specimen 1 is much more severe than the flat bottomed hole, the SIF for this specimen was calculated. To do this, the circular profile slot is approximated to a semi elliptical surface crack for which there is a solution in the literature [57]. An empirical formula derived in Ref [58] for a mode I elastic SIF was used to calculate the maximum SIF at the middle of the crack front of the most severe damage ($a/t = 0.75$). Full details of the calculations are provided in Appendix A.3. The maximum tensile stress that the specimen 1 could endure was calculated as 12 MPa assuming that the flaws are cracks and the critical SIF for the crack opening mode (K_{IC}) of the material is 50 MPa$\sqrt{\mathrm{m}}$.

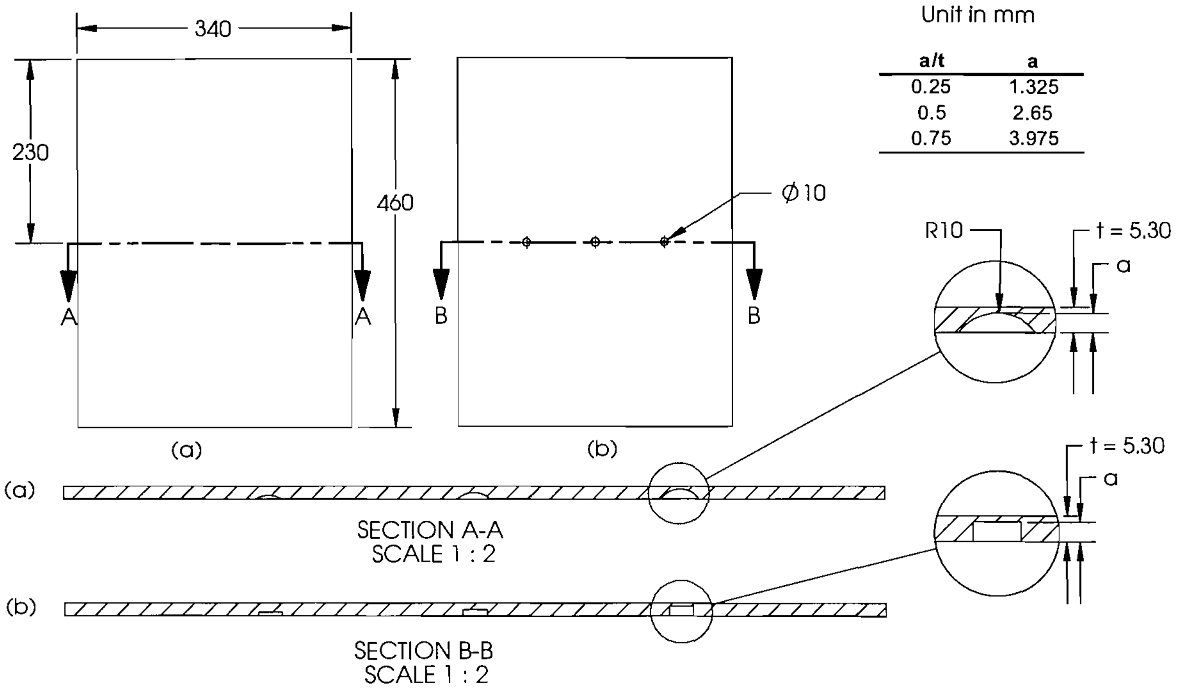

Unit in mm

a/t	a
0.25	1.325
0.5	2.65
0.75	3.975

FIGURE 4.1: Drawings of the specimens: (a) specimen no.1: the plate with multiple EDM part-through slots, (b) specimen no.2: the plate with multiple part-through holes

4.2.2 Testing arrangement and damage nomenclature

Prior to the test each specimen was coated with a very thin layer of matt black paint to enhance the surface emissivity. The specimen was then mounted in an Instron servo hydraulic test machine using a jig designed to spread the load uniformly across the width of the plate. the loading configuration is shown in Figure 4.2. The plate was secured tightly using 14 studs with threaded ends with two steel reinforcement strips at either end of the specimen. A set of thicker steel strips were attached between a universal joint and the reinforcement strips by pins to ensure a uniform load distribution across width of the plate. The universal joints connected the steel strip to the test machine hydraulic grips. This arrangement also allows the test specimen to move freely and hence eliminates any bending caused by the possibly of test machine grip misalignment.

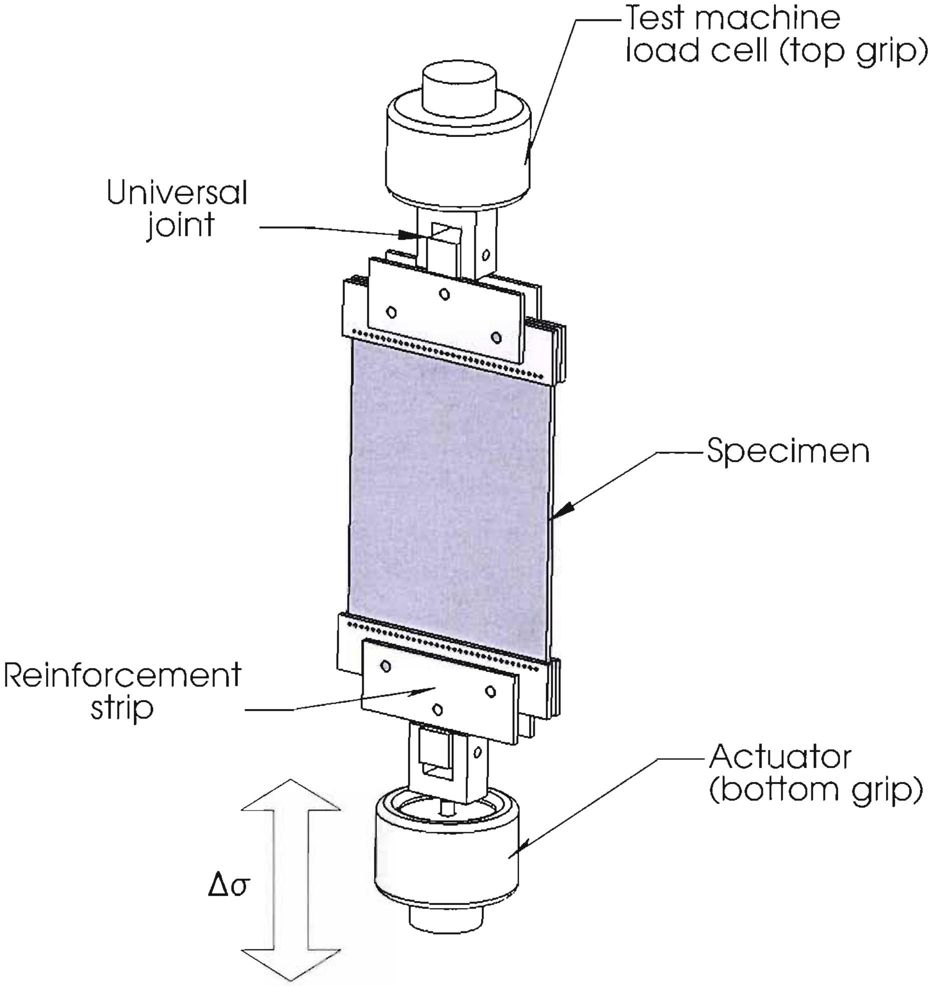

FIGURE 4.2: Test configuration of the plate specimen

Specimen 1 was tested first. The DeltaTherm system (DT1000) was used to record the thermoelastic response from both faces of the plate, i.e. damaged and non-damaged sides. The operating distance of the detector was approximately 800 mm in order to observe all three damage sites at the same time. As a consequence, the resolution of 1.8 mm per pixel was achieved. The detector operated at the sampling rate of approximately 200 frames per second, which is recommended by the manufacturer as an optimal value for most experiments [59]. The electronic shutter was set at 35 % to provide a good signal to noise ratio for the test. All integration images were captured using integration time of 30 seconds and accumulation time of 8 seconds. The details about setting the integration and accumulation times are described in the DeltaVision software online manual [59].

Initially, a load of 12 ± 10 kN was applied according to the limited stress range determined previously to prevent the specimen failure. However, the noise level in the thermoelastic data was too excessive and prevented any meaningful readings. This indicated that the stress level in the specimen was too low for this particular camera setting and the calculation based on semi-elliptical cracks described above is conservative for the EDM slots. Therefore, the load range was increased until an acceptably high signal to noise ratio was achieved (i.e. the coefficient of variation in the signal was approximately less than 10 %). As a consequence, the specimen was tested under a constant amplitude sinusoidal tensile loading of 25 ± 20 kN. This is equivalent to $\Delta\sigma = 22$ MPa.

To study the influence of loading frequency on thermoelastic response, the loading frequency was varied from 6 Hz up to 24 Hz. The loading frequency of 24 Hz was the maximum that could be achieved at this load range due to the limitations of the test machine.

After trial and error during the experiment, it was found that load range could be slightly reduced to 20 ± 15 kN ($\Delta\sigma = 17$ MPa) provided that the electronic shutter of the DeltaTherm system was increased to 53% which maintained a good signal to noise ratio, so that higher loading frequencies could be applied. Therefore, the non-adiabatic behaviour over a larger frequency range was investigated. The settings for each test are summarised in Table 4.1.

TABLE 4.1: Summary of test settings

Experimental settings	Specimen 1		Specimen 2	
	back side	front side	back side	front side
Load range (kN)	25 ± 20	20 ± 15	20 ± 15	20 ± 15
$\Delta\sigma_{\mathrm{nom}}$ (MPa)	22	17	17	17
Load freq (Hz)	6–24	6–30	6–30	6–30
Ele. Iris (%)	34	53	53	53

To examine the thermoelastic response at particular damage locations in more detail, positions of interest were identified and are indicated in Figure 4.3 (a). Three on the back side are identified as points 1, 2 and 5 and two on the front side are identified as point 3 and 4. In specimen 1 Points 3 and 4 are at the tips of the slot on the front surface of the plate, and points 1 and 2 are at the corresponding positions on the back surface. These four positions are similar in specimen 2 (Figure 4.3 (b)), i.e. points 3 and 4 are at the edge of the hole and point 1 and 2 are at the equivalent positions on the back surface. Point 5 is only defined in specimen 1 representing the projected position of the deepest front profile of the slot (i.e. equivalent to the crack-tip for growing into the plate) on the back surface. The average values of point 1 and 2 and point 3 and 4 were used as a single data point for the back and front surfaces respectively.

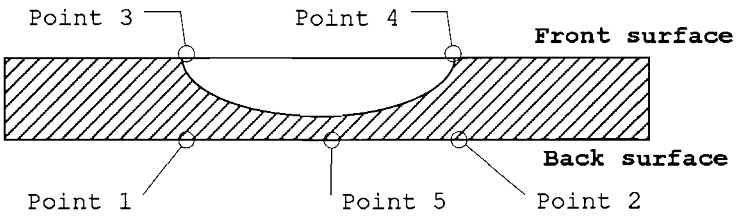

(a) Specimen 1

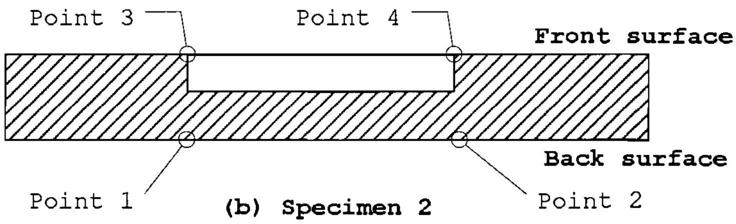

(b) Specimen 2

FIGURE 4.3: Damage nomenclature

4.3 Results

Typical thermoelastic data plots in terms of X, Y and phase images captured from the damaged and undamaged side for both plates are shown in Figure 4.4, 4.5, 4.6 and 4.7. In each figure, the image was recorded at loading frequency of 10 Hz. A line plot is taken along the damaged site (shown as Line 1 in the X-image). Line plots were also taken from the Y and phase image at the identical locations.

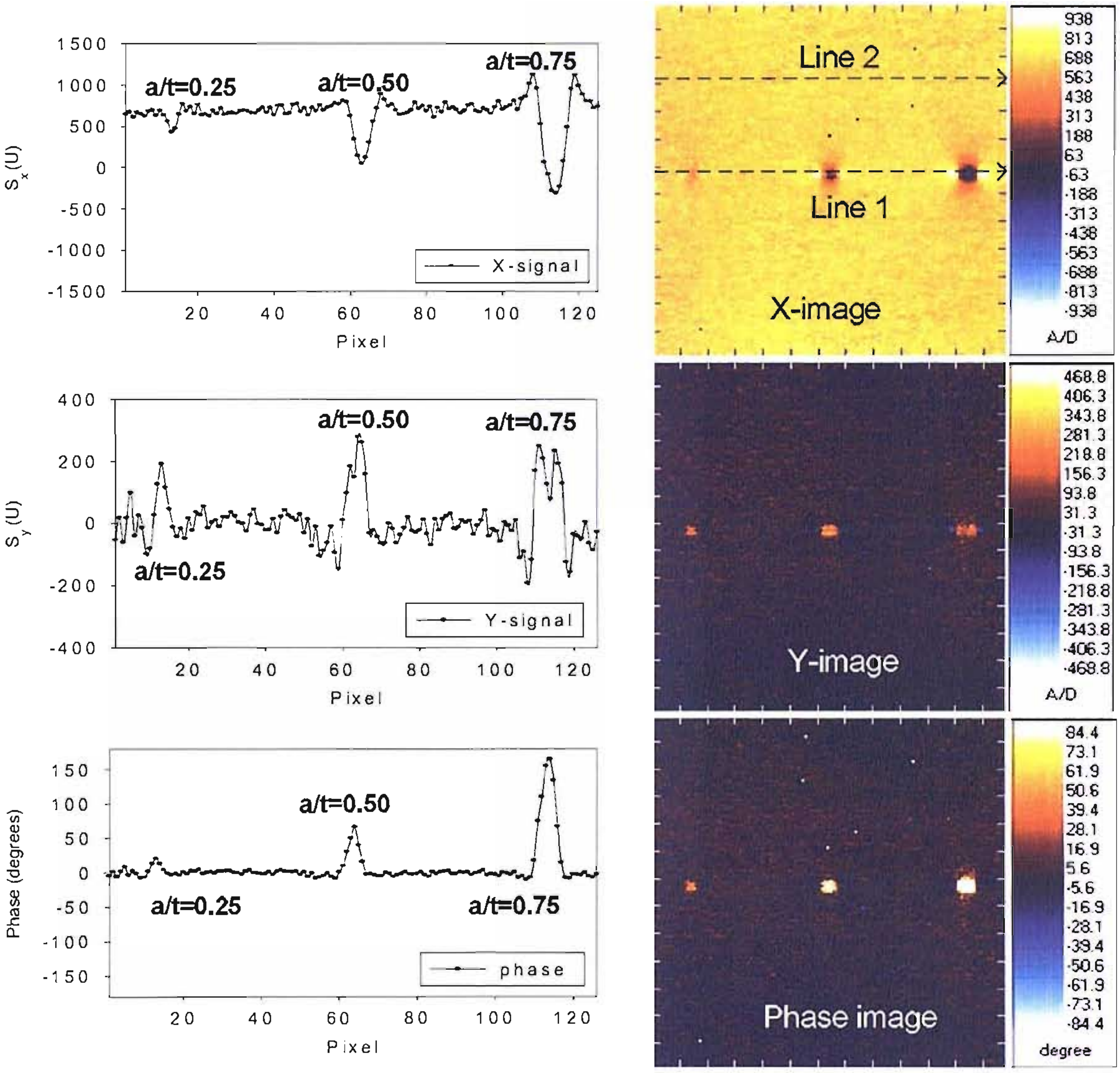

FIGURE 4.4: X, Y and phase images from specimen 1 and line plots along line 1 on the damaged side

Figure 4.4 shows the image from the front side of specimen 1. Away from the tip of the slots, the signal is fairly constant. The signal increases rapidly up to the tips of the slots. At the tip of the severest damage i.e. $a/t = 0.75$ the highest X signal is obtained while the least damage produces lower signal. The signal drop around the middle of each slot indicates that very low stress occurred.

In terms of the Y-image and phase data, the maxima occurs at the most severe damage site while the minimum occurs at the shallowest slot. A decrease in the Y signal at the crack tip is also observed. These provide further evidence that heat conduction is taking place in the region of high stress gradient near the damage sites.

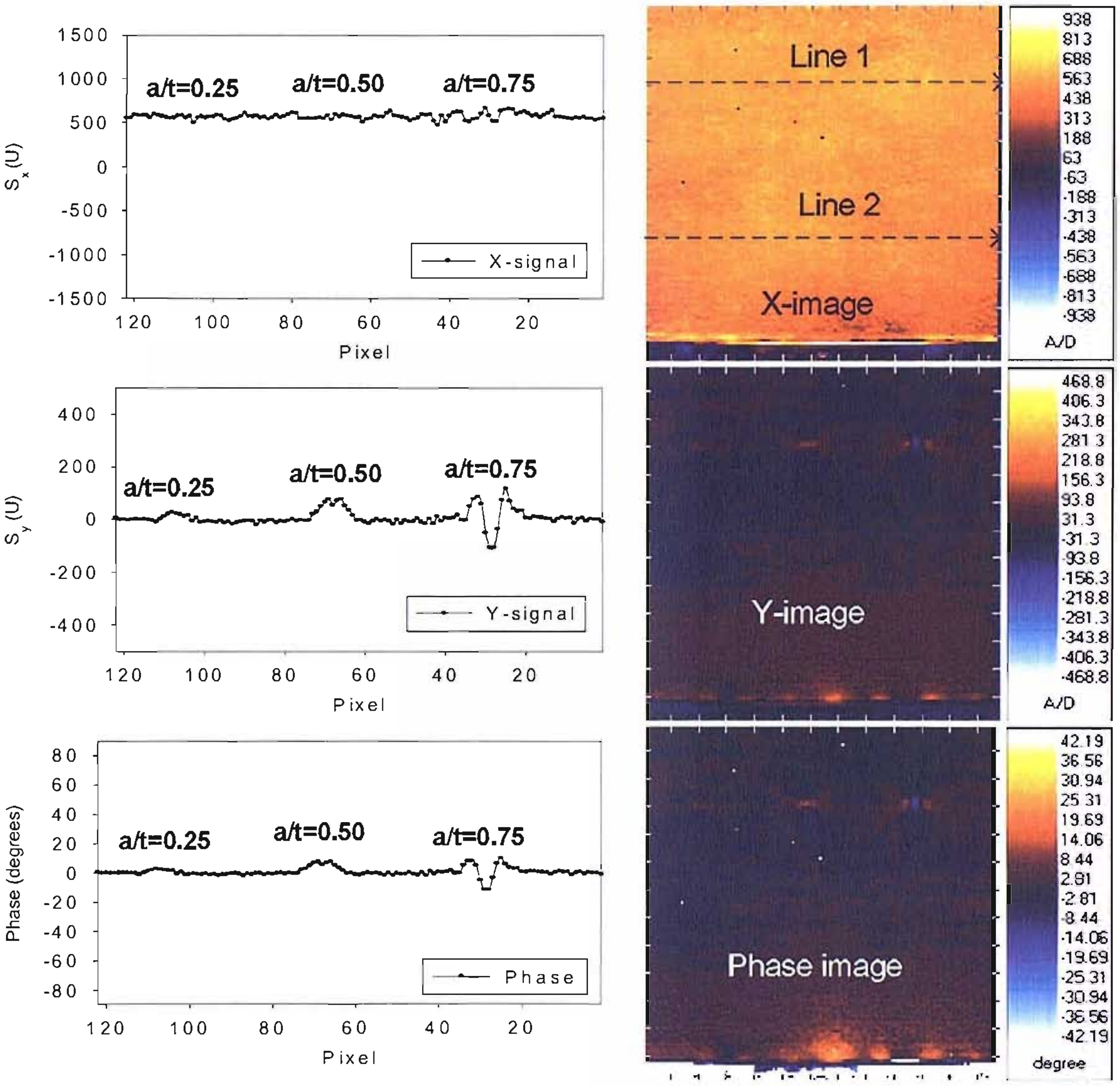

FIGURE 4.5: X, Y and phase images and from specimen 1 and line plots along line 1 on the undamaged side

In Figure 4.5 the data was captured from the other side of the specimen (i.e. the undamaged surface). Despite a small perturbation of the X signal at $a/t = 0.75$, without the prior knowledge of the damage location, it is difficult to identify the locations of damage in the X image. In the line plot of the in-phase data, the signal appears to be constant along the damage site. However, in the Y and phase data the signal at the damage locations departs from the zero condition and the location of the damage can be clearly identified. The trend is that the more severe the damage, the higher Y signal. However, at the position of point 5 shown in Figure 4.3, a decrease in signal is observed. This characteristic is evident when $a/t = 0.50$ and becomes more obvious when the damage is more severe i.e. $a/t = 0.75$, to the extent that the signal becomes negative.

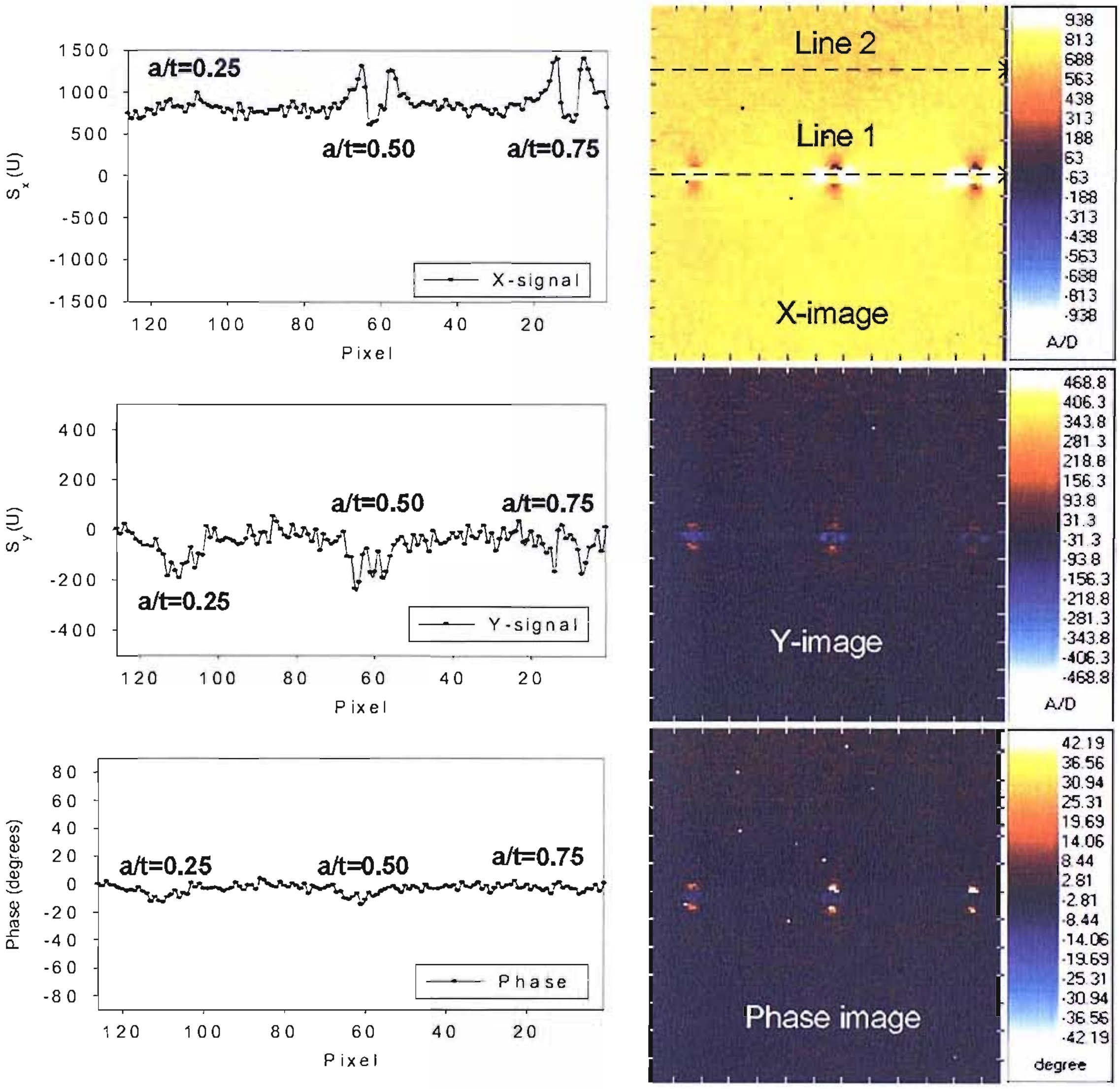

FIGURE 4.6: X, Y and phase images and from specimen 2 and line plots along line 1 on the damaged side

In Figure 4.6, data captured from the front side of specimen 2 (see Figure 4.1(b)) is shown. The data was recorded at load frequency of 10 Hz. It can be seen that the trend of the X-image is similar to that observed from the specimen 1, i.e. the signal away from the flaw is fairly constant with high signal to noise ratio, but the signal near the edge of the holes increases rapidly up to the edge of the holes. The signal increases with

a/t ratio at the damage site. The finite signal at the middle of each flaw represents the signal from the flat bottom of the hole carrying a tensile stress. In terms of the Y and phase image, the strength of the out-of-phase signal at the edge of the flaws is similar to what was observed from the first specimen (see Figure 4.4) because these are the high stress gradient regions. The gradient of the out-of-phase signal on specimen 2 was expected to be smaller than that on specimen 1, however, it is not noticeable from the plots as the resolution of the plots is too low.

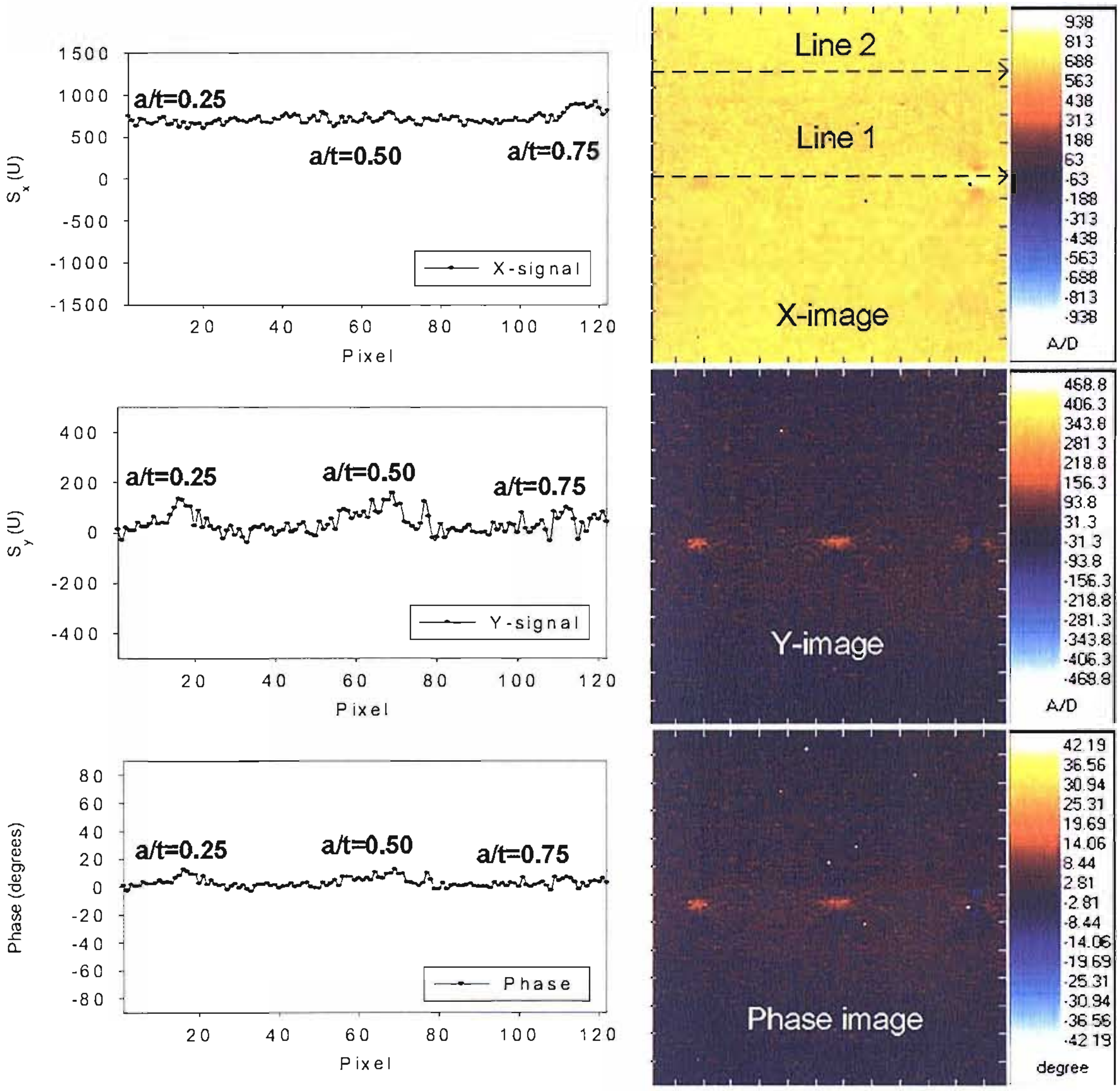

FIGURE 4.7: X, Y and phase images and from specimen 2 and line plots along line 1 on the undamaged side

TSA data recorded from the undamaged side of the specimen 2 is shown in 4.7. As expected, the X image shows only a very small indication of the damage; only at the severest damage sites can a change in S_x be observed. This might be caused by local deformation. Again, the Y image can be used to identify the damage site. In this plate, however, the gradient of the out-of-phase signal is not as large as that observed for specimen 1.

To study the influence of the loading frequency on the thermoelastic response, a number of images captured at 6, 12, 18 and 24 Hz are presented together for both plates in Figures 4.8, 4.9, 4.10 and 4.11. X and Y images are shown as well as line data across the damage sites.

Figure 4.8 shows data captured from the damaged side of specimen 1. A comparison of the X and Y images shows that the damage can be seen in the X data and the signal increases with a/t at the damage site. In the Y data away from the damage the signal is zero with some out-of-phase behaviour at the damage site. As loading frequency increases there appears to be little effect on the X image. However, in the Y image the out-of-phase data reduces with increasing loading frequency. The line plots in Figure 4.8 provide more detailed information on the effect of loading frequency. The in-phase data clearly shows that changes in frequency in the range of 6-24 Hz has little effect on the response. The increase in signal at the edges of the damage with increasing damage severity is apparent with the maximum average signal of 1150 for $a/t = 0.75$, 935 for $a/t = 0.50$ and 732 for $a/t = 0.25$. The out-of-phase data away from the damage is zero. At the damage sites the readings are non-zero, indicating a non-adiabatic response.

In Figure 4.9, a similar comparison plot of the in-phase and the out-of-phase images captured from the undamaged side of the same plate is shown. It appears that the influence of loading frequency on the in-phase signal is insignificant. The in-phase signal for various load frequencies is virtually the same. On the other hand, a change of the out-of-phase data at the damage locations is very noticeable when the loading frequency increases. The out-of-phase signal at the damage site increases with the loading frequency, but it does not change away from the damage. This indicates that the non-adiabatic response is influenced by the change of loading frequency and it can be observed readily from the undamaged side of the plate.

According to the experimental results, the out-of-phase signals at the damage of $a/t = 0.75$ and $a/t = 0.50$ are much greater than that observed from $a/t = 0.25$. The maxima of both $a/t = 0.75$ and $a/t = 0.50$ are virtually the same at the same loading frequency. These are 220 at 24 Hz, 180 at 18 Hz, 150 at 12 Hz and 50 at 6 Hz. However, the shape of each plot is completely different in that there is a sharp drop in the out-of-phase signal between the two peaks for $a/t = 0.75$ while only a single peak is observed at the damage of $a/t = 0.50$.

In Figure 4.10, thermoelastic data readings were taken from the front side of specimen 2. When the loading frequency increases, the in-phase data is virtually unchanged, which implies that adiabatic conditions are maintained. In terms of the out-of-phase data, increasing loading frequency causes a reduction of the Y-signal at the damage location. The reduction of the magnitude of the out-of-phase signal at the edge of the holes is easily distinguishable, particularly at the severest damage site. There is no influence of increasing loading frequency on the out-of-phase signal at the nominal region. This finding is similar to that for specimen 1.

In Figure 4.11, the data was captured from the back side of the plate. A comparison of in-phase and out-of-phase images on the top of the figure shows that damage locations can be detected clearly only at the severest damage from the in-phase image, but all damage location can be seen in the out-of-phase image. There are similar trends in the line plots to those for specimen 1, i.e. a double peak of S_{y} at the severest damage and a single peak at those with less severe damage. However, it is noticeable that the out-of-phase signal at the damage site of specimen 1 is more localised.

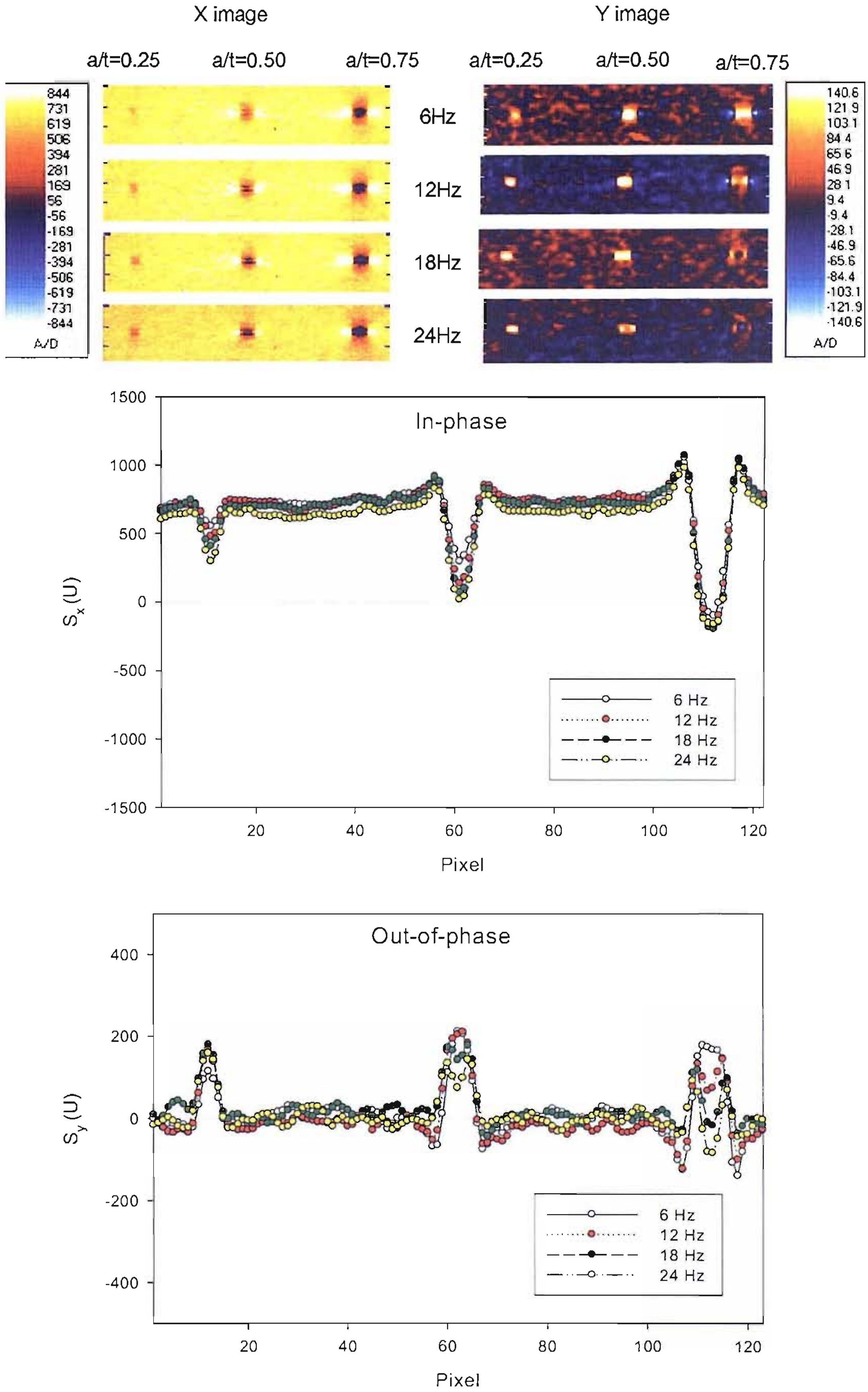

FIGURE 4.8: Thermoelastic response influenced by load frequency. The data was taken from the damaged surface of specimen 1

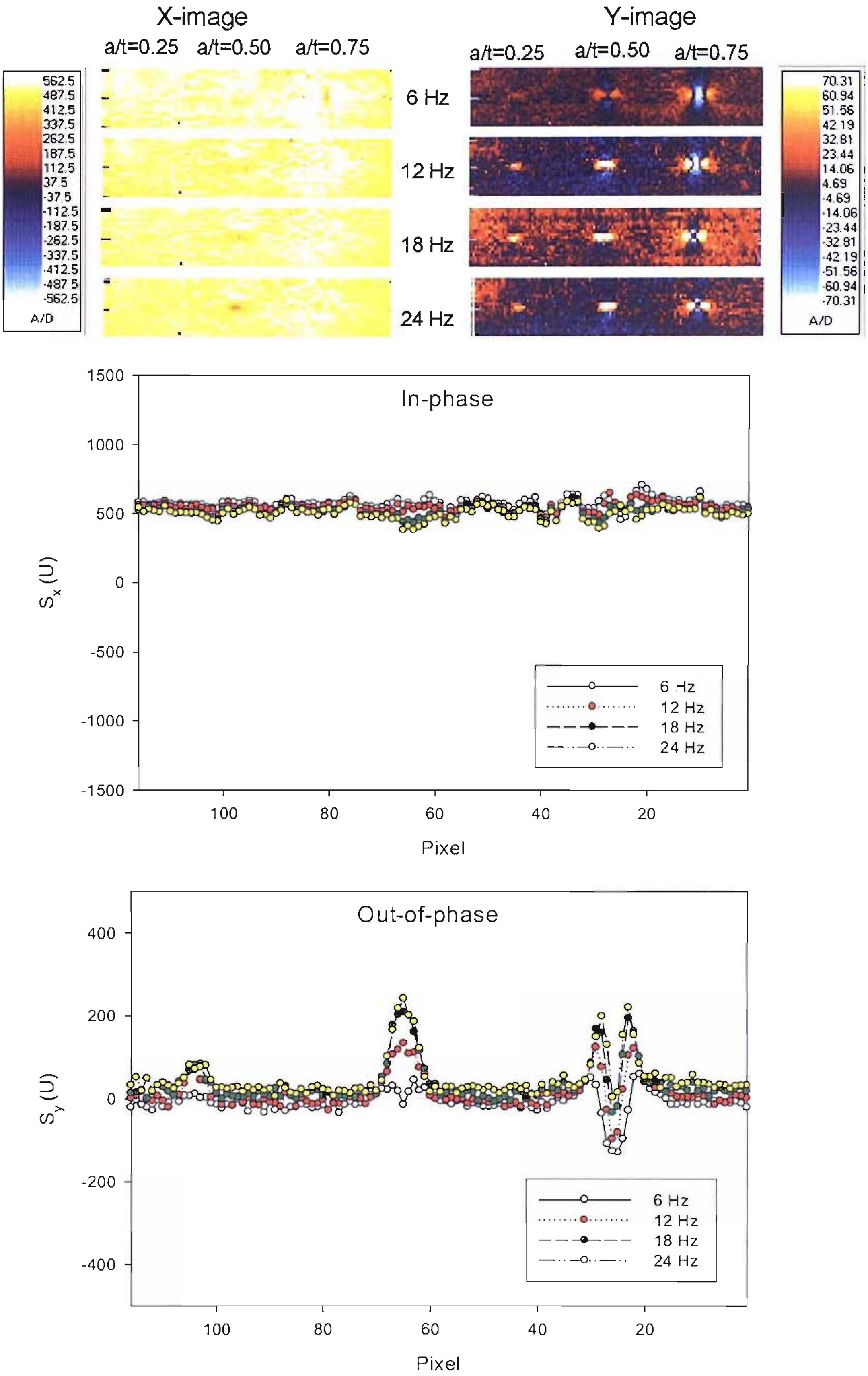

FIGURE 4.9: Thermoelastic response influenced by load frequency. The data was taken from the undamaged surface of specimen 1

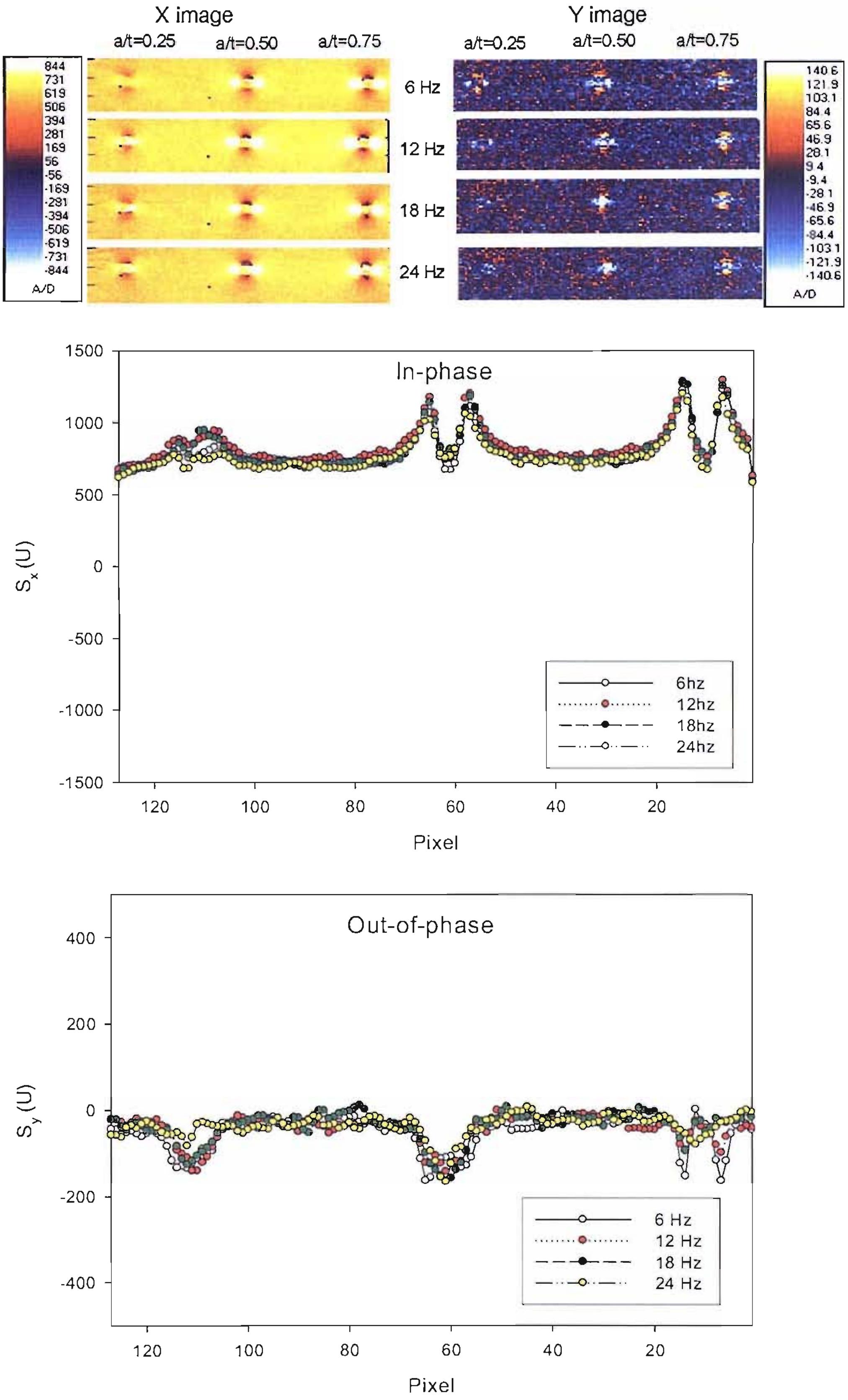

FIGURE 4.10: Thermoelastic response influenced by load frequency. The data was taken from the damaged surface of specimen 2

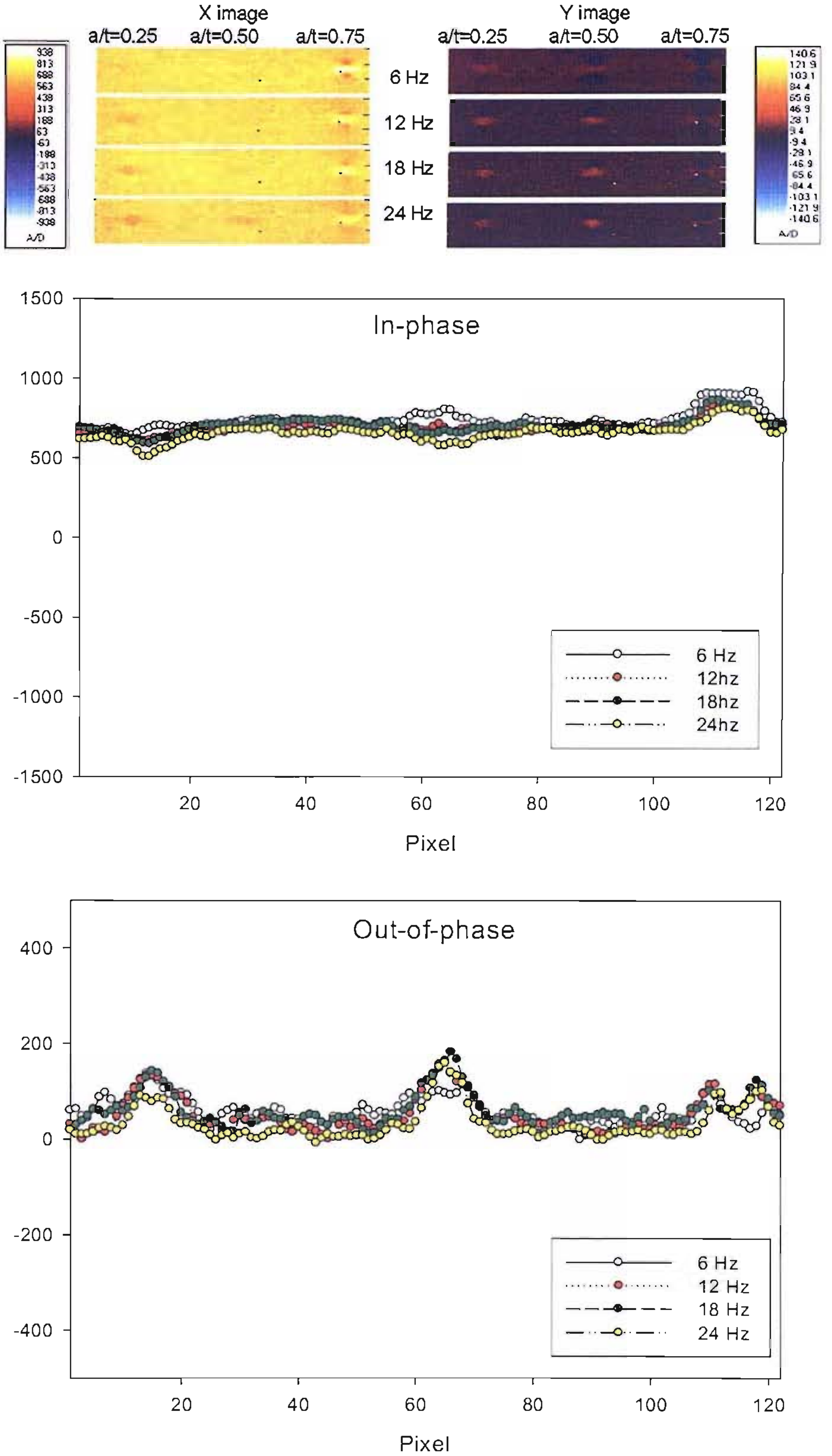

FIGURE 4.11: Thermoelastic response influenced by load frequency. The data was taken from the undamaged surface of specimen 2

4.4 Analysis of Results

In order to study the thermoelastic response in more detail around the damage over a range of frequencies, data point interrogation was carried out at the locations shown in Figure 4.3. In Figures 4.12, 4.13, 4.14 and 4.15, the thermoelastic response at these locations are plotted against loading frequency. These plots show the influence of both damage extent and loading frequency on the thermoelastic response at various points around the damage.

The nominal signal (S_{nom}) was taken from corresponding points on line 2 in the X-image as shown in Figure 4.4, 4.5, 4.6 and 4.7. S_{nom} and S_{x} are plotted together in Figure 4.12 to show the consequence of the damage on the in-phase thermoelastic measurement. In each of the plots shown in the figure, the value shown is an average of the two reading positions. Figure 4.12 (a) and (b) shows the reading from the damaged side of specimen 1 and 2 respectively. From these plots, it can be seen that S_{nom} and S_{x} is essentially constant over the range of loading frequency for each specimen. In Figure 4.12 (c) there is a clear reduction in thermoelastic signal over the frequency range. In Figure 4.12 (d) S_{x} reduces slightly, with the reduction most prominent for the severest damage. In all cases the severest damage gives the highest signal. This analysis clearly shows that a non-adiabatic response is occurring on the undamaged side of the plates as a consequence of the subsurface damage.

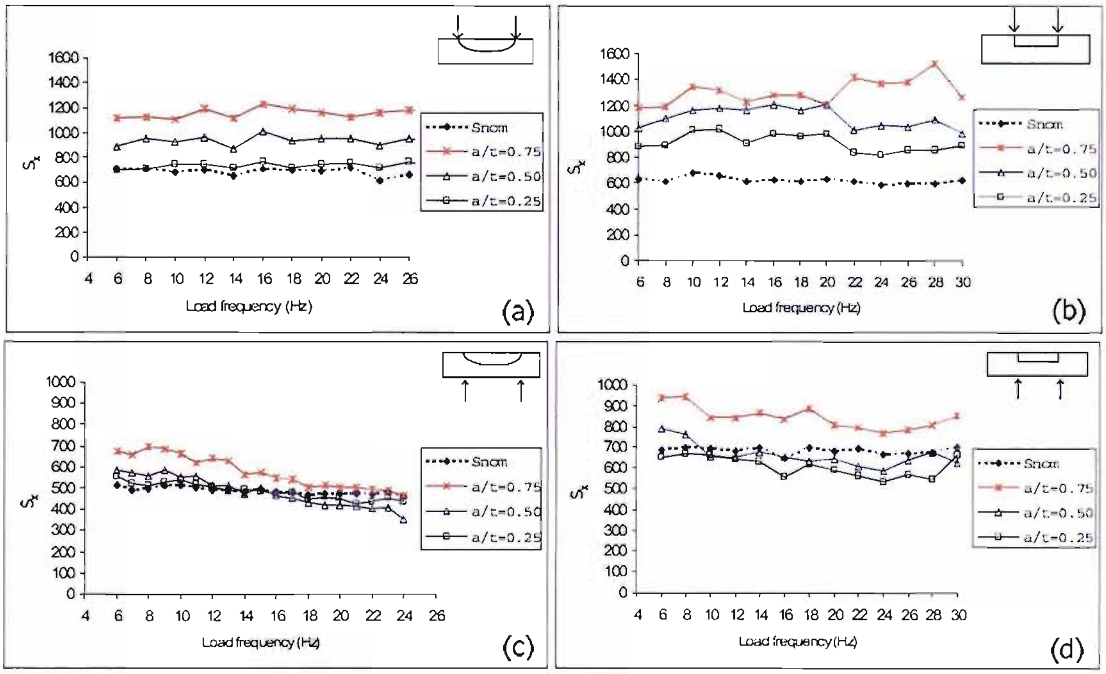

FIGURE 4.12: Influence of load frequency to the in-phase signal at positions 1-2 and 3-4 in Figure 4.3

The S_{nom} value was then used to normalised the results by dividing the signal obtained from damage sites by the average value of S_{nom}. These values can be considered as a 'stress factor'. A plot of the stress factor and corresponding phase change observed at point 1 and 2 is shown in Figure 4.13. It should be noted that the phase information is not changed by this operation. Points 1 and 2 are on the undamaged face of the plate and therefore represent readings that might be taken from a subsurface flaw. In specimen 1 this point is projected from the intersection of the slot and in specimen 2 this is the edge of the hole at the maximum stress concentration. The data from specimen 1 is plotted in Figure 4.13 (a) and (b) and that from specimen 2 is plotted in Figure 4.13 (c) and (d). In Figure 4.13 (a) all stress factors from all damage severities decrease at practically the same rate as the loading frequency increases. The stress factor of the severest damage is always the highest and that of the least damage is always the lowest. The most interesting phenomenon in the test results can be observed in Figure 4.13 (b) where the phase angle increases dramatically with loading frequency for all damage severities.

The stress factor obtained from the undamaged side of specimen 2 is shown in Figure 4.13 (c) and shows only a slightly change over the frequency range. Likewise the phase angle (Figure 4.13 (d)) appears more constant and does not show the same trend observed in specimen 1.

When similar information is analysed at the central position of specimen 1 (i.e. position 5 of Figure 4.3), the behaviour of the damage $a/t = 0.50$ and $a/t = 0.25$ are nearly the same as observed at position 1 and 2 (see Figure 4.14 (a) and (b)) but the stress factor at $a/t = 0.75$ tends to increase with load frequency and the phase angle for $a/t = 0.75$ is shifted down by approximately 20 degrees, but has the same gradient as the plot of $a/t = 0.50$. When $a/t = 0.25$ there is an initial increase in phase angle which then becomes constant at around 10 degrees.

Figure 4.15 shows similar plots as shown in Figure 4.13 but the thermoelastic data was observed from the front side instead. As expected, the stress factor (Figure 4.15 (a)) at the edge of the severest EDM slots is the largest and those of $a/t = 0.50$ is larger than those of $a/t = 0.25$. The trend of the stress factor is relatively uniform over the loading frequency range. The same trend is observed in the other specimen as well. In terms of the phase angle, the data from all damage sites appears to converge to zero degrees when the loading frequency increases.

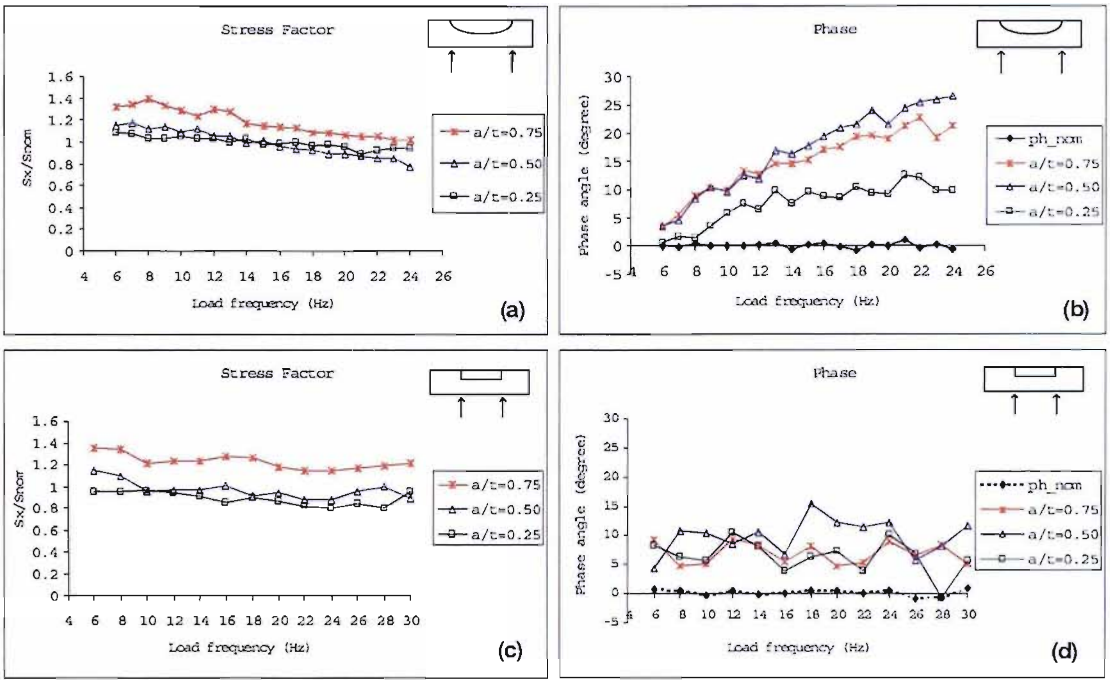

FIGURE 4.13: Stress factor and phase plot at position 1 and 2 in Figure 4.3

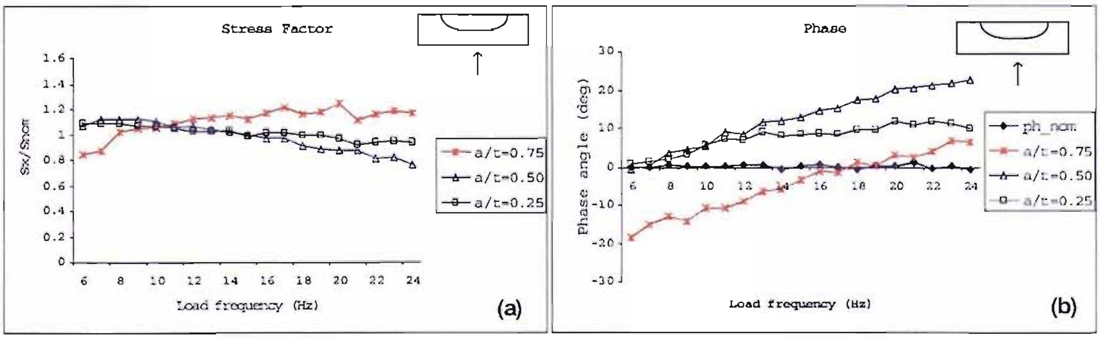

FIGURE 4.14: Stress factor and phase plot at position 5 in Figure 4.3

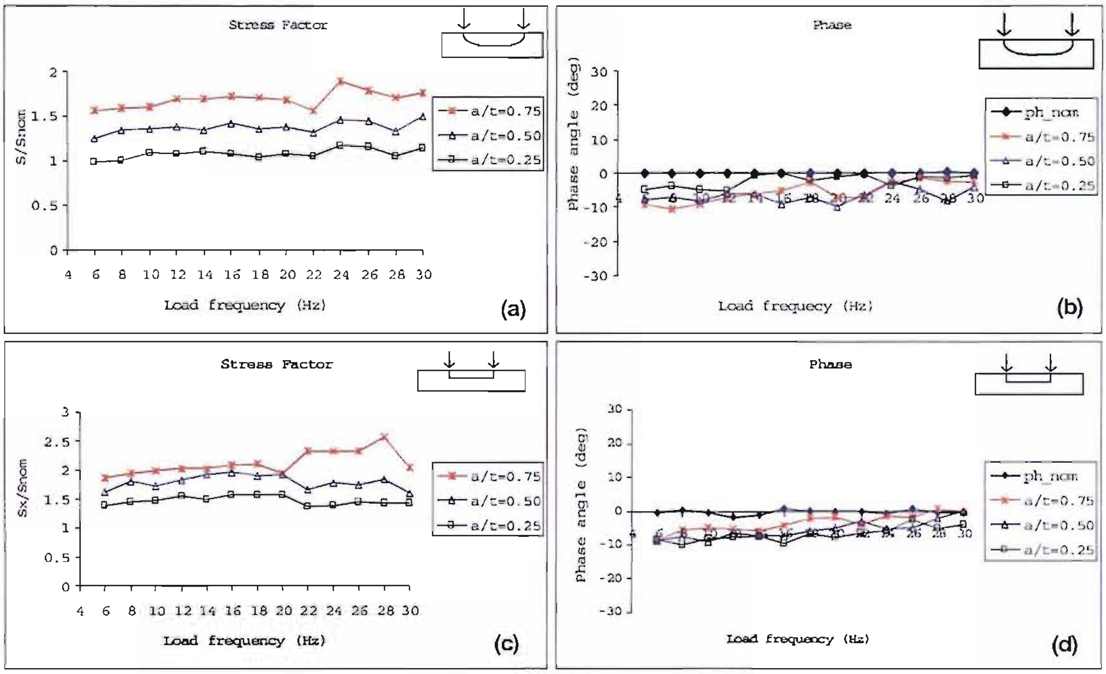

FIGURE 4.15: Stress factor and phase plot at position 3 and 4 in Figure 4.3

4.5 Summary

In this work it was shown that surface damage can be readily observed in the in-phase thermoelastic response. The magnitude of the thermoelastic signal is dependent on the damage severity. The magnitude and phase of the signal from the surface damage does not vary, demonstrating that an adiabatic response is obtained when observing surface damage.

The purpose of the thesis is to determine if sub-surface damage can be evaluated using TSA. To this end two types of sub-surface damage have been studied in this chapter: the severe case of a part-through crack-like flaw and a less severe case of a part through flat bottomed hole. The thermoelastic response on the surface of the plate at the damage site (i.e. the undamaged side of the flat plate) was shown to be highly dependent on loading frequency. Close examination of the response from each damage type showed that the out-of-phase (Y-image) was more sensitive to the damage than the in-phase data. This can be attributed to the fact that the Y-image is a sine-function of the phase angle [59] and in all cases the damage caused a departure from a zero phase angle.

It is known that non-adiabatic behaviour causes changes in the phase of thermoelastic data and it is clear from the work in this chapter that the magnitude of the phase change is related to the damage severity. Therefore it can be concluded that the non-adiabatic response can be used to determine the severity of sub-surface damage and the approach is worth pursuing.

The work on the undamaged side of the specimens in this chapter has shown that the response from sub-surface crack-like flaws is highly dependent on loading frequency. The response from the flat bottomed holes was less dependent on loading frequency. Therefore as the crack-like flaw is the most responsive and probably the most representative of actual damage, the remainder of the thesis will concentrate on this type of damage.

It has been indicated in this preliminary work that the effect of heat diffusion in the neighbourhood of the damage causes localised non-adiabatic behaviour. In order to use this effect to study the damage severity it is necessary to develop a thermoelastic equation that includes the effect of thermal diffusion. This is done in Chapter 5. Chapter 5 also shows how the DeltaTherm system respond to the effect of heat diffusion and how this can be included in the standard TSA equation. To solve this equation, a finite element approach has been developed and is described in Chapter 6. The preliminary work has also indicated that the out-of-phase response to damage is complex. To understand this further a simpler test specimen has been designed containing a 'one-dimensional' damage type. The work on this specimen is described in Chapter 7 and used as a basis for studies of damage of the type in specimen 1 which is given in Chapter 8 and 9.

Chapter 5

Development of non-adiabatic theory and its application in standard TSA

5.1 The thermoelastic effect

A volumetric deformation of any substance in nature is always accompanied by a temperature change. A compressive load produces an increase in temperature whereas a tensile load produces a decrease in temperature. The phenomenon is caused by the mechanical-thermal conversion of energy known as the thermoelastic effect, first described theoretically by Lord Kelvin [60].

A hundred years later, Biot [61] applied thermodynamic theory to improve understanding of the thermoelastic effect. He carried out a detailed investigation into the irreversible thermodynamics of the phenomenon. The study of the entropy change as the material deformed with the applied load lead to development of the classical thermoelastic equation. According to his development, the change in temperature, ΔT, caused by the volumetric deformation, $\Delta(\epsilon_{11} + \epsilon_{22} + \epsilon_{33})$, of the material can be obtained from the energy balance equation which may be described by the following expression [61]:

$$Q = \rho c_\epsilon \, \Delta T + \frac{T_0 E \alpha}{1 - 2\nu} \Delta \left(\epsilon_{11} + \epsilon_{22} + \epsilon_{33}\right) \tag{5.1}$$

where

Q	is the amount of heat absorbed by a unit element,
ρ	is the material density,
c_ϵ	is the specific heat at constant strain,
ΔT	is the temperature increment caused by the thermoelastic effect ($\Delta T = T - T_0$),
T	is the absolute temperature,
T_0	is the specimen temperature at free stress state,
E	is Young's modulus,
ν	is Poisson's ratio,
α	is the coefficient of linear thermal expansion.

If adiabatic deformation is assumed, Equation 5.1 can be reduced to a linear relationship between temperature change and change in the first strain invariant:

$$\Delta T = -\frac{T_0\, E\, \alpha}{\rho\, c_\epsilon\, (1 - 2\nu)}\, \Delta\left(\epsilon_{11} + \epsilon_{22} + \epsilon_{33}\right) \tag{5.2}$$

Equation 5.2 can be developed to obtain a linear relationship between the temperature change, the first stress invariant, $\Delta(\sigma_{11} + \sigma_{22} + \sigma_{33})$ by replacing c_ϵ with the specific heat at constant pressure, c_p, as follows:

$$\Delta T = -\frac{\alpha\, T_0}{\rho\, c_p} \Delta(\sigma_{11} + \sigma_{22} + \sigma_{33}) \tag{5.3}$$

Equation 5.3 is the standard form of the thermoelastic equation used in TSA for isotropic homogeneous materials under elastic and adiabatic deformation. A review of background theory and derivations of thermoelastic effect can also be found in Ref [62].

To make Equation 5.3 valid in practice, i.e. for TSA, the specimen is cyclically loaded at a certain frequency to ensure that the transport of heat caused by a non-uniform temperature field is insignificant. However, adiabatic conditions may not be achieved if the temperature gradient is very high or the thermal conductivity of the material is large [56], unless very high load frequencies are used.

In general, regions of high stress gradients occur in the neighbourhood of crack tips or other stress raisers. Moreover, most engineering structural materials are metals, so high thermal conductivity is to be expected. These situations result in non-adiabatic thermoelastic conditions so, Equation 5.2 or Equation 5.3 does not sufficiently describe the temperature distribution. The thermoelastic equation can be developed further to account for the existing heat transfer between volume elements by applying the Fourier law of heat conduction to the thermoelastic equation [61].

According to the law of heat conduction, the rate of heat absorbed by an element without an internal heat source can be expressed as:

$$\frac{\mathrm{d}Q}{\mathrm{d}t} = k\nabla^2 T \tag{5.4}$$

where t is time, k is the thermal conductivity and

$$\nabla^2 T \equiv \frac{\partial^2 T}{\partial x^2} + \frac{\partial^2 T}{\partial y^2} + \frac{\partial^2 T}{\partial z^2}$$

By differentiating Equation 5.1 with respect to time and combining with Equation 5.4, the generalised heat conduction equation for the thermoelastic effect without an internal heat source is obtained as follows:

$$k\nabla^2 T = \rho\, c_\epsilon\, \frac{\partial T}{\partial t} + \frac{\alpha\, T_0\, E}{1-2\nu}\, \frac{\partial\left(\epsilon_{11} + \epsilon_{22} + \epsilon_{33}\right)}{\partial t} \tag{5.5}$$

It can be seen that Equation 5.5 is in the form of a heat diffusion equation containing an effective heat source (second term on the right hand side) caused by the thermal-mechanical interaction, i.e. the thermoelastic effect. The rate of the heat generation depends on the rate of volumetric deformation. Equation 5.5 can be rewritten by replacing the heat capacity with the specific heat at constant pressure and replacing the first strain invariant with the first stress invariant i.e.:

$$k\nabla^2 T = \rho\, c_p\, \frac{\partial T}{\partial t} + \alpha\, T_0\, \frac{\partial\left(\sigma_{11} + \sigma_{22} + \sigma_{33}\right)}{\partial t} \tag{5.6}$$

Since, Equation 5.6 is derived from the entropy balance equation, it is valid for either adiabatic or non-adiabatic conditions. In the case of adiabatic conditions, as the heat flux becomes insignificant $\left(\therefore k\nabla^2 T \approx 0\right)$, Equation 5.6 can be integrated over a time period from the initial state to the final state of deformation and hence reduced to give a linear relationship between ΔT and the change in the first stress invariant, $\Delta\left(\sigma_{11} + \sigma_{22} + \sigma_{33}\right)$, resulting in Equation 5.3.

In the case of non-adiabatic conditions $(k\nabla^2 T \neq 0)$, heat transfer problem exists. Therefore, the temperature change caused by the change of the stress can be obtained by solving Equation 5.6. Equation 5.6 can be solved analytically for certain problems such as a plate subjected to pure bending vibration [63, 64]. For more complex problems it is preferable to use numerical techniques to obtain the solutions.

In summary, the development of the classical thermoelastic equation and the generalised heat conduction equation for thermoelasticity has been described. The former can be used to describe the thermoelastic effect under adiabatic conditions, i.e. Equation 5.2 or Equation 5.3. On the other hand, if the material is undergoing non-adiabatic conditions, Equation 5.6 must be applied.

5.2 Principles of IR thermal detecting for TSA

To apply TSA in practice, a component is generally loaded cyclically at a certain frequency so that the heat conduction in the material becomes insignificant. Under this loading regime, there exists a very small temperature fluctuation caused by the thermoelastic effect which can be detected by a highly sensitive thermal sensor. According to a literature review by Rocca and Bever [65], early measurements of the thermoelastic effect were made by thermocouples or other temperature-measuring systems which were considered as contacting sensors. These techniques could not provide a full-field measurement. It was Belgen [66] who first introduced the IR radiometer for temperature related stress measurement to achieve a full field non-contacting approach for TSA [1].

The fundamental basis of the technique is the fact that all substances with a temperature above absolute zero will release thermal energy in the form of electromagnetic radiation. The hotter the substance is, the the more thermal radiation it emits. If an IR detector is used to measure this thermal radiation and assumed to behave linearly, i.e. the relationship between input thermal radiance and electrical output is linear, the electrical output from the detector can be calibrated to provide the temperature value. Therefore the IR detector can be used to quantify surface temperature from the emitted thermal radiation.

To correlate the temperature change with the thermal radiation, it is assumed that the stress-associated temperature oscillation, ΔT, is very small compared to the reference temperature, T_0 (i.e. $\Delta T \ll T_0$). The relationship between the photon flux striking the detector and the temperature of the specimen surface can be obtained by dividing Planck's law with the energy carried by each photon and integrating between the associated operating wavelength of the IR detector. The relation can be simplified to [67]:

$$N_\lambda = eBT^n \tag{5.7}$$

where N_λ is the photon flux striking the detector (considered between the operating wavelength), e is the surface emissivity, B is a physical constant depending on the detector, T is the surface temperature and n is a constant which can be determined numerically or experimentally (see Ref. [67]).

Differentiating Equation 5.7 with respective to temperature gives:

$$\frac{\mathrm{d}N_\lambda}{\mathrm{d}T} = n\,e\,B\,T^{n-1} \tag{5.8}$$

It can be seen from Equation 5.8 that the relationship between the change of the number of photons detected, $\mathrm{d}N_\lambda$, and the temperature increment, $\mathrm{d}T$, is temperature dependent. However, by assuming that the mean temperature of the specimen surface, T_0, does not change appreciably with time during a standard TSA practice and the temperature change due to the thermoelastic effect is very small ($\Delta T = \mathrm{d}T$), the relationship between the number of photons and the small temperature increment becomes linear, and can be written in the form:

$$\Delta N_\lambda = n\, e\, B\, T_0^{n-1}\, \Delta T \tag{5.9}$$

Assuming a linear relationship between the signal output or thermoelastic signal, S, and the change of photon flux from the IR radiation, gives:

$$S = Z\, \Delta N_\lambda \tag{5.10}$$

where Z is denoted as a detector response factor.

Substituting Equation 5.9 into Equation 5.10, the relationship between S and ΔT is obtained:

$$S = Z\, n\, e\, B\, T_0^{n-1}\, \Delta T \tag{5.11}$$

Under adiabatic deformation, ΔT from Equation 5.3 can be substituted into Equation 5.11. The following relationship of S and ΔT is obtained:

$$\Delta\sigma_I = -\underbrace{\left(\frac{1}{n\, B\, Z\, T_0^{n-1}}\right)\left(\frac{1}{T_0\, e\, K}\right)}_{A} S \tag{5.12}$$

where $\Delta\sigma_I$ is the change of the sum of the principal stress, $\Delta(\sigma_{11} + \sigma_{22} + \sigma_{33})$ and K is the thermoelastic constant, $K = \frac{\alpha}{\rho c_p}$. All constant parameters in both brackets may be grouped together and denoted as calibration constant, A, so that a more familiar form of thermoelastic relation can be obtained as shown in Equation 1.1.

To demonstrate that the signal response, S, contains information about the amplitude of the thermal response and the phase relative to the stress change, it is necessary to express Equation 5.11 in terms of time-variable and an example is given below.

A uni-axial tensile stress generated by sinusoidal load (see Figure 5.1) can be written as:

$$\sigma \;=\; \sigma_m + \sigma_a \sin(\omega\, t) \;=\; \sigma_m + \sigma_a\, e^{j\omega t} \tag{5.13}$$

where, σ_m is a mean of the sum of the principal stress, σ_a is the amplitude of the sum of the principal stress, ω is the angular velocity ($\omega = 2\,\pi f$), f is the loading frequency, and t is time.

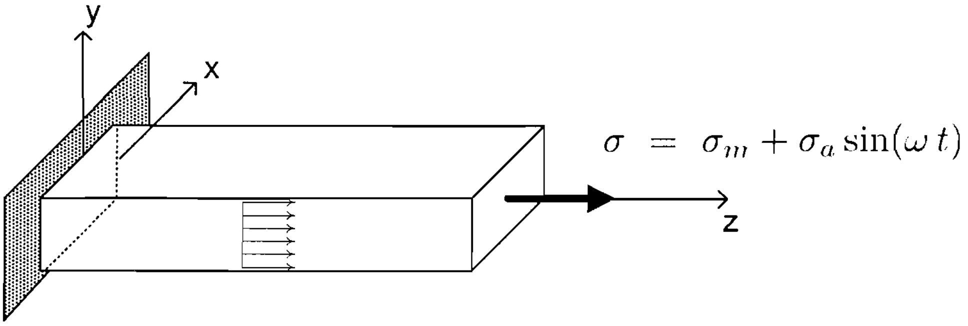

FIGURE 5.1: A beam under uniform sinusoidal load

From Equation 5.3, the heat generation rate associated with the stress change can be described as [65]:

$$\dot{q} = \rho c_p \frac{\mathrm{d}T}{\mathrm{d}t} = -\alpha T_0 \frac{\mathrm{d}(\sigma_{11} + \sigma_{22} + \sigma_{33})}{\mathrm{d}t} \tag{5.14}$$

where $\dot{q}$ is the rate of heat generated by the thermoelastic effect.

By substituting, σ from Equation 5.13 as the first stress invariant in Equation 5.14, the heat generation term becomes:

$$\dot{q} = -\alpha T_0 \omega \sigma_a \sin(\omega t - \frac{\pi}{2}) = -j \alpha T_0 \omega \sigma_a \mathrm{e}^{j\omega t} \tag{5.15}$$

The temperature response is the integral of the heat generation rate, therefore the temperature change associated with the stress change can be described in terms of a Fourier sine series as:

$$\Delta T = K T_0 \sigma_a \sin(\omega t - \pi) = K T_0 \sigma_a \mathrm{e}^{j(\omega t - \pi)} \tag{5.16}$$

The normalised relationship between excitation stress (Equation 5.13), heat generation rate (Equation 5.15) and temperature response (Equation 5.16) under adiabatic conditions is shown in Figure 5.2. The figure shows that under adiabatic conditions the temperature response is always lagging the stress excitation by π radians which corresponds with the negative sign in the standard thermoelastic equation (Equation 5.3).

To express relationship of the signal output as a function of time, Equation 5.16 is substituted into Equation 5.11 to give:

$$S = \left(Z n e B T_0^{n-1}\right) K T_0 \sigma_a \sin(\omega t - \pi) \tag{5.17}$$

In general practice, the thermoelastic data is collected for a period of time and the signal corresponding to the magnitude of the stress change is then averaged to obtain the thermoelastic signal output as the mean value. Therefore, Equation 5.17 can also be rewritten in a simpler form of the thermoelastic equation as Equation 1.1.

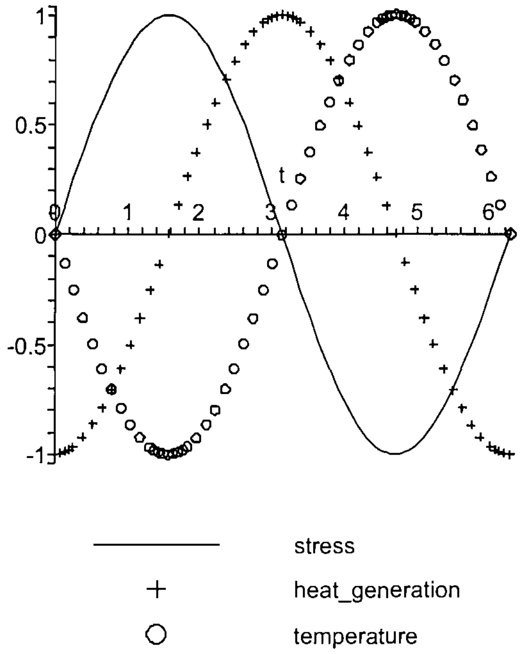

FIGURE 5.2: Stress, heat generation rate and temperature relationship in thermoelastic effect under adiabatic conditions [36]

Under non-adiabatic conditions, the temperature response must be obtained from the energy balance equation i.e. Equation 5.1 which can be rewritten in the form:

$$Q = \rho\, c_p\, \Delta T + \alpha\, T_0\, \Delta\sigma_I \tag{5.18}$$

By rearranging, Equation 5.18 becomes:

$$\Delta T = -K\, T_0\, \Delta\sigma_I + \frac{Q}{\rho\, c_p} \tag{5.19}$$

The first term on the right hand side represents the thermoelastic temperature change and the second term may be considered as an 'added temperature' contributed from the conduction of heat. The added temperature can be positive or negative depending on the direction of heat transfer during the load cycle.

By substituting ΔT from Equation 5.19 into Equation 5.11, the relationship between the measured stress and the signal output under non-adiabatic conditions is obtained as follows:

$$\Delta\sigma_I + \frac{Q}{\alpha\, T_0} = -\underbrace{\left(\frac{1}{n\, B\, Z\, T_0^{n-1}}\right)\left(\frac{1}{T_0\, e\, K}\right)}_{A} S \tag{5.20}$$

It can be seen that the standard equation for TSA (Equation 1.1) can not be used to quantify the sum of the principal stresses from the thermoelastic signal accurately. This is because the transportation heat biases the instantaneous temperature change.

Similar to the derivation of S as a function of time under adiabatic conditions, the temperature response under non-adiabatic conditions must be obtained to substitute into Equation 5.11. Since the generalised heat conduction equation is in the form of a non-homogeneous partial differential equation, analytical solutions become laborious to derive, particularly for a non-uniform stress field. However, for a simple case such as a cantilever beam under bending, the solution of Equation 5.6 can be obtained analytically.

Figure 5.3 shows a simple cantilever beam subjected to a sinusoidal force, F, applied at the edge of the beam of thickness 2L. Desiderati and Salerno [68] provide a solution for the temperature variation in the y-direction, i.e. the temperature across the cross section, at distance z_1 is as follows:

$$T(y,t) = \left[C_1\, \mathrm{e}^{\frac{(1+j)}{\gamma}\cdot y} + C_2\, \mathrm{e}^{\frac{-(1+j)}{\gamma}\cdot y} - \frac{\alpha T_0\, F_0\, z_1\, y}{\rho\, c_p\, J} \right] \mathrm{e}^{j\omega t} \tag{5.21}$$

where

$$C_1 = -C_2 = \left[\frac{\alpha \cdot T_0 \cdot F_0 \cdot z_1}{2\,\rho\, c_p \cdot J \cdot \cosh(\theta)} \cdot \frac{\gamma}{(1+j)} \right],$$

$$\theta = L \cdot \left(\frac{1+j}{\mu} \right),$$

$$\gamma = \sqrt{\frac{2\,k}{\rho\, c_p \cdot \omega}} = \text{thermal diffusion length},$$

L = beam half thickness, and

J = Moment of inertia of the beam cross section.

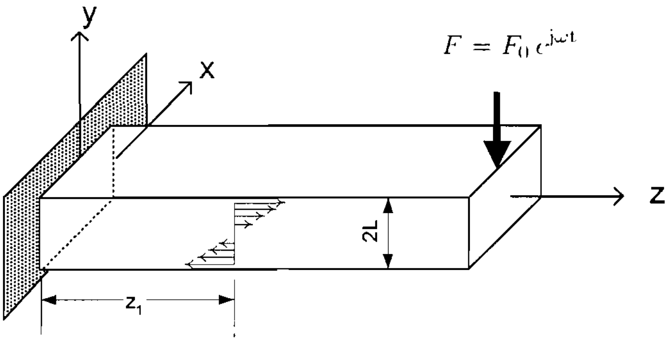

FIGURE 5.3: Cantilever beam subjected to a sinusoidal load [68]

From Equation 5.21, the temperature response at the surface of the beam, i.e. at y = L, becomes:

$$T(L,t) = \left[C_1\,\mathrm{e}^{\frac{(1+j)}{\gamma}\cdot L} + C_2\,\mathrm{e}^{\frac{-(1+j)}{\gamma}\cdot L} - \frac{\alpha\,T_0\,F_0\,z_1\,L}{\rho\,c_p\,J}\right]\mathrm{e}^{\mathrm{j}\omega\,\mathrm{t}} \tag{5.22}$$

By substituting Equation 5.21 into Equation 5.11 as ΔT, the thermoelastic signal output in this case can be expressed as follows:

$$S = Z\,n\,e\,B\,T_0^{n-1}\,\left[C_1\,\mathrm{e}^{\frac{(1+j)}{\gamma}\cdot L} + C_2\,\mathrm{e}^{\frac{-(1+j)}{\gamma}\cdot L} - \frac{\alpha\,T_0\,F_0\,z_1\,L}{\rho\,c_p\,J}\right]\mathrm{e}^{\mathrm{j}\omega\mathrm{t}} \tag{5.23}$$

It can be seen from Equation 5.23 that under non-adiabatic conditions, the magnitude and phase of the thermoelastic signal output at a point is affected by the thermal diffusion length, which is the function of loading frequency and material properties. By changing the loading frequency, a different thermoelastic response is obtained. This indicates non-adiabatic behaviour in the thermoelastic response can be monitored by the signal response from a standard TSA system.

5.3 Summary

It has been shown that non-adiabatic behaviour can be described by the generalised heat conduction equation developed above. Derivations of the signal response from a generic TSA system have been presented and shown that a non-adiabatic thermoelastic response can be monitored by a standard TSA system. This understanding is essential for developing an approach to detect and assess the sub-surface damage in which localised non-adiabatic behaviour is significant. In the following chapter, an FE simulation procedure is developed based on the generalised heat conduction equations. Therefore, the two full-field approaches can be compared and validated.

Chapter 6

Numerical simulation of the thermoelastic effect

6.1 Introduction

In the feasibility study in Chapter 4 it was shown that it is possible to assess sub-surface damage using TSA. This work also demonstrated the complex nature of the response and the requirement for a detailed knowledge of the underlying theory to interpret the data.

It is shown in Chapter 5 that the governing equation of generalised heat conduction equation for thermoelastic effect is in the form of a non-homogeneous partial differential equation (PDE), i.e.

$$k\nabla^2 T = \rho\, c_p\, \frac{\partial T}{\partial t} + \alpha\, T_0\, \frac{\partial\left(\sigma_{11} + \sigma_{22} + \sigma_{33}\right)}{\partial t} \tag{6.1}$$

To solve this equation for general cases it is necessary to use a numerical approach. In this chapter, a finite element (FE) approach, capable of solving problems governed by PDEs in various complex domains, is developed for the thermoelastic problem. The FE analysis was performed using a commercial FE package, ANSYS. The software has many FE analysis capabilities ranging from a simple linear analysis to a complex transient non-linear analysis. There are a large number of element types in the software library, however a standard element suitable for the thermoelastic problem that governs this work does not exist. Therefore a procedure to perform thermoelastic simulation by adapting the standard facilities in ANSYS is described in this chapter. The simulation procedure is validated by comparing the results with other published work as well as with experimental data.

6.2 Simulation procedure

To deal with the coupled problem of the thermoelastic effect, the FE analysis is separated into two steps. Firstly, standard FE structural stress analysis was performed to determine the sum of the principal stresses resulting from the applied load range, using linear elements. Then, the heat generation rate is calculated from the results of this model and applied to a thermal harmonic model. A schematic representation of this procedure is presented in Figure 6.1.

In the structural stress analysis, the simulation process starts with geometrical modelling and discretization. At this stage the model is constructed numerically, then the solution domain is discretized into elements and nodes. A static analysis is carried out based on the loads, boundary conditions and mechanical material properties defined for the problem. The next step is to process the solutions so that the sum of the principal stresses is calculated at each node in the model. Now, the thermal harmonic analysis can be carried out using an identical model to that in the structural analysis. The heat generation rate is calculated at each node and loading frequency using the following relationship (see Section 5.2):

$$\dot{q} = -\alpha T_0 \omega \frac{\sigma_I}{2} \sin(\omega t - \frac{\pi}{2}) \tag{6.2}$$

It is important that the FE mesh is the same so that all loading data from the individual nodes can be transferred into the thermal analysis routine. The post processing of the thermal analysis extracts the magnitude and phase of the thermoelastic response at each node in the model. After finishing this step the results are written into a data base file. Then, the next loop is started i.e. the thermal load corresponding to the next load frequency is defined and used as a new set of thermal loads and another solution is obtained. Therefore, the number of loops for thermal analysis depends on the number of loading frequencies required. Essentially at each frequency the FE simulation is solving for the stress terms and integrating over the time equivalent for the period of the cycle. Therefore the output gives a ΔT value for a given frequency to include the 'Q' term in Equation 5.19.

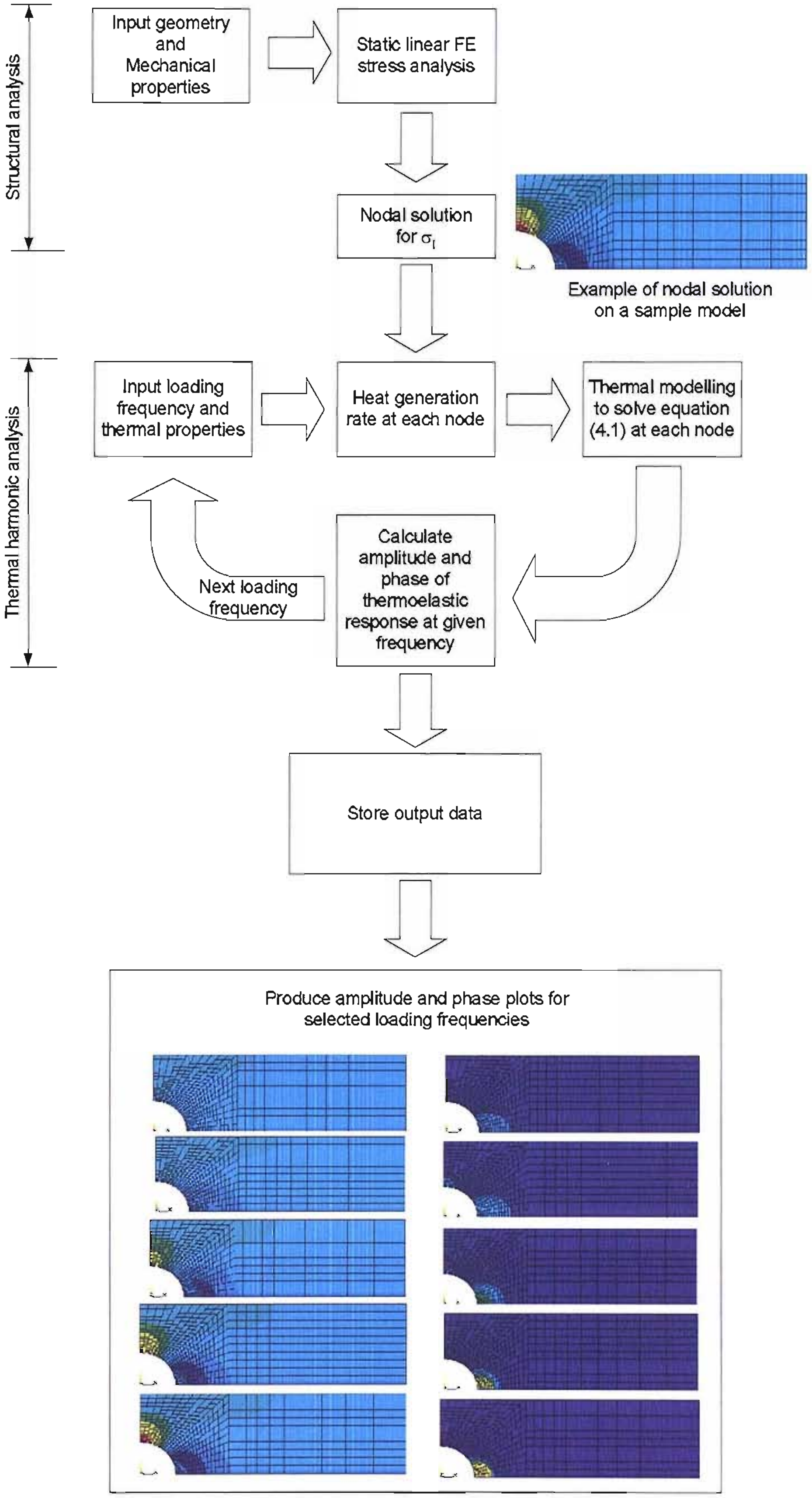

FIGURE 6.1: Flow chart of thermoelastic effect simulation

6.3 Validation of the simulation procedures

In order to validate the simulation procedure, the numerical solutions from the current model is compared with that from other published work and with experimental results. Firstly, a comparison is made with the FE model used in Ref [38]. A simple "hole in a plate" model (see Figure 6.2) which is identical to that in Ref [38] was used. A PLANE42, a 2-D 4 node solid element, was used to create the structural model. A quarter of the specimen was modelled (see Figure 6.2) as in Ref [38] and material properties are the same as those used in Ref [38] (see Table 6.1). The model was subjected to a stress range ($\Delta\sigma$) of 25 MPa as used in Ref [38].

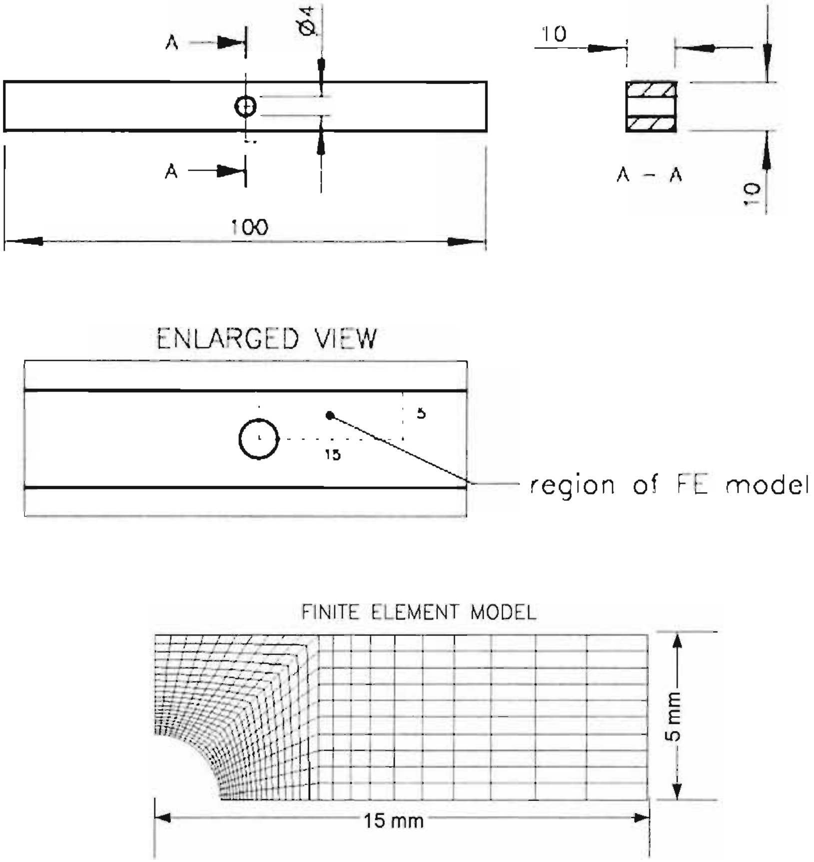

FIGURE 6.2: Geometries of the sample specimen and FE model

As illustrated in Figure 6.1, the first part of the simulation process deals with the construction of model geometries, discritization of the model as well as defining the material properties. Although ANSYS provides an adaptive meshing tool necessary for handling any complex geometry, a "mapped meshing" or "structured mesh" strategy is preferable in this situation. This is because the structured mesh technique allows complete control of mesh transition and mesh density. Therefore a finer mesh can be used in the region of expected high stress gradient, e.g. close to the hole, providing an improved quality model.

TABLE 6.1: Material properties of steel using in the FE simulation

Material Properties of steel	Value	Unit
Young's modulus, E	210	GPa
Poisson's ratio, ν	0.3	-
Specific heat at constant pressure, c_p	460	J $kg^{-1}K^{-1}$
Thermal conductivity, k	50	W $m^{-1}K^{-1}$
Density, ρ	7860	kg m^{-3}
Coefficient of linear thermal expansion, α	12E-6	K^{-1}
Reference temperature, T_0	293	K

The next step is to apply the load and boundary conditions to the model and obtain the solution. The boundary conditions at the edges A-B and C-D are set as fixed in one direction and free in the other as shown in Figure 6.3. A pressure load of 25 MPa is applied on the edge D–E of the solid model.

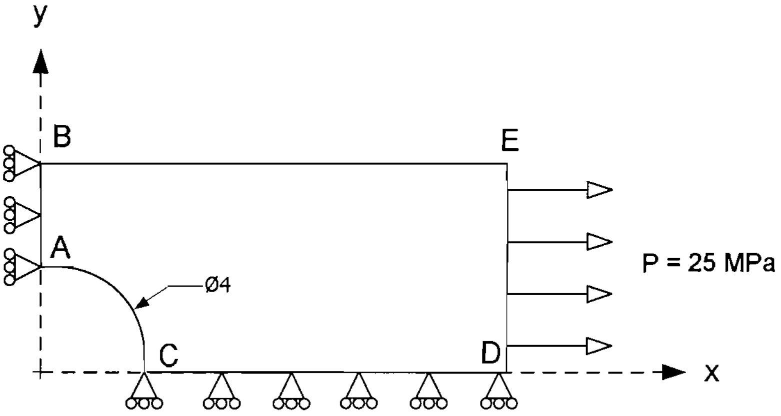

FIGURE 6.3: Boundary conditions and applied load on the model geometries

The final stage of structural analysis is obtaining the nodal results. The principal stress data is extracted from a default data base file generated by ANSYS. Then the heat generation rate at each node and frequency is calculated for the thermal analysis.

In the thermal analysis, the construction of the model geometry and the discritization procedure is carried out in the same manner as structural modelling. The element type used in the thermal modelling was a PLANE55, 2-D 4-node thermal element. Since the effect of convection and heat conduction through the paint are neglected in this model, adiabatic boundary conditions were applied to the model. Then the thermal analysis is performed as described in Section 6.2. An example of the simulated thermoelastic response is shown in Figure 6.4, giving contour plots of both ΔT and phase at a loading frequency of 10 Hz.

A comparison of the contour plot of ΔT at 1, 20 and 1000 Hz from the current work and Ref [38] is given in Figure 6.5: there is excellent agreement. It should be noted that the amplitude of the thermoelastic response plot from this simulation is the absolute value, which is equivalent to the R signal from the DT system. Therefore, the ΔT values in the compression stress zones remain positive. To validate the results, the solutions obtained from various loading frequencies along the path A–B (see Figure 6.3) are compared in terms of both ΔT and phase data and shown in Figure 6.6. The curves show a very good correspondence with the results reported in Ref [38], hence validating the modelling approach against the literature and indicating it is correct.

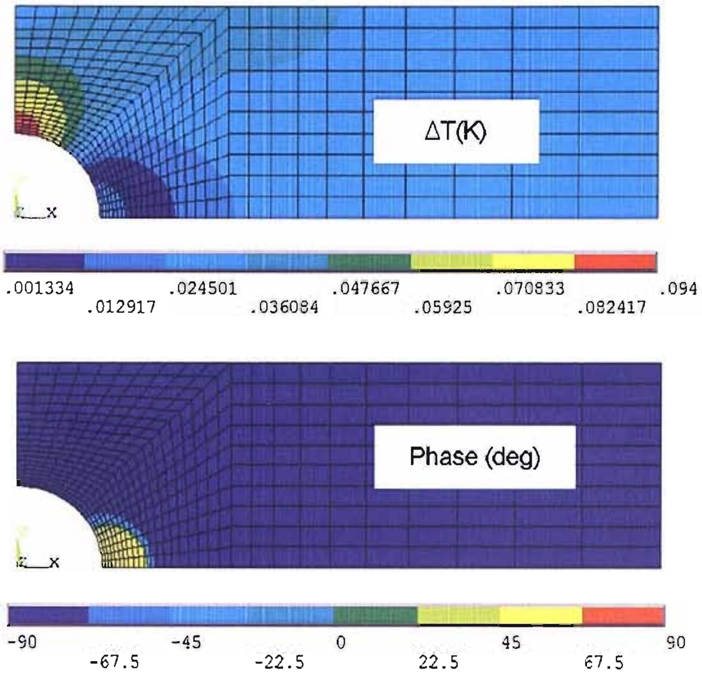

FIGURE 6.4: Contour plots from the FE simulation at a loading frequency of 10 Hz

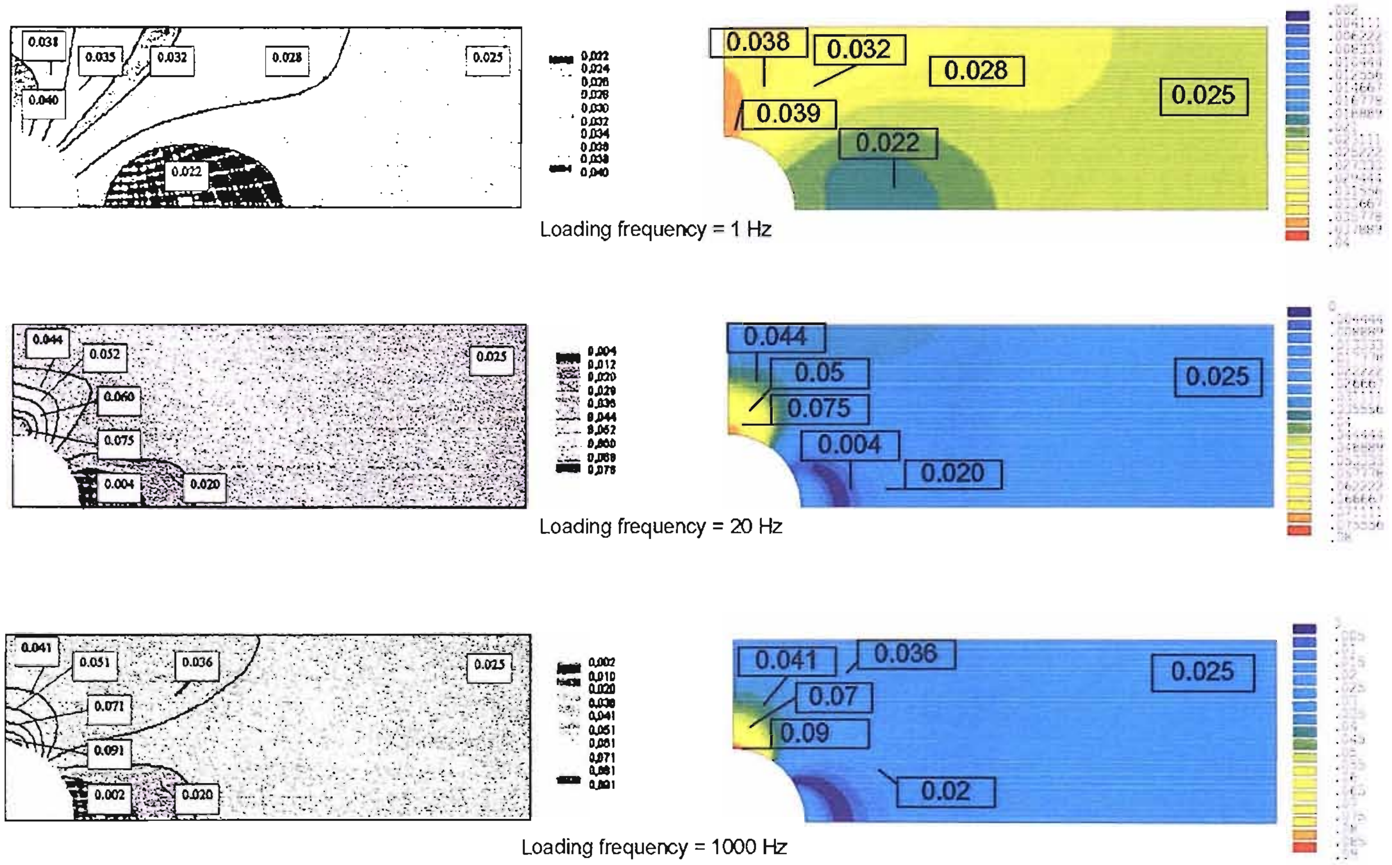

FIGURE 6.5: Contour plots of ΔT: Ref [38] (left) and current work (right)

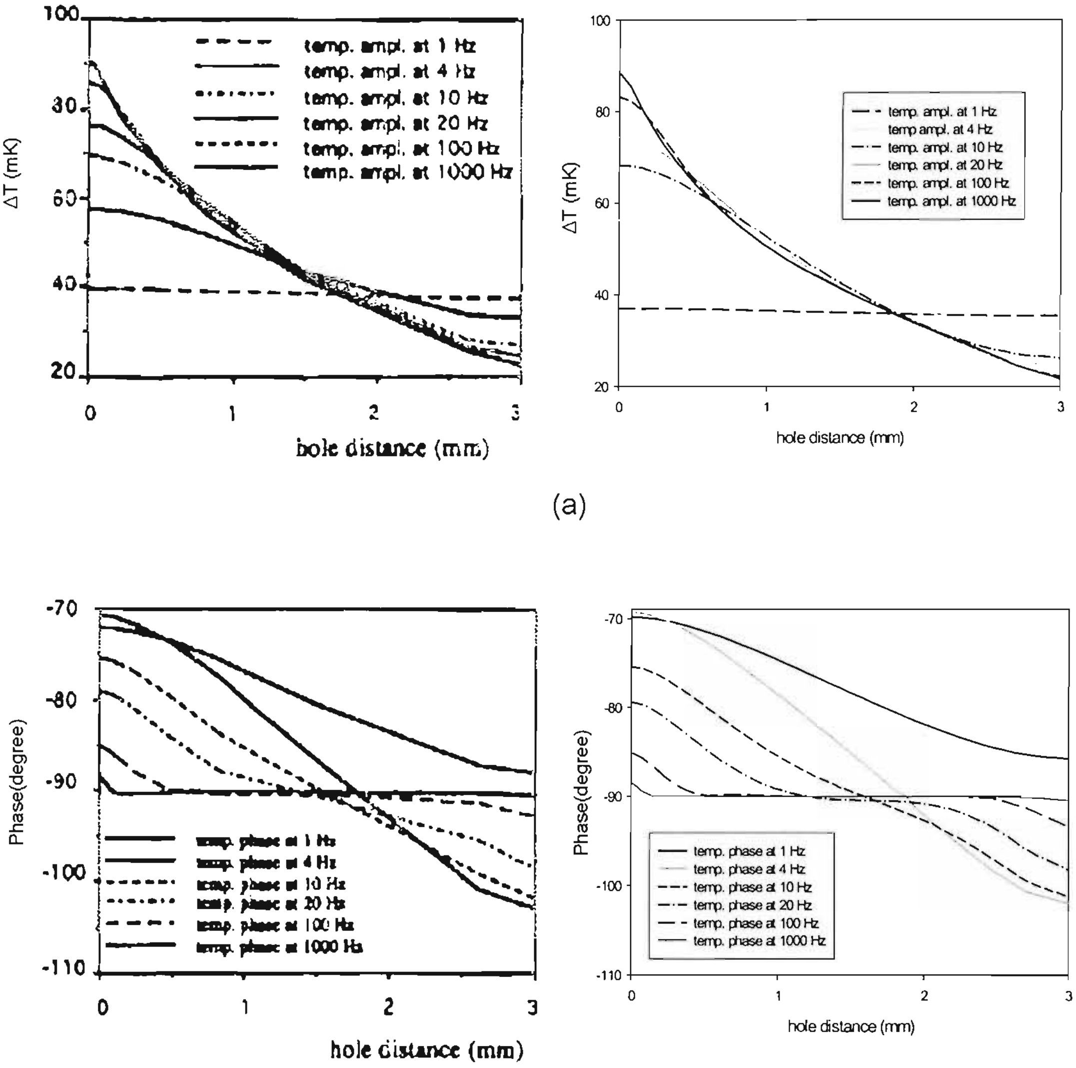

(a)

(b)

FIGURE 6.6: The ΔT and phase along path A B shown in Figure 6.3: Ref [38] (left) and current work (right)

To emphasize the validity of the simulation procedure, the model was used to predict ΔT and compared with TSA measurements from the DeltaTherm system. The specimen used in the experiment was a steel bar of 6 mm thick, 40 mm width and 300 mm length. The specimen was machined with a central hole of 12 mm diameter as shown in Figure 6.7. Prior to the experiment, the surface of the specimen was coated with a thin layer of matt black paint to enhance the surface emissivity. It is essential that the paint coating should be thin and even so that the study of non-adiabatic behaviour is not affected by the paint thickness [56]. During the experiment, a tensile load of 9 ± 8 kN was applied using a servo hydraulic testing machine. The thermoelastic response was then taken at the following loading frequencies: 1, 2, 5, 10 and 20 Hz. A calibration factor was determined so that the sum of the principal stresses was used to obtain ΔT in Equation 5.3.

To obtain ΔT from the DeltaTherm system, R-signal was used because the R-signal is independent of the phase setting. Therefore, it can be related directly to the absolute temperature change on the specimen surface.

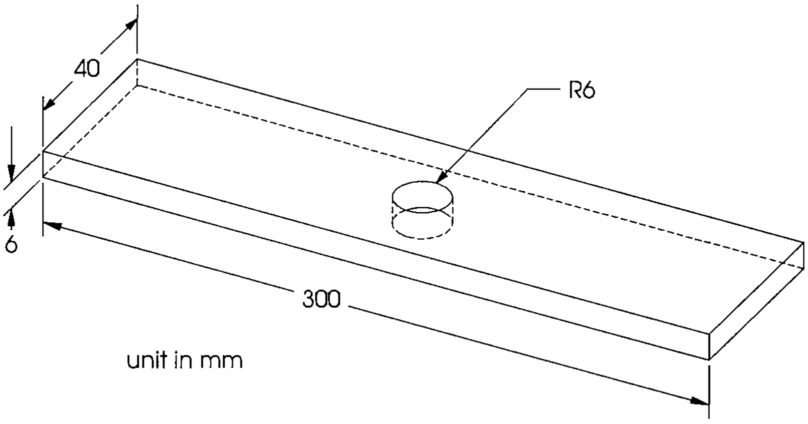

FIGURE 6.7: Dimensions of the specimen

The calibration factor, A, (see Equation 1.1) was determined using the following relationship [53]:

$$A = \frac{\Delta\sigma_{\mathrm{app}}}{S_{\mathrm{nom}}} \tag{6.3}$$

where $\Delta\sigma_{\mathrm{app}}$ is the known applied stress range, i.e. 66.67 MPa and S_{nom} is the thermoelastic signal taken in the region of a uniform stress from the experiment with the loading frequency of 20 Hz, i.e. 3800 U, Uncalibrated signal unit. From this, A was determined as 0.01754 MPa/Uncalibrated signal unit.

The FE simulation was carried out using the same material properties given in Table 6.1. The procedure of the simulation is exactly the same as described in the previous simulation except that the dimensions of the specimens and applied load were changed to correspond with the test specimen and the experiment.

The distribution of ΔT and phase data at 1 and 20 Hz from both techniques are shown in Figure 6.8. It can be seen that the agreement between the two techniques is very good. It is important to note that the phase data between the numerical result and TSA is offset by 90 degrees. This is because the reference datum of both techniques is different and offset to each other by 90 degrees. In the DeltaTherm system, the load signal from the testing machine load cell is used as a reference datum. In numerical simulation, the heat source (see Figure 5.2) is considered as a reference datum. As a consequence, the phase offset of 90 degrees is expected between the two techniques. This can be observed easily in the uniform stress region where zero degree phase data is measured from the TSA but -90 degree is predicted by the FEA.

To compare the results of both techniques in detail, ΔT and the corresponding phase response along the path A B and C D for all load frequencies are plotted and shown in Figure 6.9 and Figure 6.10 respectively. For comparison purposes, phase data from the numerical results was offset 90 degree in this plot. It can be seen that both ΔT and the phase data from FEA agree very well with those from TSA. Quantitatively, there is a small discrepancy of the ΔT values between two techniques at the edge of the hole. This may be a contribution from a small amount of motion of the specimen. In terms of phase signal, it is evident that, phase data from TSA is rather noisy and a slight phase shift is observed for the 20 Hz curve in Figure 6.9, Moreover, the largest discrepancy in the phase data is observed at 1 and 2 Hz. Likewise, in Figure 6.10, the largest discrepancy between FEA and TSA is observed at 1 and 2 Hz. Nevertheless, the trend of each curve in the phase plot corresponds well with the FEA, i.e. the largest phase shift is observed at the edge of the hole at the lowest loading frequency and the smallest phase shift is observed at the highest loading frequency.

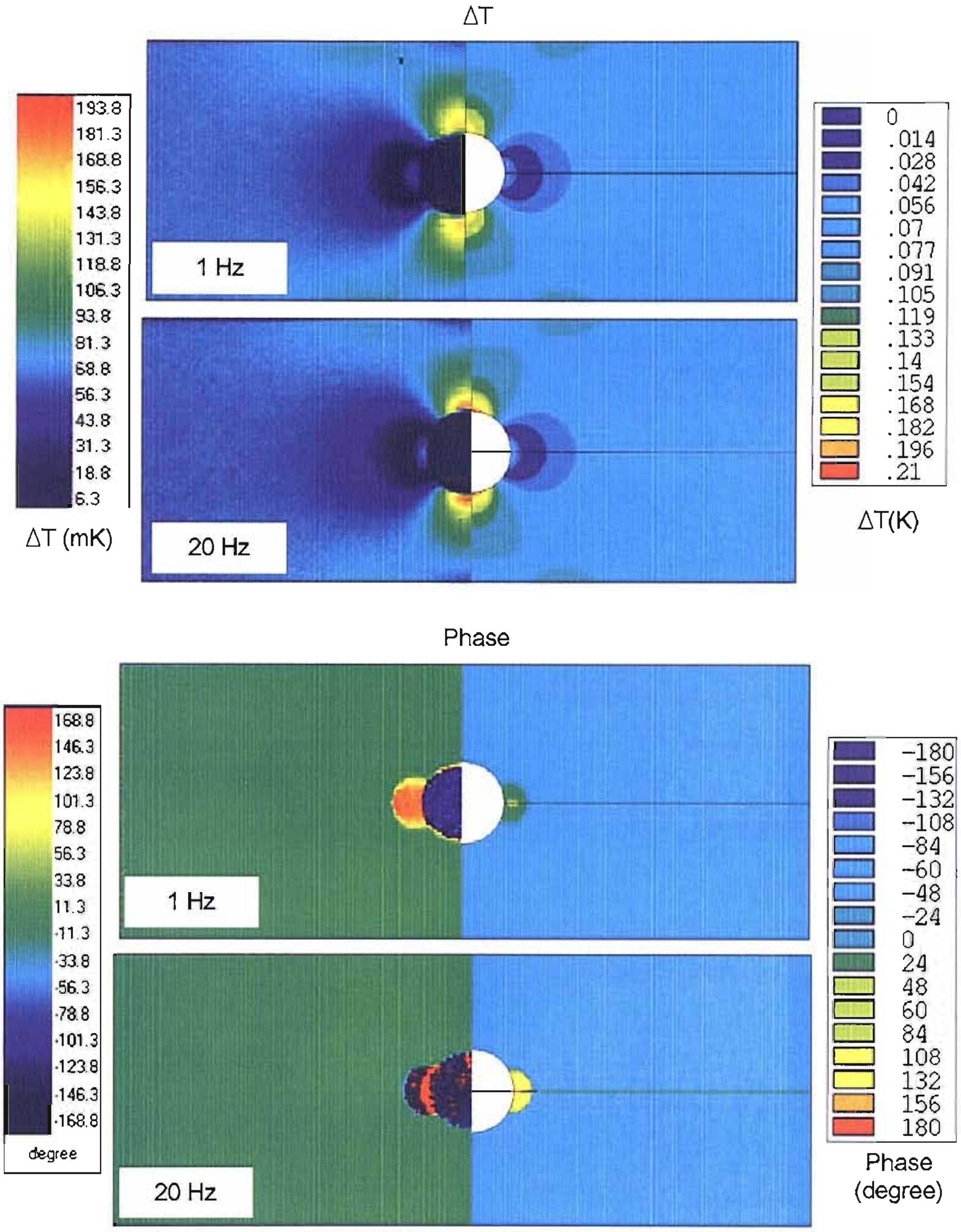

FIGURE 6.8: Comparisons of contour plot of ΔT and phase at 1 Hz and 20 Hz: TSA (left) and FEA (right)

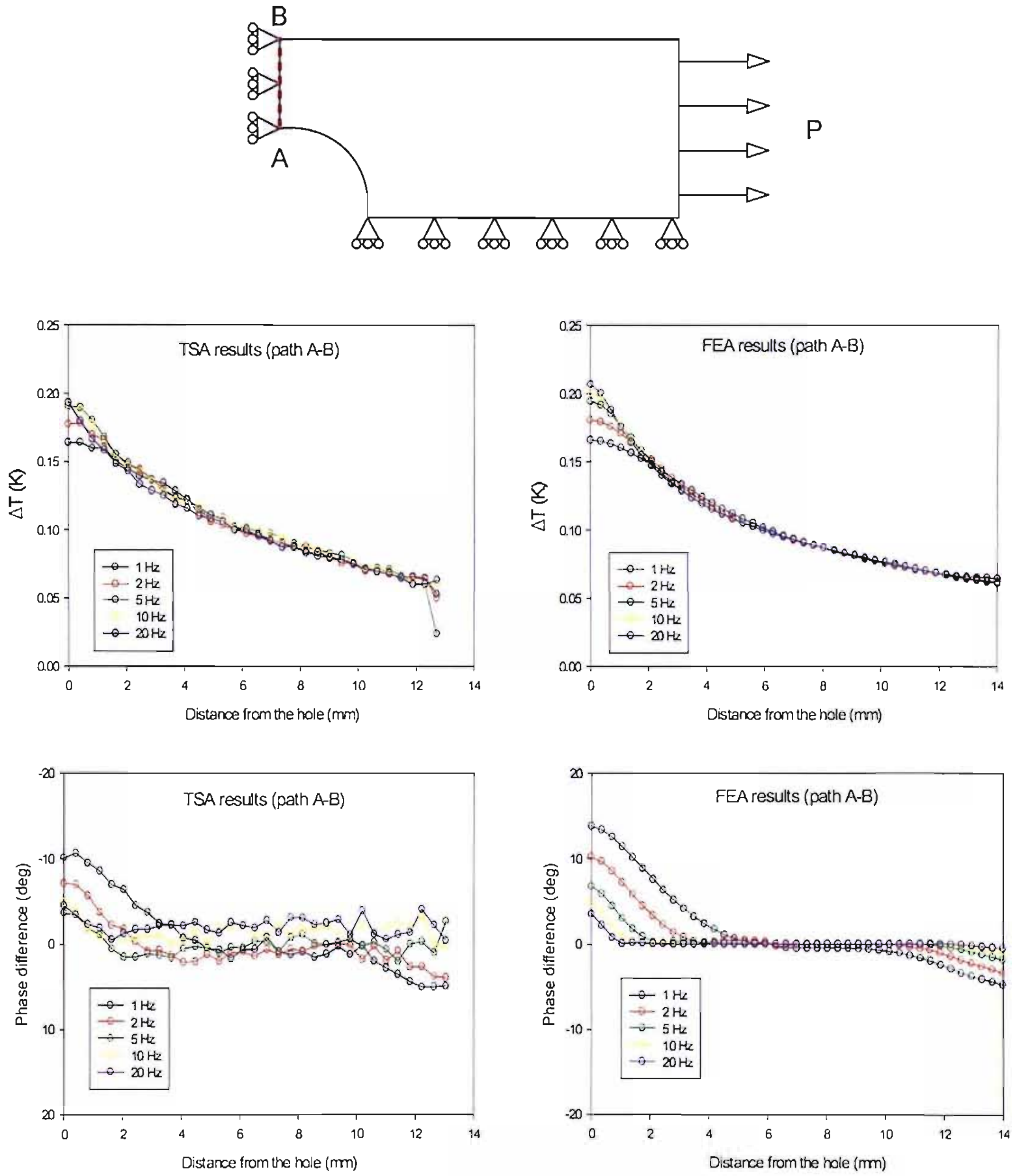

FIGURE 6.9: Comparisons of ΔT and phase response along path A–B: TSA (left) and FEA (right)

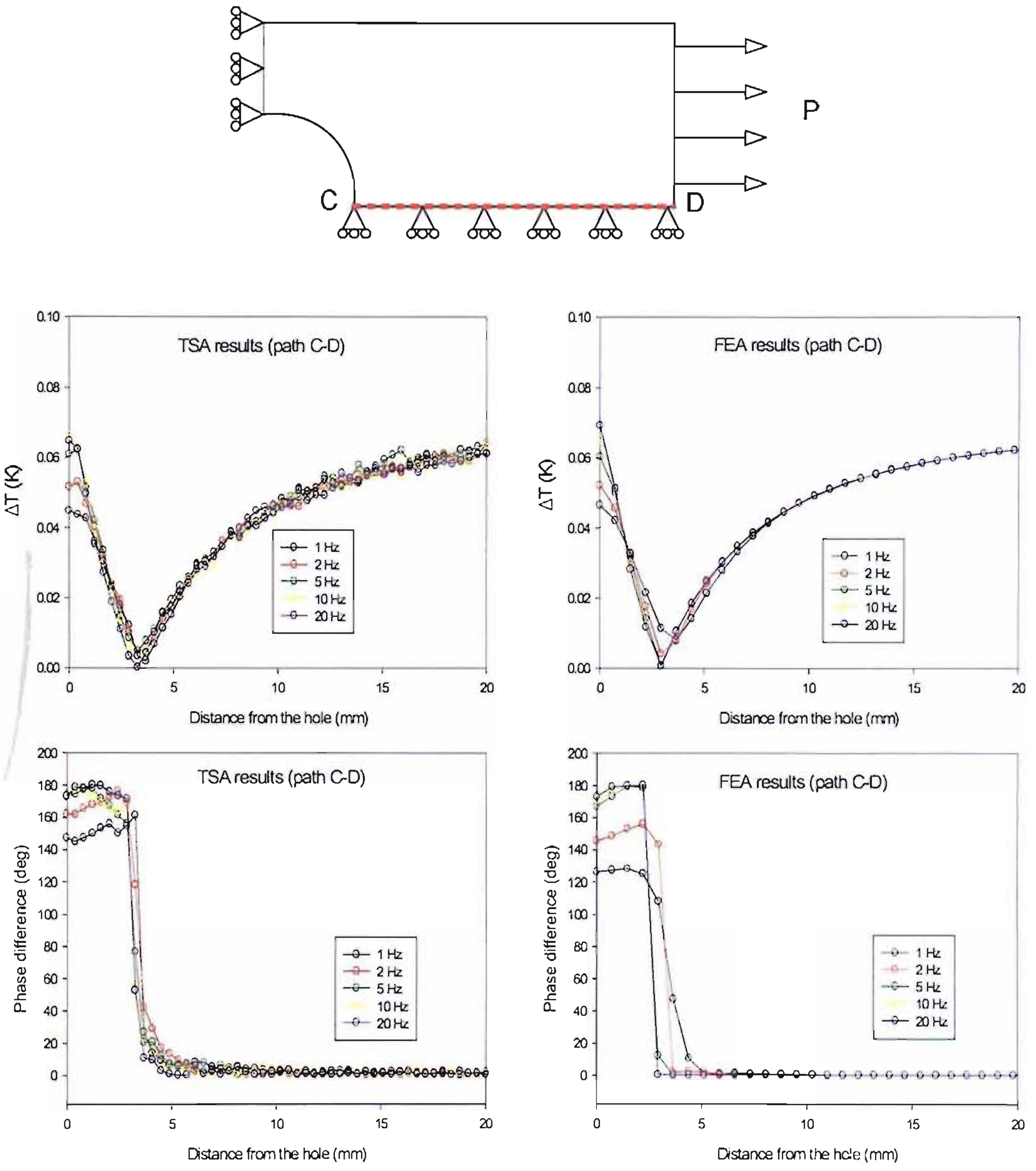

FIGURE 6.10: Comparison of ΔT and phase response along path C–D: TSA (left) and FEA (right)

According to the above comparisons with other published work as well as the experiment, it can be concluded that the simulation procedure is valid to predict thermoelastic response in a component. In the following section, the simulation technique is used to examine the influence of material properties, loading frequency and stress gradient on the non-adiabatic behaviour in order to justify the potential of the proposed approach.

6.4 Parameters that influence non-adiabatic behaviour

A parametric study was carried out using numerical simulations to examine parameters that influence non-adiabatic behaviour, i.e. material properties, loading frequency and stress gradient. Three materials are chosen in this numerical analysis i.e. an aluminium alloy, mild steel and PMMA. The generic material properties are given in Table 6.2 [55, 69].

TABLE 6.2: Material properties used in the numerical simulations

Materials	Al alloy 6082	Mild steel	PMMA
Modulus of elasticity (GPa)	70	207	2.4
Poisson's ratio	0.33	0.29	0.35
Density (kg$\cdot$m^{-3})	2700	7860	1190
Coef. of linear thermal expansion ($\times10^{-6}$)	24	12.4	70
Heat capacity(J$\cdot$kg$^{-1}\cdot$K^{-1})	896	460	1400
Thermal conductivity (W$\cdot$m$^{-1}\cdot$K^{-1})	180	50	0.17

The model used in this analysis is shown in Figure 6.7, parametric simulations were carried out by changing the material properties. Loading frequencies of 1, 2, 5, 10, 20, 30 and 1000 Hz were used. The loading frequency of 1000 Hz was used to predict the thermoelastic response for adiabatic conditions. The stress range applied to the aluminium and steel model was 66.67 MPa and 6.67 MPa for the PMMA model. Contour plots of ΔT and phase data at 1 Hz and 30 Hz for each model are given in Figure 6.11.

As expected, among these models, the maximum attenuation of ΔT occurred on the aluminium model and no attenuation of ΔT is observed in PMMA. The attenuation is also observed in the steel model, particularly at the edge of the hole. In order to see the trend of the non-adiabatic behaviour in the thermoelastic response, the solutions along path A-B and C-D for all the loading frequencies and for each material are given in Figure 6.12 and Figure 6.13 respectively.

In Figure 6.12, line data is plotted across the steepest stress gradient close to the edge of the hole, which then reduces along up to the edge of the plate. It can be seen that, at the relatively low stress gradient (middle zone of the curves), the attenuation of ΔT is not significant. The attenuation is increased as the edge of the hole is approached for all load frequencies. This confirms that the larger the stress gradient, the more non-adiabatic the behaviour.

In terms of the effect material properties, the aluminium model shows largest attenuation of ΔT while less attenuation occurs in the steel model and there is no attenuation on the PMMA model. This confirms that specimens made from materials with higher thermal diffusivity/conductivity are more prone to non-adiabatic behaviour. In view of the use of non-adiabatic behaviour for sub-surface damage evaluation, the higher the thermal

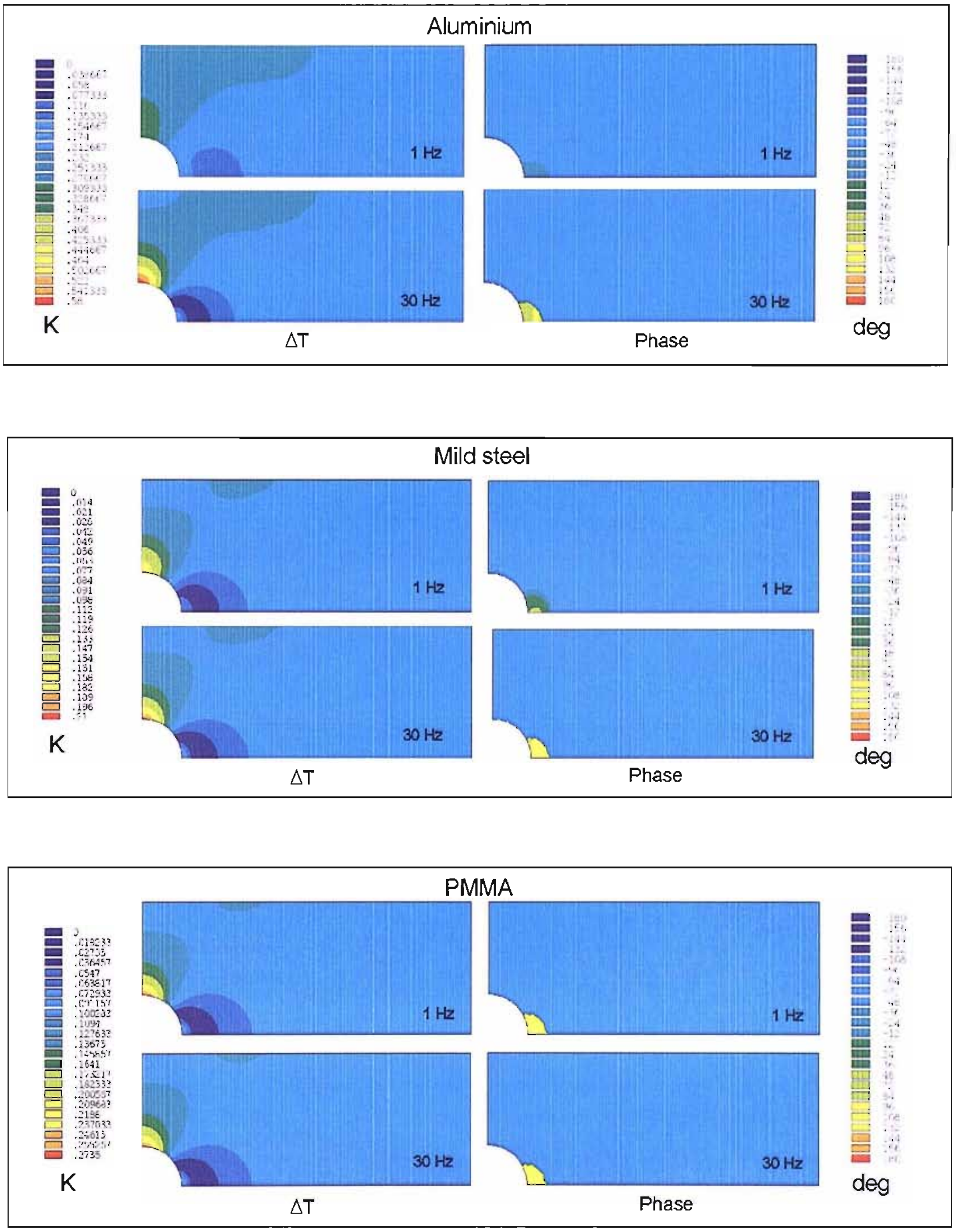

FIGURE 6.11: Thermoelastic response of an aluminium, mild steel and PMMA

diffusivity of the material, the greater the ability to detect small level of damage. With a low thermal diffusivity material such as PMMA, the approach of using non-adiabatic behaviour may not be applicable because the material exhibits adiabatic behaviour even at low loading frequencies.

In Figure 6.13, similar behaviour is observed, i.e. greatest attenuation of ΔT occurs in the aluminium model at the lowest loading frequency (1 Hz). This attenuation decreases when loading frequency is increased. At the same loading frequency, non-adiabatic behaviour reduces in materials with smaller thermal diffusivity.

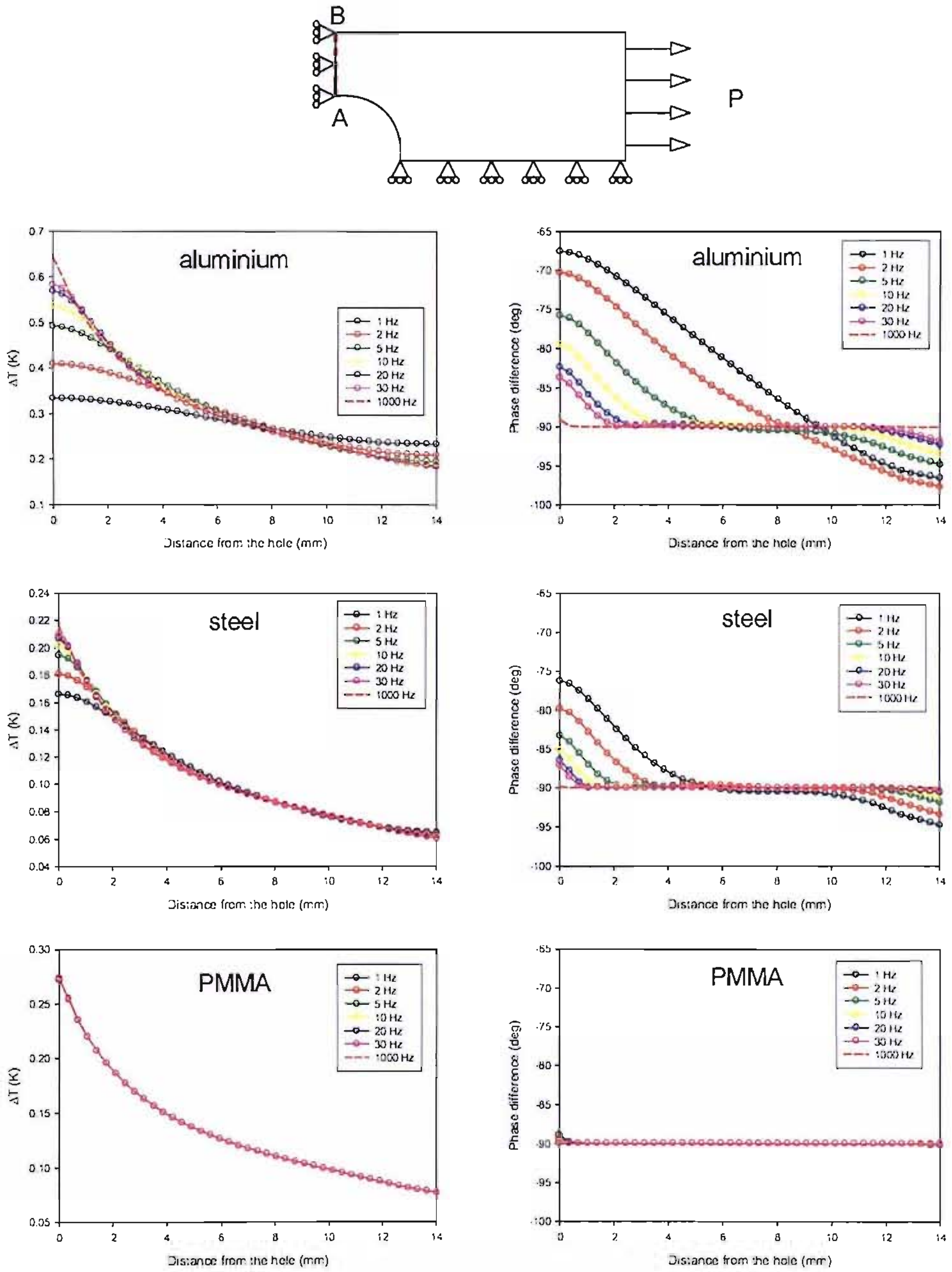

FIGURE 6.12: Thermoelastic response on path A–B

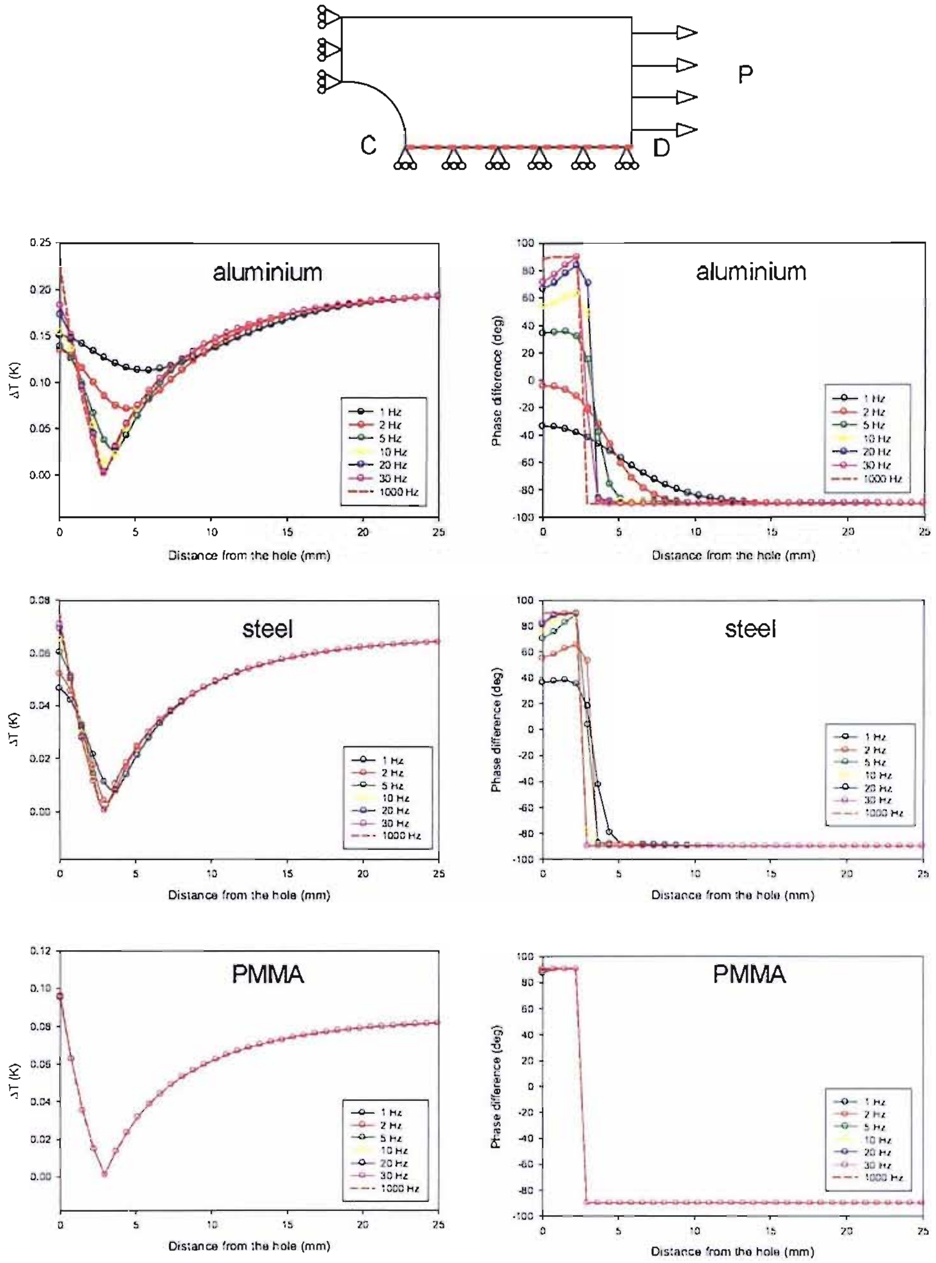

FIGURE 6.13: Thermoelastic response on path C–D

Based on the parametric study carried out in this section, it can be observed that:

- The attenuation of ΔT occurs at the largest stress gradient location in a material.
- The most severe attenuation occurs in the most conductive material at the same stress gradient and loading frequency.
- The attenuation is caused by heat conduction to the surrounding material and can also be observed by the corresponding phase response.

- For the same material, the lower the stress gradient, the lower the loading frequency is to achieve adiabatic behaviour.
- Adiabatic conditions can be achieved at a very low loading frequency if the conductivity of the material is very low.
- Loading frequency and stress gradient are the important parameters when considering non-adiabatic behaviour in a material.

6.5 Conclusions

In this chapter, a procedure to simulate the thermoelastic effect using ANSYS has been developed. The simulation procedure was validated by comparing the simulation results with results from the literature and experimentally using the DeltaTherm system. The simulation procedure can be applied to any FE model to study the thermoelastic response. A parametric study of thermoelastic effect on aluminium, steel and PMMA has been carried out. It has been shown that non-adiabatic behaviour can be influenced by various parameters. By applying the simulation procedure, the thermoelastic response can be predicted provided that material properties, loading frequencies, boundary conditions and detailed dimensions are available.

In the following chapters, the approach developed in this chapter will be used to simulate the thermoelastic response from complex specimens. It will be used as a basis to better understand the response from these specimens and enable a wider range of loading frequencies to be studied as there are no restrictions associated with the testing machines.

Chapter 7

Studies on idealised damage

7.1 Introduction

The preliminary work described in Chapter 4 has demonstrated that it is feasible to assess sub-surface damage using the thermoelastic response. It has been shown that non-adiabatic behaviour causes changes in the phase of the data and that the out-of-phase response can reveal sub-surface damage. However, the work in Chapter 4 has demonstrated that the thermoelastic response from defects that are representative of actual damage is very complex. In order to understand the nature of the thermoelastic response from sub-surface damage it is necessary to assess a simpler defect geometry. The objective of this chapter is to examine in detail the response from the neighbourhood of idealised damage to demonstrate that this can be used to assess the damage severity in terms of the sub-surface stress.

In this chapter, TSA is used to examine the thermoelastic response from sub-surface machined notches in simple bar specimens. In Chapter 6, it has been shown that the thermoelastic response is influenced by the stress distributions, loading frequency and material properties. Therefore, the experimental work described in this chapter was designed to examine the effect of specimen material and loading frequency on specimens with identical stress distributions. The FE modelling approach developed in the previous chapter is validated on the notches by comparing the results with those from the TSA. A means of identifying the contribution to the surface thermoelastic response from the sub-surface is developed. This is used to indicate the stress level at the notch and hence provide an insight into the damage severity.

7.2 Experimental work

7.2.1 Test specimens

As in the numerical study in the previous chapter three types of materials were chosen based on their thermal properties: aluminium alloy, mild steel and poly methyl methacrylate (PMMA), i.e. one with a high thermal conductivity, one with a smaller thermal conductivity and one with a practically zero thermal conductivity. Three specimens were manufactured from each material with different damage severities so that a parametric study of the effect of damage could be carried out.

To reduce the complexity of the stresses and allow simple two dimensional-numerical simulations, each specimen was of a uniform rectangular cross-section as shown in Figure 7.1. A crack-like notch was made in the metal specimens by electro-discharge wire erosion machining (EDM) to give a through notch at the centre of the specimen with a finite notch radius of 0.175 mm. For the PMMA specimen the notch was machined using an end mill to give a notch radius of 0.750 mm. Although each specimen has a through crack-like flaw, this flaw can be considered as a part-through sub-surface defect if observed from the surface normal to the plane that contains the defect, i.e. plane x-y shown in Figure 7.1. Similar to Chapter 4, the damage severity is defined by a dimensionless parameter a/t (damage length to specimen thickness ratio). Three damage severities were obtained by machining notches to different depths in the three specimens of the same material. Details of the specimen dimensions are given Table 7.1, with the material properties for each specimen provided in Table 7.2.

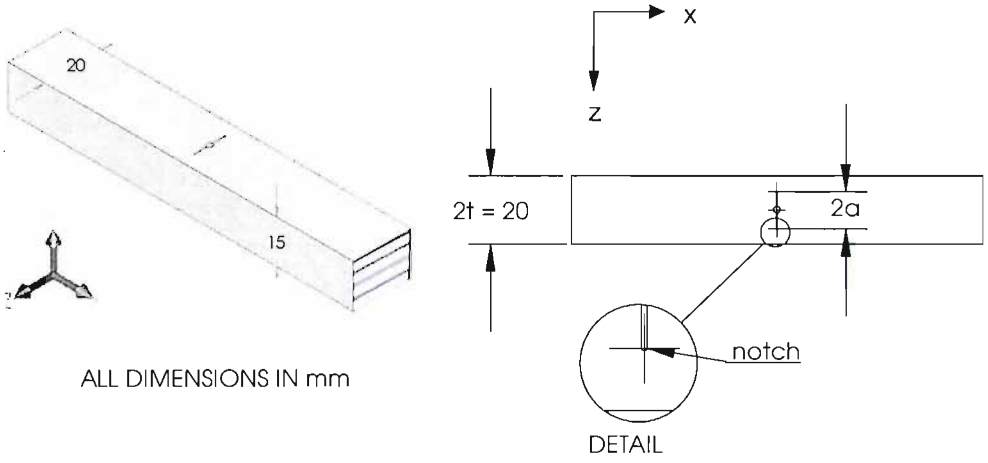

Figure 7.1: Specimen dimensions

TABLE 7.1: Specimen dimensions

Materials	Al alloy 6082			Mild steel			PMMA		
Severity Index, a/t	0.25	0.50	0.75	0.25	0.50	0.75	0.25	0.50	0.75
Defect length, a [mm]	5	10	15	5	10	15	5	10	15
Thickness, t [mm]	20	20	20	20	20	20	20	20	20
Notch radius [mm]	0.175	0.175	0.175	0.175	0.175	0.175	0.75	0.75	0.75

TABLE 7.2: Material properties

Materials	Al alloy 6082	Mild steel	PMMA
Modulus of elasticity (GPa)	70	207	2.4
Poisson's ratio	0.33	0.29	0.35
Density ($\mathrm{kg{\cdot}m^{-3}}$)	2700	7860	1190
Coef. of linear thermal expansion ($\times10^{-6}$)	24	12.4	70
Heat capacity($\mathrm{J{\cdot}kg^{-1} \cdot K^{-1}}$)	896	460	1400
Thermal conductivity ($\mathrm{W{\cdot}m^{-1} \cdot K^{-1}}$)	180	50	0.17

7.2.2 Experimental arrangement

The undamaged surface (y-z plane in Figure 7.1) of each specimen was coated with a thin layer of matt black paint to enhance the surface emissivity. The specimen was assembled into the end jigs shown in Figure 7.2. This arrangement allows the test specimen to move freely and hence eliminates any possible bending that may be caused by misalignment of the jaws of the testing machine. The specimens were loaded in uniaxial tension with the applied load ranges given in Table 7.3. These applied load ranges were selected during testing as the minimum load required to ensure that signal noise was maintained at less than 10% of the overall signal. The intention was to keep the load as small as possible to minimise plastic deformation at the notch. The extent of the plastic region was estimated using a simple SIF approach by taking the maximum stress in the cycle and assuming a sharp notch; this is given as a percentage of the ligament length, i.e. $(t - a)$ in Table 7.3. It can be seen that the largest plastic zone occurs in the steel specimen with the largest notch, but even in this case it is only 1% of the ligament length.

The DeltaTherm 1400 was used in this experiment. The detector was positioned as shown in Figure 7.3, so that the thermoelastic signal from an undamaged face (i.e. the x-y plane (see Figure 7.1)) at a remote region (away from the damage site) and at the damage site could be captured simultaneously. This results in the TSA image having resolution of approximately 0.4 mm per pixel. For each specimen thermoelastic data was recorded at the following frequencies: 2, 3, 5, 10, 20, 30 and 40 Hz.

The ΔT values associated with the sum of the principal stress away from the notch are calculated using Equation 5.3 with the material properties given in Table 7.2 and are also given in Table 7.3; these will be used to normalise the FEA results (see Section 7.3).

Table 7.3: Applied loads and calculated temperature change for each specimen

Materials	a/t	Max load (kN)	Min load (kN)	$\Delta\sigma$(MPa)	ΔT (K)	Plastic zone size (% of ligament)
Al alloy (6082)	0.25	7	1	20	0.058	0.03
	0.50	7	1	20	0.058	0.10
	0.75	7	1	20	0.058	0.54
Mild steel	0.25	11.5	0.5	36.7	0.037	0.11
	0.50	11.5	0.5	36.7	0.037	0.44
	0.75	7.5	0.5	23.3	0.023	0.99
PMMA	0.25	0.7	0.1	2	0.025	0.01
	0.50	0.7	0.1	2	0.025	0.02
	0.75	0.5	0.1	1.3	0.016	0.05

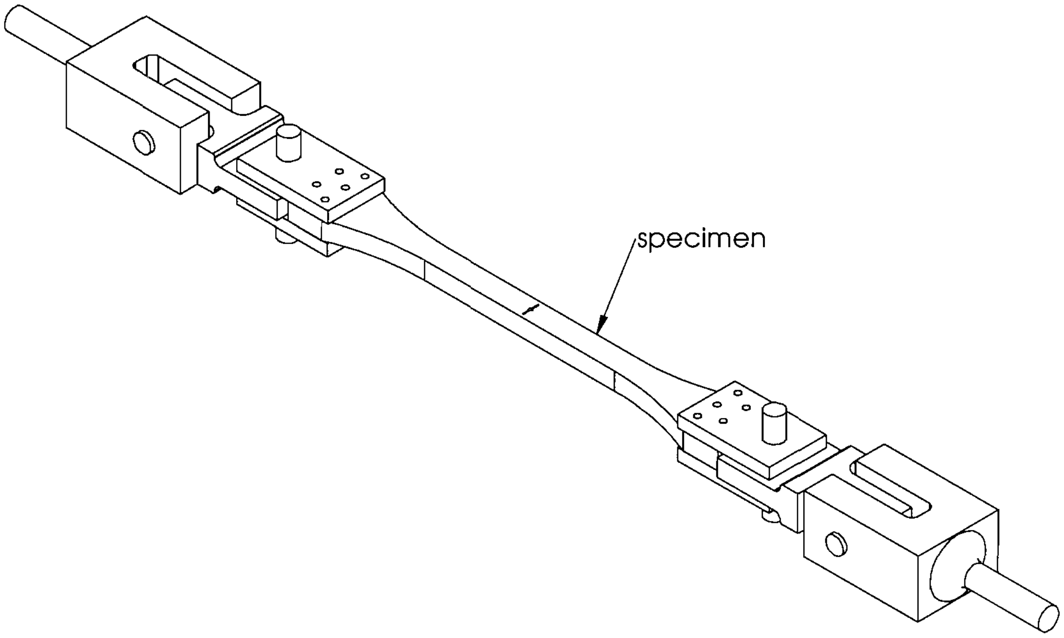

FIGURE 7.2: The specimen and loading jigs

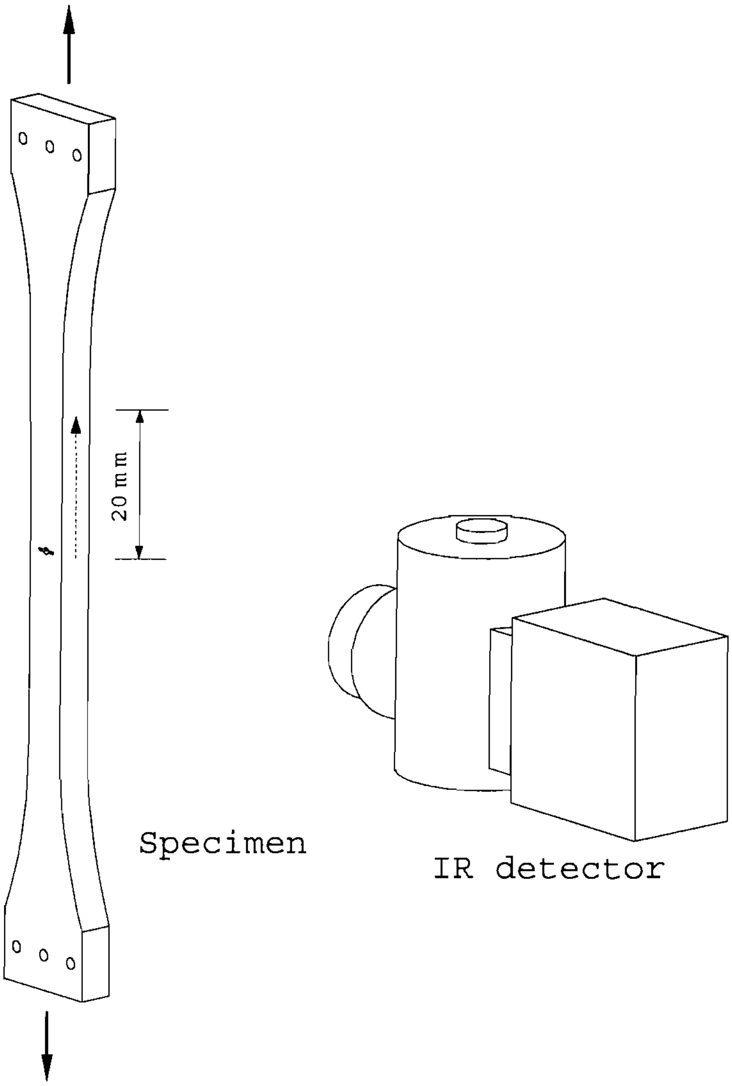

FIGURE 7.3: Detector viewing arrangement

7.2.3 Results and discussions

The results are presented in the form of signal magnitude, i.e. the R-signal data from the DeltaTherm system. This is because the R-data is not affected by the phase setting and is therefore equivalent to the absolute temperature change (see Equation 5.19). As the R-data is independent of the phase setting, any changes in the R-signal can be attributed directly to non-adiabatic behaviour. The drawback of presenting data this way is that negative stresses cannot be identified. Furthermore as the R-signal is directly related to the absolute temperature change it can be compared directly with the ΔT values obtained from the FEA. Examples of R-image and phase data are shown in Figure 7.4 for the aluminium alloy specimen, Figure 7.5 for the steel specimen and Figure 7.6 for the PMMA specimen with a/t = 0.50 at 2 or 3 and 40 Hz (readings at 2 Hz could not be obtained for the PMMA).

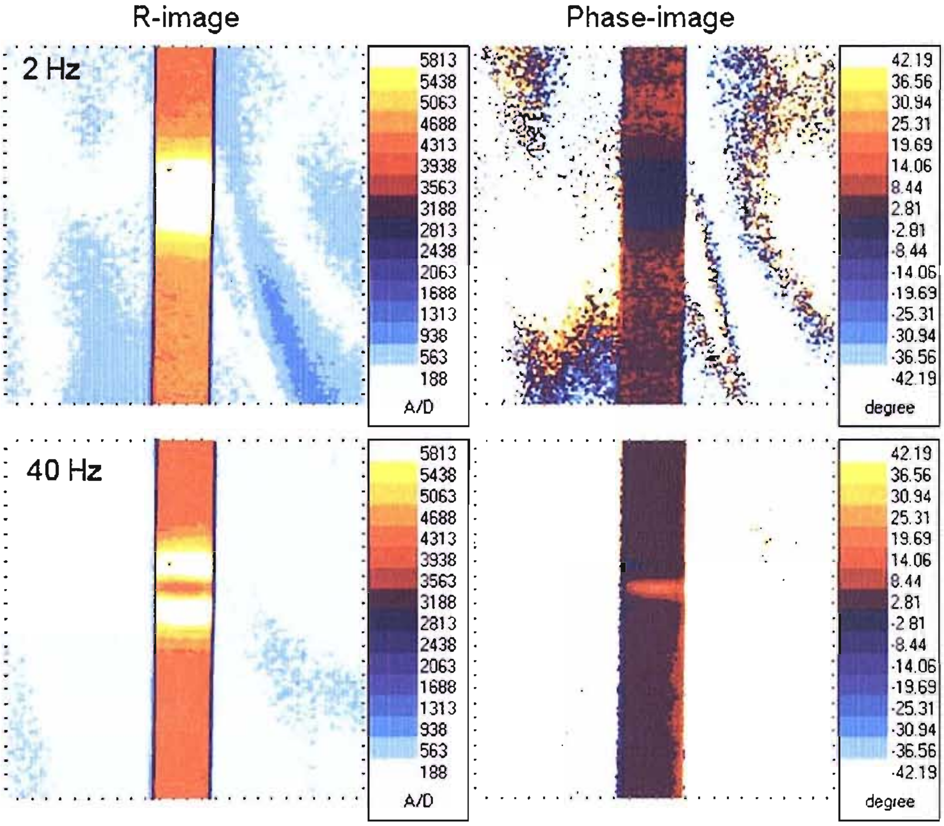

FIGURE 7.4: Aluminium alloy specimen (a/t = 0.50)

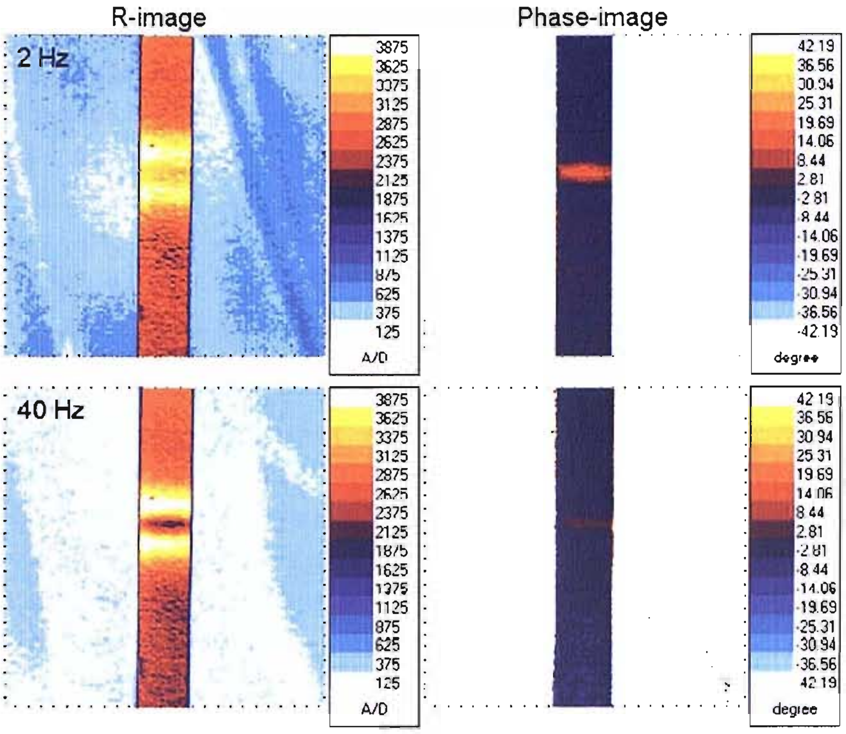

FIGURE 7.5: Steel specimen ($a/t = 0.50$)

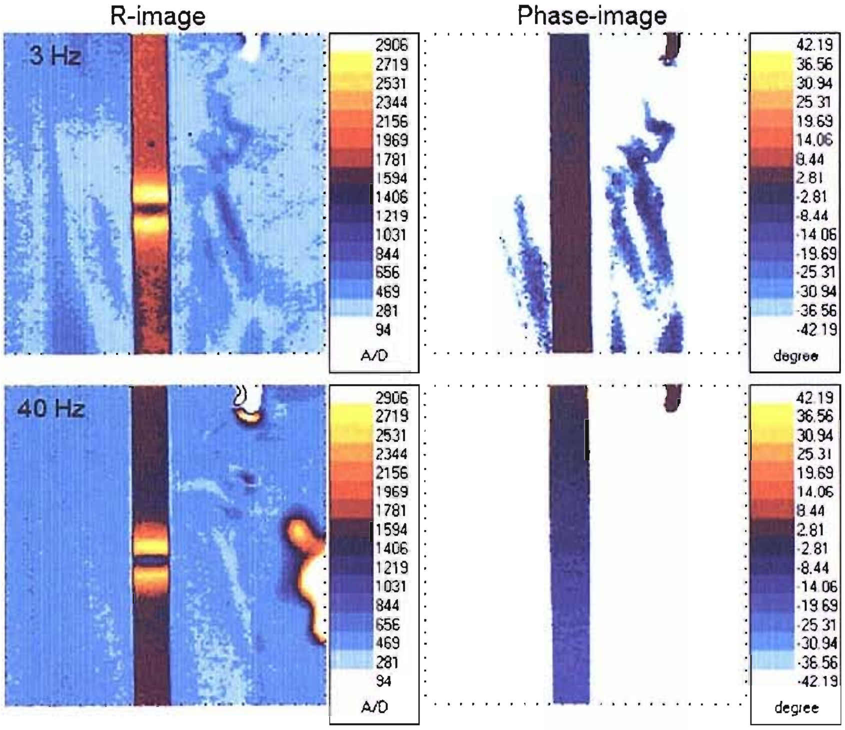

FIGURE 7.6: PMMA specimen ($a/t = 0.50$)

In the R-image for the aluminium alloy (Figure 7.4), it is very clear that the response at 2 Hz is very different to that at 40 Hz. At 2 Hz there is an increase in signal magnitude local to the damage site and at 40 Hz there is a decrease. In contrast the R-images for the PMMA are practically identical at 3 Hz and 40 Hz, both showing a decrease in signal magnitude locate to the damage site. In the phase images for the PMMA, there is no localised phase shift at the damage site, however, there is an indication of phase shift gradually across the specimen. For the steel specimen, there is a similar trend in the R-image between 2 Hz and 40 Hz to that of the PMMA specimen. However, there is a much greater difference in signal magnitude around the damage region between 2 and 40 Hz.

As each material gives a different response (i.e. has a different thermoelastic constant) and the applied stresses were different, for comparison purposes, the magnitude of the thermoelastic response must be normalised against the response away from the damaged region and plotted as *stress factors* in an identical manner to that described in Chapter 4. However, the phase of the signal is not affected by applied load range (in the elastic region); therefore phase data can be compared directly from specimen to specimen.

To compare the thermoelastic data from each test, an interrogation line along the centre line of x-y plane from a position coincident with the notch tip to a distance 20 mm away from notch tip was defined, as shown in Figure 7.3. The stress factor and phase data along the interrogated line for 2, 10, 20 and 40 Hz for aluminium, steel and for 5, 10, 20 and 40 Hz for PMMA are plotted and shown in Figure 7.7, Figure 7.8 and Figure 7.9 respectively. The reason for using 5 Hz instead of 2 Hz for the lowest loading frequency in PMMA specimens for this experiment is that the 5 Hz is the lowest loading frequency that the DeltaTherm system could be used to measure the thermoelastic signal from the PMMA specimen with $a/t = 0.75$. It is important to note that in an adiabatic situation the temperature change would be 180 degrees out of the phase with the stress change (see Equation 5.16). For presentation purposes the 180 degree phase lag has been omitted in Figure 7.7, 7.8 and 7.9 and hence the negative phase change is shown in the phase data. For all materials the shallowest notch, i.e. $a/t = 0.25$, gives the smallest variation in stress factor and phase. With the deeper notches the stress factor increases and the phase changes are more pronounced particularly over the range 2 20 Hz. This is except for the phase response from the PMMA specimens in which all the phase changes are relatively small.

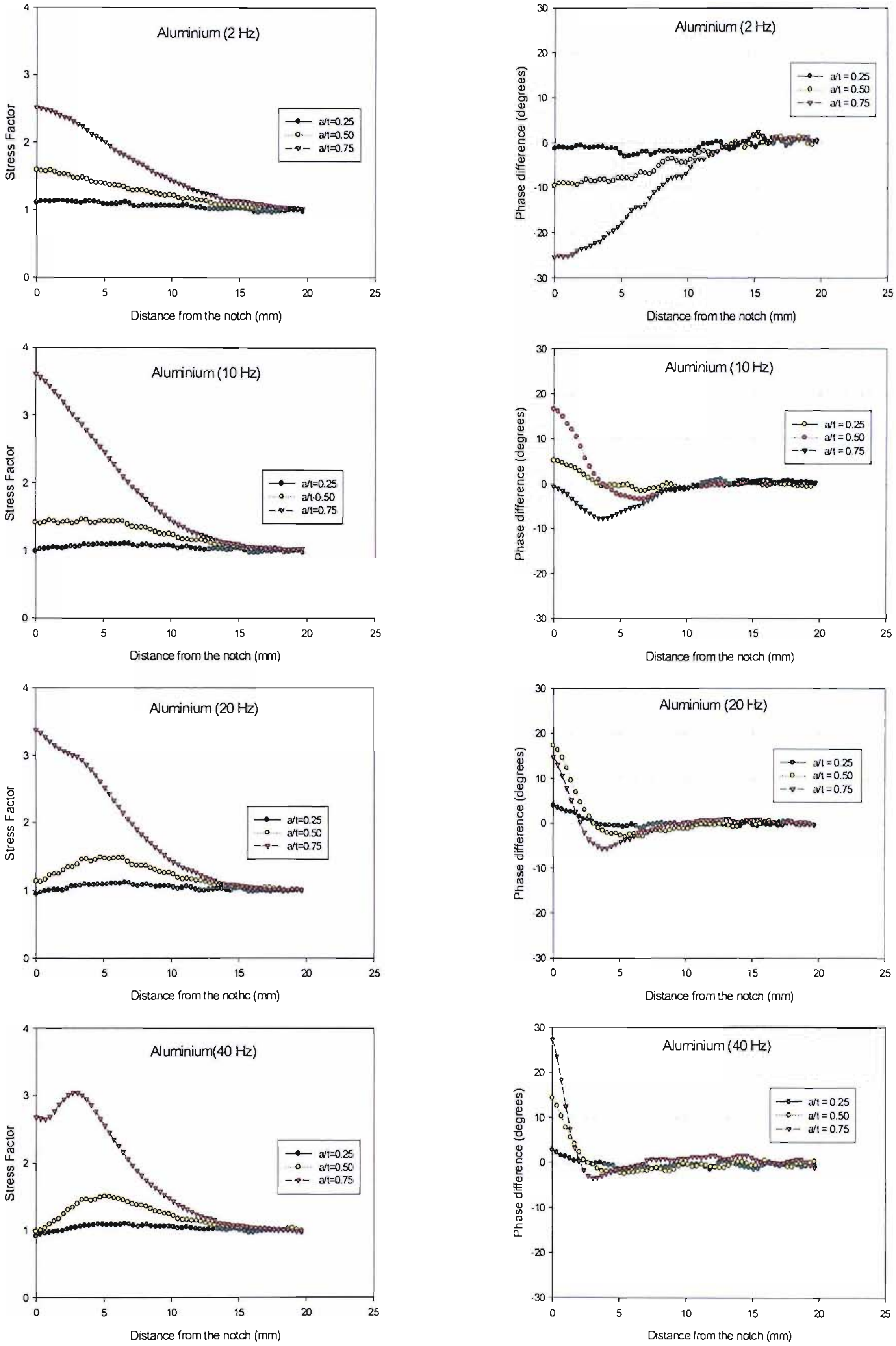

FIGURE 7.7: Stress factor and phase data from aluminium specimens

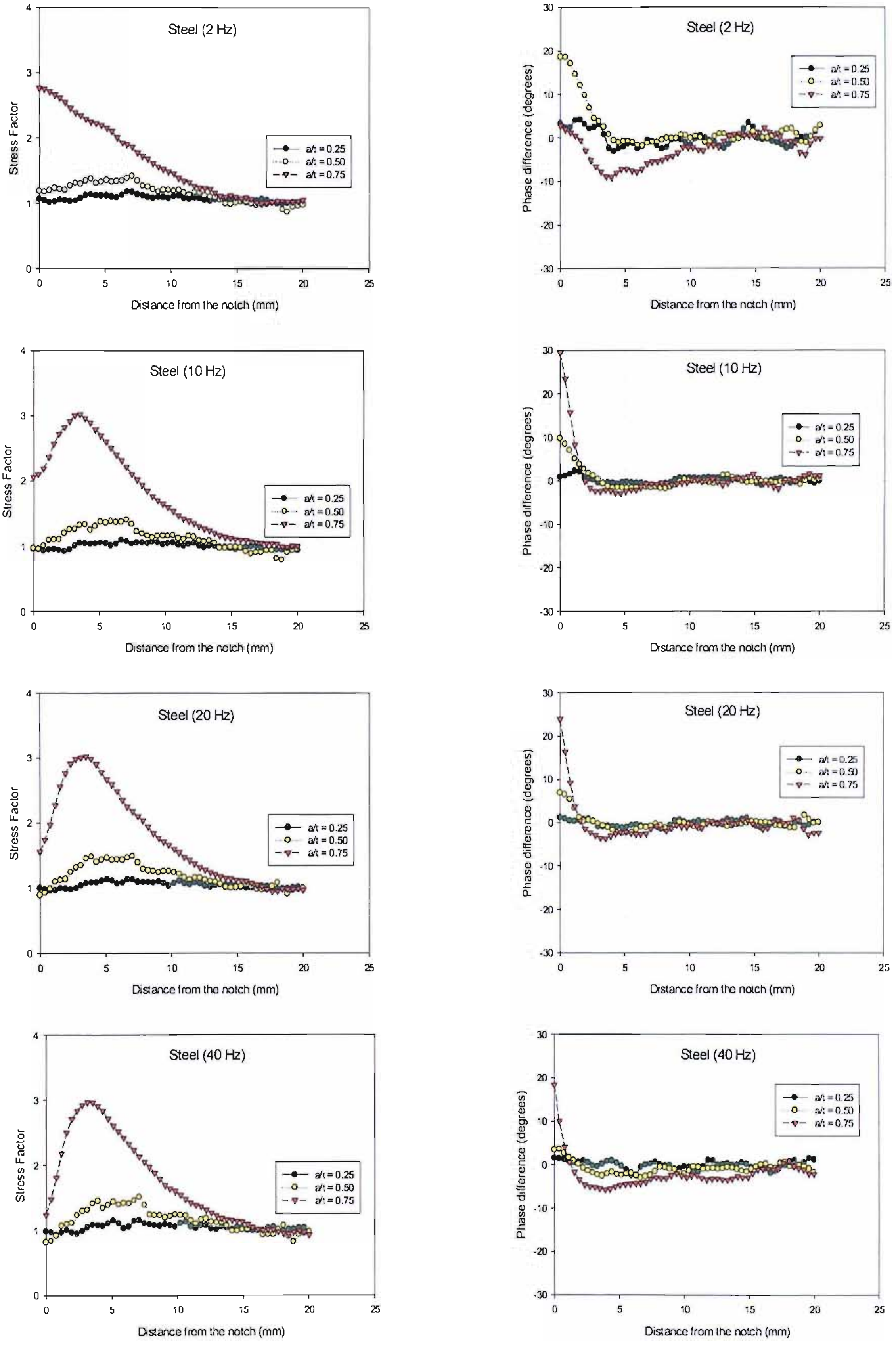

FIGURE 7.8: Stress factor and phase data from steel specimens

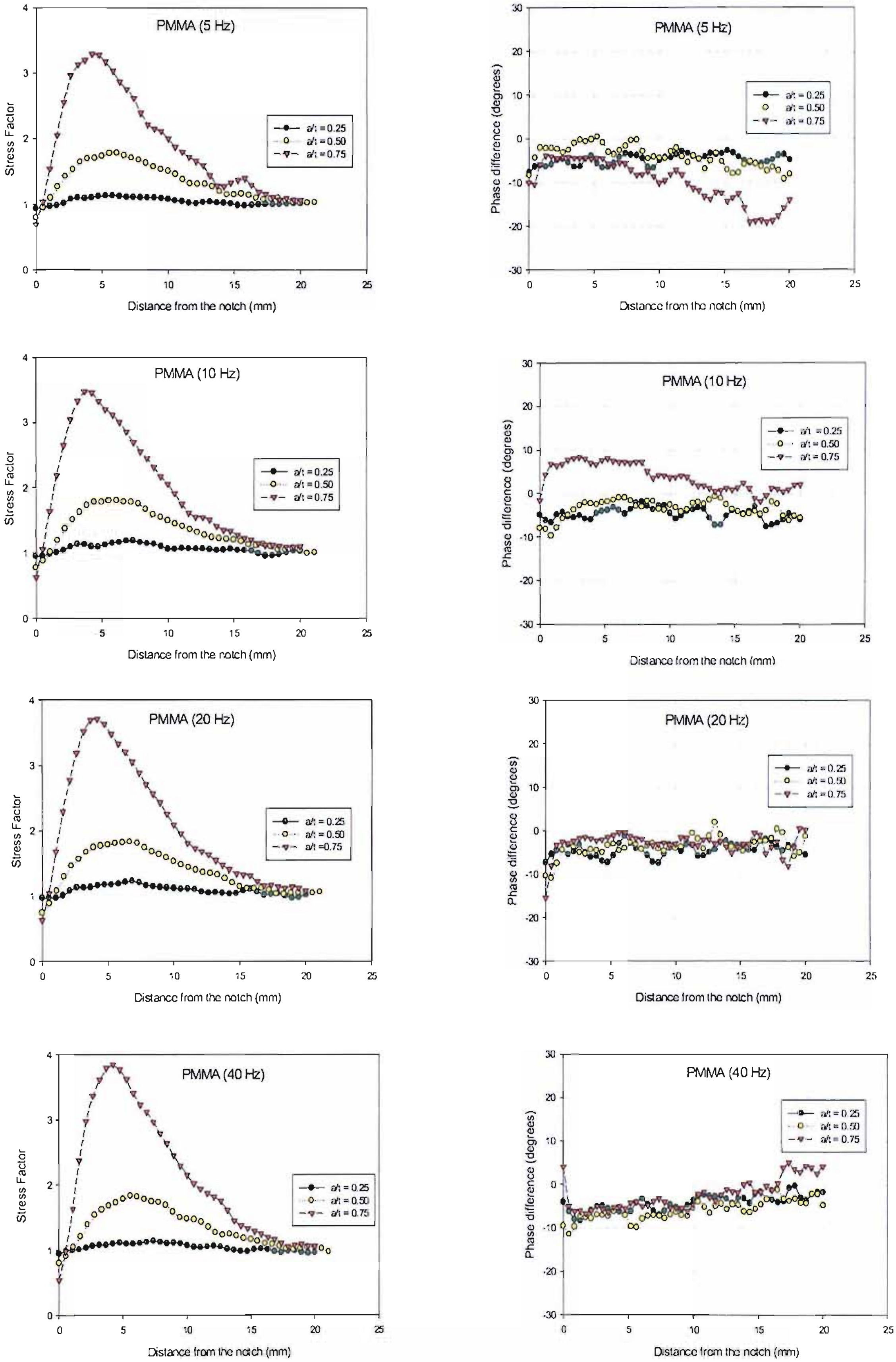

FIGURE 7.9: Stress factor and phase data from PMMA specimens

From all the plots for the PMMA (Figure 7.9), the thermoelastic response shows that the material behaves in an adiabatic manner at a relatively low loading frequency. The trend of the stress distribution for each PMMA specimen shows that the signal response is frequency independent. As the dimensions of the specimens and the through notch are very similar, therefore under adiabatic conditions, the trend of the stress distribution from all specimens is expected to be similar to that of the PMMA specimens. Although adiabatic behaviour is exhibited from the stress factor plots in Figure 7.9, there are variation in the phase data, which does not concur with the implied adiabatic conditions. An inspection of the plots shows that the a gradient across the 20 mm length is particularly pronounced at 5 Hz for a/t = 0.25 and for all specimens in the 40 Hz plot. After consultation with the equipment manufacturers it was determined that this variation in phase could be attributed to line by line data collection and the sampling rate of the detector and not non-adiabatic behaviour.

It can be seen that, on the metal specimens, particularly at relatively low load frequencies, the curves change shape at each frequency setting. To provide a clearer interpretation of the data Tables 7.4, 7.5 and 7.6 provide values of maximum stress factor value and its location relative to the centre of the notch for each a/t. Starting with the PMMA specimens it can be seen that the stress factors are relatively constant across the frequency range giving averages of 1.16 for a/t = 0.25, 1.78 for a/t = 0.5 and 3.58 for a/t = 0.75. There is a variation when a/t = 0.75 but this could be attributed to signal processing difficulties (see above) rather than non-adiabatic behaviour. The position of the maximum signal is also constant at 6.0, 5.5 and 4.0 mm from the notch tip for a/t = 0.25, 0.5 and 0.75 respectively. Accepting that the notch in the PMMA is slightly different from the notches in the steel and the aluminium, the values for the maximum stress factor and the maximum signal position obtained for the PMMA can be used as the 'adiabatic values' for each geometry. For the a/t ratio of 0.25 there is little difference in the value of the maximum stress factor across the frequency range in the aluminium alloy specimens. It is clear from the position of the maximum stress factor adiabatic conditions are achieved at 10 Hz and above. For the steel specimen when a/t = 0.25 it appears adiabatic conditions are achieved at all frequencies. The phase angle reading given in Table 7.7 indicates that the variation of phase data is within the range of noise, i.e. about ± 2 degrees. For a/t = 0.5, a similar trend is shown for both the steel and the aluminium as with a/t = 0.25. However, the steel stress factor is much lower than that of the aluminium and the PMMA. Furthermore the position of the maximum stress factor, although constant, is further away from the notch. The most interesting results are these given for the a/t = 0.75, here the aluminium does not appear to achieve adiabatic conditions and the stress factor values are once again much lower than those given by the aluminium and the PMMA. An explanation for the differences between the steel and the two other specimens may be the additional heat generated by the larger plastic zone in the steel specimen (see Table 7.3).

TABLE 7.4: Maximum stress factor and its locations for specimens with $a/t = 0.25$

Materials	Al alloy 6082		Mild steel		PMMA	
Load freq (Hz)	SF(Max.)	Pos.(mm)	SF(Max.)	Pos.(mm)	SF(Max.)	Pos.(mm)
2	1.11	0	1.17	7.0		
5	1.08	2.0	1.12	7.0	1.13	6.0
10	1.12	6.2	1.07	7.0	1.18	6.0
20	1.12	6.2	1.12	7.0	1.21	6.0
40	1.10	6.8	1.15	7.0	1.12	6.0

TABLE 7.5: Maximum stress factor and its locations for specimens with $a/t = 0.50$

Materials	Al alloy 6082		Mild steel		PMMA	
Load freq (Hz)	SF(Max.)	Pos.(mm)	SF(Max.)	Pos.(mm)	SF(Max.)	Pos.(mm)
2	1.59	0	1.30	6.2		
5	1.60	0	1.30	6.2	1.73	5.5
10	1.45	5.4	1.30	6.2	1.78	5.5
20	1.46	5.4	1.40	6.2	1.83	5.5
40	1.49	5.4	1.40	6.2	1.78	5.5

TABLE 7.6: Maximum stress factor and its locations for specimens with $a/t = 0.75$

Materials	Al alloy 6082		Mild steel		PMMA	
Load freq (Hz)	SF(Max.)	Pos.(mm)	SF(Max.)	Pos.(mm)	SF(Max.)	Pos.(mm)
2	2.51	0	2.78	0		
5	3.39	0	3.08	3.1	3.29	4.0
10	3.60	0	3.08	3.1	3.47	4.0
20	3.38	0	3.08	3.1	3.71	4.0
40	3.04	3.0	3.08	3.1	3.85	4.0

TABLE 7.7: Phase angles at notch-tip for specimens with $a/t = 0.25$

Materials	Al alloy 6082	Mild steel	PMMA
Load freq (Hz)	Phase (deg)	Phase (deg)	Phase (deg)
2	-1.2	3.2	
5	5.3	2.7	-7.0
10	5.2	0.8	-5.3
20	4.0	1.2	-7.1
40	2.8	1.5	-4.2

TABLE 7.8: Phase angles at notch-tip for specimens with $a/t = 0.50$

Materials	Al alloy 6082	Mild steel	PMMA
Load freq (Hz)	Phase (deg)	Phase (deg)	Phase (deg)
2	-9.4	18.6	--
5	6.9	12.4	-8.0
10	16.7	9.8	-8.0
20	17.3	6.9	-10.4
40	14.4	3.4	-9.5

It is clear from this work, taking into account the erratic phase response from the PMMA

TABLE 7.9: Phase angles at notch-tip for specimens with $a/t = 0.75$

Materials	Al alloy 6082	Mild steel	PMMA
Load freq (Hz)	Phase (deg)	Phase (deg)	Phase (deg)
2	-25.4	2.7	-
5	-12.3	25.5	-10.2
10	0	29.4	-1.5
20	14.7	23.9	-15.4
40	27.4	18.4	4.2

specimens, the PMMA data shows no real phase change and demonstrates that for materials with low thermal conductivities the approach described in this thesis cannot be used to ascertain the damage severity in components made from similar materials. This is because the heat transfer due to the thermal gradient is not significant in a material with a very low thermal conductivity as demonstrated in the parametric study in Section 6.4. In view of this, the remainder of this analysis in this chapter will concentrate mainly on the aluminium and steel specimens.

At low loading frequencies, an out-of-phase signal is observed from a much larger area around the damage than at higher frequencies. Figure 7.10 show a comparison of phase difference of the aluminium specimens at 2 and 20 Hz. This shows that at higher loading frequencies the non-adiabatic behaviour becomes more localised. This is because adiabatic conditions are achieved at the lower stress gradient regions, i.e. away from the notch. As the loading frequency is increased the damage can be located by examining the phase difference in the signal. This pattern could be used to locate the existence of sub-surface damage. Therefore an interesting feature of the work is the observation that phase change can be used to precisely locate the damage at higher frequencies.

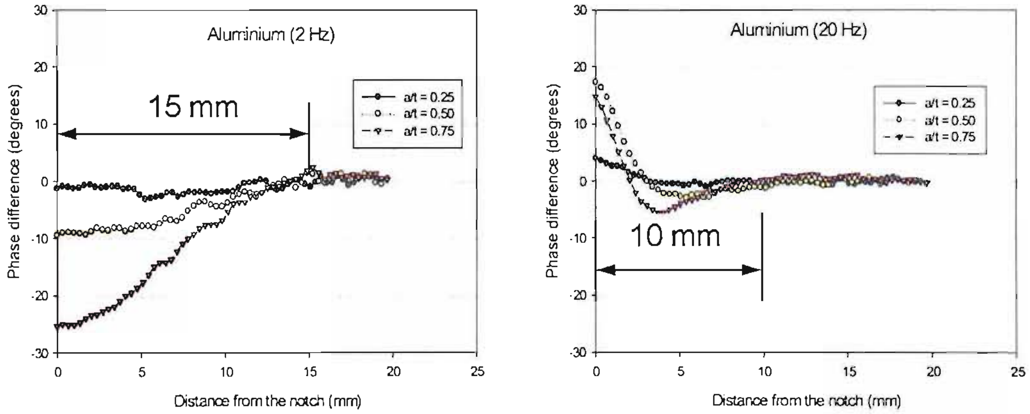

FIGURE 7.10: A comparison of the non-adiabatic response regions at 2 Hz and 20 Hz on the aluminium specimens

By inspecting Tables 7.7–7.9 it can be seen that at the lower frequencies, it is not always the deepest notch that gives the greatest phase change. In fact it is difficult to discern any relationship between the frequency and the phase in the data. This warrants further investigation. As changes in the phase must be an indication of non-adiabatic behaviour and in view of the difficulties in obtaining accurate and constant phase data, (as illustrated in Table 7.7 to Table 7.9) in the next section it was decided to study the thermoelastic response numerically using the approach described in the previous chapter.

7.3 Numerical simulation of thermoelastic effect on damaged specimens

By taking advantage of symmetry only a quarter of the specimen was modelled, which was constrained at the boundaries as shown in Figure 7.11. The damage severity and notch radius of individual models were defined using the values given in Table 7.1. For each material type, three models with damage severities of a/t = 0.25, 0.50 and 0.75 were produced. The material properties used in the analysis were taken from Table 7.2 and the model was constructed as described in Chapter 6.

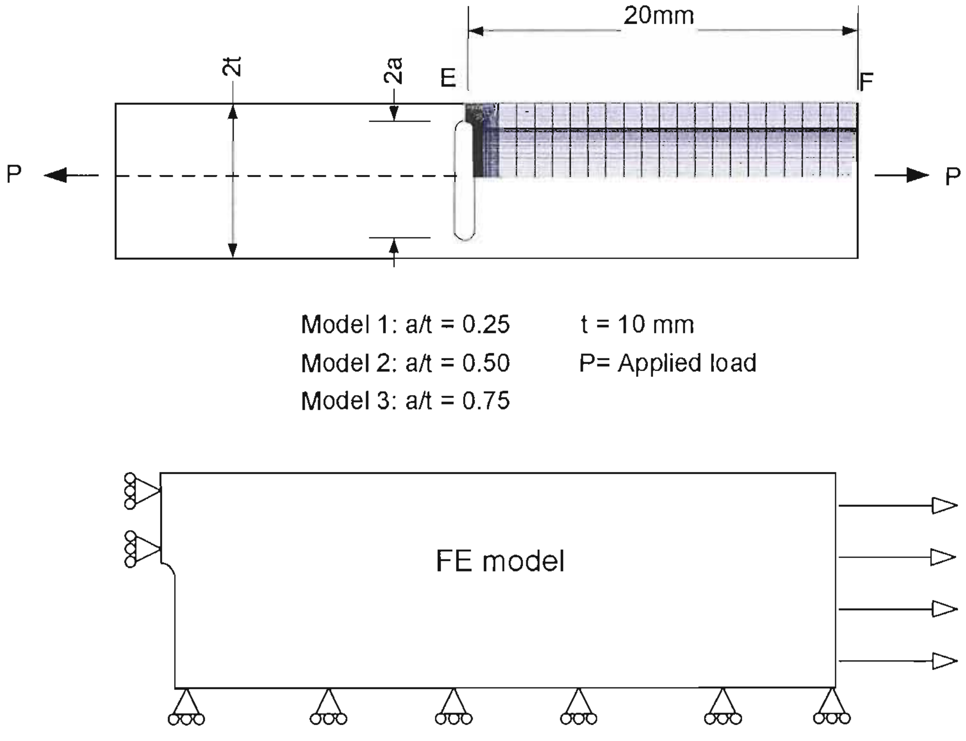

FIGURE 7.11: Geometries of the models for TSA

In this analysis the model contains a small radius notch, where a large stress gradient exists, therefore model discretization is essential. The mesh transition and density of the mesh around the notch must be fine enough to capture the high stress/thermal gradient. In view of this, convergence tests (see Appendix A.2) were carried out prior to the simulation in order to ensure the optimum mesh size.

To compare the TSA and the FEA results, both data sets were normalised against values obtained from the area of uniform stress away from the notch. The TSA data was normalised using the signal away from the notch and plotted as stress factors. The FE data was normalised against ΔT (see Table 7.3) calculated from the applied stress away from the notch and the material properties. Examples of the results from the simulation are given in Figure 7.12, using data from the path E-F shown in Figure 7.11, at 2 and 5 Hz for the aluminium and steel specimens. It can be seen that the correspondence of the results from TSA and FEA is excellent in most cases. The trends of the stress factor curves and the phase data are the same. However, some discrepancy can be observed at the location of the notch tip. Therefore, a detailed examination of the data at locations close to the notch tip has been carried out to observe the trends in the data from both techniques for all loading frequency range.

To compare the FE results with the TSA at specific locations, four points on the surface around the damage site were selected from locations on the x–y plane of the aluminium specimen and steel specimens with $a/t = 0.75$. Readings were taken coincident with the notch tip and 0.67 mm, 2 mm and 4 mm away from the notch tip (see Figure 7.13) for frequencies from 2 to 40 Hz. The normalised thermoelastic signal magnitude from TSA and the normalised temperature response from FEA are plotted in Figure 7.14. The plot shows that the experimental data is behaving as predicted by Equation 5.6 providing confidence in the phase readings given in Figure 7.15. To further confirm the validity of the phase readings given in the experiments, the corresponding phase data are also provided in Figure 7.15. In this figure, the agreement at the notch in the phase data from the FE and TSA for the steel specimen is poor. The only explanation in this case may be that of the largest plastic zone estimated in the steel specimen with $a/t = 0.75$ in Table 7.3 which contributes extra heat and is not considered in the FE simulation. For the aluminium specimen at the notch and in all other cases the agreements are very good, confirming the validity of the FE simulation.

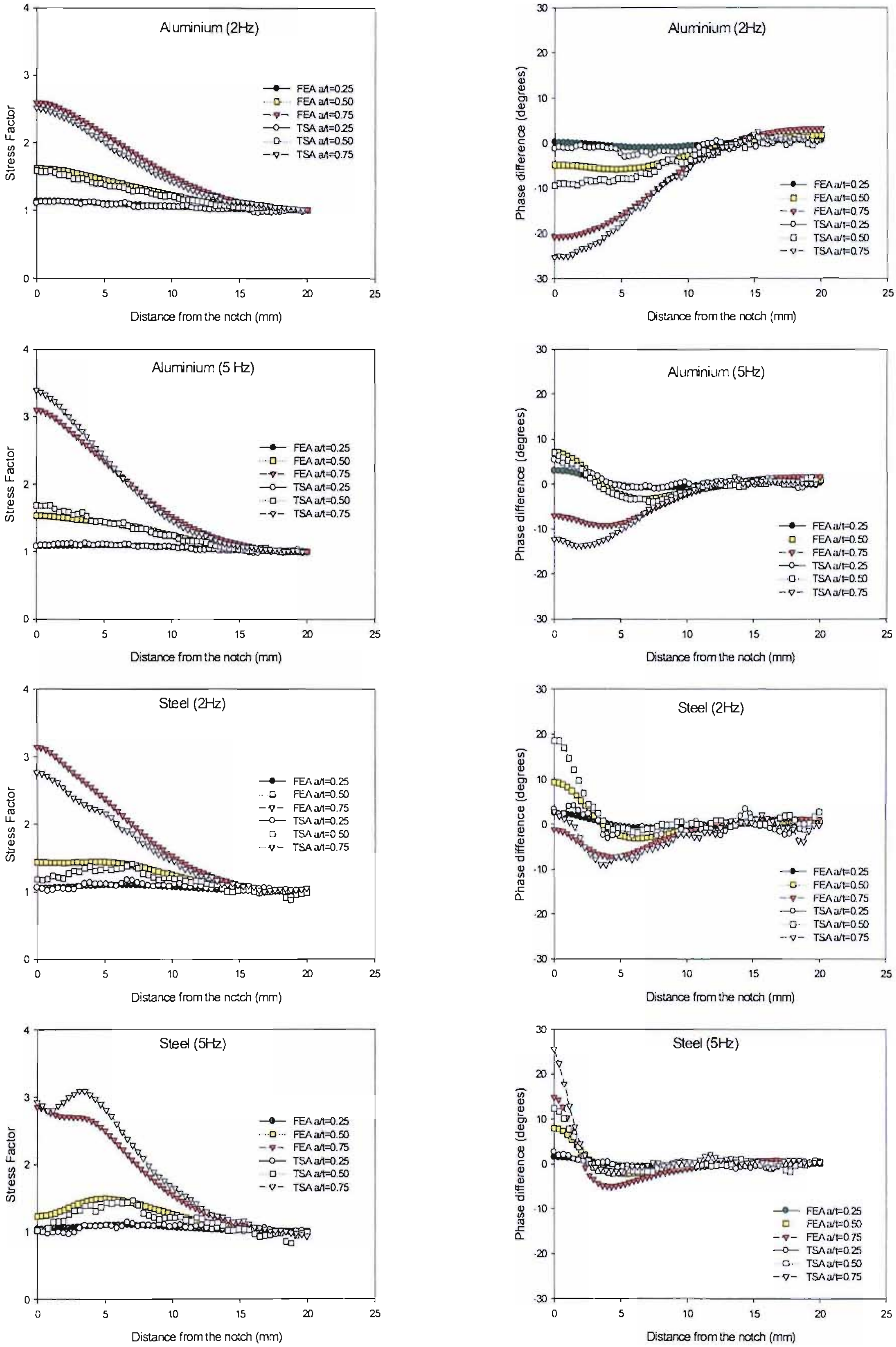

FIGURE 7.12: FEA results compared with TSA for aluminium and steel specimens

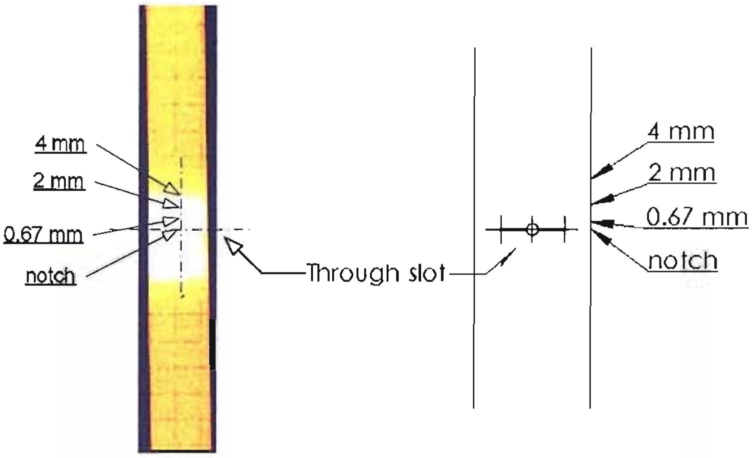

FIGURE 7.13: Locations of the measuring point from TSA data and FE model

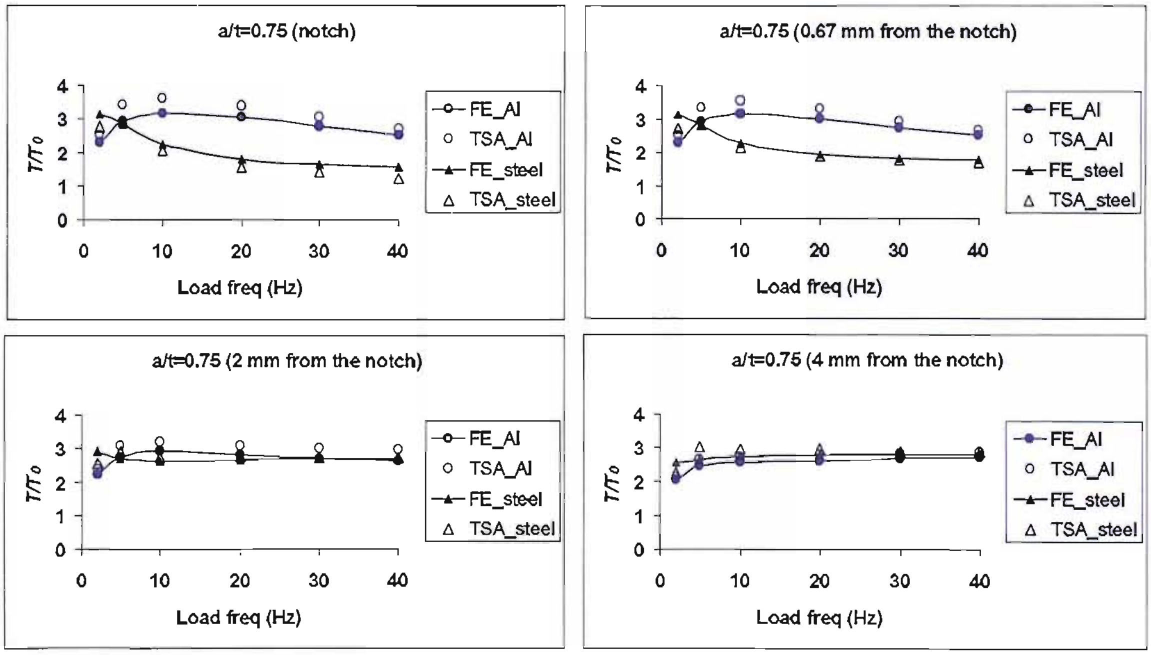

FIGURE 7.14: Data point comparisons between FEA and TSA results (stress factor)

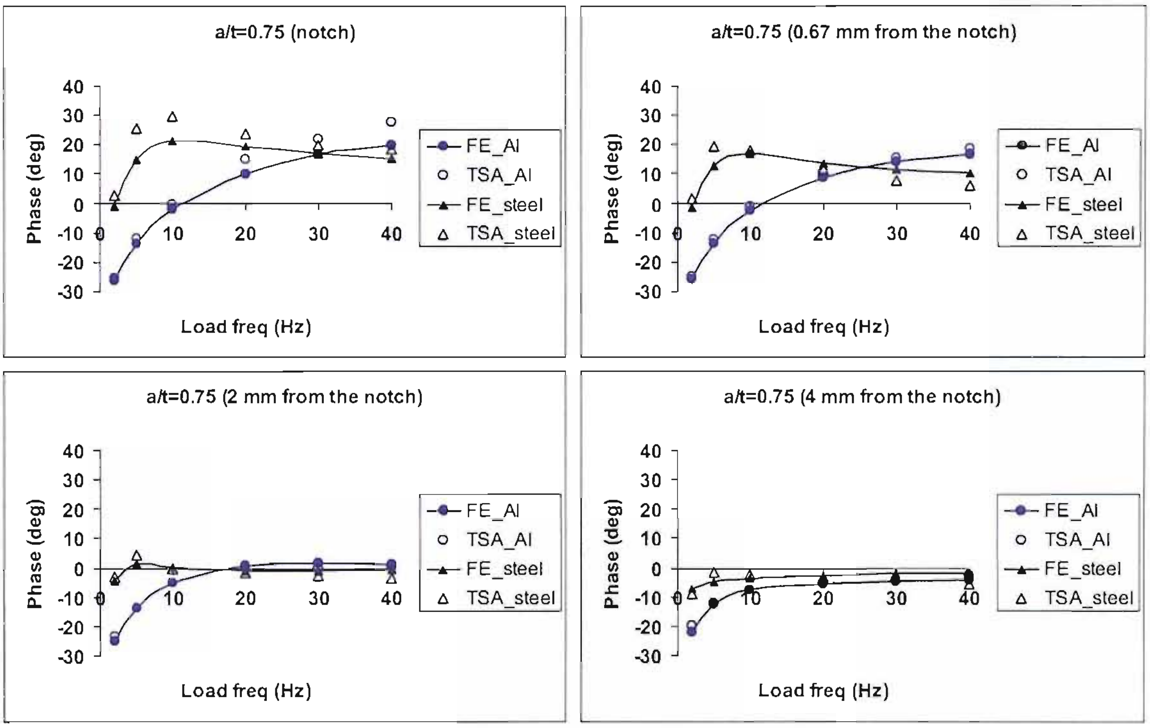

FIGURE 7.15: Data point comparisons between FEA and TSA (phase)

7.4 Damage Analysis

In all of the work described in this chapter it is difficult to identify any relationship between the damage severity and the non-adiabatic thermoelastic response. However, it is clear that non-adiabatic behaviour is frequency dependent. To fully investigate the non-adiabatic behaviour at the notch, FE simulations were carried out over a wider range of loading frequencies, i.e. from 1 Hz to 1000 Hz, than were available from experimentation. It is assumed that 1000 Hz is sufficient to achieve fully non-adiabatic behaviour in all specimens. Inspection of the experimental results show that material properties and the notch depth play a significant role in the response. In order to eliminate the influence of material properties and notch depth, it was decided to plot the phase data from the surface at the notch (see Figure 7.13) against the thermal diffusion length, $\gamma = \sqrt{\frac{k}{\rho c_p \pi f}}$, ($f$ is the loading frequency), divided by the ligament length, i.e. the distance between the notch tip and the surface, $(t - a)$. The plot of the phase data obtained from FE simulations against this quantity is shown in Figure 7.16.

In Figure 7.16 a very revealing trend emerges. There are three distinct curves representing each notch depth. The zero point in this curve represents fully adiabatic behaviour at high frequencies. It is difficult to see the PMMA[1] results in Figure 7.16 as they are grouped around the zero position so a zoomed plot is also provided in Figure 7.16. This clearly shows the PMMA points on the curves according to their notch depth. As the quantity $\gamma/(t-a)$ increases, the non-adiabatic behaviour in the specimen is also increasing. The turning point at 0.25 in all three curves is an important feature. Accepting that the non-adiabatic contribution to thermoelastic signal comes from beneath the surface then the turning point could indicate when a greater proportion of the signal is obtained from beneath the surface. Therefore, taking signal readings from when $\gamma/(t - a)$ is greater than 0.25 opens up the possibility of obtaining data that is directly related to the sub-surface stress.

---

[1] The notch radius of the PMMA models are the same as aluminium and steel models to eliminate the effect of different geometries, i.e. the notch radius.

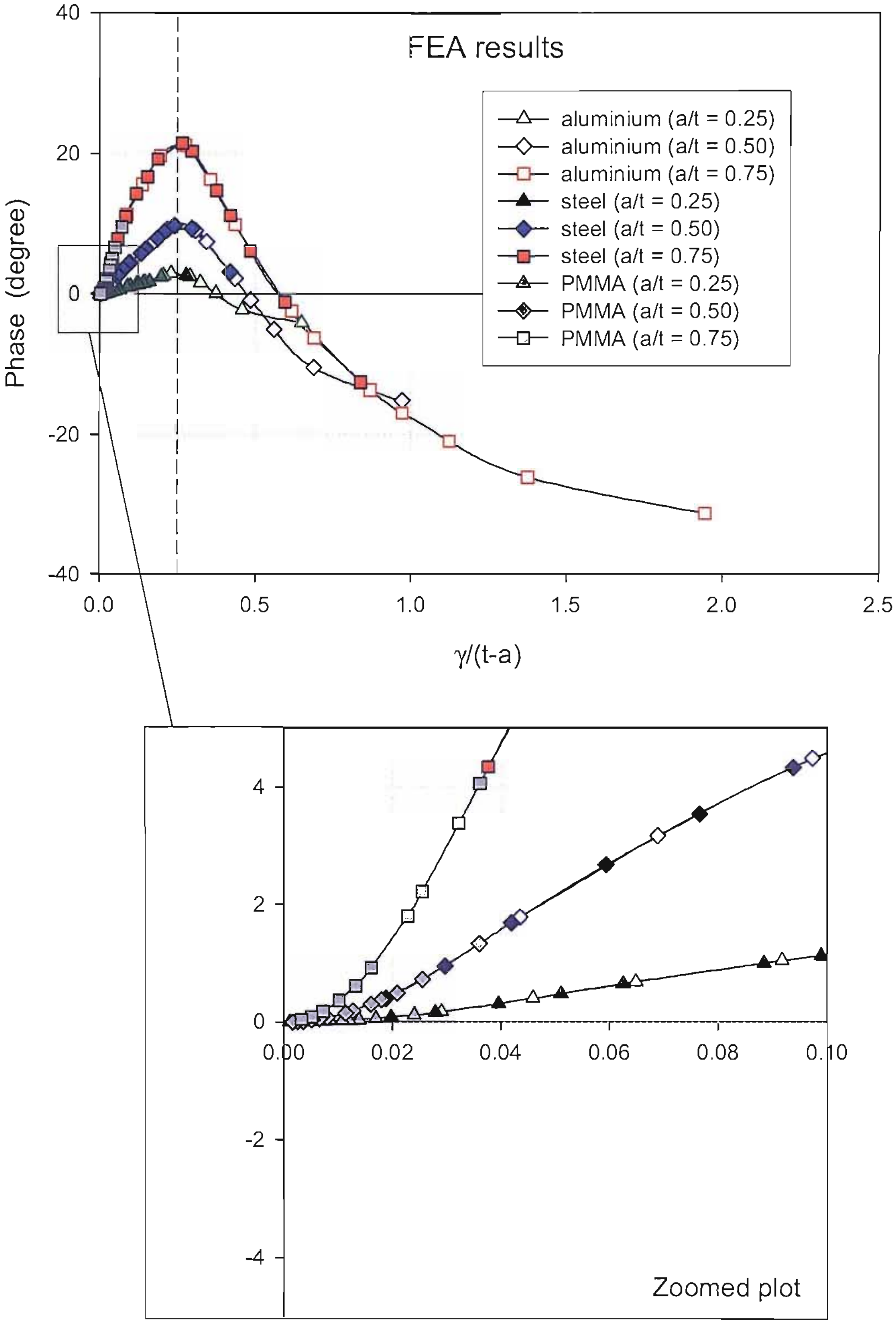

FIGURE 7.16: Phase response from FEA

re 7.17 shows a plot of the experimental data obtained for the steel and the aluminium. A 'best fit' curve is also provided for each notch depth and it can be seen that there are three distinct curves. The loading frequency for the 2 Hz and 40 Hz conditions are indicated in the plot. The underline and non-underline label represents the loading condition for the aluminium and steel specimen respectively. With the exception of the aluminium $a/t = 0.75$ notch, the 40 Hz conditions lies in the range $0 \leq \gamma/(t-a) < 0.25$. Likewise, the 2 Hz values all lie above $\gamma/(t-a) = 0.25$ with the exception of the $a/t = 0.25$ for the steel specimen. For comparison the FEA data is presented in the same way in Figure 7.18 and shows identical trends. However, the magnitude of the phase change in the experimental data is much greater than that given by the FEA. The only physical explanation for this is the omission of the plastic zone characteristic at the notch in the FEA. However, the means by which the DeltaTherm system software obtains the phase is also questionable and could be contributing to the difference.

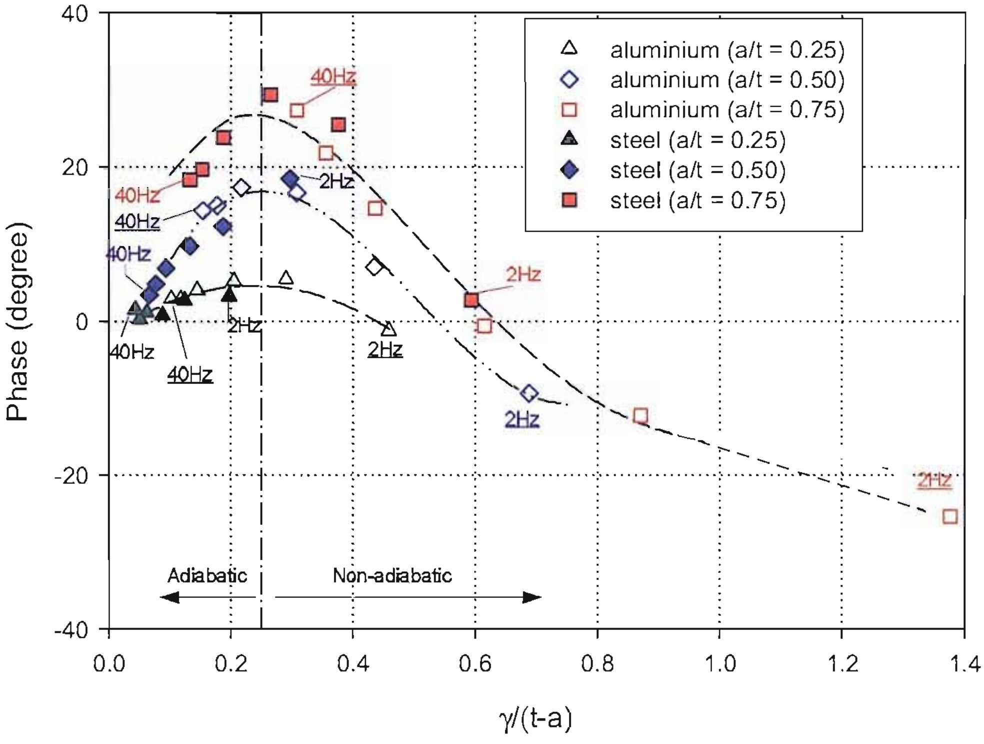

FIGURE 7.17: Phase response from TSA

Equation 5.19 in Section 5.2 shows that thermoelastic signal obtained under the effect of non-adiabatic behaviour is biased by the extra heat content caused by heat conduction, i.e. from the sub-surface in this case. Therefore, a subtraction of TSA signal between the one obtained at high frequency (more adiabatic) and one obtained at low frequency could be used to reveal the contribution caused by the additional heat content from the sub-surface and may provide an opportunity for stress analysis at the notch.

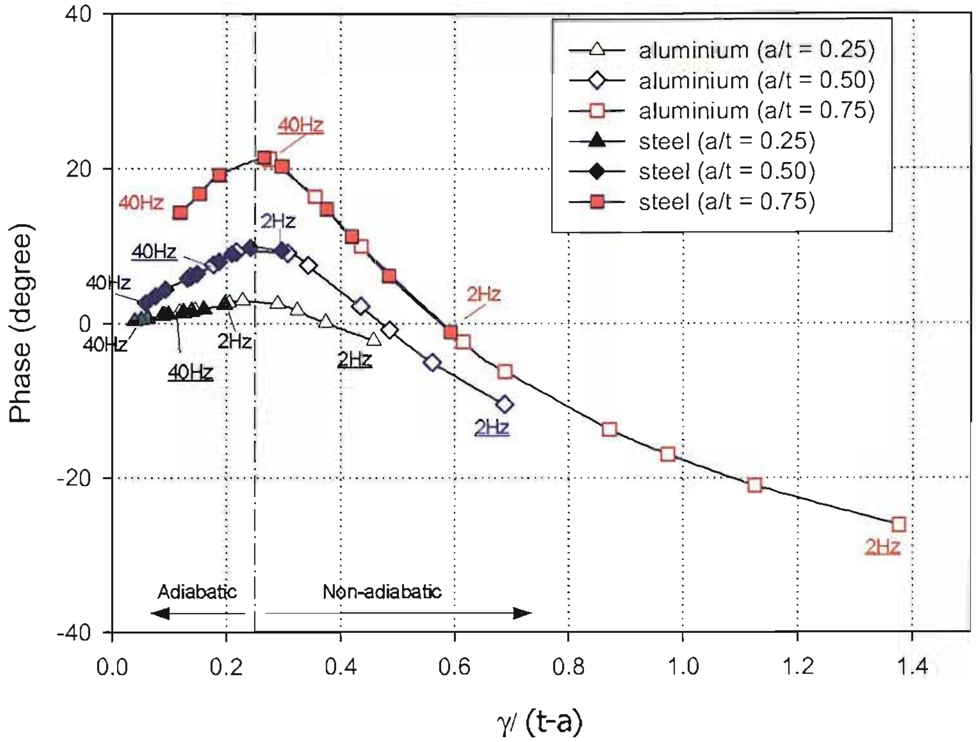

FIGURE 7.18: Phase response from FEA

To investigate if subtracting the two signal data sets will provide data related to the subsurface stress, the remaining R signal from subtracting the data at 40 Hz away from the data at 2 Hz is given in Figure 7.19. The remaining R signal from the aluminium specimen with a/t = 0.25, 0.50 and 0.75 is shown in Figure 7.19 (a), (b) and (c) respectively. Similarly, the remaining data from steel specimens with a/t = 0.25, 0.50 and 0.75 is shown in Figure 7.19 (d), (e) and (f) respectively. In all of the plots a peak in remaining R signal is evident at the notch, with the exception of the a/t = 0.75 aluminium data. To assess if this peak is related to the stress, results from the FEA static analysis at the subsurface are also show in the figure. For the aluminium a/t = 0.25 and a/t = 0.50 and the steel a/t = 0.75, a sharp increase in signal is evident at the notch of a similar nature to that given by the FEA. For these specimens it can be seen in Figure 7.17 and Figure 7.18 the 2 Hz reading is in the 'non-adiabatic' region, i.e. $\gamma/(t-a) > 2.5$ and the 40 Hz is in the 'adiabatic' region, i.e. $\gamma/(t-a) < 0.25$. For the steel where $a/t = 0.25$ the increase in the thermoelastic data is barely apparent; in Figure 7.17 and Figure 7.18 both the 2 Hz and 40 Hz reading are located in the $\gamma/(t-a) < 0.25$. When $a/t = 0.50$ in the steel specimen there is an increase in the signal at the notch but not as sharp as that seen in the FEA. In this case the 2 Hz reading is positioned very close to $\gamma/(t-a)$ = 0.25 indicating only a small contribution from the subsurface to the surface response. Finally for $a/t = 0.75$ in the aluminium specimen the thermoelastic response is negative compared to that given by FEA. In Figure 7.17 and Figure 7.18 the 2 Hz and the 40 Hz values are both in the region where $\gamma/(t-a) > 0.25$. Moreover, the 2 Hz condition is located further away from the turning point which indicates severe non-adiabatic condition. However, the flaw can still be observed. Interestingly, it can be seen that if the two points are located nicely each side of the turning point such as aluminium specimens of $a/t = 0.25$ and 0.50 and steel specimen of $a/t = 0.75$, the subtracted R-signal is very well represent the severity of the sub surface stress.

Although the thermoelastic data in Figure 7.19 is not calibrated, when interpreted in terms of the data given in Figure 7.17 and Figure 7.18 it clearly shows that there is potential to reveal the subsurface stress using the non-adiabatic response. The magnitude of the thermoelastic signal difference between a mainly adiabatic signal i.e. when $\gamma/(t-a) < 0.25$ and a mainly non-adiabatic signal $\gamma/(t-a) > 0.25$ could be used as a measure of the damage severity.

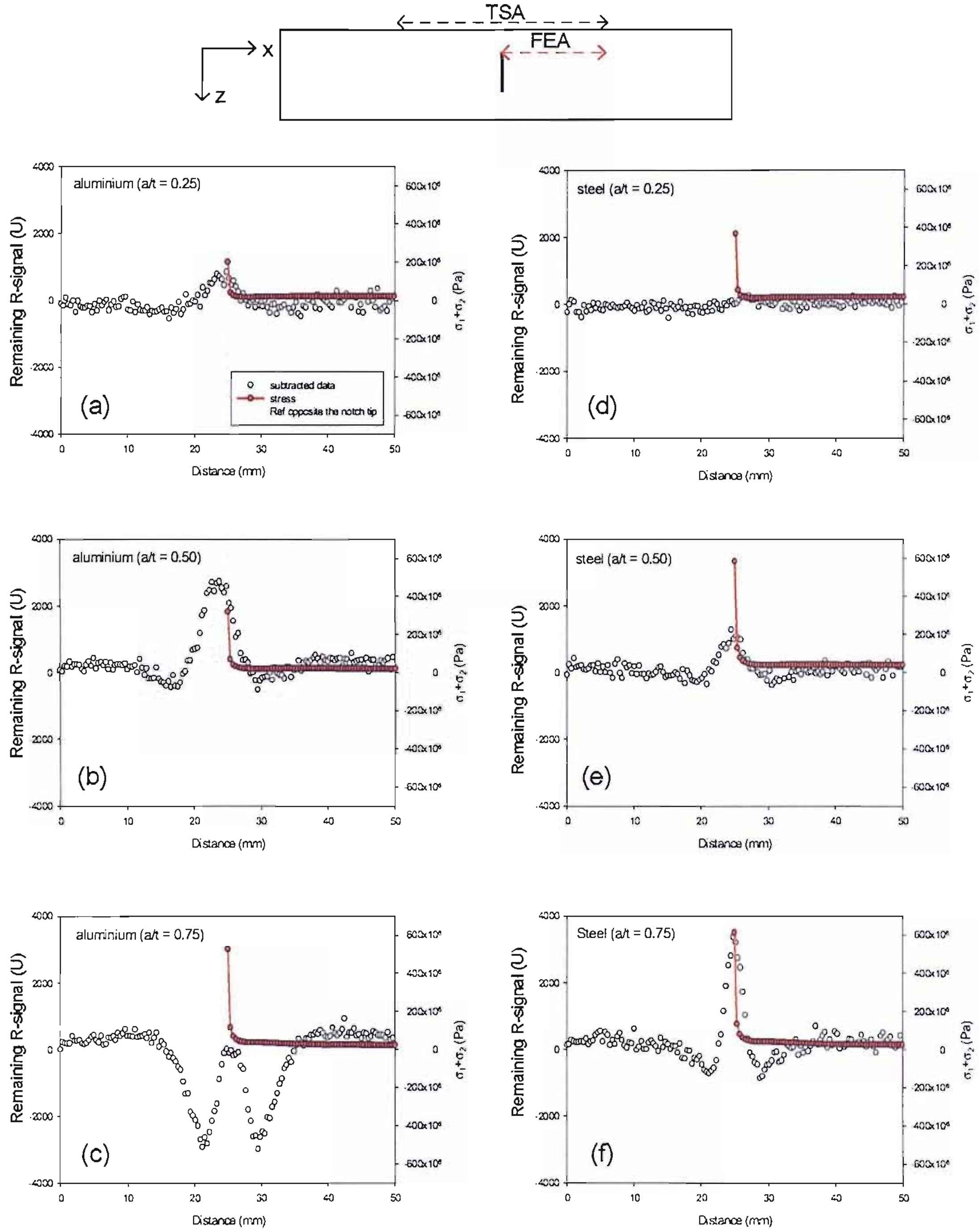

FIGURE 7.19: Sub-surface heat contribution on aluminium and steel specimens

7.5 Conclusions

The work in this chapter has demonstrated that materials with low thermal conductivities such as PMMA do not exhibit a non-adiabatic responses even at very low frequencies, hence the approach described for damage severity evaluation can only be applied to materials with high thermal conduction.

Experiments have shown that there is no direct relationship between the phase change in the thermoelastic data, notch depth and loading frequency. An FE model has been produced that simulates the thermoelastic response over a larger range of frequencies other than those available from experiments. This has been validated against experimental data and shown to be in very close agreement. The FE model has been used as a basis for identifying the contribution that is made to the surface signal from the sub-surface of material. A new parameter ($\gamma/(t-a)$) has been developed and it is shown that when this is plotted against phase change can indicate the level of contribution to the response from the sub-surface. $\gamma/(t-a) = 0.25$ was shown as the turning point in the curves and subtraction of one data set from $\gamma/(t-a) = 0.25$ can provide data that is related to the sub-surface stress and hence provide a measure of damage severity.

The material is shown to have an important effect on the interpretation of the data. Hence, the next step in the work will examine only one material type. The damage examined in this chapter concentrates on idealised damage. Therefore the next chapter of the thesis will examine more realistic damage.

Chapter 8

Detection and evaluation of damage in flat plates

8.1 Introduction

It has been shown in the previous chapter that the proposition of using TSA to detect and evaluate sub-surface damage is viable. Before moving on to the problem of internal sub-surface flaws on a curved shell structure of a pipe section, the next logical step is to test the approach on a more realistic shaped defect in the form of a sub-surface flaw in a flat plate. This is to investigate behaviour of the thermoelastic response of such damage on a simple plate structure and to confirm the applicability of the approach on a realistic sub-surface flaw. Therefore, in this chapter, a study of the non-adiabatic behaviour of a sub-surface flaw in the form of a semi-circular slot of a similar form to those described in Chapter 4 is carried out.

In Chapter 7 it was shown that the material thermal conductivity played an important role. To study the thermoelastic response from a wider range of damage severities, the work in Chapter 7 indicated a material of relatively high conductivity is preferable. This is because the higher the conductivity of the material, the smaller the level of damage that can be detected. Therefore, an aluminium alloy was chosen to be the test specimen material. In this chapter, six damage severities of a/t = 0.15, 0.20, 0.40, 0.60, 0.80 and 0.85 (see Chapter 4) were investigated. As in Chapter 4 and 7, TSA was used to observe the thermoelastic response from the undamaged surface of the specimen at various loading frequencies. The thermoelastic response was also investigated using the numerical simulation technique developed in Chapter 6.

8.2 Experimental work

8.2.1 Test specimen

An aluminium flat plate of 10 mm thickness, 340 mm width and 450 mm length was fabricated. Surface flaws were introduced in the plate by the EDM technique. The semi-circular slots of width 0.175 mm were machined using a electrode of radius 15 mm. Locations of each slot and its dimensions are shown in Figure 8.1. A dimensionless parameter of damage severity is defined in the same way as in the preliminary study in Chapter 4, i.e. a/t is referred to as the ratio of the slot depth to the plate thickness.

8.2.2 Experimental arrangement

The specimen was coated with a thin layer of matt black paint to improve and standardise the surface emissivity. The specimen was then mounted into the servo hydraulic test machine. As the specimen was the same width as the specimens used in Chapter 4 it was mounted in an identical manner as described in Section 4.2.2. A loading of 15 ± 14 kN, equivalent to $\Delta\sigma = 8.23$ MPa was applied for all frequencies: 2, 5, 10, 20 and 30 Hz. The loading frequency of 30 Hz is the maximum frequency that the testing machine can achieve for this test. The DeltaTherm (DT1400) detector was positioned at a distance so that all damage locations could be observed in one reading. This results in an image resolution of approximately 0.83 mm per pixel. The detector operated at a sampling rate of 142 frames per second. The electronic shutter was adjusted at 35% to provide a good signal to noise ratio for the test. Based on these settings, an average thermoelastic signal of 1260 U was obtained at a uniform stress region on the specimen. The average signals (S_{ave}), standard deviation (SD) and coefficient of variation from each test reading at a uniform stress away from the damage are given in Table 8.1.

TABLE 8.1: Thermoelastic signals at a uniform stress region

Test No.	Freq. (Hz)	Signal, S_{ave} (U)	SD	Coef of variation
1	2	1273	123	9%
2	5	1247	124	10%
3	10	1187	124	10%
4	20	1347	119	8%
5	30	1233	140	11%

8.2.3 Results

An example thermoelastic response in terms of R-image and phase image from the experiment at 5 Hz is shown in Figure 8.2. A set of R-images and phase images around the damage regions at these loading frequencies are given in Figure 8.3 and Figure 8.4

respectively. By inspecting only the R-image, the smallest level of damage that can be observed is $a/t = 0.40$. On the other hand, in the phase image, the damage of $a/t = 0.20$ can be also detected at 5 Hz and 10 Hz. A general characteristic of the phase profile around the damage is that the change of phase become more localised when the loading frequency increases, once again indicating that the phase response can be used to locate the damage.

For $a/t = 0.20$ and 0.40, the phase change at the damage approaches zero at a loading

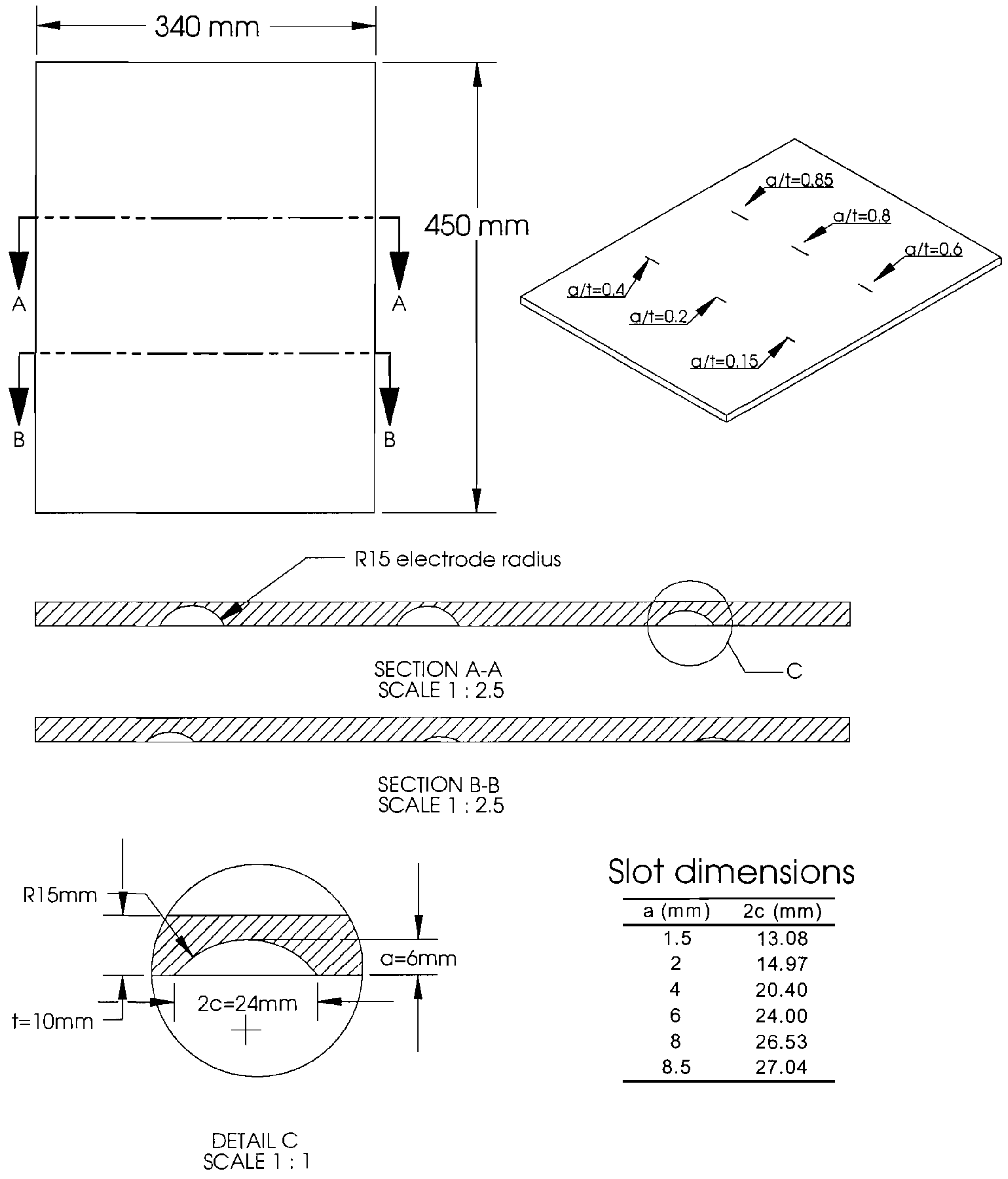

Slot dimensions

a (mm)	2c (mm)
1.5	13.08
2	14.97
4	20.40
6	24.00
8	26.53
8.5	27.04

FIGURE 8.1: Technical drawing of the specimen. The enlarged detailed C shows a cross-sectional view of the damage at $a/t = 0.60$

frequency of 10 Hz, which indicates that the condition at the damage zone is becoming more adiabatic. To visualise the phase behaviour at the damage site, the phase signal at the middle of the notch location (see Figure 4.3 position 5) was plotted in Figure 8.5. The phase data of the damage $a/t = 0.15$ is not included in the plot because it can not be identified by TSA. For the damage of $a/t = 0.60$, 0.80 and 0.85 there is no sign of adiabatic behaviour at the notch tip within the range of 2-30 Hz. To further examine the thermoelastic response from the damage numerical simulation is necessary because of the limitation of the testing machine.

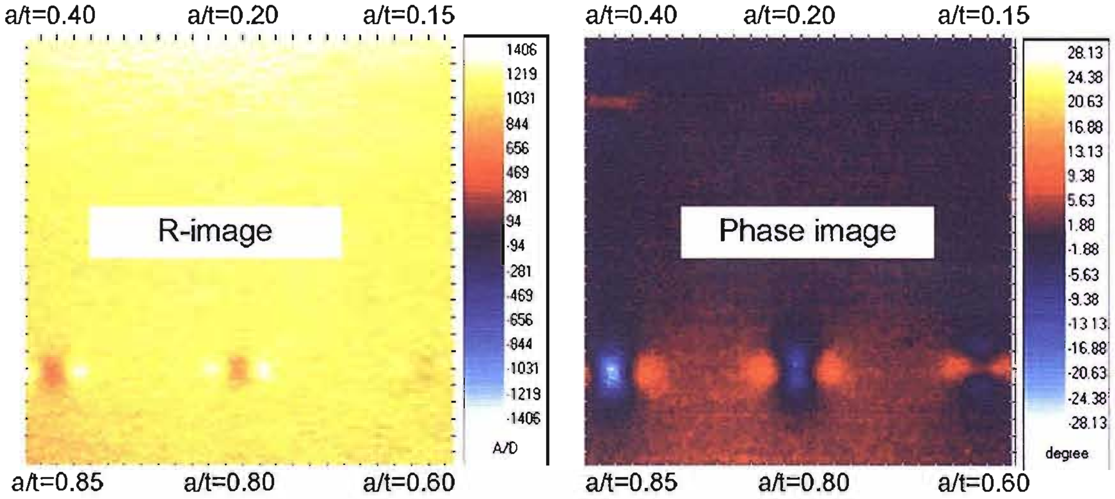

FIGURE 8.2: Example R-image and phase image from TSA

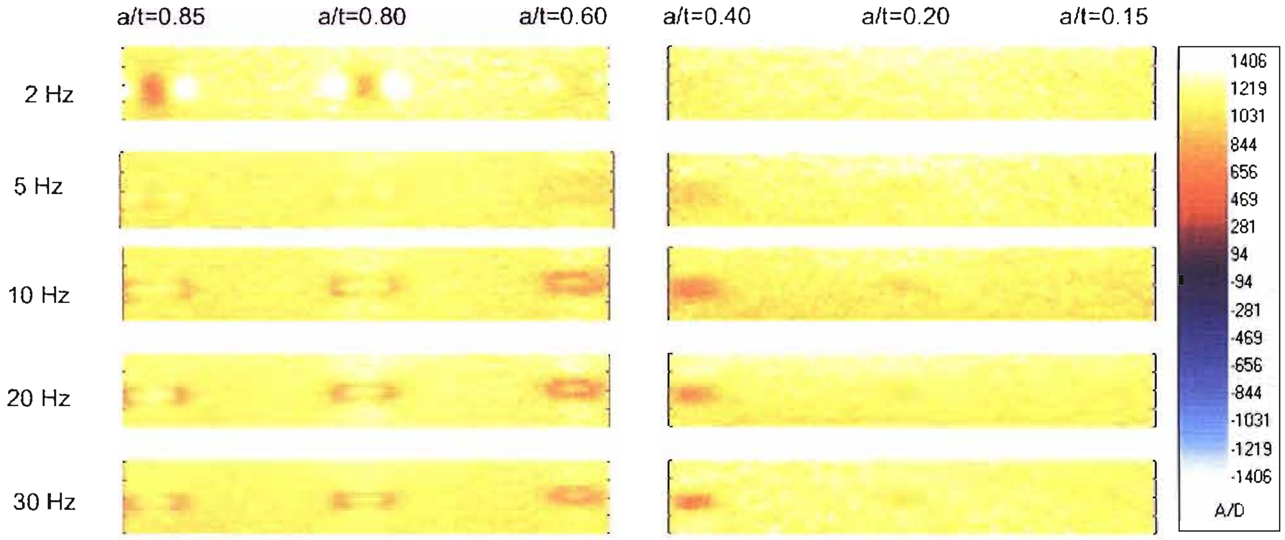

FIGURE 8.3: R-signal results

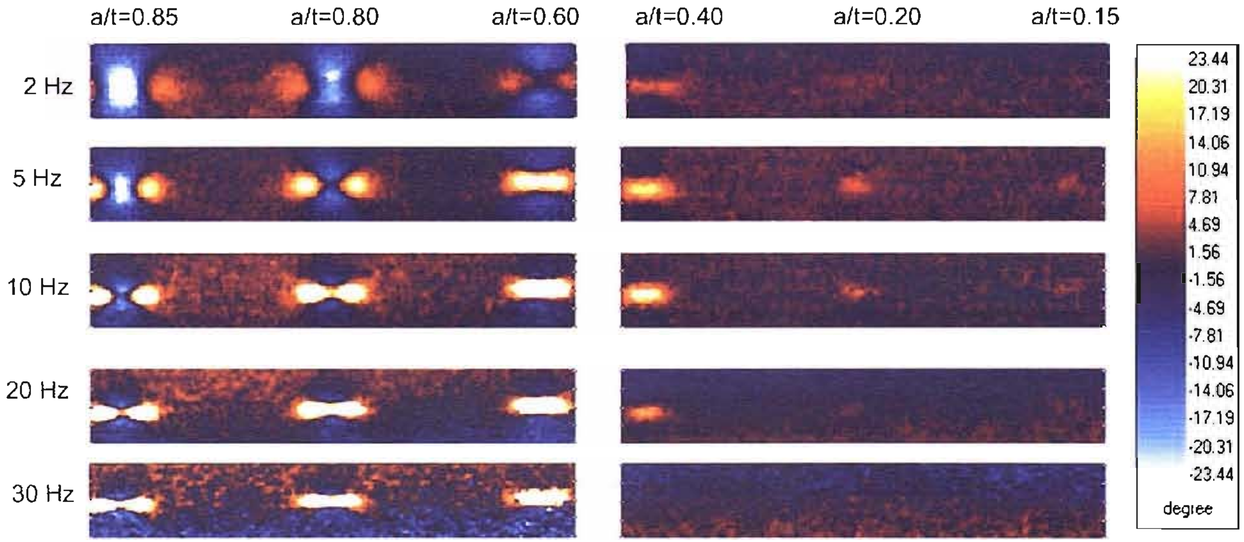

FIGURE 8.4: Phase readings

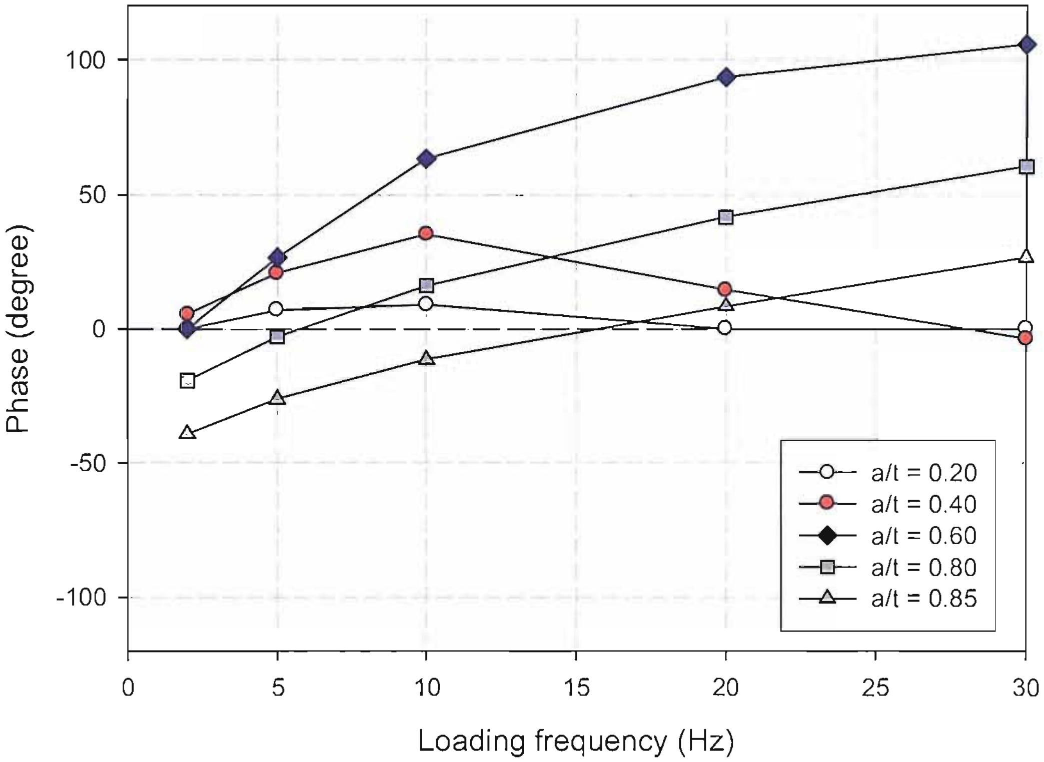

FIGURE 8.5: Phase signal at the back surface opposite to the notch tip

8.3 Numerical and experimental investigation of subsurface damage in a flat plate

8.3.1 3-D modelling of damage in a plate structure and FE simulation

Modelling a crack like flaw in three dimensions is much more demanding than in two dimensions. In a 3-D model, the mesh transition at the region of expected large stress gradient, i.e. around the notch, must be controlled effectively in three dimensions in order to avoid an irregular element shape (i.e. taper, skew, large aspect ratio or warping element) which is a fundamental source of error. Some modeller software packages specially designed for FE simulation in fracture mechanics can be used to mesh a crack model automatically, as well as provide automatic refinement process at the region with various cracks geometries. Examples of FEA crack software are Zencracks[1] and Structural Reliability Technology (SRT) FEA-crack [2]. However, the main purpose of these software packages is to mesh the crack front with a special element type to obtain a good SIFs approximation at the singular point and they are not suitable to simulate thermoelastic effect at a notch.

The approach used here is to build a solid model from scratch and mesh the model manually. A damaged section of the specimen is defined as shown in Figure 8.6. It is assumed that the the damaged section is subjected to the same stress distribution experienced at the remote region away from the damage zone. A solid model was then constructed as a quarter of the damaged section containing the flaw as shown in Figure 8.7. The meshed model was constructed ensuring that the resulting stress distribution in the notch region was smooth and continuous across the element. The meshing process was carried out by trial and error of changing element size as well as moving the nodes, particularly in the notch region until there was no excessive element distortion in the model. As a result, meshing the damage in order to obtain a high quality mesh is a time consuming task.

The steps to simulate the thermoelastic effect are the same as described in the Chapter 6 except 3-D elements were used. A 3-D structural solid element (SOLID45) was used for the model in the structural analysis and a 3-D thermal solid element (SOLID70) was used for thermal harmonic analysis. The applied load on the model is equivalent to the cyclic tensile load on the specimen of 15 ± 14 kN or $\Delta\sigma = 8.2$ MPa. Material properties of the specimen used in the simulation are given in Table 8.2.

Due to the fact that meshing process was carried out manually, the higher a/t ratio, the too many elements are required to maintain a good quality mesh. As a results, a model of the damage larger than of $a/t = 0.60$ for this damage dimensions has not

---

[1] http://www.zentech.co.uk/zencrack.htm

[2] http://www.srt-boulder.com/software.htm

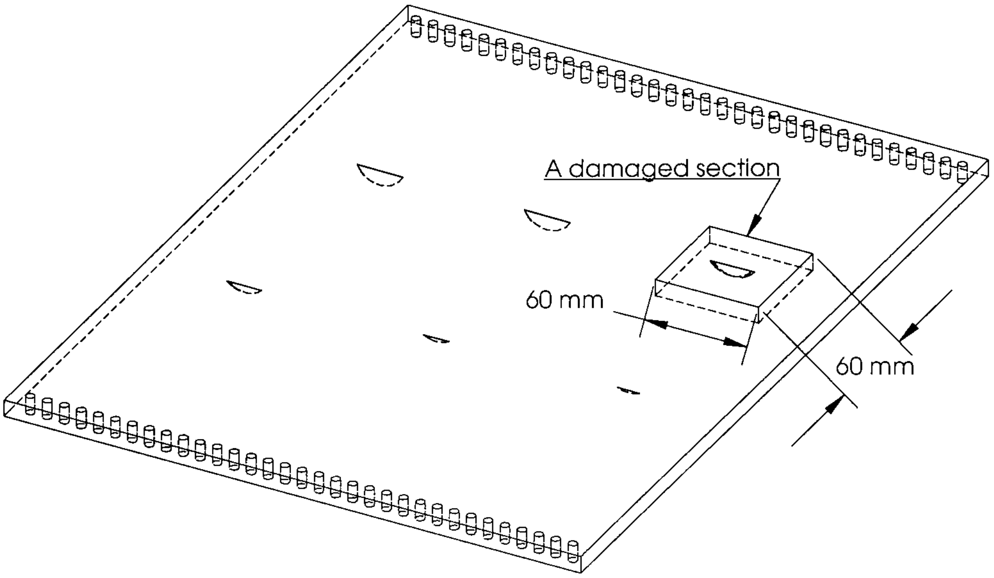

FIGURE 8.6: A defined damaged section in the specimen for FE idealisation

been meshed successfully. Therefore, only two FE models were created, i.e. the model with $a/t = 0.40$ and $a/t = 0.60$. The former is selected in order to examine if the FE model can be used to predict the non-adiabatic behaviour of this type of damage. The later is chosen to perform further analysis of non-adiabatic behaviour at higher loading frequencies, that can not be done experimentally.

TABLE 8.2: Material properties of aluminium alloy using in the FE simulation

Material Properties of aluminium	Value	Unit
Young's modulus, E	70	GPa
Poisson's ratio, ν	0.33	-
Specific heat at constant pressure, c_p	896	J / kg K
Thermal conductivity, k	180	W / m K
Density, ρ	2700	kg/ m^3
Coefficient of linear thermal expansion, α	24E-6	1/K
Reference temperature, T_0	293	K

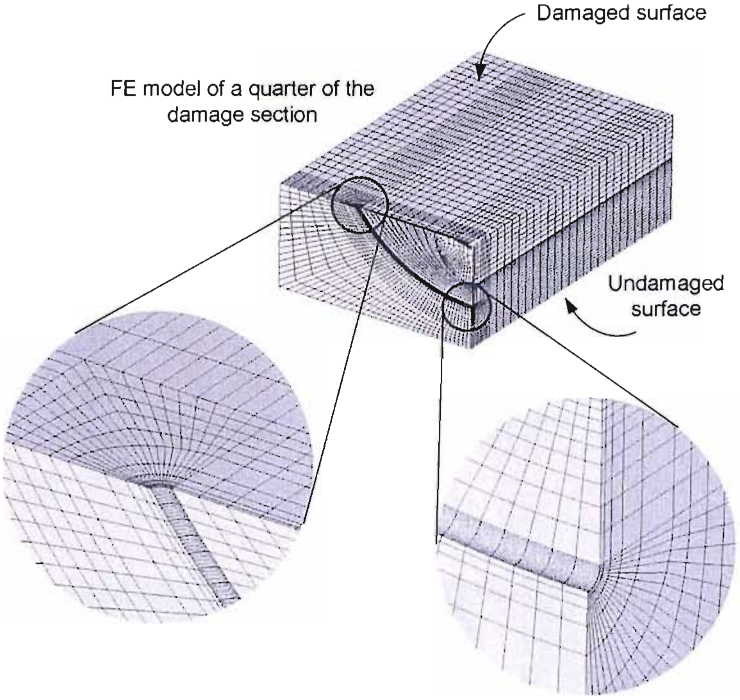

Figure 8.7: FE model of a quarter of the damaged section defined in Figure 8.6

8.3.2 Results and damage analysis

Figure 8.8 shows contour plots of the sum of the principal stress plotted from both calibrated TSA data and 3-D FEA results (static analysis). The boxes indicated in the TSA data correspond to the damaged-section dimensions defined in Figure 8.6. To compare the results between two approaches, the thermoelastic data obtained from the line profiles indicated in the figure are plotted together with the data obtained from the FE model at the equivalent location in terms of stress factor and phase data and given in Figure 8.9 and Figure 8.10 for a/t = 0.40 and a/t = 0.60 respectively. From both figures, it can be seen that the simulation results agree well with the experimental results.

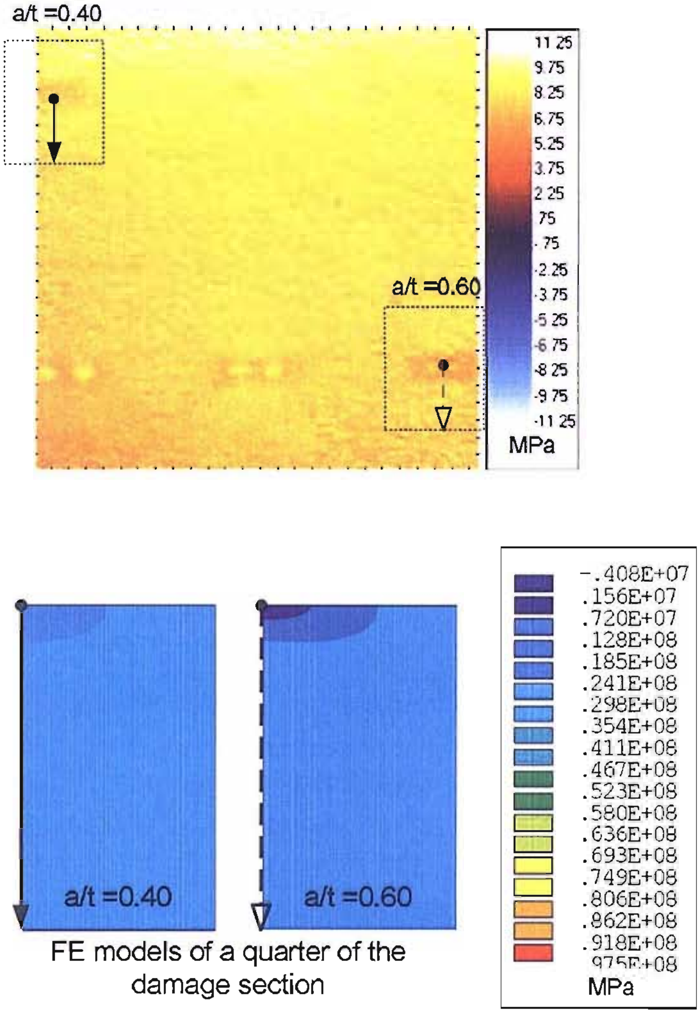

FIGURE 8.8: Locations of the profiles where the data is interrogated

To analyse the sub-surface stress from the sub-surface flaw, phase data is plotted against the proposed characteristic length ($\gamma/(t-a)$). TSA data from Figure 8.5 and FE results are plotted in Figure 8.11 and Figure 8.12 respectively. In Figure 8.11, the curves representing the damage of a/t = 0.20 and 0.40 reach a turning point at $\gamma/(t-a) \approx 0.2$

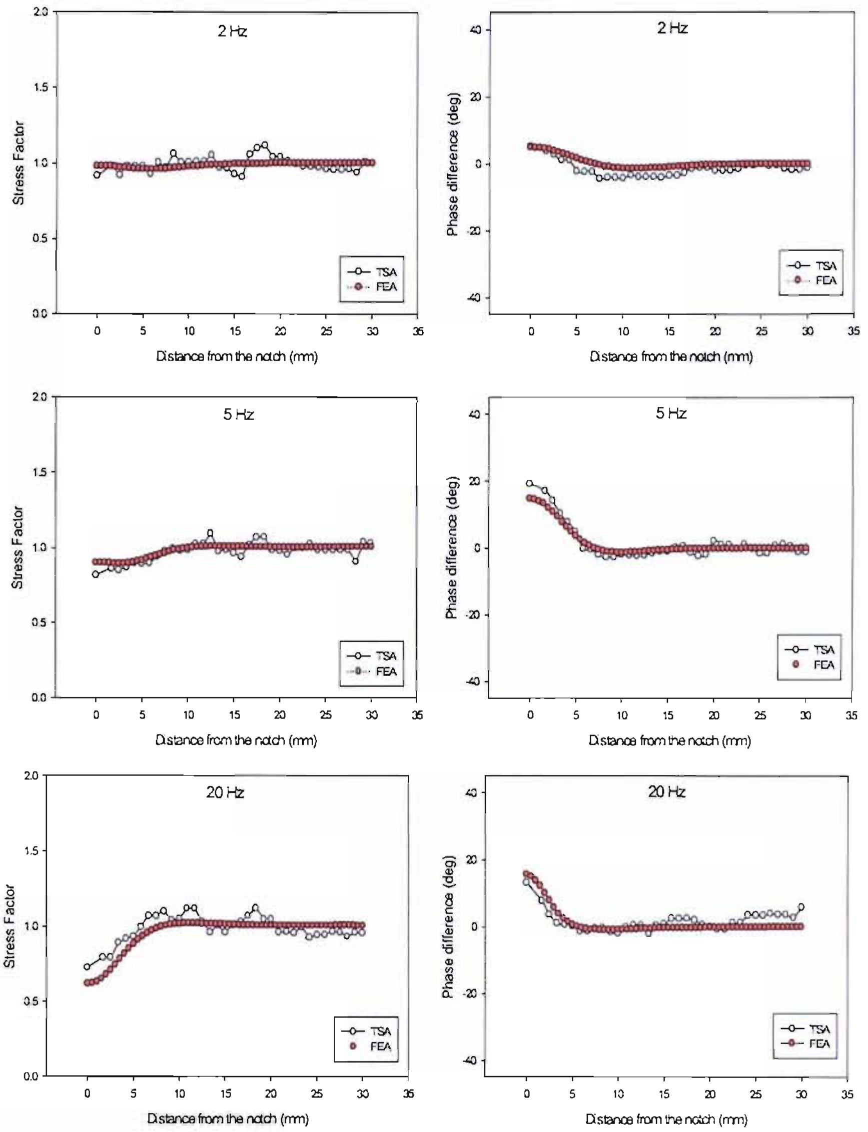

FIGURE 8.9: FE results compared with TSA (a/t = 0.40)

and 0.26 respectively. The curve of the damage with $a/t = 0.60$ appears to reach the maximum phase change at a frequency of 30 Hz, but this cannot be confirmed experimentally. This requires FE simulation. Therefore additional FE simulation was carried out to simulate the thermoelastic response of $a/t = 0.60$ at the following loading frequencies: 50, 100, 200, 500 and 1000 Hz. This additional simulation results are also included in Figure 8.12. It can be seen that for the damage extent of $a/t = 0.60$, the loading frequency required to diminish the contribution of non-adiabatic behaviour is higher than 40 Hz. To show the agreement between the TSA data and the FE prediction, the data for the damage of $a/t = 0.40$ and 0.60 are plotted in Figure 8.13.

To show the contribution of the sub-surface stress, the approach for damage analysis introduced in Section 7.4 is applied. For the damage with $a/t = 0.40$, $\gamma/(t-a) \approx 0.26$) is

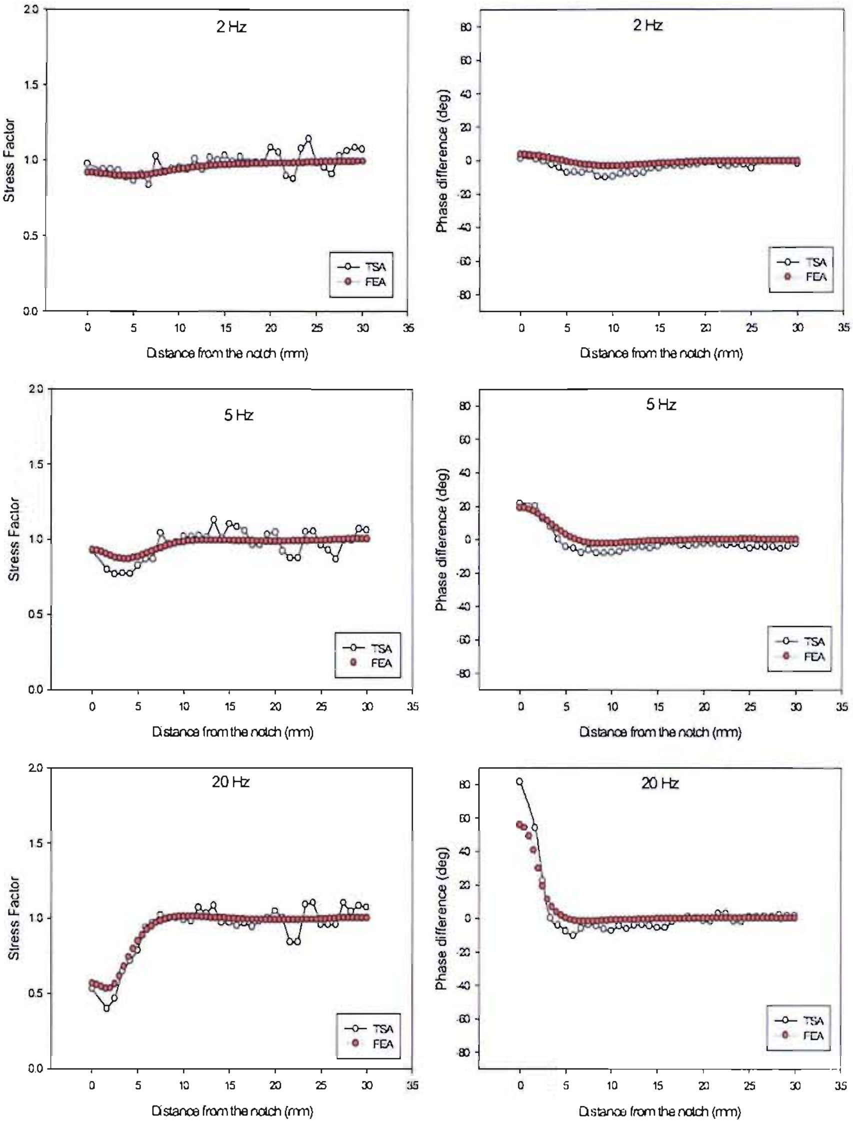

FIGURE 8.10: FEA results compared with TSA (a/t = 0.60)

obtained from both FEA and TSA as a turning point of phase response for this damage. The R-signal at 2 Hz ($\gamma/(t-a) > 0.26$) was subtracted from the R-signal at 30 Hz ($\gamma/(t-a) < 0.26$). The remaining R-signal is plotted in Figure 8.14 (top) along with the internal stress obtained from FEA at the tip of the slot. It can be seen that the remaining R-signal clearly shows a contribution of subsurface stress. A similar procedure was applied for the R-signal from $a/t = 0.60$, i.e. the R-signal from 2 Hz was subtracted from that of 30 Hz and the remaining R-signal is plotted in Figure 8.14 (bottom). Here, the remaining R-signal curve does not show a similar trend as obtained in the previous curve ($a/t = 0.40$). This is because the R-signal used for the subtraction was positioned in the 'more non-adiabatic' zone.

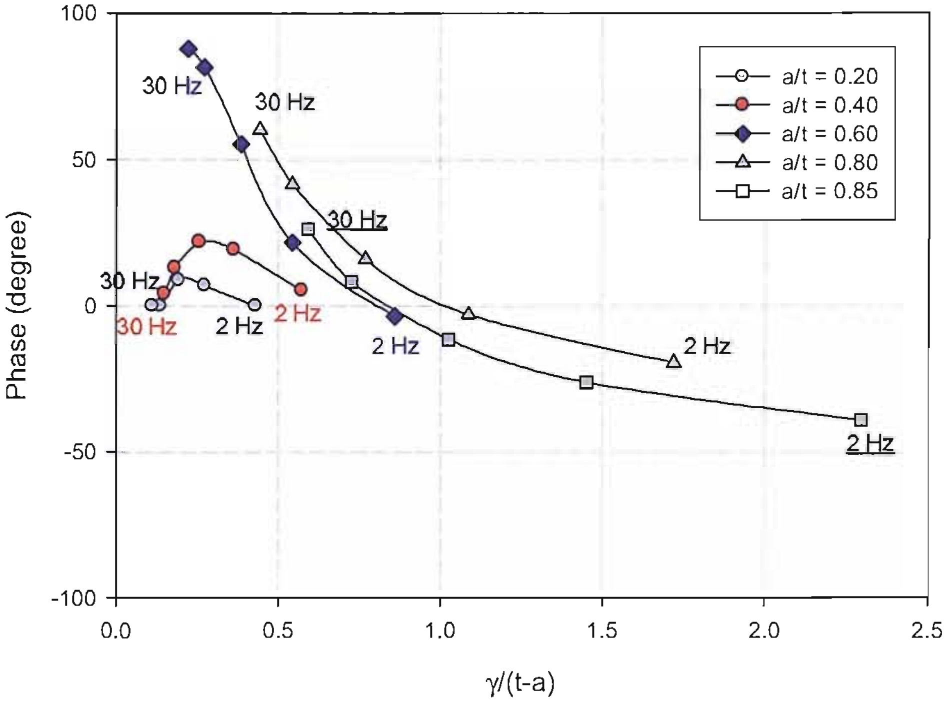

FIGURE 8.11: TSA results

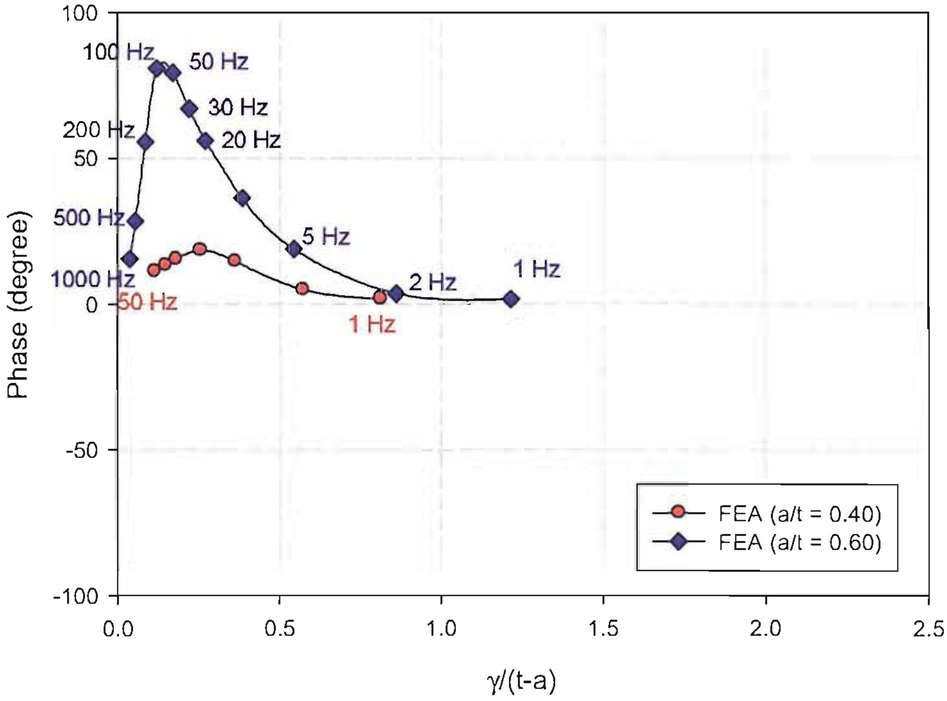

FIGURE 8.12: FEA results

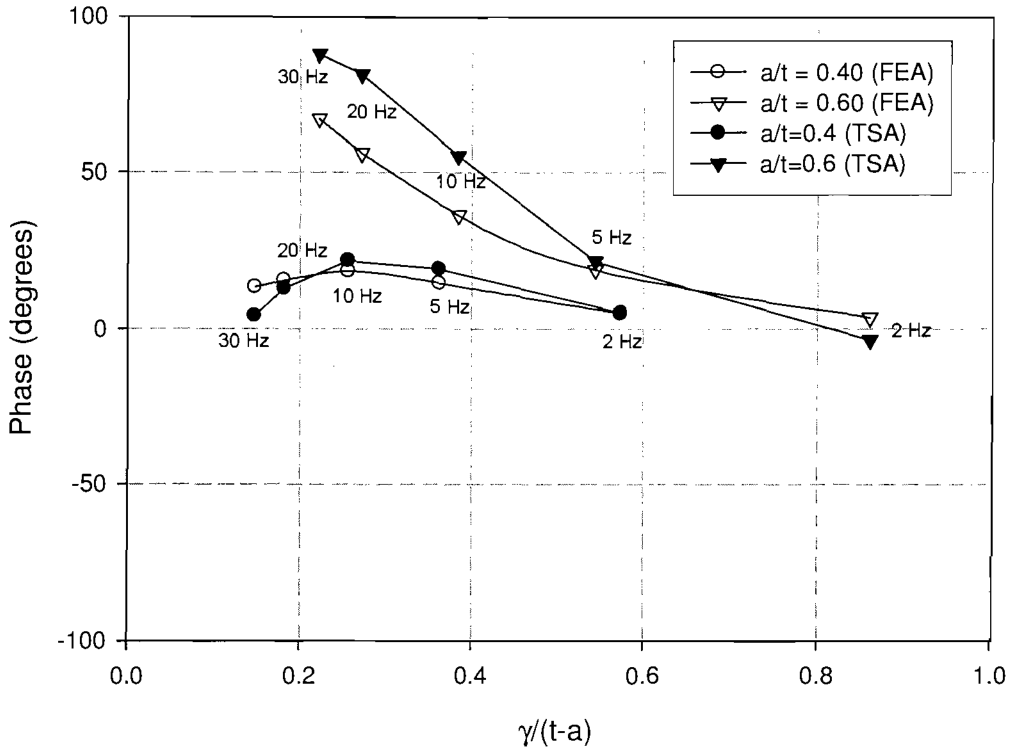

Figure 8.13: TSA and FEA results at the same loading frequency range

8.4 Conclusions

It has been shown that non-adiabatic behaviour from defect with more realistic geometries can be predicted successfully using 3-D FE simulation. However, the use of an FE approach for this complex geometry is time consuming, due to the complex meshing required, especially for the cracks or very sharp slots in a large structure. Therefore, a more efficient technique for modelling and meshing a damaged geometry needs to be developed.

From the thermoelastic work carried out in this chapter, it can be seen that the non-adiabatic thermoelastic response for realistic defects is much more complicated than that of idealised damage as described in Chapter 7. However, the validity of the proposed approach has been demonstrated and it can be seen that the subsurface stresses at the damage site can be predicted by subtracting the adiabatic response from the non-adiabatic response and hence a damage severity factor can be determined. In the next chapter, this approach of using non-adiabatic behaviour to assess the damage will be applied to a pipe structure.

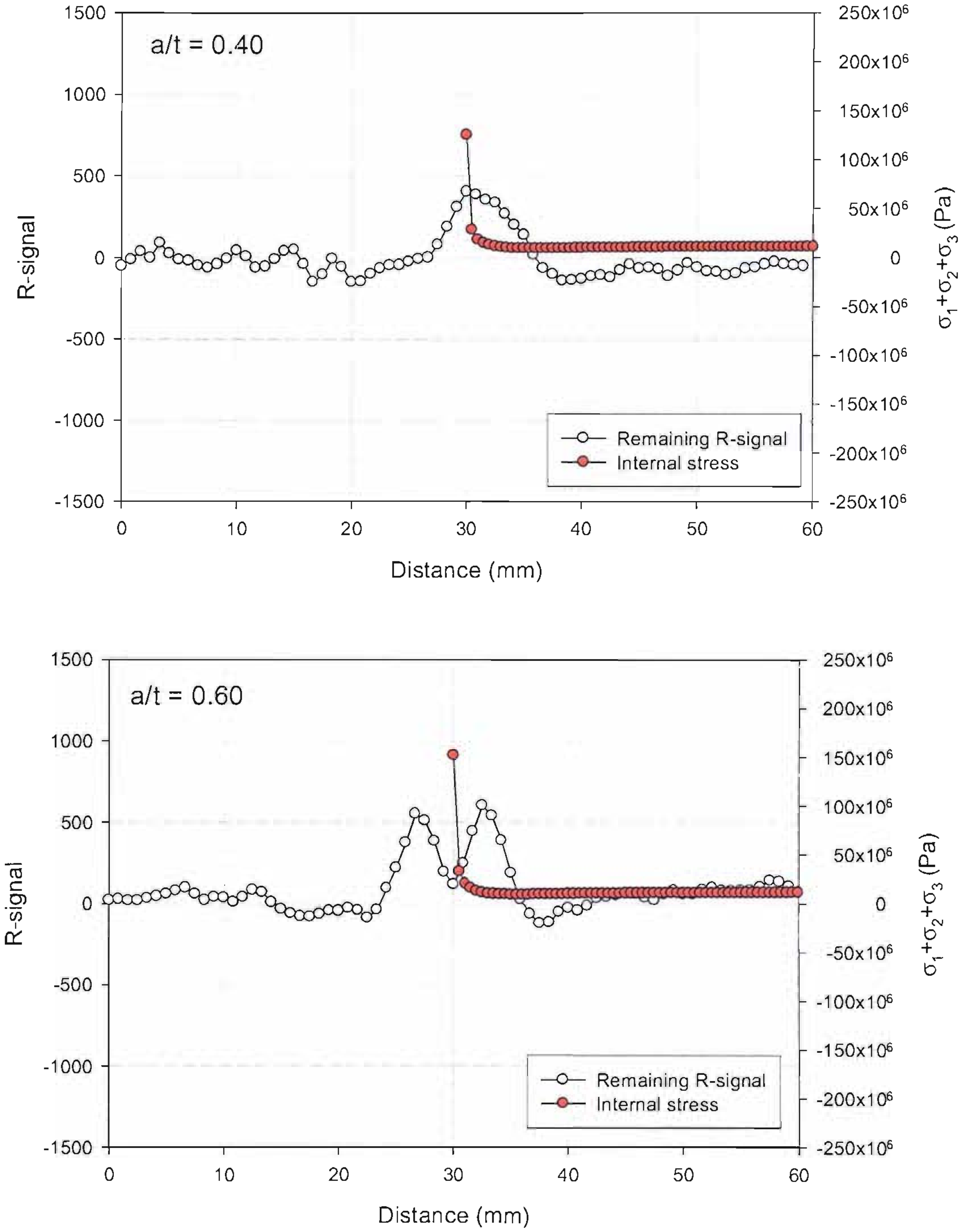

FIGURE 8.14: Remaining R-signal(from TSA) and internal stress (FEA)

Chapter 9

Detection and evaluation of damage in a pressurised cylindrical component

9.1 Introduction

Following on from the work on the flat plates described in the previous chapter, the next logical step is to apply the approach of using TSA to detect and evaluate damage to a cylindrical component, i.e. a pipe section with internal-surface flaws. To perform an experiment on such a component, two difficulties have to be overcome: first, a cyclic pressure must be applied to the specimen and secondly, surface flaws must be created on the inner surface of the pipe component. The first difficulty has been addressed in previous work by the author described in Ref [70] by the design and fabrication of a pressure rig which can be used with an existing servo-hydraulic testing machine. However, some modifications have been made in the course of current work to improve the functionality and performance of the system. The second problem was solved by cutting a pipe specimen in half and machining an EDM slot on the internal surface and then welding the pipe back together. Details of the manufacturing of the specimen are discussed in this chapter. The TSA experiment was then carried out on the 'damaged' pressurised pipe specimen and the non-adiabatic thermoelastic response used to identify the damage.

The objectives of this chapter are: firstly, to describe the work on upgrading of the pressure transmission rig and provide a full validation (described in Section 9.2 9.3) and secondly, to demonstrate the applicability of the devised approach damage characterisation on pressurised components. The design of a specimen with internal flaws is described in Section 9.4. The detail of the experimental procedure, results and discussion are provided in Section 9.5 and 9.6 respectively.

9.2 Pressure device modification

The rig was designed and built for the purpose of using TSA to investigate the stress distribution on an enclosed pressurised structure under dynamic loading. The function of the rig is to transform the force applied by a servo-hydraulic testing machine actuator into fluid pressure. This is achieved by utilising a heavy duty hydraulic ram. A photograph of the rig assemblies and hydraulic circuit diagram is provided in Figure 9.1.

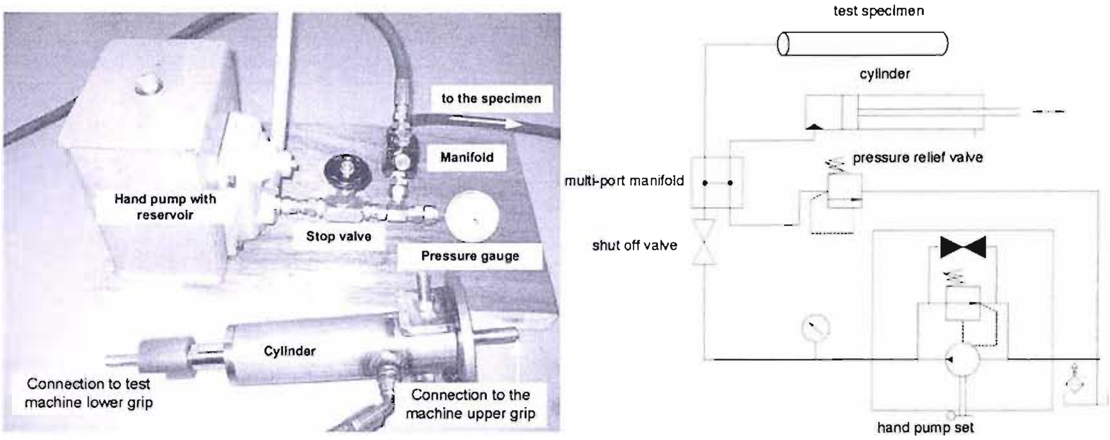

FIGURE 9.1: Pressure rig assemblies and circuit diagram

Essentially, the rig is composed of three components: pressure ram, hand pump and test specimen arrangement. The pressure ram is used to apply cyclic pressure load to the specimen. Both sides of the ram are fixed with the grippers into an Instron 8800 servo-hydraulic test machine. The hand pump is included in the design to allow the operator to control the mean operating pressure in the system manually. Moreover, it is used to flush and circulate hydraulic oil in order to remove any entrapped air bubbles from the system. The last component is the test specimen assembly which consists of the support fixture and the specimen. This is explained in detail in Section 9.3.1. The pressure rig described above needed to be modified to improve its performance so that a larger cyclic stress could be applied. The objective of the modification was to increase the so called *bulk modulus* of the hydraulic system. A shortcoming of the previous design was the deformation of the type SAE 100R2 hydraulic hoses shown in Figure 9.2. When these were subjected to internal pressure of near to 10 bar, the radial deformation of the hoses was approximately 1 mm,which was too large for the intended purpose. Also, there was a small leak at the pressure relief valves (see Figure 9.1 (circuit diagram)) at high pressure caused by the low quality of the valve seat.

Both deficiencies caused a displacement of the test machine hydraulic actuator of up to 10 mm,which was too large as this restricted the tests to low loading frequencies of up to a maximum of 3 Hz only. The reason for the restriction was that the piston displacement

FIGURE 9.2: Fluid power hose used in the rig: SAE 100R2 was used in the previous design and it was replaced by SAE 100R10 to prevent excessive hose expansion.

exceeded the operational envelope of the testing machine at higher loading frequencies (see Figure 9.3).

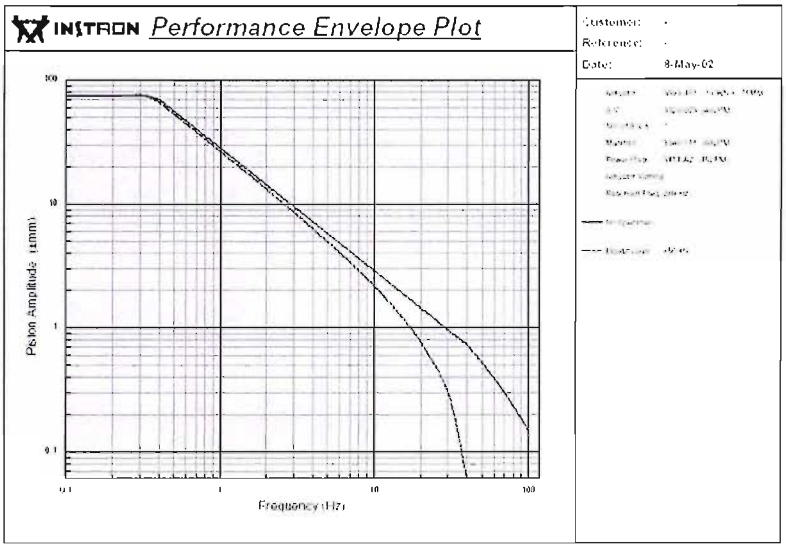

FIGURE 9.3: Envelope performance plot (Instron 8802)

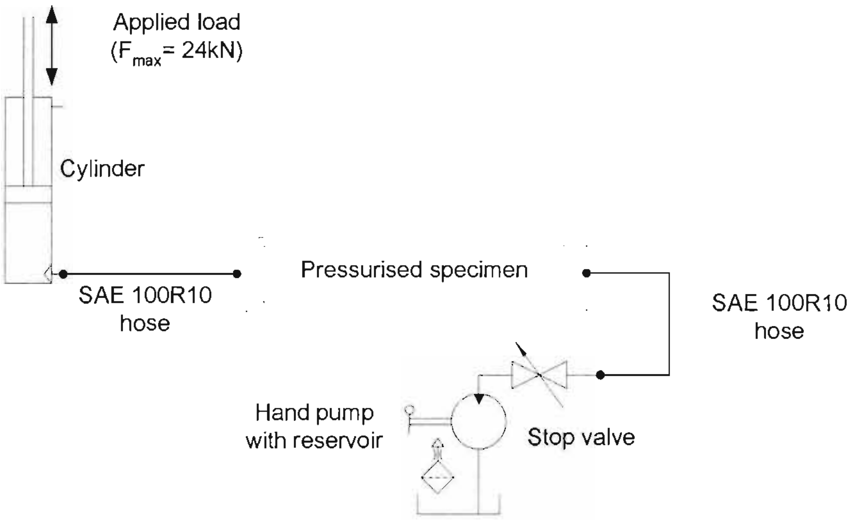

FIGURE 9.4: Simplified hydraulic circuit

To eliminate these deficiencies, the hydraulic circuit has been simplified by removing the safety valve and manifold (a diagram of the modified circuit is provided in Figure 9.4) and all hoses have been changed to a stronger type (SAE100R10). This type of hose consists of very high density wire reinforcement: 4-spiral plies of heavy wire wrapped in alternating directions as shown in Figure 9.2. The use of fixed copper tubes instead of hydraulic hoses is probably the best option to solve the problem, but this would have resulted in a less portable design. Therefore, this option was not pursued. Although the safety relieve valve has been removed from the system, safe operation is maintained provided that the test machine control system limiters are set to restrict the movement of the actuator within a safe operating range.

The rig was tested after the modification. The movement of the actuator was reduced to 2 mm when the maximum testing-load is applied. This is well within the range of operational envelope of the test machine and allows testing at higher loading frequencies of up to 10 Hz. One minor difficulty still exists in that it is impossible to remove all of air bubbles from the oil. However, with careful assembling this has been minimised and has a negligible effect on the results.

9.3 Test rig validation

9.3.1 Test specimen and fixtures

In order to validate the rig a simple test specimen was chosen. It is of a cylindrical form and is shown in Figure 9.5. The specimen was cut from a typical seamless low carbon steel pipe of 75 mm internal diameter and 5 mm thickness, a section of the specimen has been machined at both ends to remove the cutting edges and provide a smooth contact surface.

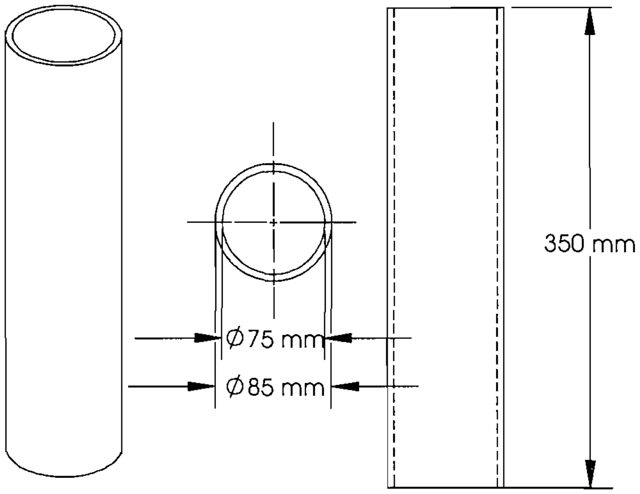

FIGURE 9.5: The steel pipe specimen for validation test

A set of support fixtures was designed so that when the specimen was subjected to an internal pressure, the longitudinal stress was minimized. This was achieved by an open-end configuration as shown in Figure 9.6. Two steel plates are used to prevent the aluminium plugs from slipping out when the pipe is subjected to internal pressure. This configuration allows free deformation in both radial and axial directions and as the specimen is not constrained axially the longitudinal stress is eliminated. O-rings were used to prevent leakage between the pipe-ends and the aluminium end-caps. A standard o-ring groove was machined in each aluminium end-cap,therefore the maximum load achievable is dictated by the o-ring performance. This means that the test can be performed for a static pressure of up to 80 bar. That is to say the maximum load that can be applied to the piston rod of the ram is limited to 24 kN.

To independently evaluate the stress in the specimen, a two-gauge orthogonal strain gauge rosette was bonded to the surface of the cylinder along the principal stress axes in order to record the hoop strain ($\epsilon_{\text{hoop}} = \frac{\sigma_{\text{hoop}}}{E}$) and the axial strain ($\epsilon_{\text{axial}} = -\nu\frac{\sigma_{\text{hoop}}}{E}$).

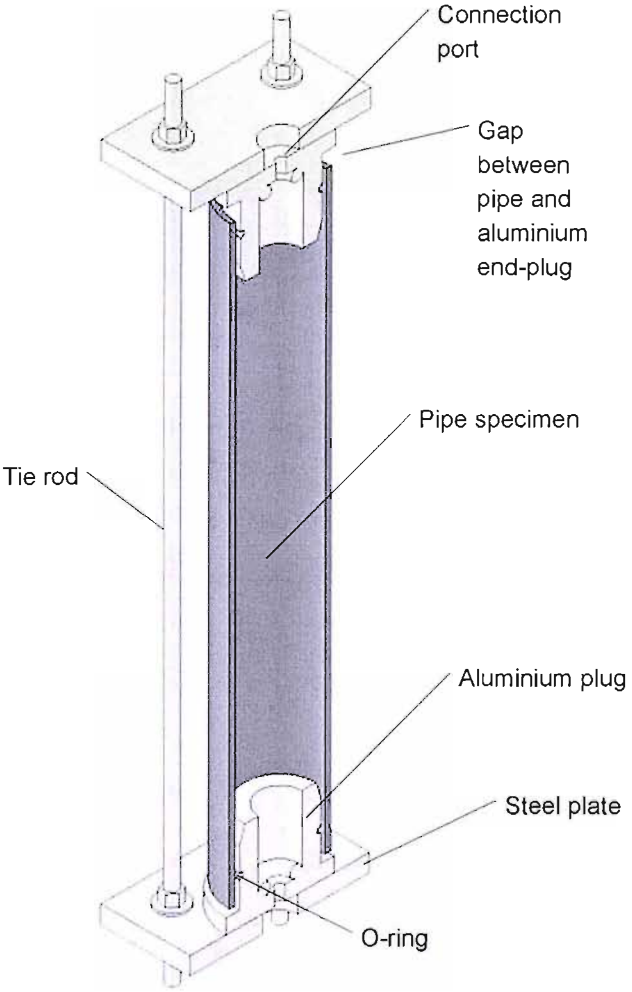

FIGURE 9.6: Cross-sectional view of the specimen assembly

9.3.2 Hydrostatic validation

The rig and test specimen were assembled and tested. Figure 9.7 shows the test setup. In the first place, the static load was increased gradually to ensure that the internal pressure and stresses developed in the specimen can be controlled effectively by the Instron test machine control panel. The surface strain from the strain gauges was monitored and recorded via a computer controlled data acquisition system.

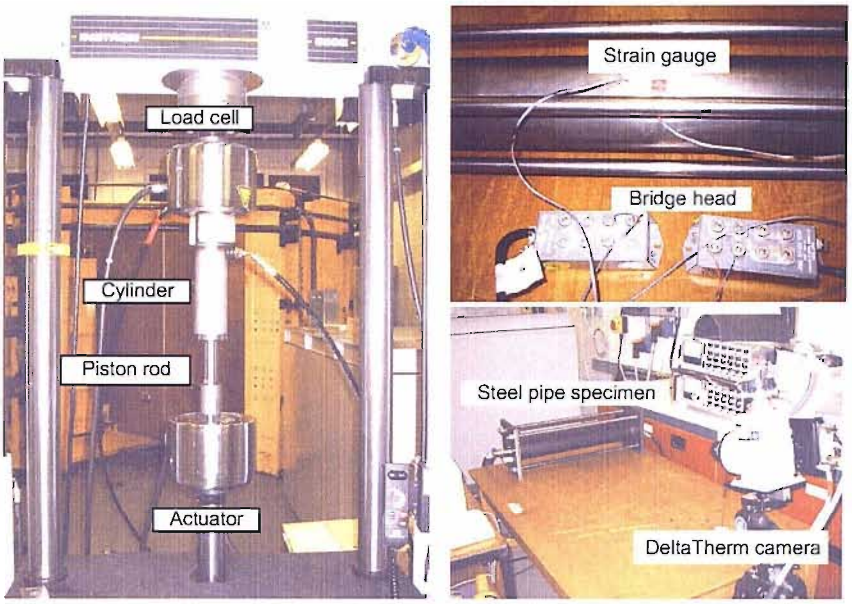

FIGURE 9.7: Pressure test set-up

The strain developed due to the hydrostatic internal pressure was recorded and is given in Appendix A.4 and plotted in Figure 9.8. Taking $\nu = 0.3$, it can be seen that ϵ_{axial} is approximately $-0.3\,(\epsilon_{\text{hoop}})$,as expected.

Stresses in both principal directions at each load step can be calculated from the measured strain. They were calculated using the classical stress strain relationship with the stress in the z direction is zero (normal to the specimen surface) and assuming E = 207 GPa and $\nu = 0.3$ [69]:

$$\sigma_{\text{hoop}} = \frac{E}{1-\nu^2}\left(\epsilon_x + \nu\epsilon_y\right) \tag{9.1}$$

$$\sigma_{\text{axial}} = \frac{E}{1-\nu^2}\left(\epsilon_y + \nu\epsilon_x\right) \tag{9.2}$$

The values obtained from the gauges were compared with theory, for a thick-walled cylinder the stresses are as follows [69]:

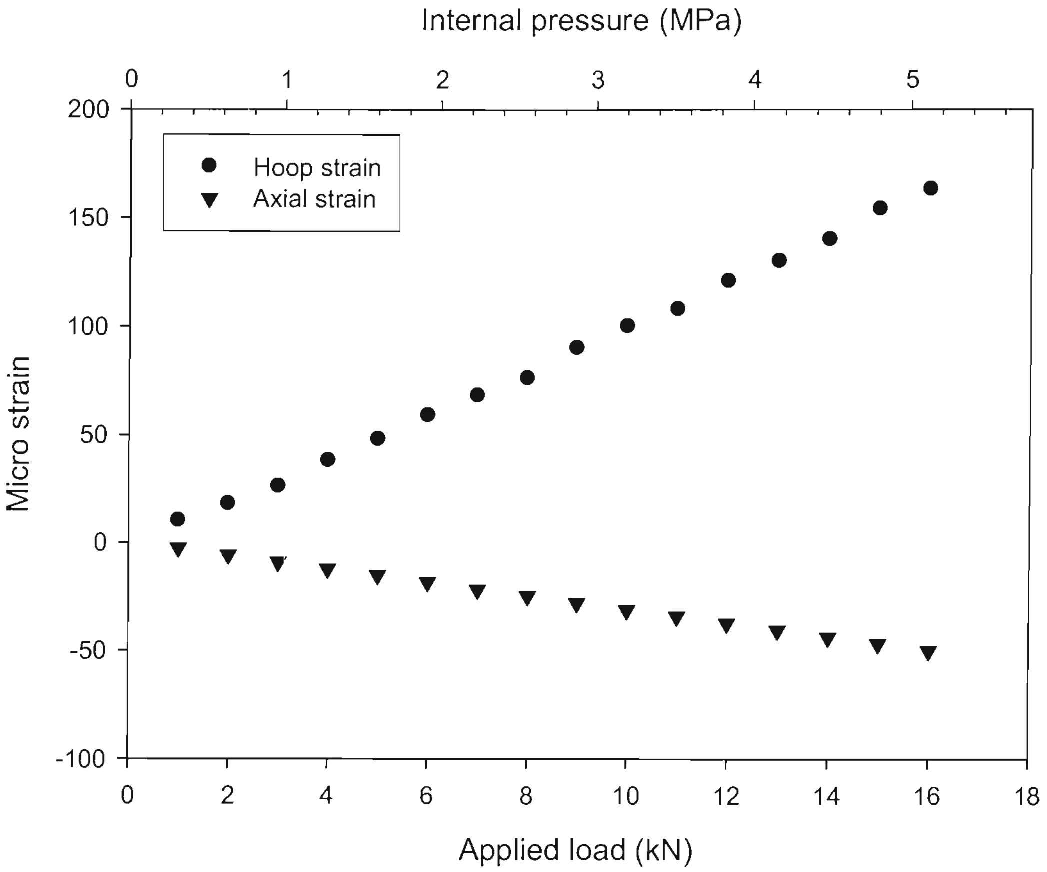

FIGURE 9.8: Strain data

$$\sigma_{\text{hoop}} = \frac{p_i}{(\frac{r_o}{r_i})^2 - 1}\left(1 + \frac{r_o^2}{r^2}\right) \tag{9.3}$$

$$\sigma_{\text{radial}} = p_i \, \frac{r_i^2 \, (r^2 + r_o^2)}{r^2 \, (r_o^2 - r_i^2)} \tag{9.4}$$

$$\sigma_{\text{axial (open end)}} = 0 \tag{9.5}$$

where σ_{hoop} is the hoop stress, σ_{radial} is the radial stress and σ_{axial} is the axial stress, p_i is internal pressure, r_i is the inner radius, r_o is the outer radius and r is the radial position where the stress are calculated.

The internal pressure was calculated simply by:

$$p_i = \frac{P}{A_{\text{ram}}} \tag{9.6}$$

where P is the applied load and $A_{\text{ram}}(= 3117\,\text{mm}^2)$ is the cross sectional area of the piston of the heavy duty hydraulic ram.

In theory, in this configuration, σ_{radial} at $r = r_o$ is zero as the cylinder is under internal pressure and σ_{axial} is zero as the cylinder is not constrained axially. The calculated and measured values at the surface of the cylinder are plotted in Figure 9.9 and show a good agreement. The small divergence from theory may be caused by the misalignment of the strain gauge to the principal directions. So it can be concluded that the rig is working properly and the stress developed in the specimen can be controlled directly from the test machine control panel.

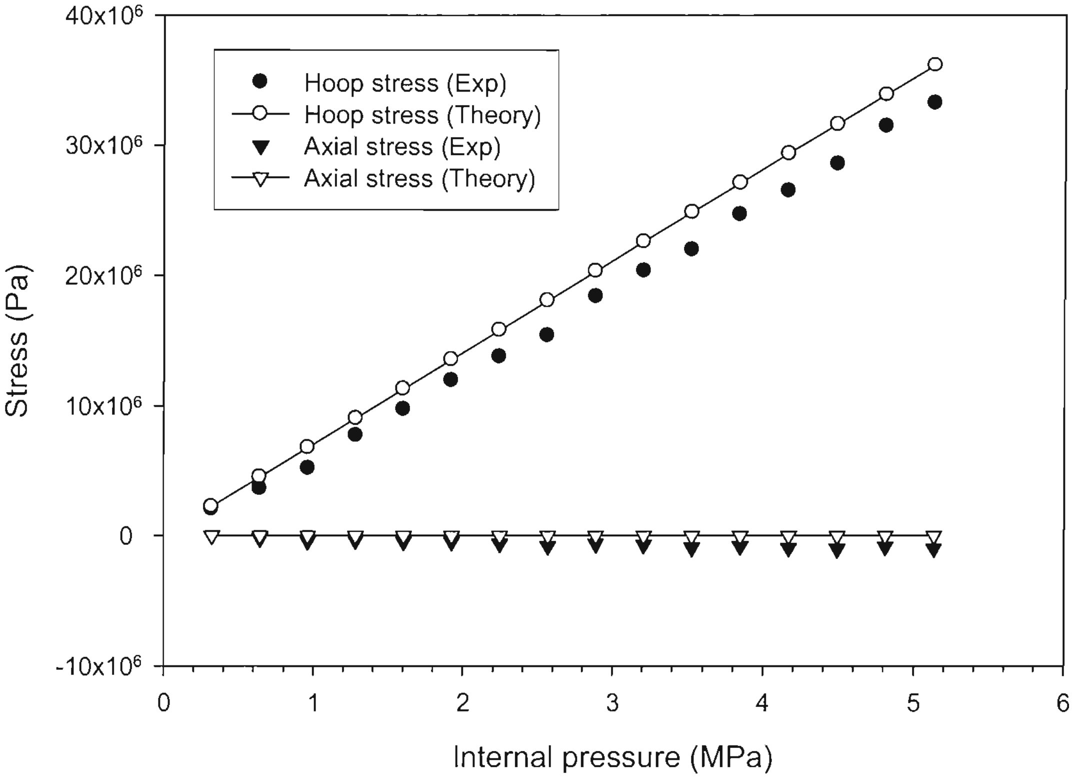

FIGURE 9.9: Hoop and axial stresses derived from strain gauges compared with theory

9.3.3 TSA validation

In order to verify that the pressure rig is capable of applying a cyclic pressure for TSA, it is necessary to carry out two tests:

- a simple compressive test on a cylinder of the same material
- a cyclic pressure test using the cyclic pressure testing facilities of the rig

The experimental settings for both the compression and pressure tests are summarised in Table 9.1. In both cases to enhance the surface emissivity, the pipe surface was coated with a very thin layer of matt black paint.

TABLE 9.1: Summary of the test setup

Setting	Compressive test	Pressure test
Load (kN)	12 ± 10	10 ± 6
$\Delta\sigma_{\mathrm{app}}$ (MPa)	15.9	28.9
Loading frequency (Hz)	10	10
Electronic Iris	47	47
Image type	AC Integrate	AC Integrate

The aim of the compressive test is to evaluate a *calibration factor*, A from the thermoelastic equation (Equation 1.1) for the pipe material. By loading an identical pipe in uniaxial compression as shown in Figure 9.10 a uniaxial stress field is obtained and the calibration factor can be determined as:

$$A = \frac{\Delta\sigma_{\mathrm{app}}}{S} \tag{9.7}$$

where, $\Delta\sigma_{\mathrm{app}}$ is the applied stress change due to the applied cyclic load.

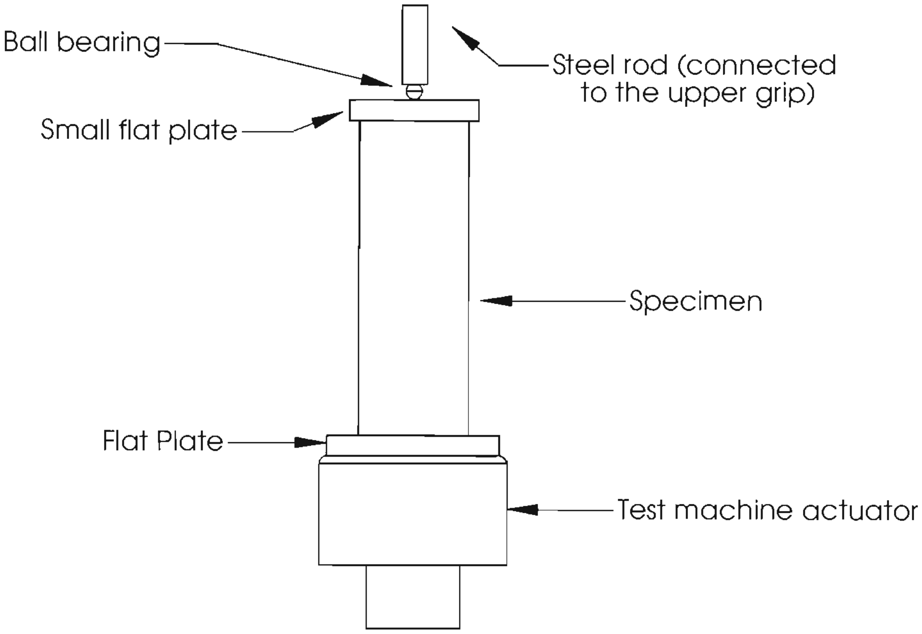

FIGURE 9.10: Compressive loading

The specimen was loaded between flat plates as shown in Figure 9.10 to give $\Delta\sigma_{\mathrm{app}} =$ 15.9 MPa. Figure 9.11(a) shows a DeltaTherm image of the compressive test. The image shows a stress concentration at the base of the pipe due to the contact region between the flat plate and the specimen. Clearly the end of the cylinder is not perfectly square and this results in the non-uniform stress distribution at the end of the pipe. A reasonably uniform signal distribution is achieved away from the end of the pipe. The average signal was obtained from an area indicated by the rectangle in Figure 9.11(a) as 203 ± 42 uncalibrated units, i.e. coefficient of variation of 20%. The calibration factor was calculated from Equation 9.7 as 0.0784 MPa/U.

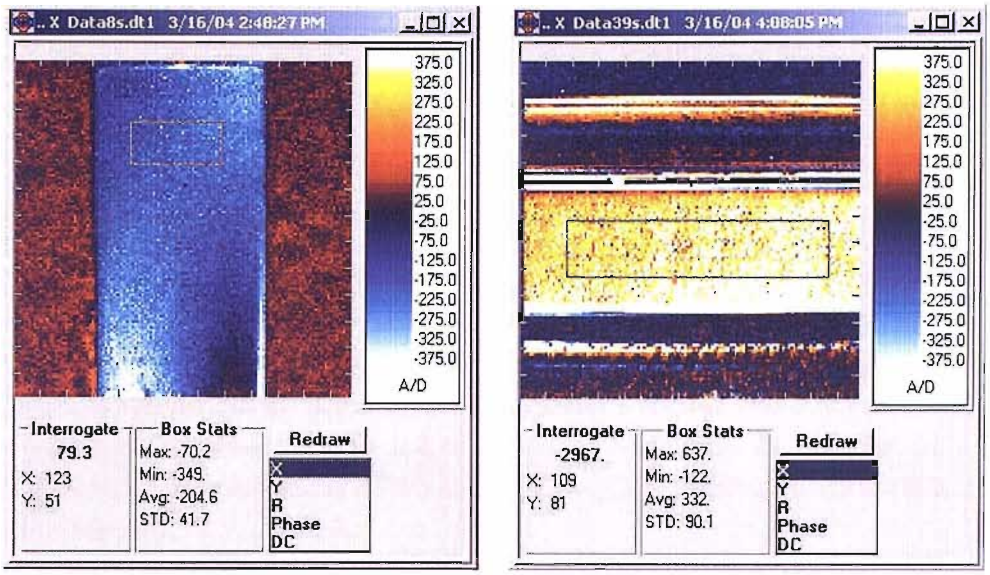

Interrogate
79.3
X: 123
Y: 51

Box Stats
Max: -70.2
Min: -349.
Avg: -204.6
STD: 41.7

Interrogate
-2967.
X: 109
Y: 81

Box Stats
Max: 637.
Min: -122.
Avg: 332.
STD: 90.1

(a) compressive test (b) pressure test

FIGURE 9.11: Sample of captured images from the experiment

In the cyclic pressure test, the same specimen as the previous hydrostatic test was used. The test setting was identical to the hydrostatic test but a cyclic load of 10 ± 6 kN ($\Delta\sigma = 28.87$ MPa) was applied. An average signal of 332 ± 90 units was obtained from the region indicated in a rectangular box shown in Figure 9.11(b). The coefficient of variation was 27%. Using the uncalibrated signal from the pressure test ($S_{\text{ave}} = 332$ U) and the calibration factor, the stresses in the pressurized specimen can be be evaluated by applying Equation 1.1. The principal stress in longitudinal direction is assumed to be zero due to the open-end configuration therefore a hoop stress of 26 MPa is obtained from the thermoelastic data.

To validate the use of the rig for TSA, the load was applied through the ram and controlled by testing machine control panel. The stresses on the wall of the cylinder associated with the applied load was then evaluated. The stress results from the TSA were compared with that from the strain gauge readings, theory and an ANSYS FE model. Firstly, the thick-walled theory was applied to obtain $\Delta\sigma_{\text{hoop}}$ using on internal pressure of 3.85 MPa, i.e. the range of cyclic pressure. Secondly, strain gauges were used to determine the stress; it was assumed that the pressure change due to the cyclic load produced the same strain at the corresponding static load. Thirdly, the FE approach was also used to predict $\Delta\sigma_{\text{hoop}}$, by modelling a 'slice' of the cross-section of the pipe. A quarter of the pipe cross-section was modelled in ANSYS using a 2-D plane element

(PLANE42) under plane stress condition (see Figure 9.12). The model was subjected to internal pressure load of 3.85 MPa and the plane stress condition meant there was no stress in the longitudinal direction. The code and validation for this model is given in Appendix A.5. All results are given in Table 9.2.

TABLE 9.2: Solutions for $\Delta\sigma_{\text{hoop}}$ from various methods

Methods	$\Delta\sigma_{\text{hoop}}$(MPa)	% error from TSA
Thick-walled theory	27.1	+4 %
FEA	27.0	+4 %
Strain gauge	24.9	−4 %
TSA	26.0	

The stresses measured by the TSA technique agree well with the results obtained from the other techniques. The TSA value is 4% less than the thick-wall theory. In comparison with the thick-walled theory, the error observed from the strain gauge technique is of the order of 8% and the error in the TSA technique is around 4%. This clearly shows that the rig is providing the expected cyclic pressure and that the readings from the TSA, although noisy, are giving sufficient signal to give an accurate value for the cyclic stress in the pipe.

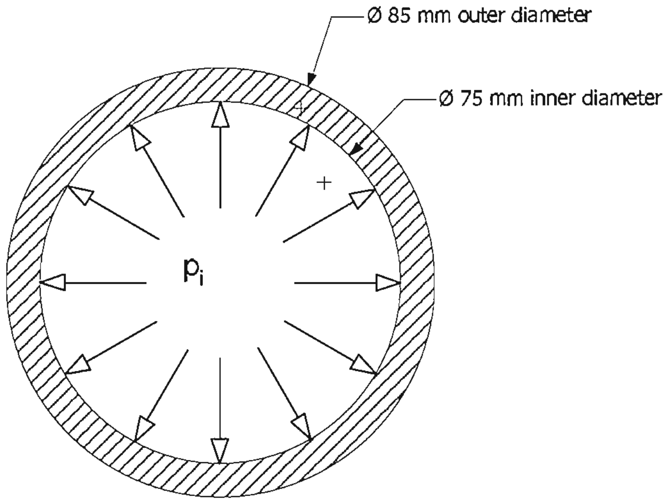

Thick-wall pipe under internal pressure

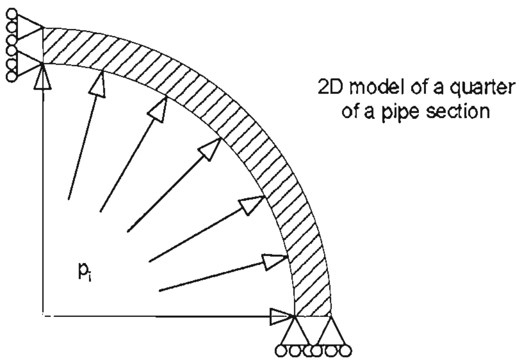

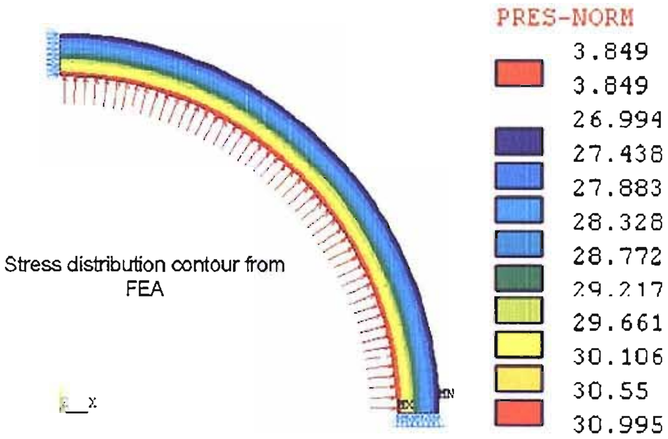

FIGURE 9.12: FE model of stress distribution through pipe thickness

9.4 Design of the damaged pipe specimen with simulated damage

To test the approach demonstrated in Chapters 7 and 8 on pressurised pipework, a pipe specimen with surface flaws needed to be fabricated. Steel is the material considered here because most of the pipework in marine industries is made from steel. A longitudinal crack-like internal surface flaw was simulated in the pipe by a part-through EDM slot. As a result of the findings on steel specimen in Chapter 7, two flaws of different damage severities ($a/t = 0.25$ and $a/t = 0.75$) were chosen, i.e the one that give the minimum and maximum heat contribution from the sub-surface flaw (see Figure 7.19). As it is not feasible to put the electrode inside a cylindrical section, this specimen was made by cutting the pipe in half along the pipe axis and then machining the EDM slot on the inner surface of the pipe as shown in Figure 9.13. Cross sectional views across the EDM flaw are also provided in the figure. Finally, the pipe sections were welded together to re-form a pipe specimen with internal surface flaws. Care must be taken at the weld region during the manufacturing process so that no discontinuity or defect is formed that results in a large stress concentration and so a butt weld was used to minimise the possibility of this.

Because the pipe was cut and welded back together, the prior circular shape of the round pipe deformed. Therefore, the internal end of the pipe was machined to reshape to a circular shape. One inherent problem is that there is no standard o-ring size for the customised pipe diameter. Consequently, the o-rings had to be made in-house and this caused the maximum pressure rating to be invalid. Static test was carried out to ensure safety and define the maximum pressure that the pipe assembly could withstand. From these tests on the damaged pipe, the maximum pressure was approximately 3.5 MPa.

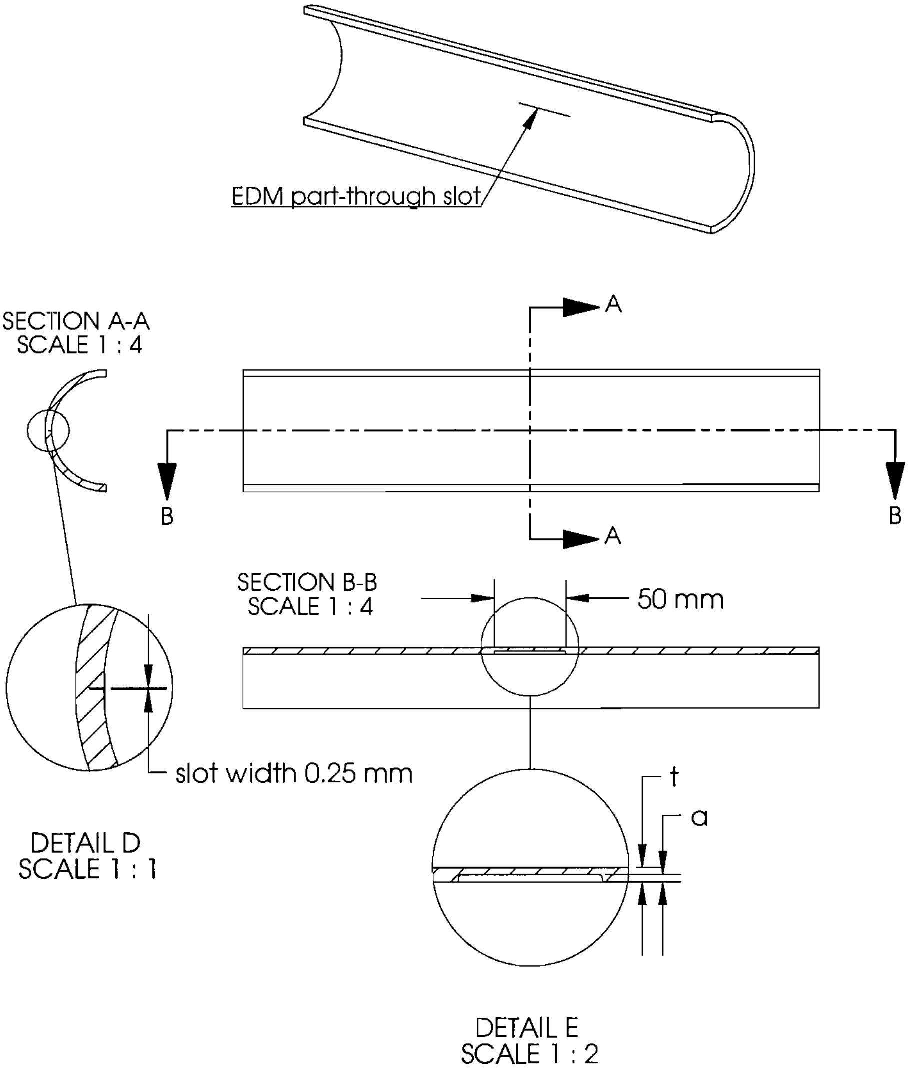

FIGURE 9.13: Technical drawing of one section of a damaged pipe specimen

9.5 Experimental work

Experimental procedures and the experimental arrangements for TSA was the same as the validation test described in Section 9.3.2, i.e. the damaged pipe specimen was assembled into the fixture shown in Figure 9.14, the specimen surface was cleaned and coated with a very thin layer of matt black paint to enhance the surface emissivity. The cyclic internal pressure load 1.6 ± 1.3 MPa ($\Delta\sigma$ = 18 MPa) was applied. The thermoelastic data were recorded at a resolution of approximately 1 mm per pixel. The test was carried out at loading frequencies between 0.5 and 8 Hz. The loading frequency of 8 Hz is the maximum loading frequency that could be attained with the non-standard o-rings.

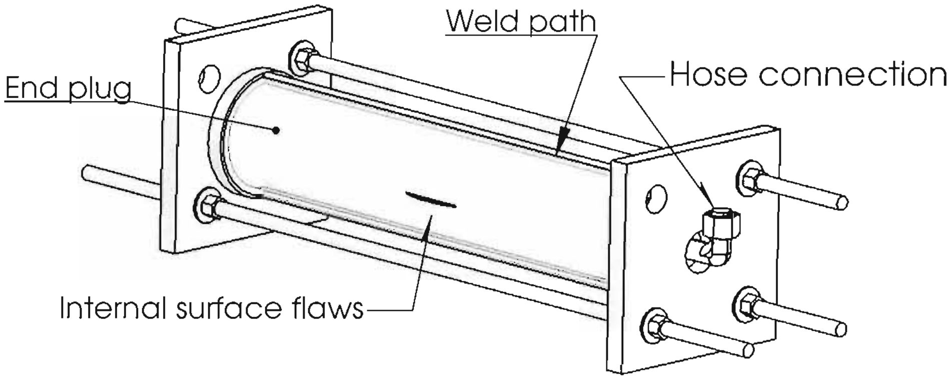

FIGURE 9.14: Damaged pipe assembly

9.6 Results and discussion

Figure 9.15 shows a typical contour plot of R-signal and phase data. It can be seen that, in general a relatively uniform signal distribution is observed from the R-images. No sign of internal damage is shown. The non-uniform contour at the top and bottom edges of the specimen was due to the discontinuity of stress distribution developed from the weld path. This is more pronounced when it is observed from the phase image.

To examine the non-adiabatic behaviour in the thermoelastic response from the pipe section, a series of the thermoelastic images from the middle section (see Figure 9.15) of the pipe were obtained. The signal magnitude and phase images from different load frequencies are provided in Figure 9.16 and Figure 9.17 for the flaw of a/t = 0.25 and the flaw of a/t = 0.75 respectively. In Figure 9.16, both the R-images and phase images across the loading frequencies when a/t = 0.25 show very consistent results with no indication of the damage. This is as expected from Figure 7.19, hence demonstrating that the technique can not detect defects of a/t = 0.25 and less in steel.

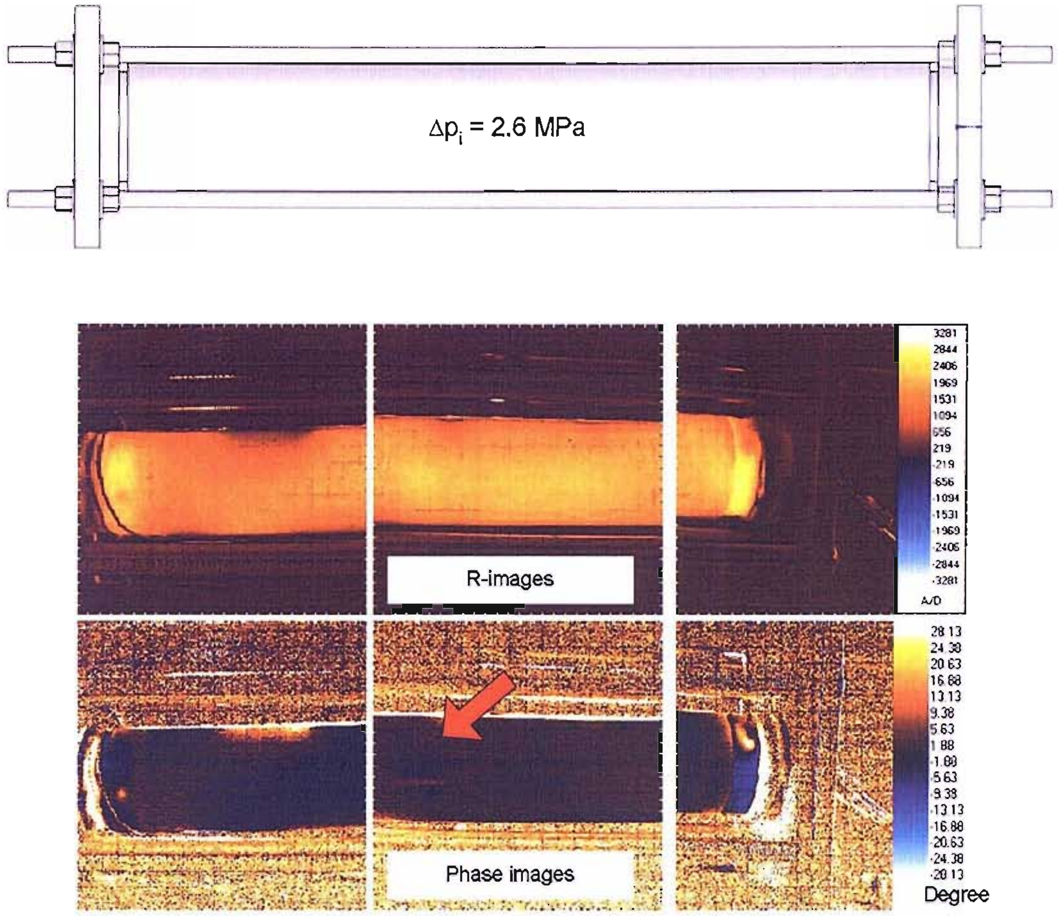

FIGURE 9.15: TSA results: R-images across the pipe shown no sign of internal damage but phase image reveals discontinuity at the damage site of the damage with $a/t = 0.75$

In Figure 9.17, there is practically no indication of the damage in the R-image, apart from at 8 Hz. However, the presence of the damage is clearly visible in the phase data. As the frequency is increased the location of the damage is revealed in the phase plots. The non-adiabatic behaviour can be observed clearly from the phase signal in Figure 9.17, which indicates the presence of sub-surface damage. To observe the effect of loading frequency with the thermoelastic response at the damage site, a line plot across the flaw is shown in Figure 9.18 for each loading frequency. In order to examine the trend of the phase data at the middle of the flaw due to the change of load frequency, the value of the phase data at the middle of the flaw is plotted together and shown in Figure 9.19. It can be seen that the phase response at the tip of the damage increases with loading frequency and becomes constant at 5 Hz. A similar procedure to that used in Chapter 7, to obtain the plot of phase data at the middle of the damage site against the dimensionless parameter $(\gamma/(t-a))$, was carried out and this plot is given in Figure 9.20. According to this data, the trend of the curve obtained from a test across a range of loading frequencies is consistent with the findings in Chapter 7 and Chapter 8. Here, the curve turns at $\gamma/(t-a) \approx 0.7$. The R-signal at 8 Hz is subtracted from the one at 0.5 Hz. The result is shown in Figure 9.21. It can be seen that the contribution from the subsurface stress is very difficult to observed in this case. Two main reasons can be contributed to this. Firstly the applied load is too small, i.e. only 7% of the yield stress. Secondly, the stress distribution across the thickness is not evenly distributed and causes more complex situations to this approach. One solution to the former is to increase the applied load range. The later requires an in-depth study on the influence of nominal stress distribution to the damage zone. However, it can be seen that the approach is very promising in that the damage can be observed from the non-adiabatic behaviour, i.e. from the phase response. The behaviour of the phase response a the damage is similar to what have been observed in the previous chapters, i.e. the turning point was revealed from a series of tests at various loading frequencies.

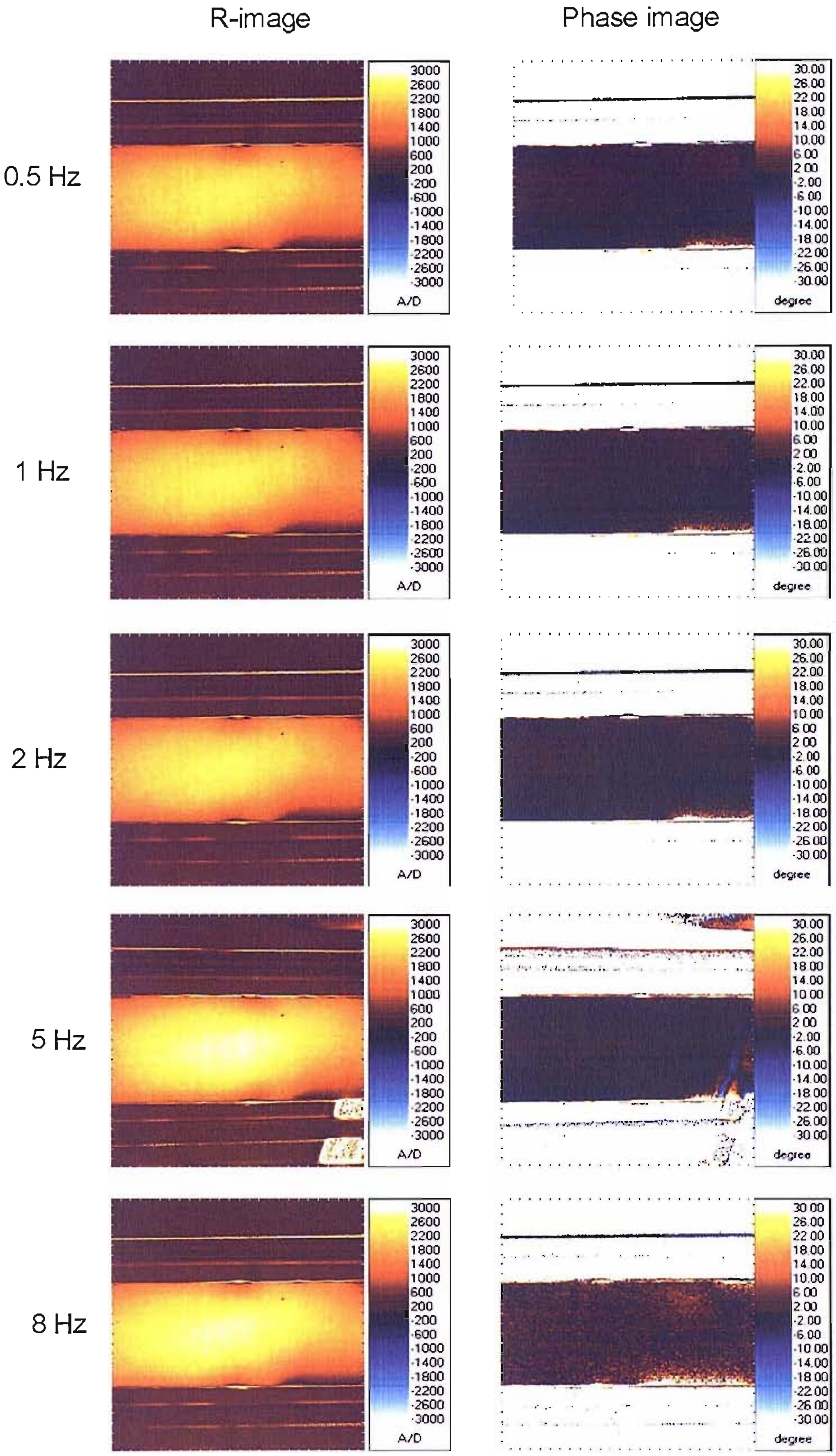

FIGURE 9.16: Results from TSA from various load frequencies (with a/t = 0.25)

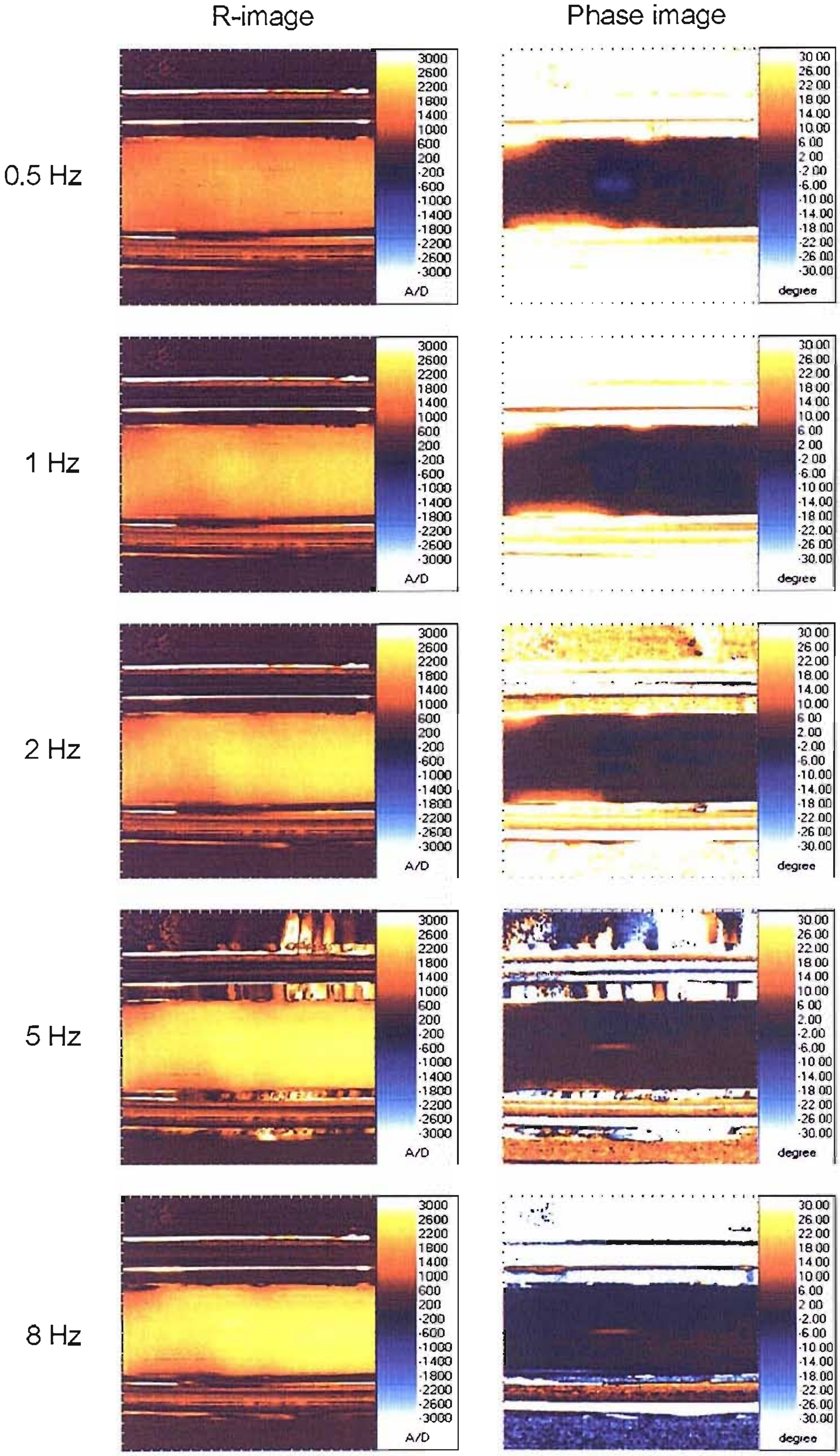

FIGURE 9.17: Results from TSA from various load frequencies(with a/t = 0.75)

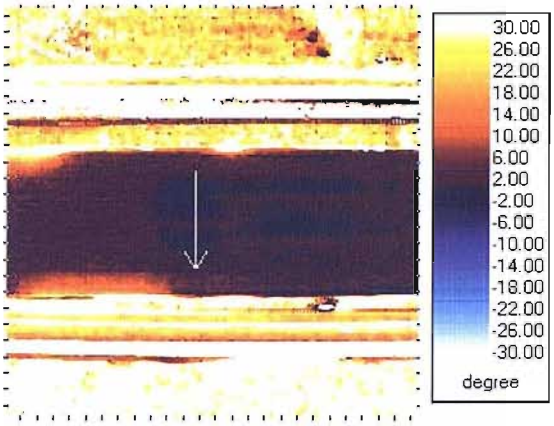

Interrogation line for plotting phase data

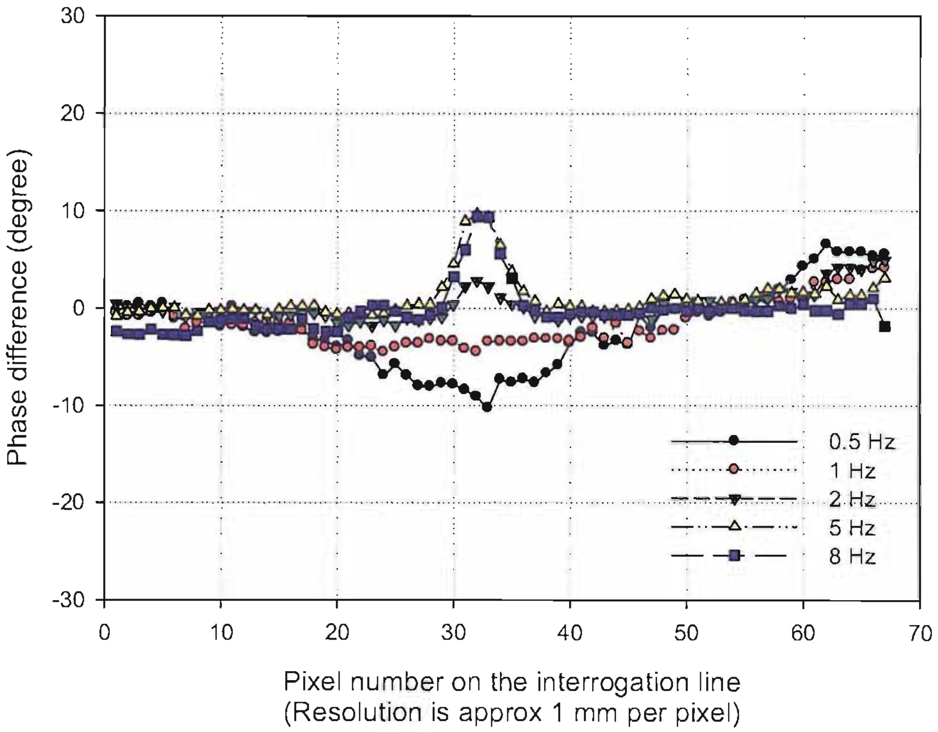

FIGURE 9.18: Phase response in thermoelastic signal at the damage region

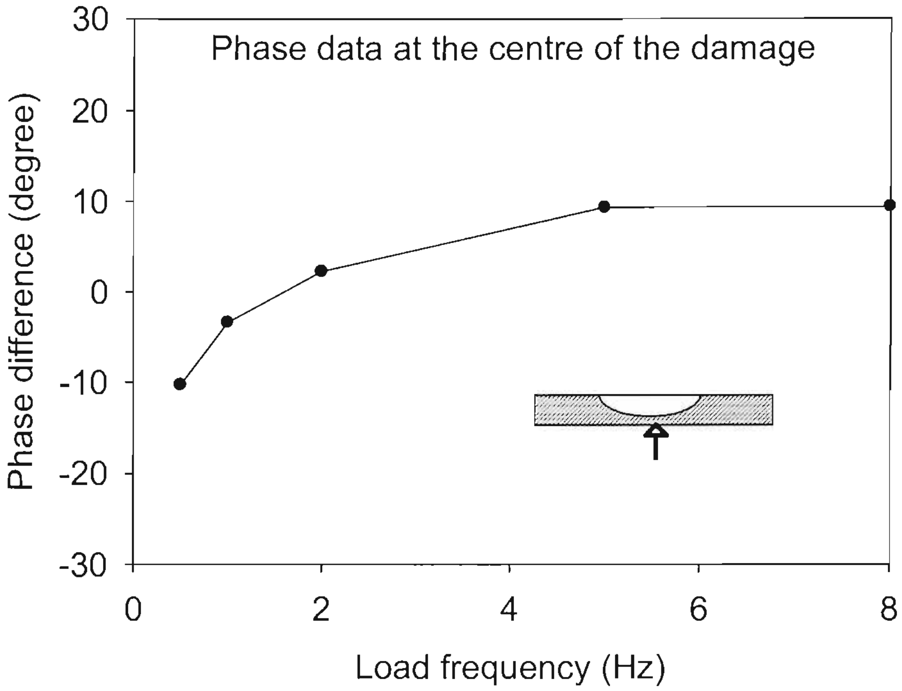

FIGURE 9.19: Phase data at the centre of the flaw

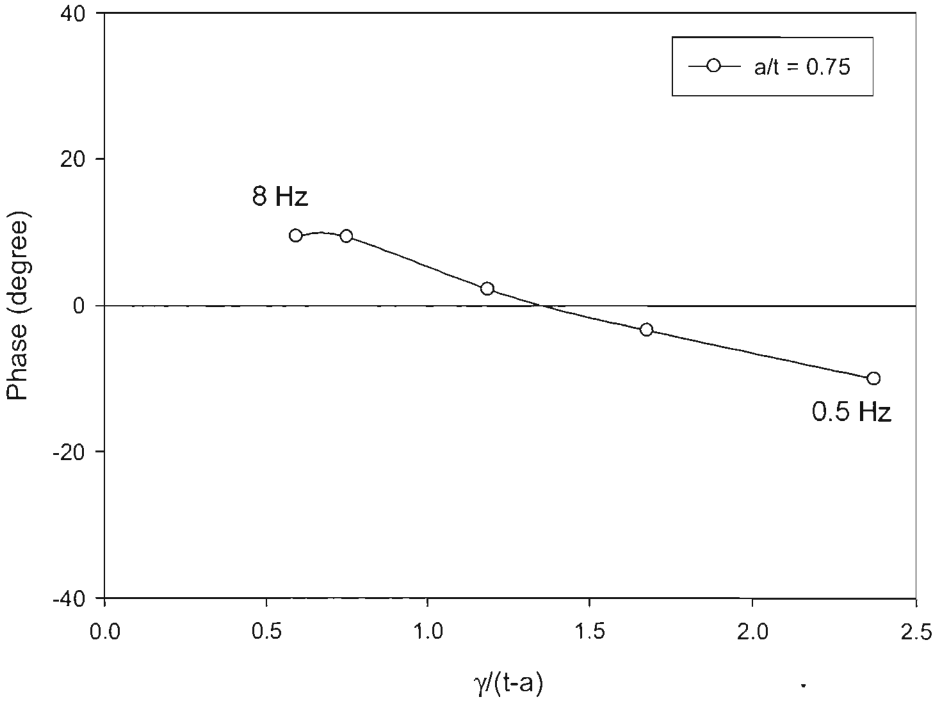

FIGURE 9.20: Phase plot against the dimensionless parameter $\gamma/(t-a)$

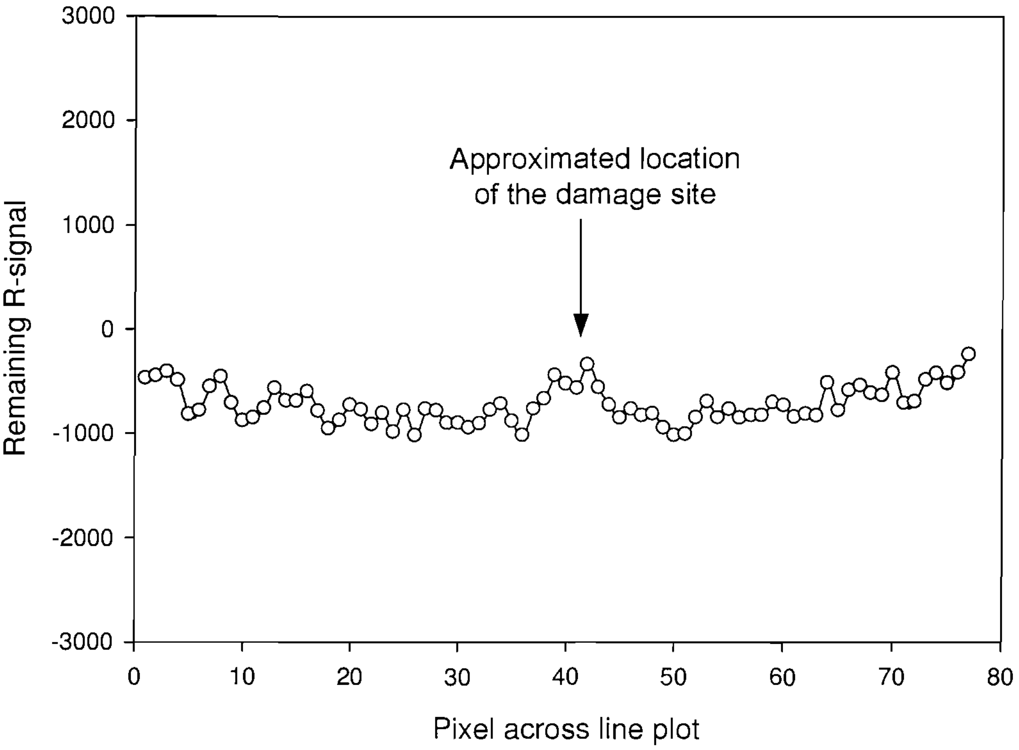

FIGURE 9.21: Subtracted R-signal on the steel pipe specimen

9.7 Conclusions

A test rig designed for the purposed of applying cyclic pressure to piping component has been upgraded and higher quality components have been installed. The rig has been validated by testing under both static and dynamic pressures. Static tests showed that the desired pressure load can be achieved by adjusting the testing machine control panel and that the stresses obtained in the specimen correspond to the loading. The TSA results from the cyclic test have been validated against theory and other experimental data; an FEA has also confirmed the results. Therefore, it can be concluded that the pressure rig is working well with the servo-hydraulic testing machine and can be used for investigations of stresses in cylindrical sections using the TSA technique.

The TSA damage detection on the steel pipes with longitudinal artificial cracks has shown that the TSA approach can be used to detect sub-surface damage successfully. In this case study, the TSA technique was used to detect the damage of $a/t = 0.75$ by using the phase data. The characteristic of the thermoelastic effect was similar to that found in the idealised damage and flat plate specimen, i.e. a phase shift at the tip of the damage that increases with load frequency up to certain level before starting to converge, i.e. contribution of sub-surface heat content becomes weaker. The severity of the sub-surface flaw can also be qualified by the same approach used in the previous chapters. Based on the experimental results, the location of the turning point of phase data is approximately 0.7, which is not consistent with the findings in the work done on the idealised damage (Chapter 7) and the damage in a flat plate (Chapter 8). It can be concluded that this value is also dependent on the geometry of the structure which causes a nominal radial stress distribution through the thickness whereas the nominal stress distribution in the flat plate was uniform. However, this initial work has demonstrated the potential for TSA to be used on actual pipe structures that experience a fluctuating pressure loading.

Chapter 10

Recommendations for future work

10.1 Summary

The work in this thesis has demonstrated the possibility of using a standard TSA system as a damage assessment tool. The study explored the theory behind the TSA and a new approach of damage identification and evaluation has been developed. The approach exploits non-adiabatic behaviour in the thermoelastic data to assess the internal stress caused by subsurface damage. This enables TSA to be used as a tool to examine sub-surface defects in enclosed structures such as pipes and pressure vessels. In addition, a feasibility study on the use of TSA to evaluate the stresses in a GRP Tee-intersection pipe section was carried out. In the following sections some suggestions for future work are made based on the findings on this thesis.

10.2 Damage Assessment in metal

The next logical step from the work done on damage evaluation using the non-adiabatic thermoelastic effect is to apply the approach to real cracks. It can be seen that the comparison of results between TSA and FE simulation in Chapter 7 shows some disagreement at the tip of the slots, particularly on the maximum damage extent. This could be caused by the omission of plasticity in the FE simulation. Valuable research work would be on the development of a numerical technique to include the heat generation component, due to plasticity, which is not reversible, at the crack tip region. As the real crack is arbitrary in shape and orientation, depending on the structure and stress conditions, further study into the effect of these factors on the non-adiabatic behaviour is also worth pursuing so that the approach can be used to detect and characterise, as well as evaluate of the sub-surface damage on real structure.

In view of the FE simulation of the thermoelastic effect, the FE approach would be much simpler if mesh modeller software were available so that a complex structure containing crack can be modelled and meshed automatically. Figure 10.1 shows a solid mesh of a complex structure containing a crack using ZenCrack software [1]. This will allow quick evaluation of the thermoelastic response for a range of different crack dimensions as well as crack orientations. This will allow an alternative hybrid technique of using FEA and TSA to evaluate crack geometry.

The current work has demonstrated that it is possible to obtain sub-surface stress information from the thermoelastic response. To fully exploit this it is essential that a calibration routine is developed that allows the determination of actual stress values from the sub-surface stresses.

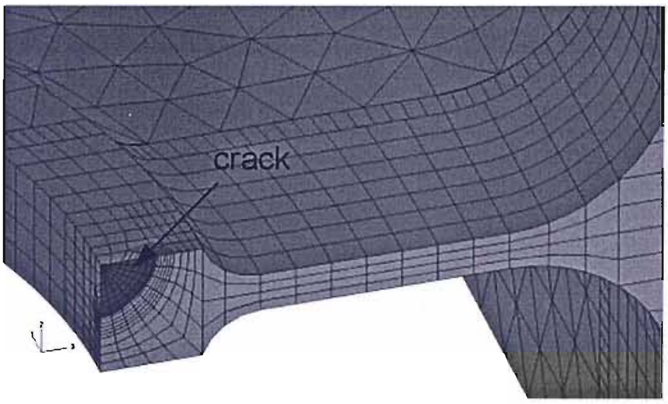

FIGURE 10.1: Example of damage mesh in a complex structure

---

[1] www.zentech.co.uk/zencrack.htm

10.3 Application of damage assessment to pipework

In Chapter 9 it can be seen how effective the damage assessment approach is when used on a real enclosed structure. However, it was speculated that the nominal stresses distributed across the pipe thickness plays an essential role in non-adiabatic behaviour as well, therefore the effect of nominal stresses across the thickness containing damage requires further study. This is because the nominal stress distribution on a pipe section in a real pipework is much more complex, due to the complex routing and geometries as shown in Figure 10.2. The approach could then be extended to evaluate the crack at the weld toe of a pipe intersection.

FIGURE 10.2: Example of pipework in an engine room

Chapter 11

Conclusions

In this thesis, the TSA technique has been advanced for use as a damage assessment tool. A new approach of damage evaluation using TSA has been developed. The approach exploits the non-adiabatic thermoelastic effect, which can be observed via phase data from a standard TSA system and used to assess the severity of subsurface damage. For this purpose, the thermoelastic expression is expressed in terms of a generalised heat conduction equation so that it can be used to describe the thermoelastic response in both adiabatic and non-adiabatic conditions. An FE simulation procedure was also developed in order to simulate the thermoelastic effect under non-adiabatic conditions. The approach has been validated by comparing experimental test results with the numerical simulation over a range of case studies. The study of the non-adiabatic thermoelastic effect shows that for a particular damage extent there exits a condition in which the phase shift is maximised and this can be used to identify the situation where non-adiabatic behaviour starts to reduce. This can be observed clearly from the plot between phase response against the parameter $\gamma/(t-a)$. The case studies carried out on typical surface flaws in flat plates and internal sub-surface damage on cylindrical sections show that the approach is applicable in practice. Further analysis of subsurface stress was carried out to show that, by using this new parameter ($\gamma/(t-a)$), the thermoelastic data containing 'non-adiabatic' components can be categorised. Therefore, subtraction between the data containing 'more non-adiabatic component' from the one containing a 'more adiabatic component' is used to evaluate the contribution of the sub-surface stress and that can be related to the severity of the sub-surface stress.

On the application of TSA on the composite pipe intersection, the study shows that it is feasible to apply TSA as a stress analysis tool on large composite structures. Although the work presented in this thesis does not contain the quantitative stress-strain information from the specimens, a comparison of normalised signal from TSA with a normalised stress from FEA indicates that TSA can be used to evaluate stress concentration on this complex structure. The proposed 'stress factor' technique allows quick evaluation of pipe performance. If a calibration technique around the complex region is available, detailed stress components from TSA can be obtained.

References

[1] Harwood, N. and Cummings, W. M. *Thermoelastic Stress Analysis.* Adam Hilger, Bristol, 1991.

[2] Bream, R. G., Gasper, B. C., Lloyd, B. E., and Page, S. W. I. The SPATE 8000 thermoelastic camera for dynamic stress measurement on nuclear plant components. In *Proceedings of 2nd International Conference on Stress Analysis by Thermoelastic Techniques*, pages 132–148, 1987.

[3] Angerer, S. and Kolitsch, C. Thermoelastic stress analysis for testing of motor-vehicle components. In *Proc.9th GESA/VDI-Bericht Symp.*, pages 265–277, 1985.

[4] Dulieu-Smith, J. M., Quinn, S., Shenoi, R. A., Read, P. J. C. L., and Moy, S. S. J. Thermoelastic stress analysis of a GRP tee joint. *Applied Composite Materials*, 4:283–303, 1997.

[5] Owens, R. H. Applications of thermoelastic effect of typical aerospace composite materials: Stress analysis by thermoelastic techniques. In *Proceedings of SPIE-The International Society for Optical Engineering*, volume 26 of *NDT & E International*, pages 74–86, London, 1987.

[6] Stanley, P. and Chan, W. K. The determination of stress intensity factors and crack-tip velocities from thermoelastic infra-red emissions. In *Proceedings of International Conference on Fatigue of Engineering Materials and Structures*, pages 105 114, Sheffield, 1986.

[7] Dulieu-Barton, J. M. and Stanley, P. Development and applications of thermoelastic stress analysis. *Journal of Strain Analysis for Engineering Design*, 33(2):93 104, 1998.

[8] Raju, I. S. and Newman, J. C., Jr. Stress intensity factors for a wide range of semi elliptical surface cracks in finite thickness plates. *Engineering Fracture Mechanics*, 11:817–829, 1979.

[9] Shlyannikov, V. N. Fatigue shape analysis for internal surface flaw in pressurized hollow cylinder. *International Journal of Pressure Vessels and Piping*, 77:227—234, 2000.

[10] Luo, J. and Bowen, P. A probabilistic methodology for fatigue life prediction. *Acta materialia*, 51(12):3537–3550, 2003.

[11] Knox, E. M., Lafferty, S., Cowling, M. J., and Hashim, S. A. Design guidance and structural integrity of bonded connections in grp pipes. *Composites, Part A: applied science and manufacturing*, 32:231–241, 2001.

[12] Silva, L. F. M., Goncalves, J. P. M., Oliveira, F. M. F., and de Castro, P. M. S. T. Applicability of the spate technique to the detection of hidden cracks. *NDT&E International*, 33:7–13, 2000.

[13] Stanley, P. and Chan, W. K. The application of thermoelastic stress analysis to composite materials. *Journal of Strain Analysis*, 23:137–143, 1988.

[14] Zhang, D., Enke, N. F., and Sandor, B. I. Thermographic stress analysis of composite materials. *Experimental Mechanics*, 30:68–73, 1990.

[15] Lin, S. T. and Rowlands, R. E. Thermoelastic stress analysis of orthotropic composites. *Experimental Mechanics*, 35:257–265, 1995.

[16] EL-Hajjar, R. and Haj-Ali, R. A quantitative thermoelastic stress analysis method for pultruded composites. *Composites Science and Technology*, 63:967–978, 2003.

[17] Lesniak, J. R., Boyce, B. R., and Sandor, B. I. Thermoelastic stress analysis/ nde via focal-plane-array detectors. Final Report WISP-0915-JL1, Stress Photonics, Inc, September 1991.

[18] Rooke, D. P. and Cartwright, D. J. *Compendium of Stress Intensity Factors*. Her Majesty's Stationery Office, London, 1976.

[19] Sih, G. C. *Handbook of Stress Intensity Factors*. Institute of Fracture and Solid Mechanics, Lehigh University, Bethlehem, Pennsylvania, 1973.

[20] Murakami, Y. *Stress Intensity Factor Handbook*, volume 2. Pergamon Press, New York, 1987.

[21] Tada, H., Paris, P. C., and Irwin, G. *The Stress Analysis of Cracks Handbook*. Del Research Corp., Hellertown, Pennsylvania, 1973.

[22] Altluri, S. N. and Kathiresan, K. 3D analyses of surface flaws in thick-walled reactor pressure-vessels using displacement-hybrid finite element method. *Nuclear Engineering and Design*, 51:163–176, 1978.

[23] Raju, I. S. and Newman, J. C., Jr. Stress-intensity factors for internal and external surface cracks in cylindrical vessels. *ASME Journal of Pressure Vessel Technology*, 104:293–298, 1982.

[24] Janssen, M., Zuidema, J., and Wanhill, R. J. H. *Fracture Mechanics*. Delft University Press, Delft, 2 edition, 2002.

[25] Nishioka, T. and Altluri, S. N. Analysis of surface flaw in pressure vessels by a new 3-dimensional alternating method. *ASME Journal of Pressure Vessel Technology*, 104:299–307, 1982.

[26] Chen, D. H., Nisitani, H., and Mori, K. Stress-intensity factors for an internal semi-elliptical surface crack in cylindrical pressure vessels. *ASME Journal of Pressure Vessel Technology*, 117:213–221, August 1995.

[27] Zheng, X. J. and Glinka, G. Weight functions and stress intensity factors for longitudinal semi-elliptical cracks in thick-wall cylinders. *ASME Journal of Pressure Vessel Technology*, 117:383–389, 1995.

[28] Lampman, S. R., editor. *ASM Handbook : Fatigue and Fracture*. ASM international, 1997.

[29] Tomlinson, R. A. and Olden, E. J. Thermoelasticity for the analysis of crack tip stress fields- a review. *Strain*, 35(2):49–55, May 1999.

[30] Stanley, P. and Chan, W. K. Thermoelastic evaluation of a proposed K_{II} specimen. In *Proceedings of 2nd International Conference on Stress Analysis by Thermoelastic Techniques*, volume 731, pages 102–109, London, 1987. SPIE.

[31] Stanley, P. and Dulieu-Smith, J. M. Progress in the thermoelastic evaluation of mixed mode stress intensity factors. In *Proceedings of the SEM spring conference on experimental mechanics*, pages 617–626, Dearborn, 1993.

[32] Lin, S. T., Feng, Z., and Rowlands, R. E. Thermoelastic determination of stress intensity factors in orthotropic composites using the J-integral. *Engineering Fracture Mechanics*, 56(4):579–592, 1997.

[33] Tomlinson, R. A., Nurse, A. D., and Patterson, E. A. On determining stress intensity factors for mixed mode cracks from thermoelastic data. *Fatigue and Fracture of Engineering Materials and Structures*, 20(2):217–226, 1997.

[34] Diaz, F. A., Patterson, E. A., Tomlinson, R. A., and Yates, J. R. Measuring stress intensity factors during fatigue crack growth using thermoelasticity. *Fatigue and Fracture of Engineering Materials and Structures*, 27:571–583, 2004.

[35] Pang, H. L. J. Experimental stress analysis of fatigue cracks by SPATE. *Experimental Techniques*, 17:20–22, 1993.

[36] Lesniak, J. R. Internal stress measurement. In *Proceedings of VI International Congress on Experimental Mechanics*, pages 825–829. SEM, BETHEL CT., 1988.

[37] Dunn, S. A. On the effects of through-thickness thermal conduction on stress measurement by thermoelastic techniques. *Experimental Mechanics*, 33:32–36, 1993.

[38] Offermann, S., Beaudoin, J. L., Bissieux, C., and Frick, H. Thermoelastic stress analysis under non-adiabatic conditions. *Experimental Mechanics*, 37:409–413, 1997.

[39] Inoue, H. and Kishimoto, K. The effect of heat conduction in thermoelastic stress analysis. In *Proceedings of the 12th International Conference on Experimental Mechanics*, pages 742–743, Italy, 2004.

[40] Salerno, A. and Desiderati, S. Procedure proposal for the correction of nonadiabatic thermoelastic stress analysis results. *Review of scientific instruments*, 75(2):507–514, 2004.

[41] Stanley, P. and Chan, W. K. A novel study of the stress distribution in a thin freely-formed pressure vessel end. In *Proceedings of the the 6th International Conference on Pressure Vessel Technology*, pages 485–500, Beijing, China, 1988.

[42] Blake, J. I. R. Practicality and economics of using FRP pipes in ships. Technical Report SSA ITMC Project No. 42, University of Southampton, June 2003.

[43] Kitching, R. and Tang, W. M. Comparison of glass reinforced plastic t-junction/straight pipe combinations for offshore use. *International Journal of Pressure Vessels and Piping*, 71:263–283, 1997.

[44] Xue, M., Lu, Q. H., Zhuang, R. Q., and Wei, Z. Z. Stress and strength analysis by fem of fibre reinforced plastic pipe tees subjected to internal pressure. *International Journal of Pressure Vessels & Piping*, 67:11–15, 1996.

[45] Tsai, S. W. and Wu, E. M. A general theory of strength for anisotropic materials. *Journal of Composite Materials*, 5:58–80, 1971.

[46] Mackin, T. J. and Roberts, M. C. Evaluation of damage evolution in ceramic-matrix composites using thermoelastic stress analysis. *Journal of the American Ceramic Society*, 83(2):337–343, 2000.

[47] Cunningham, P. R., Dulieu-Barton, J. M., Dutton, A. G., and Shenoi, R. A. Thermoelastic characterisation of damage around a circular hole in a GRP component. In *Proceedings of the 4th International Conference on Damage Assessment of Structures*, Cardiff, Wales, 2001.

[48] Dulieu-Barton, J. M., Earl, J. S., and Shenoi, R. A. Determination of the stress distribution in foam cored sandwich construction composite tee joints. *Journal of Strain Analysis*, 36(6):545–556, 2001.

[49] Paynter, R. J. H. and Dutton, A. G. The use of a second harmonic correlation to detect damage in composite structures using thermoelastic stress measurements. *Strain*, 39(2):73–78, 2003.

[50] Wong, A. K. A non-adiabatic thermoelastic theory for composite laminates. *Journal of Physics and Chemistry of Solids*, 52(3):483–494, 1991.

[51] Cunningham, P. R., Dulieu-Barton, J. M., Dutton, A. G., and Shenoi, R. A. The effect of ply lay-up upon the thermoelastic response of laminated composites. *Key Engineering Materials*, 221–222:325–336, 2002.

[52] Sfantsikopoulos, M. Stress analysis of metal pipework used in marine engineering applications: Finite element and thermoelastic stress analysis of welded piping junctions. MSc Thesis, University of Southampton, 2002.

[53] Dulieu-Smith, J. M. Alternative calibration techniques for quantitative thermoelastic stress analysis. *Strain*, pages 9–16, February 1995.

[54] Schapery, R. Thermal expansion coefficients of composite materials based on energy principles. *Journal of Composite Materials*, 2:380–404, 1968.

[55] Callister, W. D., J. *Materials Science and Engineering : An Introduction*. John Willey & Sons Inc, 4 edition, 1996.

[56] Quinn, S. and Dulieu-Barton, J. M. Identification of the sources of non-adiabatic behaviour for practical thermoelastic stress analysis. *Journal of Strain Analysis for Engineering Design*, 37(1):59–71, 2002.

[57] Smith, F. W. and Alave, M. J. Stress-intensity factors for a part-circular surface flaw. In *The First International Conference on Pressure Vessel Technology*, pages 793–800. Pressure Vessel Division of ASME, 1969.

[58] Newman, J. C., Jr. and Raju, I. S. An empirical stress intensity factor equation for the surface crack. *Engineering Fracture Mechanics*, 15:185–192, 1981.

[59] *DeltaTherm system manual*. Stress Photonics Inc, Madison, USA, 2004.

[60] Thomson, W. On the dynamical theory of heat. *Transactions, Royal Society of Edinburgh*, 20:261–288, 1853.

[61] Biot, M. A. Thermoelasticity and irreversible thermodynamics. *Journal of Applied Physics*, 27:240–253, March 1956.

[62] Pitarresi, G. and Patterson, E. A. A reveiw of the general theory of thermoelastic stress analysis. *Journal of Strain Analysis*, 38(5):405–417, 2003.

[63] Belgen, M. H. Infrared radiometric stress instrumentation application range study. Technical Report NASA CR-1067, NASA, 1968.

[64] McKelvie, J. Consideration of the surface temperature response to cyclic thermoelastic heat generation. In *Proceedings of 2nd International Conference on Stress Analysis by Thermoelastic Techniques*, pages 44–53, London, 1987.

[65] Rocca, R. and Bever, M. The thermoelastic effect in iron and nickel as a function of temperature. *Transactions AIME*, 188:327–333, Feb 1950.

[66] Belgen, M. H. Structural stress measurements with an infrared radiometer. *ISA Transactions*, 6:49–53, 1967.

[67] Dulieu-Barton, J. M., Quinn, S., Eyre, C., and Cunningham, P. R. Development of a temperature calibration device for thermoelastic stress analysis. *Applied Mechanics and Materials*, 1–2:197–204, 2004.

[68] Desiderati, S. and Salerno, A. Quantitative thermoelastic stress analysis in non-adiabatic conditions. In *Proceedings of the SPIE*, volume 5405, pages 466–475, 2004.

[69] Boresi, A. P. and Schmidt, R. J. *Advanced Mechanics of Materials*. Wiley, 6 edition, 2002.

[70] Sathon, N. Design of pressure vessel testing equipment for use with thermoelastic stress analysis. MSc Thesis, University of Southampton, 2002.

Appendix A

Supporting materials

A.1 Plastic zone size calculation

The plastic zone size in Chapter 7 was calculated using an approximated solution of a finite width (W) specimen with a centre crack length ($2a$) as shown in Figure A.1 from Ref. [24].

$$r_{y,\text{plane strain}} = \frac{1}{6\,\pi}\left(\frac{K_I}{\sigma_{ys}}\right)^2 \tag{A.1}$$

where σ_y is yield stress of the material, K_I is mode one stress intensity factor calculated from:

$$K_I = K_I = C\sigma\sqrt{\pi a}$$

$$C = 1 + 0.0256\left(\frac{a}{W}\right) - 1.152\left(\frac{a}{W}\right)^2 + 12.2\left(\frac{a}{W}\right)^3$$

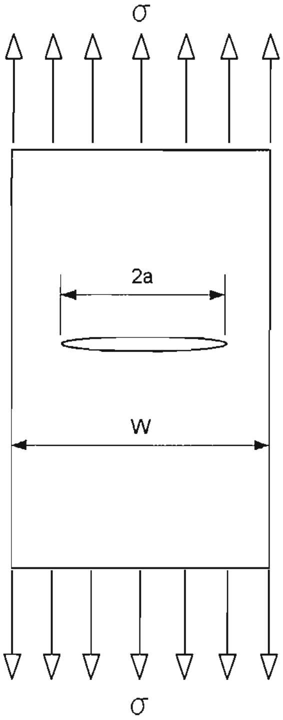

FIGURE A.1: The finite width centre cracked specimen

A.2 Convergence test of the Finite Element Model

To assure optimum mesh size of the model, the process of mesh refining was carried out. The mesh was refined until the variation in the results is less than a specific value. In this analysis, Von-Mises Stress convergence was used. An example of a convergence test is shown in Figure A.2. The plot of the maximum Von-Mises stress at the notch tip converges to a constant value of approximately 170 MPa.

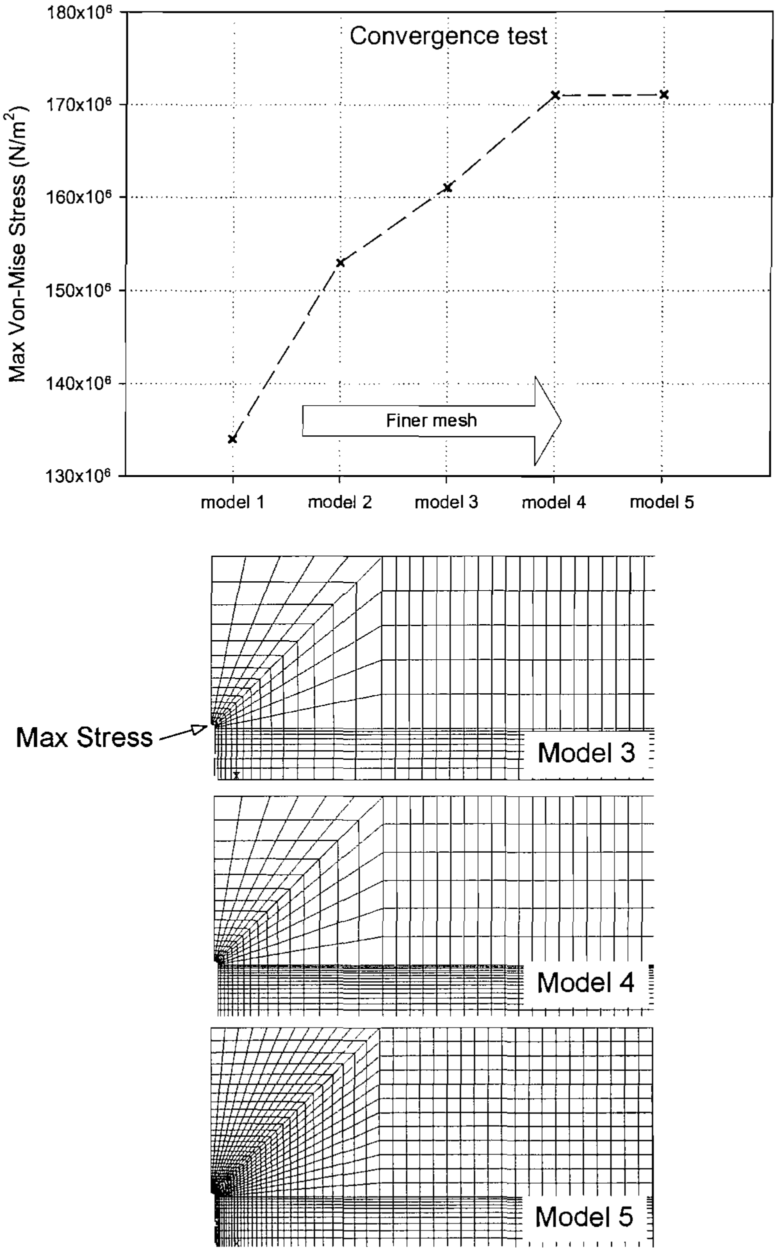

FIGURE A.2: Convergence test of the model with a/t=0.25

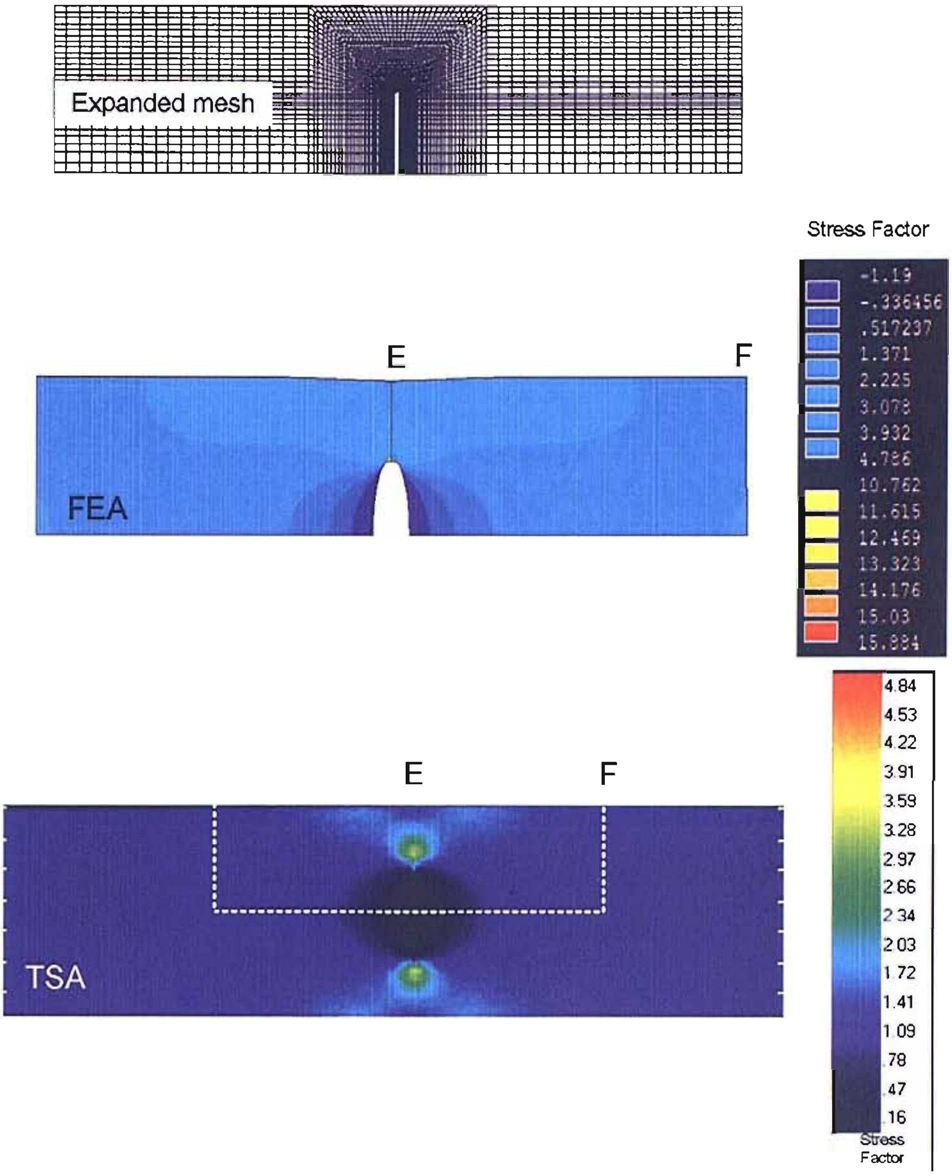

FIGURE A.3: Stress factors plot on the side view of the damage

A sample of the stress distribution in terms of stress factor from FE analysis and TSA is given in Figure A.3. The figure shows the mesh density at the notch is high enough to capture the sharp increase of stress at the notch region.

A.3 Stress Intensity Factors calculation

There are a number of well known Stress Intensity Factor solutions available for various situations. The following solution is for semi-elliptical surface crack in tension as shown in Figure A.4 from Ref [58]. A Matlab script file for the calculation is also given.

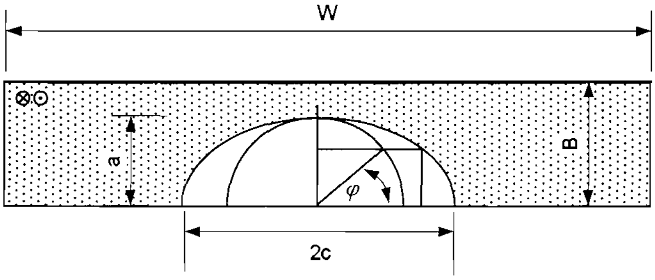

FIGURE A.4: Diagram for a crack under Mode I

$$K_I = \sigma\sqrt{\pi\frac{a}{Q}}F\left(\frac{a}{B},\frac{a}{c},\frac{c}{W},\varphi\right)$$

$$Q = 1 + 1.464\left(\frac{a}{c}\right)^{1.65}$$

$$F = \left\{C_1 + C_2\left(\frac{a}{B}\right)^2 + C_3\left(\frac{a}{B}\right)^4\right\}f_\varphi C_4 f_w$$

$$C_1 = 1.13 - 0.09\left(\frac{a}{c}\right)$$

$$C_2 = -0.54 + \frac{0.89}{0.2 + a/c}$$

$$C_3 = 0.5 - \frac{1.0}{0.65 + a/c} + 14\left(1.0 - \frac{a}{c}\right)^{24}$$

$$C_4 = 1 + \left\{0.1 + 0.35\left(\frac{a}{B}\right)^2\right\}(1 - \sin(\varphi))^2$$

$$f_\varphi = \left\{\sin^2\varphi + \left(\frac{a}{c}\right)^2\cos^2\varphi\right\}^{\frac{1}{4}}$$

$$f_w = \left\{\sec\left(\frac{\pi c}{W}\sqrt{\frac{a}{B}}\right)\right\}^{\frac{1}{2}}$$

for

$$\frac{a}{B} < 1$$

$$\frac{a}{c} \le 1$$

$$\frac{c}{W} < 0.25$$

$$0 \leq \varphi \leq \pi$$

```
% This is an M-file to be run on matlab
% Stress Intensity Factors at maximum depth of semi elliptical crack
% Define Parameters
sigma=24.97           % nominal stress MPa
a=2.65                % crack depth
B=5.3                 % thickness
W=150                 % plate width
c=7                   % half crack width
angle=90              % angle at max SIF max depth
Phi=angle*pi/180      % change degree to radius
fw=(sec(((pi*c)/W)*sqrt(a/B)))^0.5            % FUNCTION OF PLATE WIDTH
fphi=((sin(Phi)^2)+((a/c)^2*cos(Phi)^2))^0.25  % FUNCTION OF ANGLE PHI
C4=1+(0.1+0.35*(a/B)^2)*(1-sin(Phi))^2
C3=0.5-(1/(0.65+a/c))+14*(1-a/c)^24
C2=-0.54+0.89/(0.2+a/c)
C1=1.13-0.09*(a/c)
F=(C1+C2*(a/B)^2+C3*(a/B)^4)*fphi*C4*fw
Q=1+1.464*(a/c)^1.65
K=sigma*sqrt(pi*(a/Q))*F                       % SIF mode I
```

A.4 Stress-strain data from pressure experiments

TABLE A.1: Static strain/stress measurement

Load	Strain ($\mu\epsilon$)		Stress (Pa)	
(kN)	SG.1	SG.2	SG.1	SG.2
1	10	-2.7997	2.06E+06	6.71E+01
2	18	-5.9464	3.65E+06	-2.03E+05
3	26	-9.0931	5.24E+06	-4.05E+05
4	38	-12.2398	7.73E+06	-3.58E+05
5	48	-15.3865	9.77E+06	-4.35E+05
6	59	-18.5332	1.20E+07	-4.50E+05
7	68	-21.6799	1.38E+07	-5.90E+05
8	76	-24.8266	1.54E+07	-7.93E+05
9	90	-27.9733	1.84E+07	-6.20E+05
10	100	-31.12	2.04E+07	-6.97E+05
11	108	-34.2667	2.20E+07	-9.00E+05
12	121	-37.4134	2.47E+07	-7.90E+05
13	130	-40.5601	2.65E+07	-9.30E+05
14	140	-43.7068	2.86E+07	-1.01E+06
15	154	-46.8535	3.15E+07	-8.35E+05
16	163	-50.0002	3.33E+07	-9.75E+05

A.5 FEA of a pressurised steel pipe

Finite Element modelling details can be found in the comments in the code.

Note: To verify the FE model, an analytical solution is also available for a thick-walled shell and pressure vessel. The stress distribution through the thickness in a pressurized thick-walled cylinder with end caps [1] is calculated by:

$$\sigma_\theta = \frac{p_i}{k^2 - 1}\left(1 + \frac{r_o^2}{r^2}\right)$$

where, the ratio between inner and outer radius is defined by $k = r_o/r_i$, p_i is the internal pressure and r is an arbitrary radius between r_i and r_o.

```
!==============================================================
!This is a modelling of a pipe under pressure test on April 04 !to
compare with other solutions. !units used in this model: mm, MPa,
and Newton
!==============================================================
/filnam, pipe_section
/title, section pipe under pressure /PREP7
!====define internal and external diameter
R_IN=75/2 !unit in mm
R_OUT=85/2
R_mesh=50  ! number of division to mesh radius direction
!number of devision to mesh thickness direction
T_MESH= 8
EX=207E3 !Young's modulus unit in MPa
PRXY=0.3                !Poisson ratio
PRESSURE=3.849  ! applied pressure unit in MPa, Force/3117 sqmm.
! create only a quarter of the cylinder section
CYL4,0,0,R_IN,0,R_OUT,90 ! model only a quater of the pipe
!=============control mesh size LSEL,S,,,1,3,2
!select line curves
LESIZE,ALL,,,R_mesh
LSEL,ALL
LSEL,S,,,2,4,2
!select line thickness
LESIZE,ALL,,,T_MESH
LSEL,ALL
ET,1,PLANE42,1,,0,,,
```

---

[1] PP Benham, RJ Crawford and CG Armstrong, Mechanics of Engineering Materials, 2nd edition, Prentice Hall, page 386-387

```
! define element type and keyopt(3)=0 for plain stress
MP,EX,1,EX ! Young's modulus of linear material
properties
MP,PRXY,1,PRXY ! Poisson ratio
AMESH,ALL
/SOLU  ! Solution section
ANTYPE,STATIC
DL,2,,UX,0
DL,4,,UY,0
SFL,3,PRES,PRESSURE ! apply pressure on line number 3 in the model
solve
```

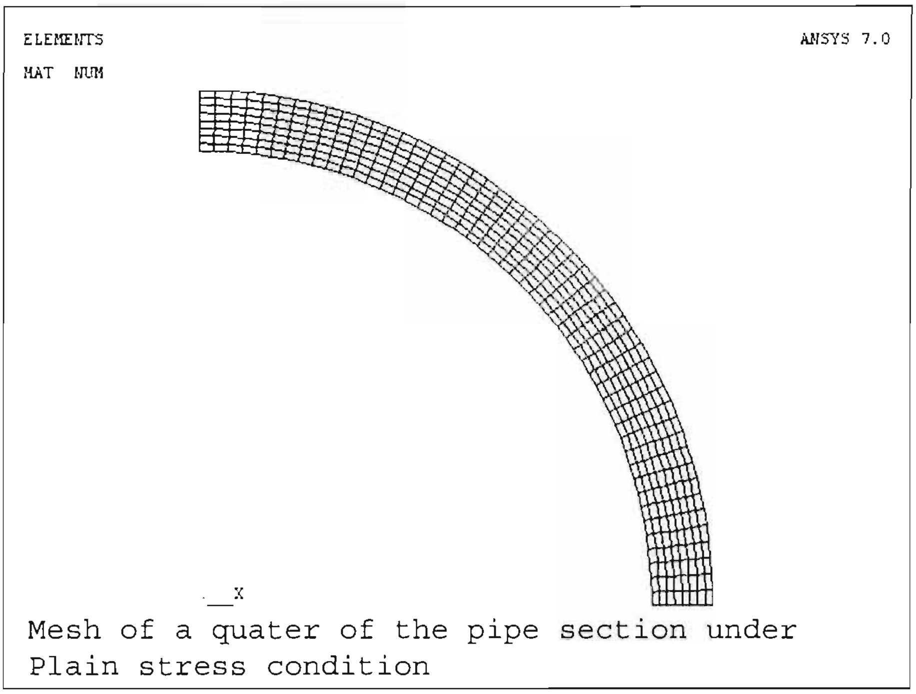

FIGURE A.5: FE mesh

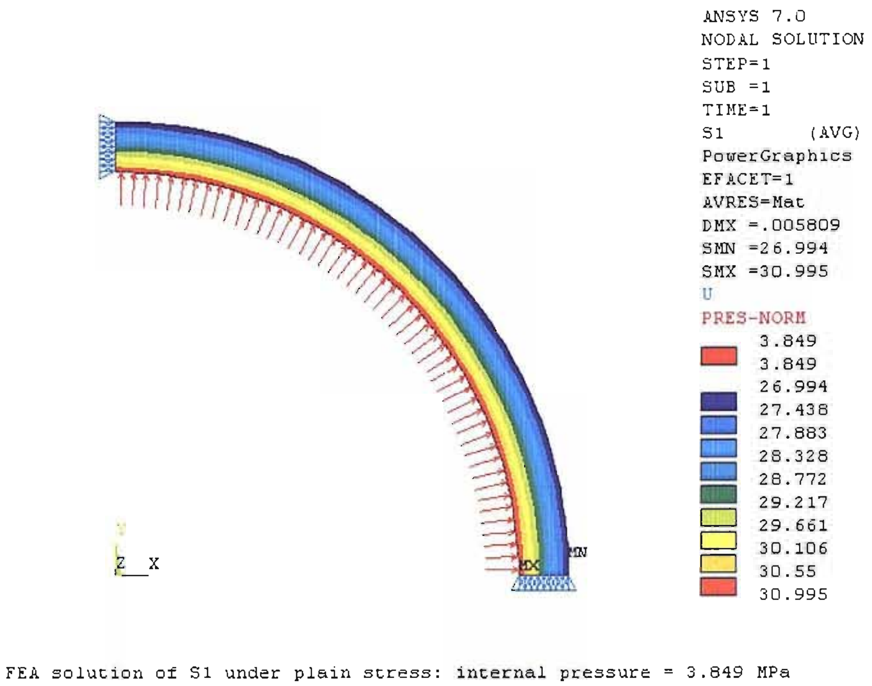

FIGURE A.6: Nodal solution of S_1

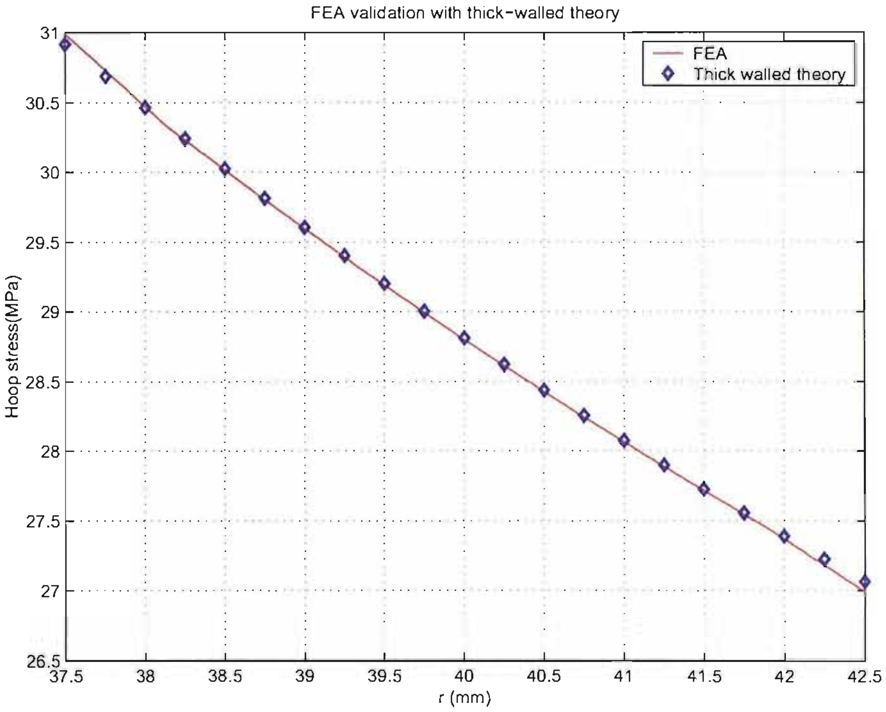

FIGURE A.7: hoop stress plot from FEA and theory

A.6 Coefficient of thermal expansion

According to the calculation of α_{11} and α_{22} used in section 3.5 for the GRP pipe using in the experiment. By using the formulation proposed by *Schapery*, the coef. of thermal expansion in the principal directions of laminar are obtained[2]. Then it is necessary to transform these values in to the principal stress direction occurred on the straight pipe. By using the standard tensorial transformation and substitute the symmetric winding angle from zero to 90 degrees, the relationship between coef. of thermal expansion in both directions and winding angle can be plotted in figure A.8

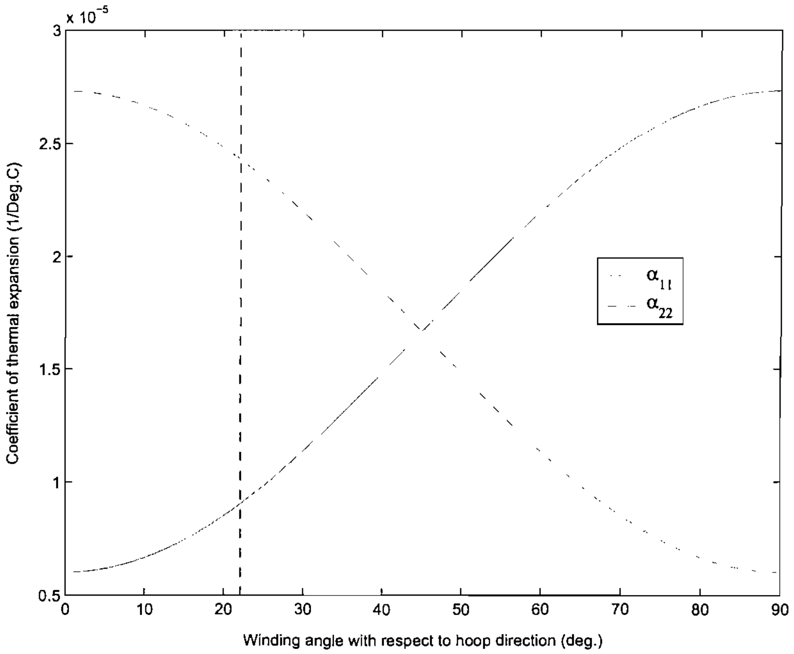

FIGURE A.8: Coefficient of thermal expansion

---

[2] J. M. Dulieu-Smith, S. Quinn, R. A. Shenoi, P. J. C. L. Read, and S. S. J. Moy. Thermoelastic stress analysis of a GRP tee joint. Applied Composite Materials, 4:283-303, 1997.

A.6.1 Matlab code for plotting CTE

```
Ef=80e12; %Young modulus of fibre
alpha_f=5e-6; %CTE of fibre
Vf=0.7; % Vol fraction of fibre
Em=3.5e12; % Young modulus of matrix
alpha_m=60e-6; % CTE of matrix
Vm=0.3; % Vol fraction of matrix
PRf=0.27; %Poisson ratio of fibre
PRm=0.37; % Poisson ratio of matrix
PR12=(PRf*Vf)+(PRm*Vm); % Poisson ratio of composite
alpha_p=((Ef*alpha_f*Vf)+(Em*alpha_m*Vm))/(Ef*Vf+Em*Vm)
% CTE parallel to fibre direction
alpha_t=(alpha_f*(1+PRf)*Vf)+(alpha_m*Vm*(1+PRm))-PR12*alpha_p
% CTE transverse direction
for i=1:1:90;
phi=i*pi/180; % winding angle in degree 22.5
alpha_11=alpha_p*cos(phi)^2+alpha_t*sin(phi)^2;
alpha_22=alpha_p*sin(phi)^2+alpha_t*cos(phi)^2;
A11(i,1)=alpha_11
A22(i,1)=alpha_22
end
x=1:90
plot(x,A11,'b-', x,A22,'b--');legend('a_1_1','a_2_2')
```

A.7 Stress factor approach

This section provides procedures to evaluate stress factor along the top surface of the pipe adopted in section 3.7.1. The example shown here is the procedure to evaluate stress factor for the steel pipe (T-05). A comparison with FEA is also given in Figure A.9.

Procedure to obtain stress factor plot:

1. The Uncalibrated signal from TSA is plotted and shown in Figure A.10 (top). The figure also shows the linear range, which was used to calculate nominal signal (S_{nom}).
2. A best fit line along the linear region is extrapolated up to the joint region (see Figure A.10 (top)). This could be considered as a reference signal due to a linear stress condition on an *equivalent straight pipe* subjected to simple bending load.
3. The stress factor is the ratio between the signal output from TSA and the reference line created previously. The stress factor is plot in Figure A.10 (bottom).

The stress factor from experiment is then compared with those evaluated from an FE model and shown in Figure A.9. The discrepancy between FEA and TSA at the maximum stress shown in the figure is caused by the high stress concentration at the weld path which cannot be modelled accurately in a simple FEA.

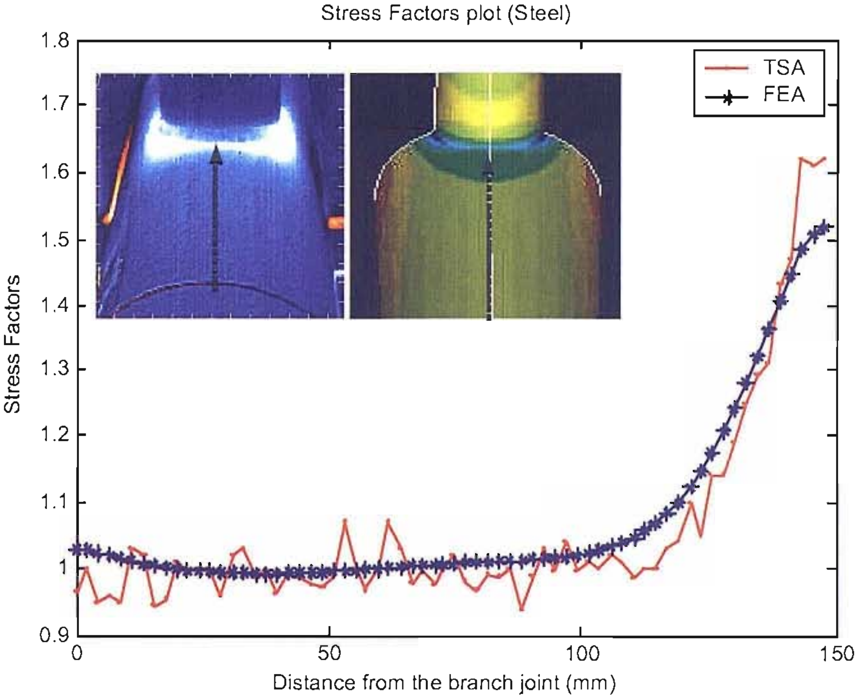

FIGURE A.9: Stress Factor from TSA and FEA

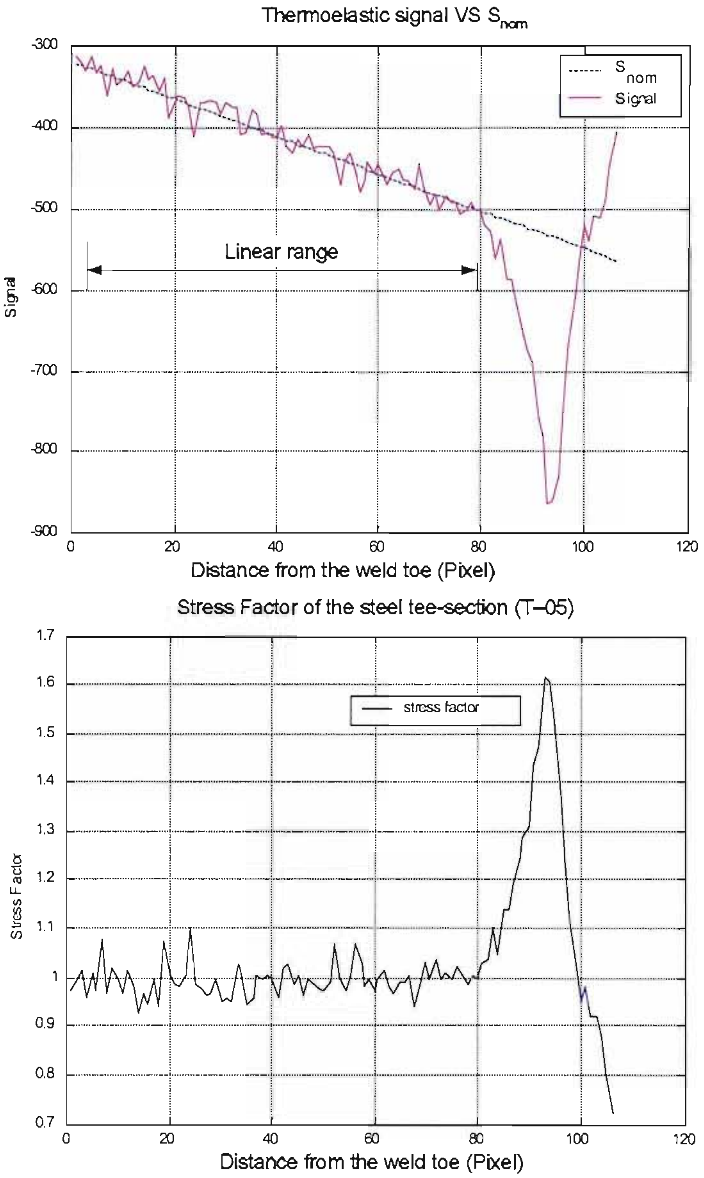

FIGURE A.10: Thermoelastic signal with an extrapolated line plot (top) and stress factor (bottom)

Appendix B

Technical drawings

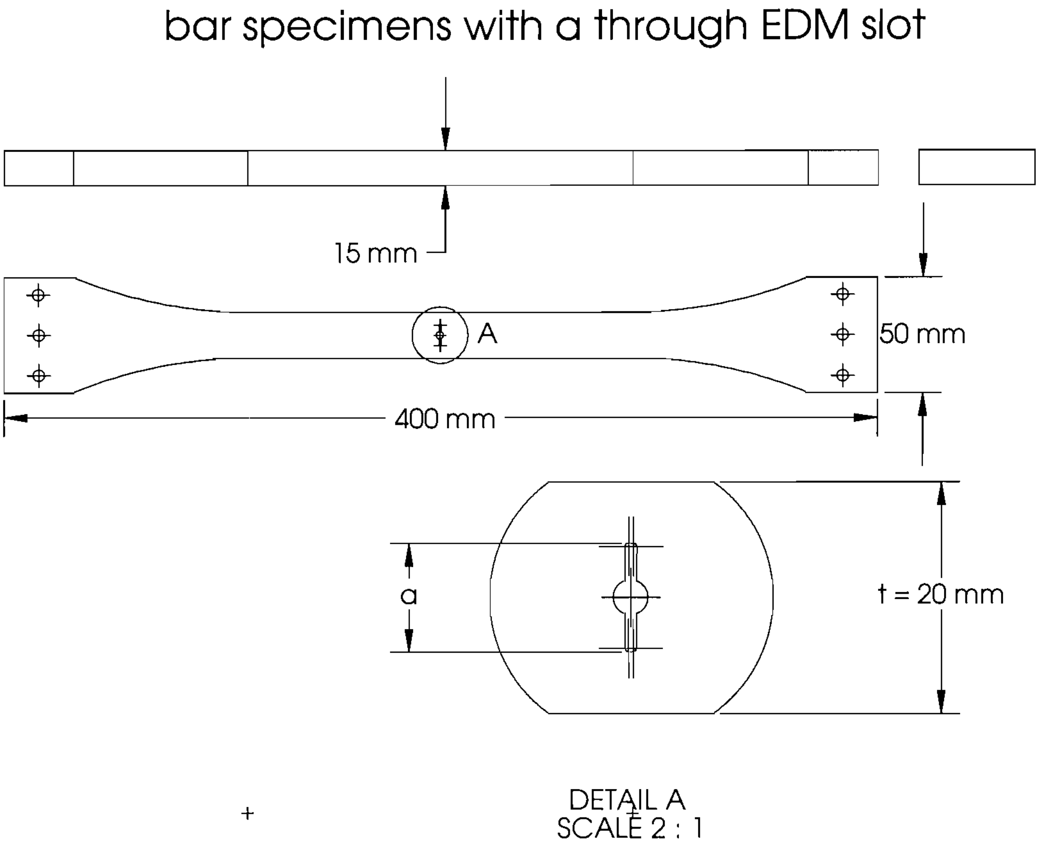

a/t	a (mm)
0.25	5
0.5	10
0.75	15

material	tip radius (mm)
aluminium	0.175
steel	0.175
PMMA	0.75

FIGURE B.1: Damaged beam specimen dimensions

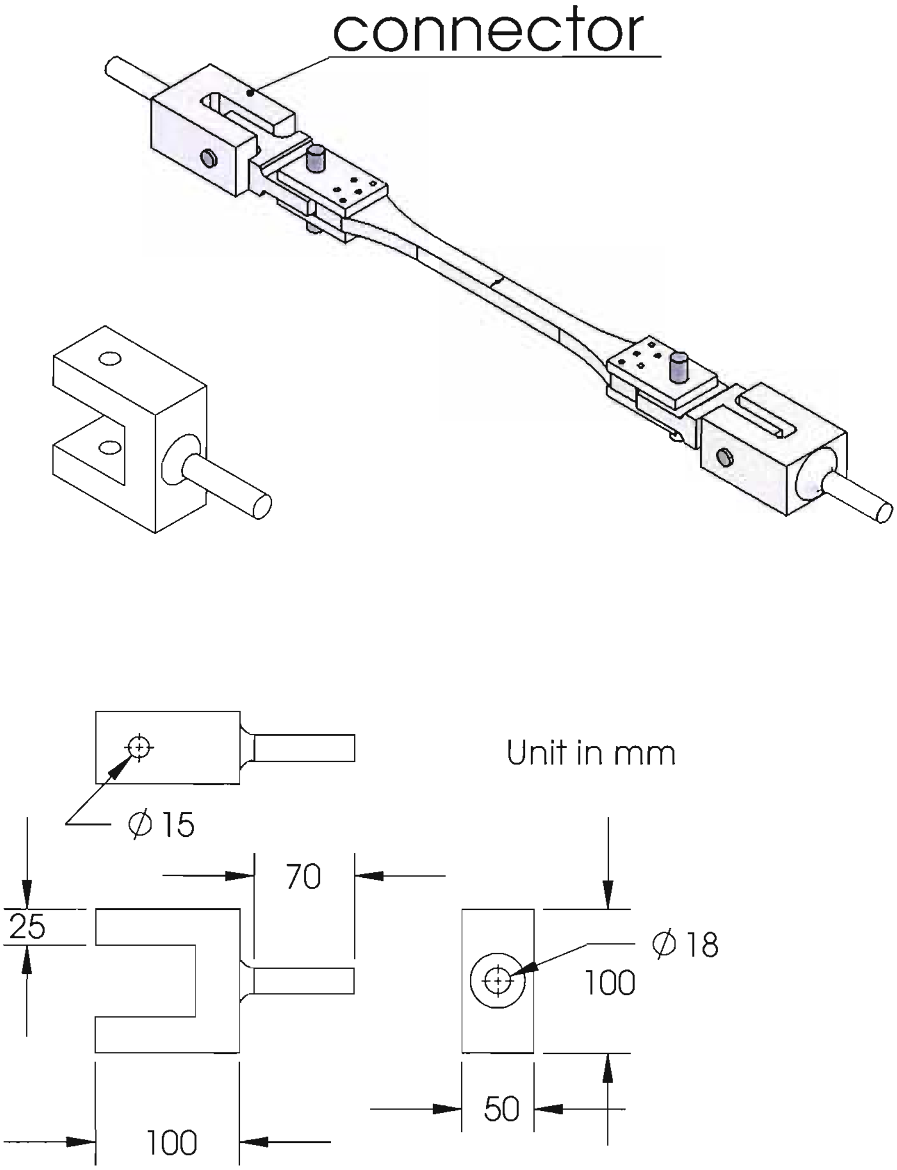

FIGURE B.2: connector

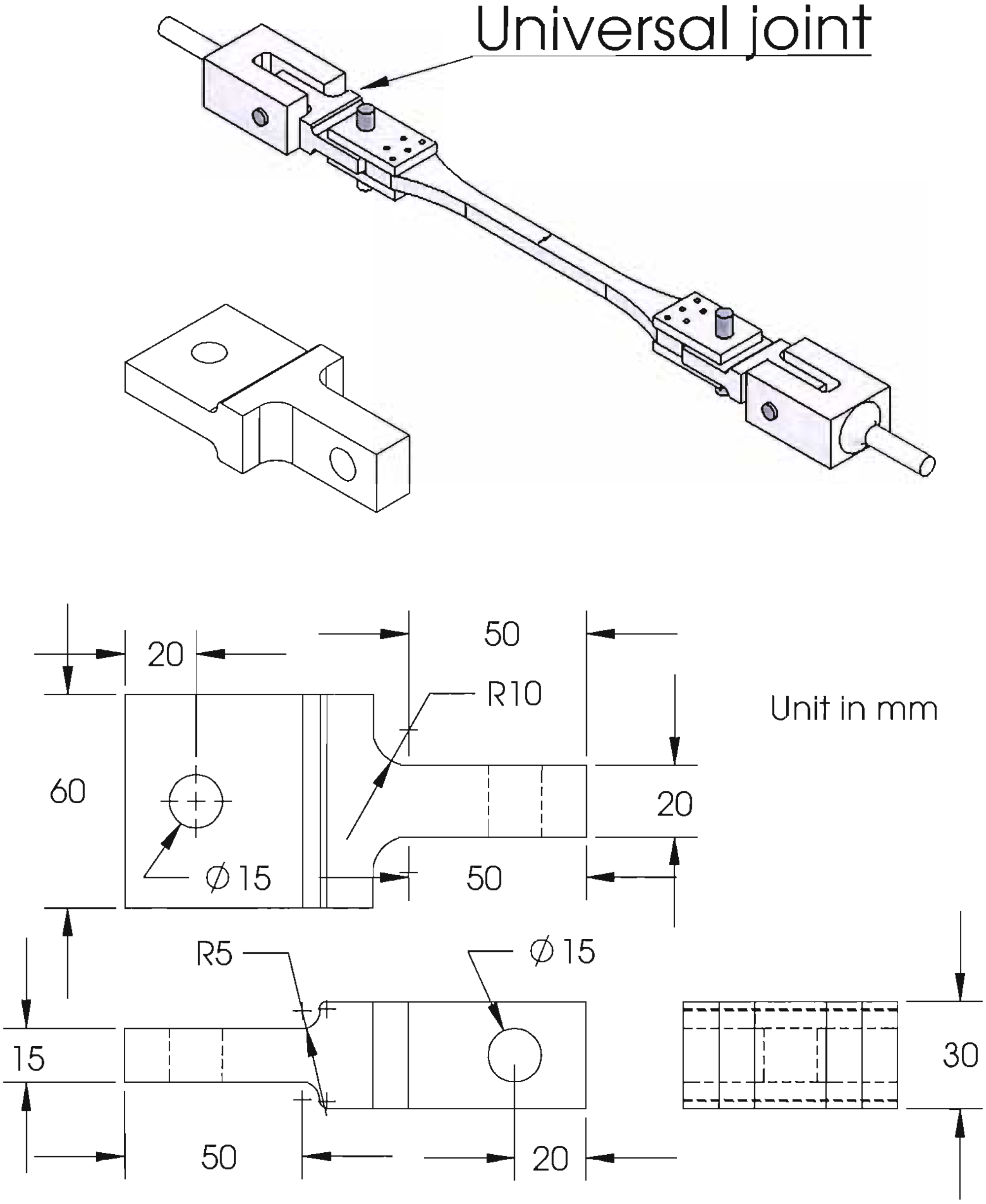

FIGURE B.3: Universal joint

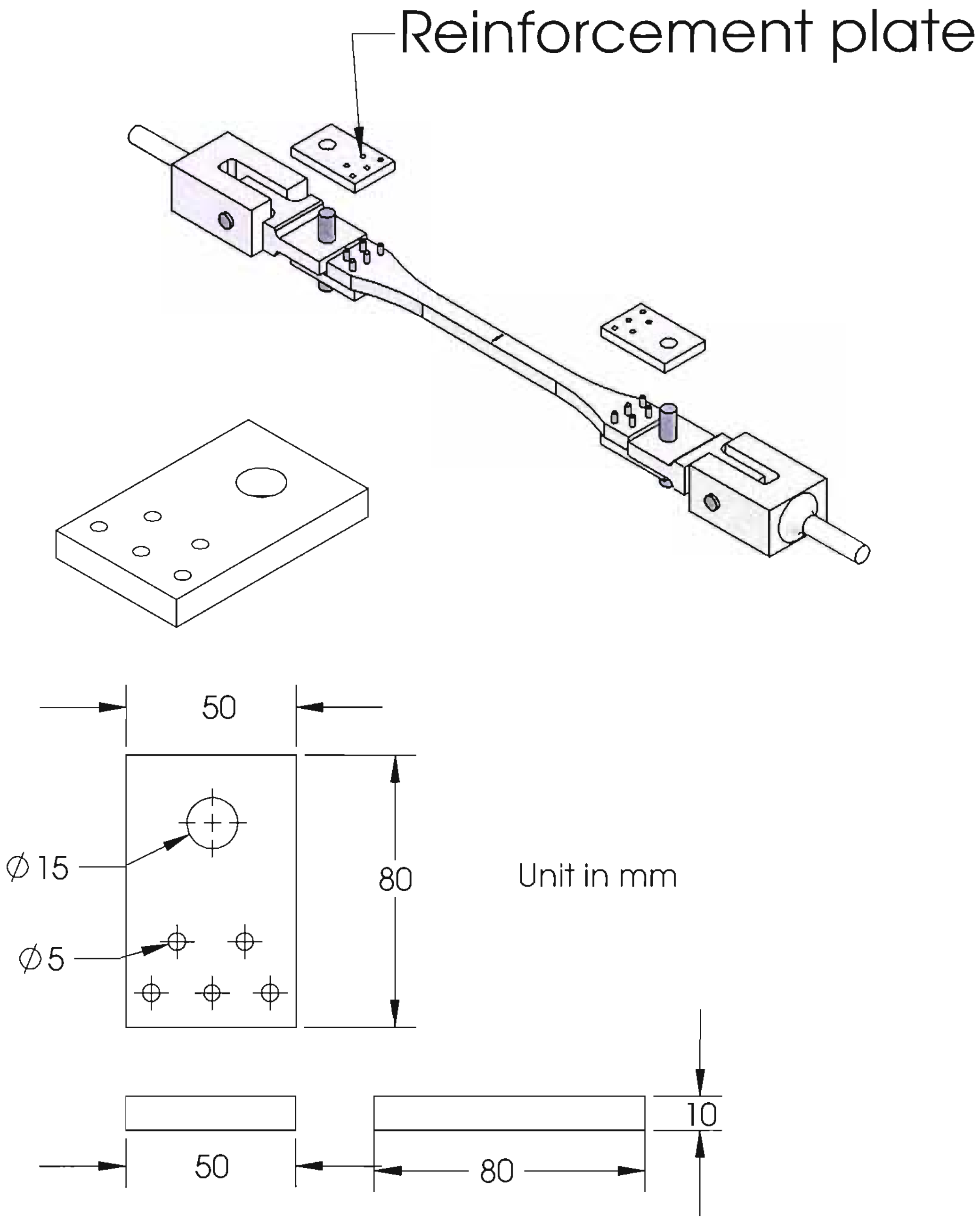

FIGURE B.4: Reinforcement plate

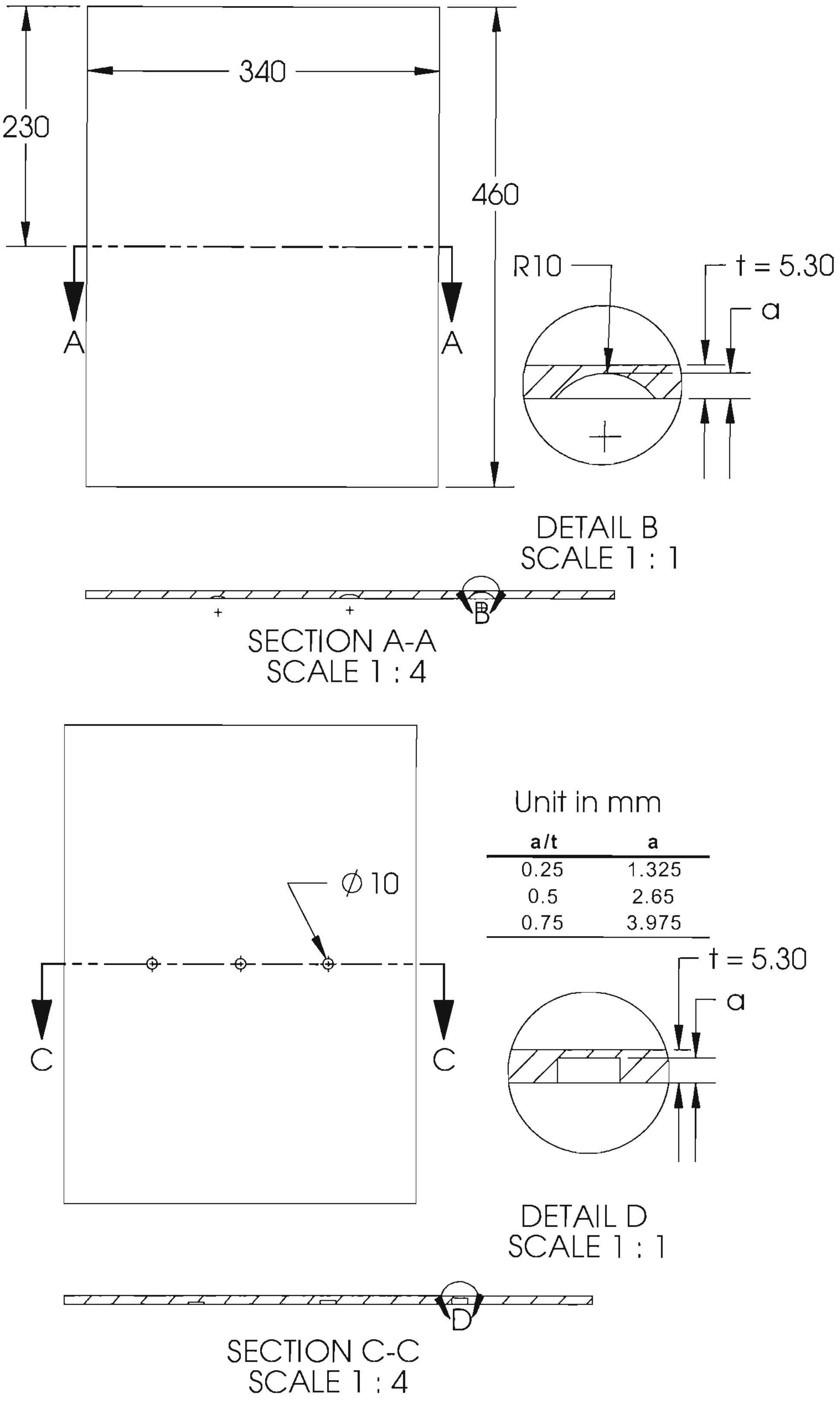

a/t	a
0.25	1.325
0.5	2.65
0.75	3.975

Figure B.5: Plate specimens: with semi-circular slots and with part-throug hole

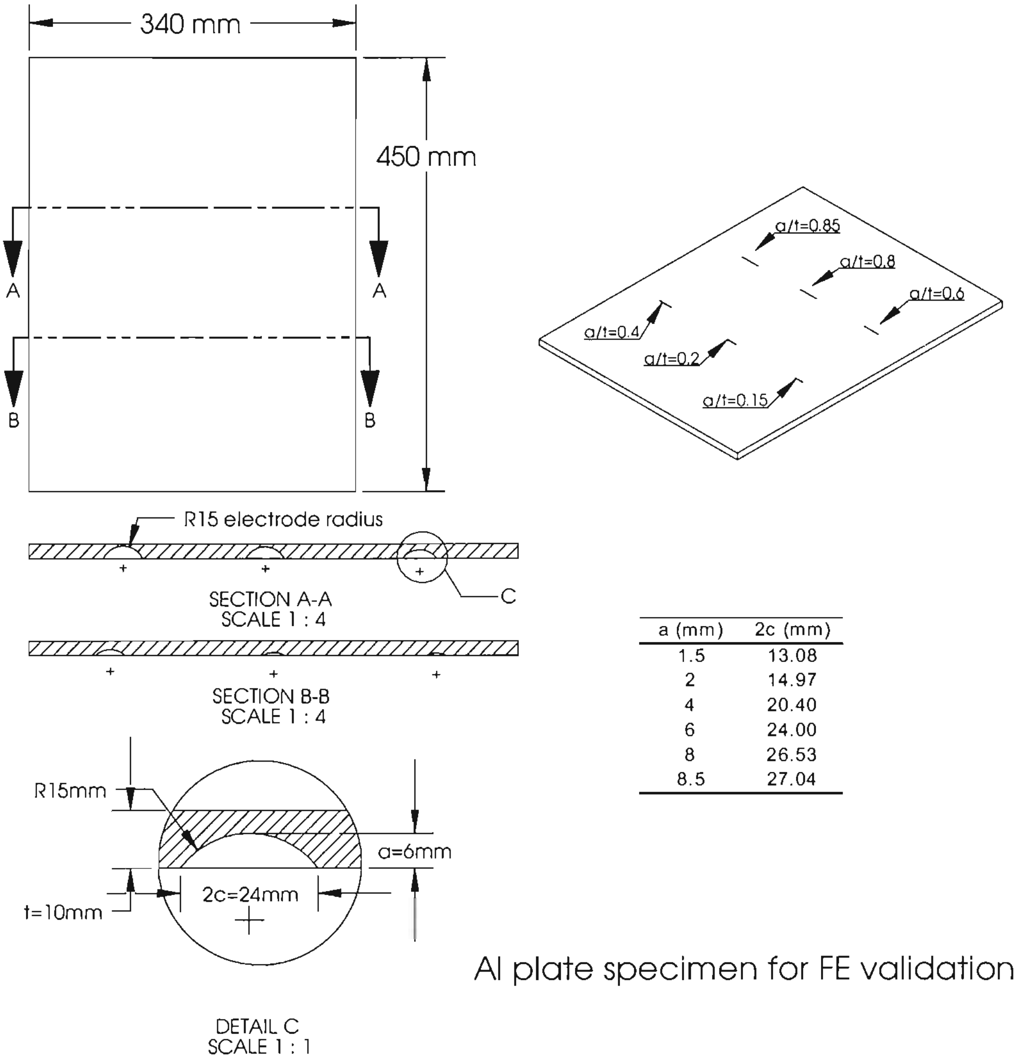

a (mm)	2c (mm)
1.5	13.08
2	14.97
4	20.40
6	24.00
8	26.53
8.5	27.04

FIGURE B.6: Al plate specimen with multiple damage for FE validation

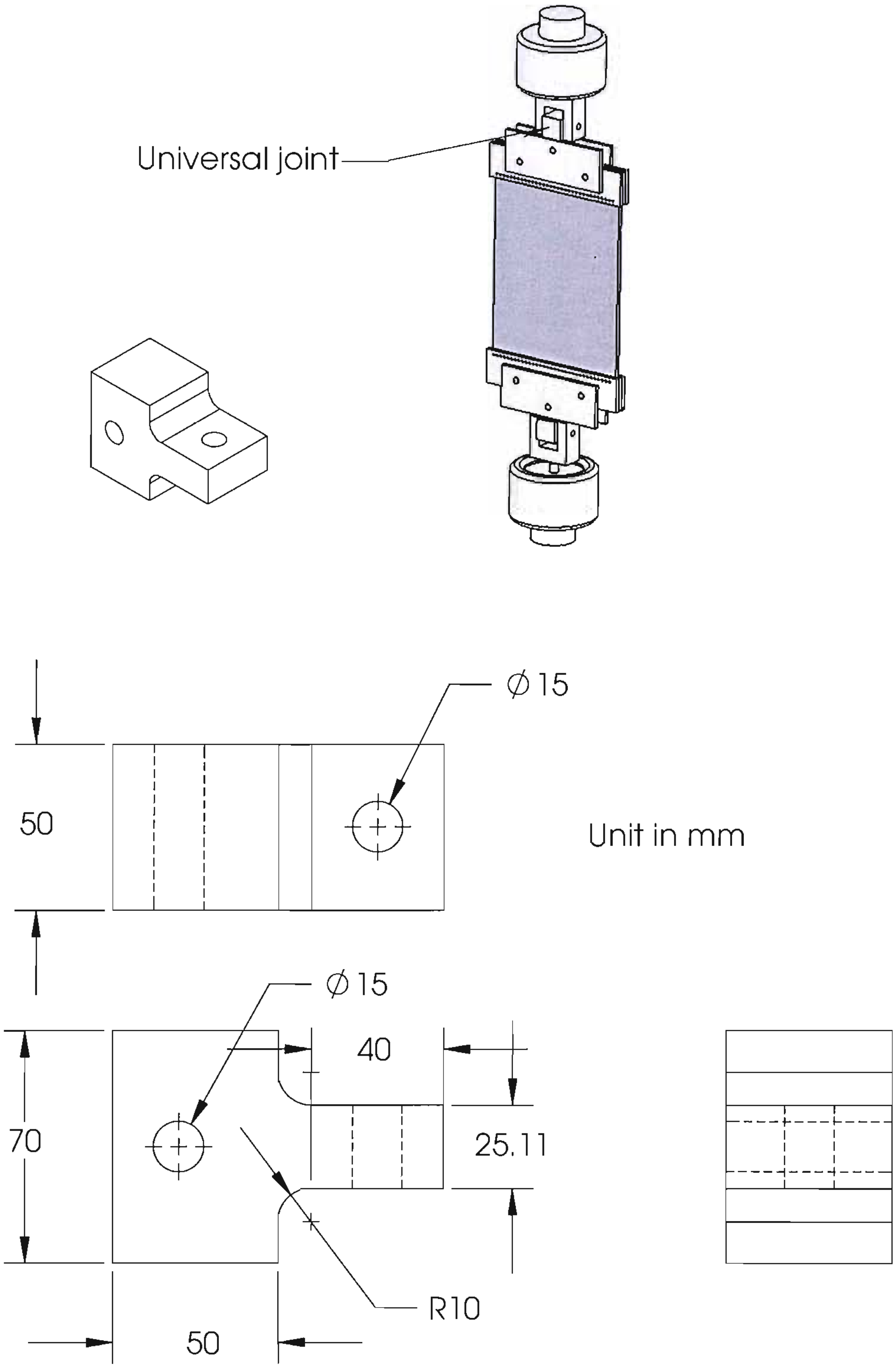

Figure B.7: Universal Joint

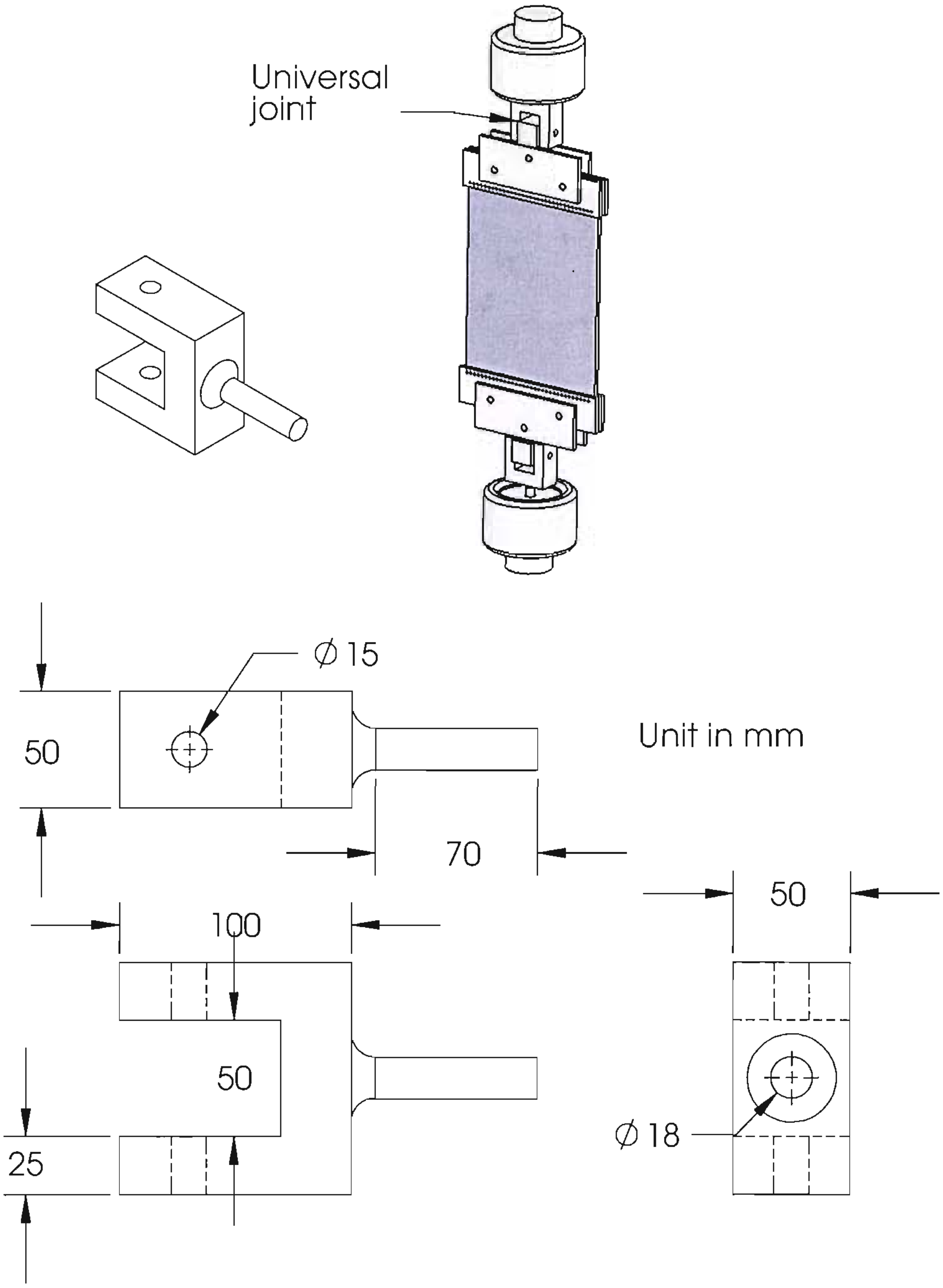

FIGURE B.8: Universal joint connector

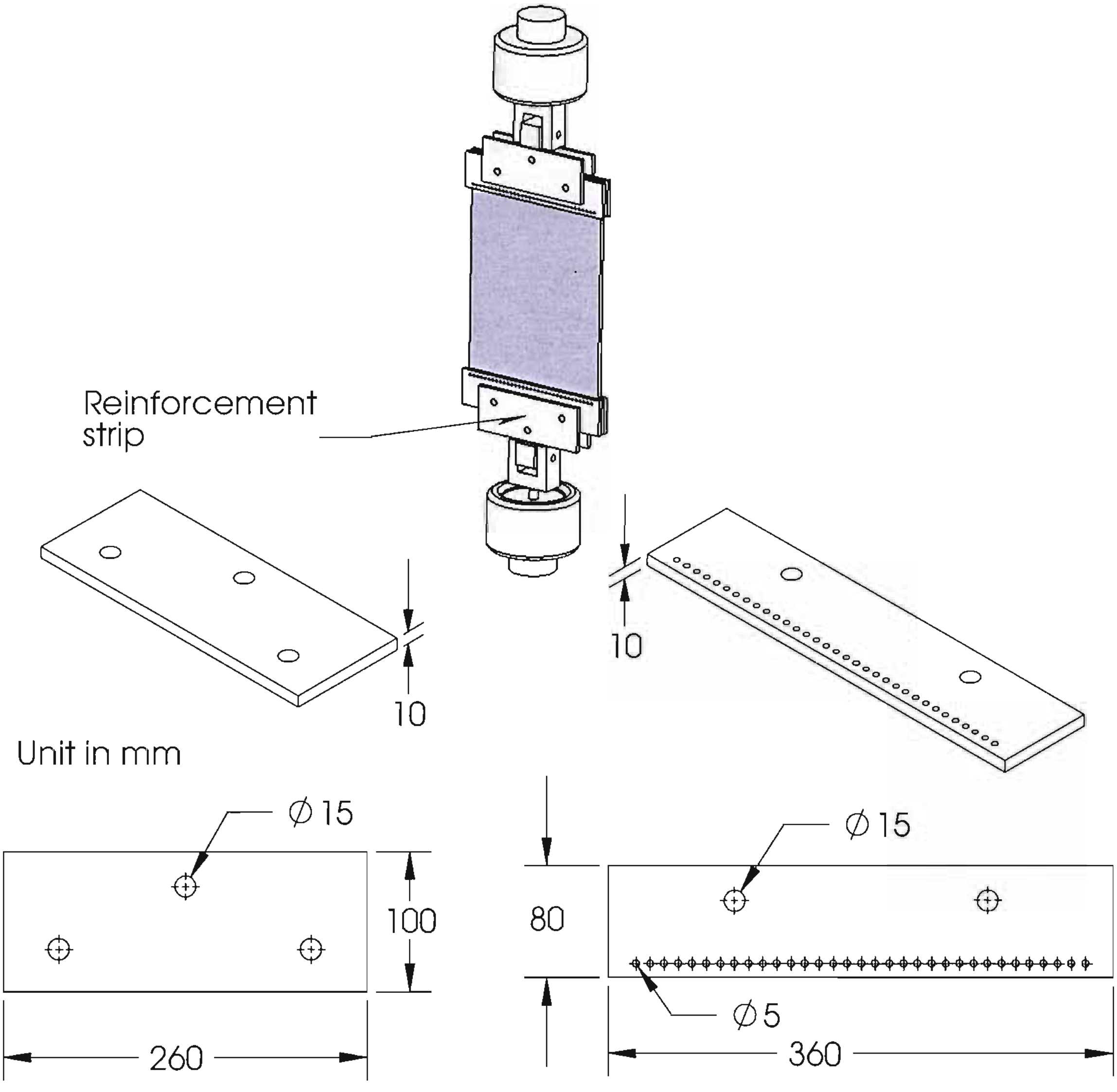

FIGURE B.9: Reinforcement strips

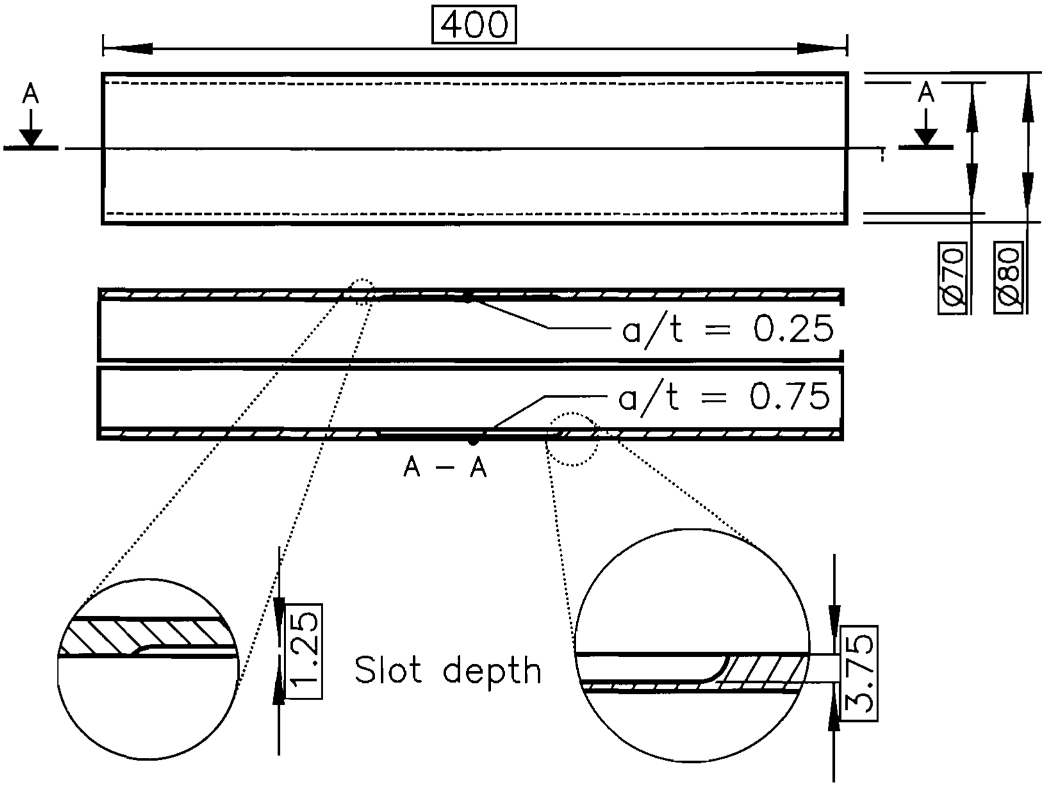

FIGURE B.10: Damaged pipe specimen dimensions

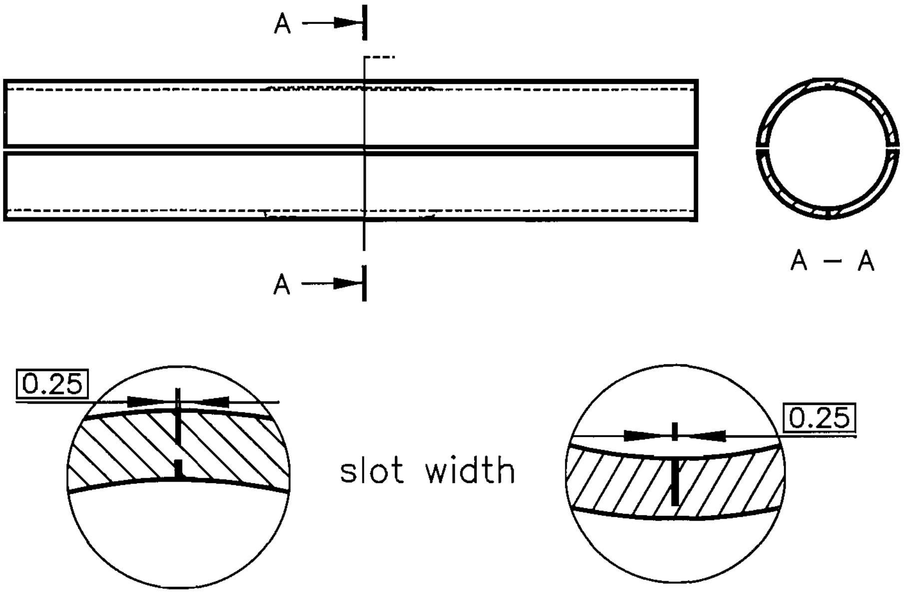

FIGURE B.11: Damaged pipe specimen dimensions

Appendix C

Publications

1. Sathon, N. and Dulieu-Barton, J.M. In Proceedings of the 12th International Conference on Experimenal Mechanics (ICEM12) Bari, Italy, 29th August - 2nd September 2004. McGraw Hill, 736-737.
2. Sathon, N. and Dulieu-Barton, J.M. (2005) Damage analysis of internal surface flaws using thermoelastic stress analysis. In Proceedings of the 6th International Conference on Damage Assessment of Structures (DAMAS 2005) Gdansk, Poland, 4th to 6th July 2005. Switzerland, Trans Tech Publications, 279-288. (Key Engineering Materials 293-294)